Wave motion in elastic enriched medias based on the second strain gradient formulation

Bo Yang

Numéro d'ordre NNT: 2022LYSEC016 Année: 2022

THESE DE DOCTORAT DE L'UNIVERSITÉ DE LYON
OPÉRÉE AU SEIN DE L'ÉCOLE CENTRALE DE LYON

ÉCOLE DOCTORALE MEGA

Mécanique, Enegétique, Génie civil et Acoustique

Spécialité: Mécanique

Soutenue le 09/05/2022 par

Bo YANG

Wave Motion in Elastic Enriched Medias Based on the Second Strain Gradient Formulation

---

Devant le jury composé de:

Mohamed Ali Hamdi	Professeur, UTC	Rapporteur
Najib Kacem	Maître de Conférence, FEMTO-ST, UFC	Rapporteur
Marie Annick Galland	Professeure, LMFA, ECL	Présidente
Christophe Droz	Chercheur, INRIA	Examinateur
Noureddine Bouhaddi	Professeur, FEMTO-ST, UFC	Invité
Mohamed Ichchou	Professeur, LTDS, ECL	Directeur
Abdelmalek Zine	Maître de Conférence, ICJ, ECL	Co-directeur

Acknowledgements

Foremost, I would like to thank all the professors of the defense committee, for their valuable help to this thesis. I would like to express the sincere gratitude to my supervisor Prof. Ichchou Mohammed for the continuous support of my Ph. D. research, for his patience, immense knowledge, motivation and enthusiasm. His guidance helped me in all the time of research and writing of this thesis.

I would also like to thank my co-supervisor Prof. Zine Abdelmalek, for offering me the professional guidance. Thanks for his warm support and encouragement in the last three years. Besides, I would like to express thanks to my co-advisor Prof. Droz Christophe. His dynamism, sincerity and motivation have deeply inspired me.

I am grateful to all of those with whom I have had the pleasure to work during my project. I would like to express my thanks to many colleagues in our laboratory LTDS in the last three years. Prof. Bareille Olivier, he helped me a lot for my comité de suivi de thèse. Pascal Fossat, he provided me with many valuable references and ideas for my Ph. D. research.

I thank my fellow labmates in LTDS: Cui Dongze, Zhang Xiaoyan, Wu Qichen, Li Xuefeng, Zhu Boyao, Shao Lun and Giulia Mazzeo, for the stimulating discussions, and for all the fun we have had in the last three years.

In the past three years, the care of my friends has made my life full of color. Dennis Adriao, without his support, I might lose the courage to smile at life. Liu Liqun and Yang Zihua, they came to Lyon with me together three years ago. We always encourage and help each other.

Nobody has been more important to me in the pursuit of my Ph. D. research than the members of my family. I would like to thank my parents, whose love and guidance are with me in whatever I pursue. They are the ultimate role models. Also, I wish to thank my little sister, Yang Meixia, and her husband, Xu Qin, who provide unending inspiration.

At last, I would like to acknowledge China Scholarship Council (CSC) for providing the funding source of my Ph. D. research.

Abstract

In this work, the Second Strain Gradient (SSG) theory proposed by Mindlin is used within a Wave Finite Element Method (WFEM) framework for dynamic analysis of enriched medias. Strong forms of continuum models including governing equations and boundary conditions for one-dimensional (1D) micro-sized Euler-Bernoulli bending beam and torsion bar are derived respectively by using Hamilton's principle. New "non-local" Lattice Spring Models (LSM) are expounded, giving unified description of the SSG models for bending and torsion. Weak forms for bending and torsion are established based on SSG theory. WFEM is used to formulate wave propagation characteristics of 1D periodic structures.

A two-dimensional (2D) micro-sized beam grid, which is restricted to out-of plane vibration, is introduced through SSG theory. The strong formulas of continuum model are derived. A valuable long-range LSM formed by interactions of nearest, next-nearest and next-next-nearest neighbors is elaborated. Weak formulas are established within the framework of SSG theory and the global dynamic stiffness matrix of a unit cell is assembled. The band structure and slowness surfaces, confined to the irreducible first Brillouin zone, are studied in frequency spectrum under WFEM. In addition, the energy flow vector fields and wave beaming effects are analyzed by SSG and Classical Theory (CT) of continuum mechanics.

The dynamical behaviors of a three-dimensional (3D) micro-sized slender beam are investigated. The constitutive relations of 3D micro-sized model are introduced within the SSG theory framework and the weak formulations including element stiffness, mass matrices and force vector are calculated. Free wave propagation characteristics are expressed by solving eigenvalue problems through the direct WFEM. Diffusion matrix for a simple coupling condition and a complex coupling condition are confirmed. Wave dispersion, diffusion including reflection and transmission are introduced.

The wave propagation characteristics in a micro-sized 2D full plate are predicted under SSG theory. An eigenvalue solving approach called Contour Integral (CI) method is applied to illustrate the Nonlinear Eigenvalue Problem (NEP) and to conform the band structure and iso-frequency contours. A Sensitivity Analysis (SA) is introduced to investigate the effects of higher order parameters on the dispersion relation.

Keywords: Micro-sized periodic structures; Second strain gradient theory; Wave finite element method; Wave propagation; Reflection and transmission

Résumé

Dans ce travail, la théorie du Second Strain Gradient (SSG) proposée par Mindlin est utilisée dans le cadre de la Wave Finite Element Method (WFEM) pour l'analyse dynamique de médias enrichis. Des formes fortes de modèles de continuum comprenant des équations gouvernantes et des conditions aux limites pour la unidimensionnelle (1D) de taille micro poutre de flexion Euler-Bernoulli et la barre de torsion sont dérivées respectivement en utilisant le principe de Hamilton. Un nouveau Lattice Spring Model (LSM) est présenté, donnant une description unifiée des modèles SSG pour la flexion et la torsion. Les formes faibles pour la flexion et la torsion sont établies sur la base de la théorie SSG. WFEM est utilisé pour formuler les caractéristiques de dispersion des ondes des structures périodiques 1D.

Une grille de faisceau bidimensionnelle (2D) de taille micro qui est limitée aux vibrations hors du plan est introduite par la théorie SSG. Les formules fortes du modèle continu sont dérivées. Un LSM à longue portée précieux formé par les interactions des voisins les plus proches, les plus proches et les plus proches est élaboré. Des formules faibles sont établies dans le cadre de la théorie SSG et la matrice de rigidité dynamique globale d'une maille élémentaire est assemblée. La structure de bande et les surfaces de lenteur, confinées à la première zone irréductible de Brillouin, sont étudiées en spectre de fréquence sous WFEM. De plus, les champs de vecteurs de flux d'énergie et les effets de faisceau d'ondes sont analysés par SSG et CT.

Les comportements dynamiques d'une poutre élancée tridimensionnelle (3D) de taille micro sont étudiés. Les relations constitutives du modèle 3D micro-taille sont introduites dans le cadre de la théorie SSG et les formulations faibles comprenant la rigidité des éléments, les matrices de masse et le vecteur de force sont calculées. Les caractéristiques de propagation des ondes libres sont exprimées en résolvant des problèmes de valeurs propres via le WFEM direct. La matrice de diffusion pour une condition de couplage simple et une condition de couplage complexe sont confirmées. La dispersion des ondes, la diffusion incluant la réflexion et la transmission sont introduites.

Les caractéristiques de propagation des ondes dans une plaque pleine 2D de taille microscopique sont prédites selon la théorie SSG. Une approche de résolution des valeurs propres appelée méthode Contour Integral (CI) est appliquée pour illustrer le problème des Nonlinear Eigenvalue Problem (NEP) et pour conformer la structure de la bande et les contours isofréquences. Une Sensitivity Analysis (SA) est introduite pour étudier les effets des paramètres d'ordre supérieur sur la relation de dispersion.

Mots-clés: Structures périodiques microscopiques; Second strain gradient theory; Wave finite element method; Propagation des ondes; Réflexion et transmission

Contents

Acknowledgements **i**

Abstract **iii**

Résumé **v**

List of abbreviations **xi**

Introduction **1**

1 Literature survey **5**
1.1 Introduction 5
1.2 Micro-sized periodic structures as a class of enriched medias 6
1.2.1 Engineering micro-sized periodic structures 7
1.2.2 Free wave propagation characteristics in periodic structures 7
1.3 Existing methods to study micro-sized structures 9
1.3.1 Non-classical continuum theories of elasticity 10
1.3.2 Lattice spring model theory 21
1.4 Existing methods to study periodic structures 24
1.4.1 Plane-wave expansion 24
1.4.2 Modified transfer matrix method 26
1.4.3 Wave finite element method 27
1.4.4 Model order reduction technique 34
1.4.5 Homogenization methods 35
1.5 Conclusions 37

2 Wave motion analysis of second strain gradient elasticity through a wave finite element approach for one-dimensional structures **39**
2.1 Introduction 39
2.2 Bending vibration analysis for Euler-Bernoulli beam 40
2.2.1 Continuum model by second strain gradient elasticity 40
2.2.2 Lattice spring model by second strain gradient elasticity 44

2.3 Torsional vibration analysis for a bar 46
2.3.1 Continuum model by second strain gradient elasticity 46
2.3.2 Lattice spring model by second strain gradient elasticity 49
2.4 One-dimensional wave propagation characteristics 50
2.5 Numerical applications and discussions 51
2.5.1 Bending vibration of Euler-Bernoulli beam 51
2.5.2 Torsional vibration of a bar 55
2.6 Conclusions 58

3 Multi-scale modelling based on second strain gradient elasticity for a two-dimensional beam grid 59
3.1 Introduction 59
3.2 Strong formulas for out-of plane vibration 60
3.2.1 Continuum model by second strain gradient elasticity 60
3.2.2 Lattice spring model by second strain gradient elasticity 61
3.3 Wave finite element method for 2D structures 62
3.3.1 Finite element procedure 62
3.3.2 2D wave propagation analysis 64
3.4 Numerical examples and discussions 65
3.4.1 Band structure 66
3.4.2 Slowness surfaces 67
3.4.3 Energy flow vector fields 68
3.4.4 Wave beaming effects 70
3.4.5 Wave shapes 74
3.5 Conclusions 75

4 Numerical investigation on multi-mode propagation and diffusion in a three-dimensional beam 77
4.1 Introduction 78
4.2 Second strain gradient theory for 3D model 78
4.2.1 Calculation of constitutive relations 78
4.3 Discretization and element matrices 80
4.4 Diffusion calculation based on second strain gradient elasticity 82
4.4.1 Diffusion with simple coupling condition 83
4.4.2 Diffusion with complex coupling condition 84
4.5 Numerical applications and discussions 86
4.5.1 Dispersion relation 87
4.5.2 Effects of higher order parameters 88

4.5.3 Diffusion through a simple coupling element 91
4.5.4 Diffusion through a complex coupling element 92
4.5.5 Forced response 93
4.5.6 Wave shapes 94
4.6 Conclusions 95

5 Dynamic and sensitivity analysis of a two-dimensional full plate 97
5.1 Introduction 97
5.2 2D wave propagation analysis 98
5.2.1 Inverse form of 2D wave finite element method 98
5.2.2 Direct form of 2D wave finite element method 98
5.2.3 Sound transmission by second strain gradient elasticity 101
5.2.4 Numerical simulations of a 2D full plate 103
5.3 Sensitivity analysis of higher order parameters 109
5.3.1 Fourier amplitude sensitivity test formulation 109
5.3.2 Numerical applications of sensitivity analysis 111
5.4 Conclusions 117

6 Conclusions and perspectives 119
6.1 Conclusions 119
6.2 Perspectives 120

Appendix A Expressions of the coefficients A, B and C in Eq.1.68 123

Appendix B Transform the bending LSM to continuum model 125

Appendix C Governing equation and associated boundary conditions of a torsional bar by SSG theory 127

Appendix D LSM vibration analysis for torsion 129

Appendix E The wave shapes in Chapter 3 131

Appendix F Definition of matrices A, B and C in Chapter 4 133

List of figures 137

List of tables 141

Bibliography 142

List of abbreviations

- CI: Contour Integral
- CT: Classical Theory of continuum mechanics
- CMS: Component Mode Synthesis
- DMM: Diffusion Matrix Method
- DOF: Degree of Freedom
- FAST: Fourier Amplitude Sensitivity Test
- FASTC: Fourier Amplitude Sensitivity Test with Correlation
- HFEM: Hierarchical Finite Element Method
- IBZ: Irreducible Brillouin Zone
- κ-space: Wavenumber space
- LSM: Lattice Spring Model
- MOR: Model Order Reduction
- MCS: Modified Couple Stress theory
- NEP: Nonlinear Eigenvalue Problem
- NSD: Normalized Standard Derivation
- PCs: Phononic Crystals
- SG: First Gradient Theory of Elasticity
- SSG: Second Gradient Theory of Elasticity
- SA: Sensitivity Analysis
- SFE: Spectral Finite Element
- SAFE: Semi-Analytical Finite Element
- TMM: Transfer Matrix Method
- TSI: Total Sensitivity Index
- WFEM: Wave Finite Element Method
- 1D: One Dimension
- 2D: Two Dimension

Introduction

Enriched medias are a class of medias with local mechanical behavior, global mechanical behavior, heterogeneity and size effects caused by multi scale features. As the typical enriched medias, periodic structures which are constructed by repeating a basic unit cell to form regular patterns are widely used in engineering fields. Initially, studies focused on the field of solid-state physics at macro-sized level based on Classical Theory (CT) of continuum mechanics. For example, the characteristics of fatigue issues and acoustic radiation for periodic systems need to be known in engineering applications. The study of maximizing and localizing band gaps or stop bands in some specific frequency ranges has also attracted many researchers.

But for the micro-sized structures (e.g., periodically positioned nano-sized Silicon resonator and nanobio-sensors) with size effects caused by multi scale features, long-range or non-local interaction between micro-particles is an important feature in the structure's deformation process. On the other hand, the micro-displacements such as micro-rotation, micro-stretch caused by micro-material can influence the mechanical behavior of micro-structure. What is more, due to the very large ratio between the surface and volume of micro-structure, the surface tension, produced by atoms with associated energy on the free surface, has a significant effect on the micro-structure's behavior. Last, the characteristic length scales associated with conventional $Lam\acute{e}$ parameters and additional higher order parameters can generate higher order deformations in the micro-structure. These properties of micro-structure can no longer be reasonably explained by CT.

Therefore, the non-classical continuum theories of elasticity that can interpret the properties of micro-sized structures have been proposed. Generally, these non-classical continuum theories of elasticity can be categorized into non-local elasticity theory, micro-continuum theory, surface elasticity theory and strain gradient family. Mindlin established one of the strain gradient theories called First Strain Gradient (SG) theory in which the potential energy density composed of strain and first gradient of strain is considered, but only for micro-sized noncentro-symmetric materials. In order to explore the properties of centro-symmetric materials, the Second Strain Gradient (SSG) theory was put forward, which offers a reasonable explanation for the transforming of strain or tension on a solid plane surface. The potential energy density in SSG theory is a function of strain, first gradient of strain and second gradient of strain. The

equilibrium equation is a high order partial differential function with classical and non-classical boundary conditions.

In order to derive the mathematical and mechanical models including governing equations and boundary conditions for micro-sized structures, the continuum theories are widely used. On the other hand, Lattice Spring Model (LSM) theory is also a valuable approach to interpret the dynamic characteristics for micro-sized medias. The continuum equation of motion with derivatives can be determined by long-range interactions in LSM.

However, there exist difficulties to interpret the physical properties of complex periodic structures through analytical solutions, especially for the micro-sized medias. Therefore, the numerous methods such as Finite Element Method (FEM) have been established to study the homogeneous or periodic structures. But the whole structure needs to be meshed, which requires excessive computing time. Subsequently, a Wave Finite Element Method (WFEM) that can effectively avoid the above defect has been proposed based on the periodic structures theory. The view of WFEM is to reduce a global periodic structure into a single substructure or unit cell. The resulting stiffness and mass matrices are post processed to offer the dynamic stiffness matrix. The dynamical properties of the periodic structure can be reflected through the spectral analysis of the unit cell.

Thesis contributions

The main contributions of the work in this thesis are:

1. The SSG theory is used within WFEM framework for dynamic analysis of 1D Euler-Bernoulli bending beam and torsional bar. Strong forms of continuum models including governing equations and boundary conditions for bending and torsion cases, respectively, are derived using Hamilton's principle. New "non-local" LSM are expounded, giving unified description of the SSG models for bending and torsion.

2. The dynamical properties of a 2D micro-sized beam grid, which is restricted to out-of plane vibration, are analyzed. Weak formulas including element stiffness and mass matrices are established within the framework of SSG theory and the global dynamic stiffness matrix of a unit cell is assembled. The WFEM is applied for the vibrational analysis of 2D periodic wave-guides.

3. The multi-mode propagation and diffusion of a 3D micro-sized beam are illustrated.

The constitutive relation of 3D model is introduced. The displacement vector is derived by employing the six quintic Hermite polynomial shape functions. The weak formulations including element stiffness, mass matrices and force vector are calculated. The dynamical characteristics such as dispersion relations, forced response are analyzed. Wave diffusion under a simple coupling condition and a complex coupling condition is introduced by SSG theory.

4. The WFEM is used to predict wave propagation characteristics in a micro-sized 2D full plate through SSG theory. An eigenvalue solver based on the Contour Integral (CI) method is applied to confirm the dispersion relations under different wave propagation directions.

5. A Sensitivity Analysis (SA) is performed on a 2D full plate to investigate the effects of higher order parameters on the models outputs such as dispersion relation. These parameters are associated with the non local characteristics of micro-sized structure. Statistics of the output set and SA results with correlated inputs are discussed through SSG theory.

Thesis outline

Chapter 1 presents the results of the conducted literature survey. The survey concerns the review of previous researches on enriched medias, of existing methods on the studying of micro-sized medias. The existing methods for studying micro-sized structures including continuum model and LSM are introduced. What is more, the plane wave expansion, modified Transfer Matrix Method (TMM), WFEM, Model Order Reduction (MOR) method and homogenization methods are discussed for the research of periodic structures.

Chapter 2 provides a method which combines SSG theory with WFEM to analyse the dynamic behavior of 1D micro-sized structures. A continuum model for Euler-Bernoulli bending beam and torsional bar are introduced by SSG theory. The strong forms including governing equations and boundary conditions are illustrated by applying the variation method. The LSMs of a micro-sized Euler-Bernoulli bending beam and torsional bar are discussed, respectively. After Fourier series transforming, the continuous governing equations of motion are determined and the variational, or weak, formulations are then calculated. The dispersion relations and forced responses for bending and torsion in micro-sized structures are calculated by SSG theory.

Chapter 3 illustrates the dynamical behaviors of a 2D beam grid within the WFEM framework. The analysis is restricted to out-of plane vibration including bending and torsion. The

weak formulas of an element are illustrated and the global dynamic stiffness matrix of a unit cell is assembled. WFEM inverse form for 2D periodic systems is introduced. Dynamic behaviors of the beam grid such as band structure, slowness surfaces, energy flow vector fields and wave beaming effects are discussed.

Chapter 4 investigates the dynamical behaviors of a 3D slender beam. The constitutive relations of 3D micro-sized model are introduced within the SSG theory framework and the weak formulations including element stiffness, mass matrices and force vector are calculated. Afterwards, free wave propagation characteristics are expressed by solving eigenvalue problems in the direct WFEM framework, diffusion matrix for a simple coupling condition and a complex coupling condition are confirmed. Wave dispersion and diffusion, effects of higher order parameters and forced response are introduced.

Chapter 5 predicts the wave propagation characteristics in a micro-sized 2D full plate under SSG theory. An eigenvalue solving approach called CI method is applied to illustrate the Nonlinear Eigenvalue Problem (NEP) and to conform the band structure and iso-frequency contours. A SA method is introduced for this 2D full plate to investigate the effects of higher order parameters on the dispersion relation.

Finally, the conclusions and perspectives are drawn in chapter 6.

Chapter 1

Literature survey

Chapter contents

1.1 Introduction 5
1.2 Micro-sized periodic structures as a class of enriched medias 6
1.2.1 Engineering micro-sized periodic structures 7
1.2.2 Free wave propagation characteristics in periodic structures 7
1.3 Existing methods to study micro-sized structures 9
1.3.1 Non-classical continuum theories of elasticity 10
1.3.2 Lattice spring model theory 21
1.4 Existing methods to study periodic structures 24
1.4.1 Plane-wave expansion 24
1.4.2 Modified transfer matrix method 26
1.4.3 Wave finite element method 27
1.4.4 Model order reduction technique 34
1.4.5 Homogenization methods 35
1.5 Conclusions 37

1.1 Introduction

Periodic structures as the typical enriched medias are widely applied in engineering fields. The dynamical properties of periodic structures have been studied over the past decade especially in the field of acoustics and electromagnetic. Initially, studies focused on the solid-state physics at macro-sized level based on CT of continuum mechanics [1, 2]. But for the micro-sized structures, it is well known that one of their noticeable features is size-dependent mechanical behavior [3, 4], which can not be observed in macro-structures. CT fails to describe those

physical phenomena in which non-local or long-range interaction plays a non-negligible role in the deformation process.

The chapter begins with a review about the studies on micro-sized periodic structures, which is then followed by a literature survey of engineering application and wave propagation characteristics. Subsequently, attention is paid on existing methods of studying the micro-sized structures by continuum model and LSM. Finally, the plane wave expansion, modified TMM, WFEM, MOR method and homogenization methods are discussed for the research of periodic structures.

1.2 Micro-sized periodic structures as a class of enriched medias

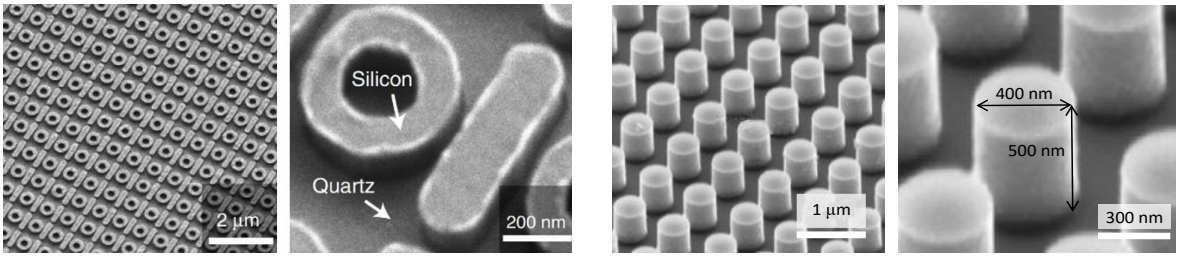

(a) Each unit cell is composed of a ring and a bar. (b) Each unit cell is composed of a cylinder.

Fig. 1.1. Periodically positioned nano-sized Silicon resonators [5].

Mechanical periodic mediums consist of macro-sized periodic structures and micro-sized periodic structures. The macro-sized periodic structures include Phononic Crystals (PCs), com-

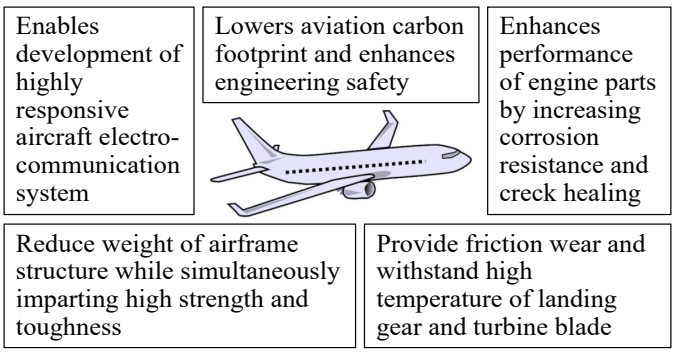

Fig. 1.2. Nano-coatings for aerospace materials [6].

posite sandwich panels, stiffened plates, truss beams, perforated plate, multi-story building and multi-span bridges, periodic foundation for buildings and so on. The micro-sized periodic structures include nano-sized PCs, periodically positioned nano-sized Silicon resonator [5], nano-coatings [6] and so on.

1.2.1 Engineering micro-sized periodic structures

Lots of structures employed in various engineering domains can be considered as micro-sized periodic. For example, as shown in Fig.1.1, the periodically positioned nano-sized Silicon resonators which are applied in nano-sensors for detection of atoms / molecules, nano-pumping devices for molecular transportation. The advantages of nano-resonators are low cost, earth-abundant and very small or even negligible light energy losses, as well as the ultra-high frequency, high sensitivity and high stability.

On the other hand, the micro-sized material can be used in aerospace, as shown in Fig.1.2, the nano-coating with ample benefits: First, enables development of highly responsive aircraft electro-communication system. Second, reduce weight of airframe structure while simultaneously imparting high strength and toughness. Third, provide friction wear and withstand high temperature of landing gear and turbine blade. Fourth, enhances performance of engine parts by increasing corrosion resistance and creak healing. Last, lowers aviation carbon footprint and enhances engineering safety.

Micro-sized structures have been widely investigated for their dynamic behaviors [7–9]. Initially, the research of micro-structures was mainly focused on stop band phenomena. Then, attention was devoted to wave propagation within the pass bands, such as negative refraction, super-lens effects, acoustic cloaks. The exploration for quantum spin Hall effect [10] and topological insulators [11] has become a hot spot for current research.

1.2.2 Free wave propagation characteristics in periodic structures

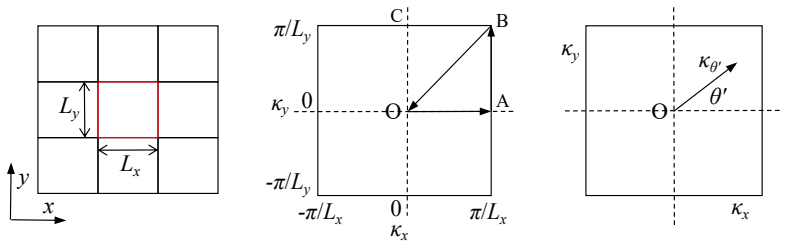

(a) A unit cell in the 2D periodic structure. (b) The first Brillouin zone and IBZ (O–A–B–O). (c) Plane wave.

Fig. 1.3. A unit cell in the 2D periodic structure and its first Brillouin zone.

The Bloch wave theory, used in the photonics crystal and quantum mechanics, has been widely applied in engineering periodic structures [12]. The description of free wave propagation characteristics is the following: The periodic reciprocal lattice can restrict wave vectors in certain regions of the reciprocal lattice called first Brillouin zone [13]. As a result, wave vectors can be expressed in terms of the reciprocal lattice basis. Fig.1.3(a) illustrates a unit cell in 2D periodic structure with size $L_x \times L_y$. The behaviour is usually described using propagation

constants λ_x and λ_y which are related to the wavenumbers κ_x and κ_y in following manner:

$$\begin{aligned} \lambda_x &= e^{-\mathrm{i}\kappa_x L_x}, \\ \lambda_y &= e^{-\mathrm{i}\kappa_y L_y}. \end{aligned} \tag{1.1}$$

The wave-numbers κ_x and κ_y change within the first Brillouin zone $[-\pi/L_x, \pi/L_x]$ and $[-\pi/L_y, \pi/L_y]$ and are discretised into (κ_x^i, κ_y^j), with κ_x^i being the i-th term, κ_y^j being the j-th term. Due to the symmetric properties in the reciprocal lattice, the wave vectors may be restricted to the Irreducible Brillouin Zone (IBZ) as presented in Fig.1.3(b). In some descriptions of the free wave propagation characteristics, the free wave propagates along the contour of IBZ (O-A-B-O) is considered. The plane wave propagates with wave-number $\kappa_{\theta'}$ in angle θ' as shown in Fig. 1.3(c). The $\kappa_{\theta'}$ can be described as:

$$\begin{aligned} \kappa_x &= \kappa_{\theta'} \cos\theta', \\ \kappa_y &= \kappa_{\theta'} \sin\theta'. \end{aligned} \tag{1.2}$$

Furthermore, The band structure, formed by the wave number with respect to frequency along the contour of IBZ, represents the backbone of electronic structure theory [14]. In mechanics, a band structure is a description of dispersion relation reflecting the property of free wave propagation in an elastic (or acoustic) structure. For 1D periodic structures, the term "dispersion relation" is employed and the free wave propagates along one direction only. For 2D periodic structures, "band structure" is utilized and the free wave propagates along two directions.

There exist some important features in dispersion relation or band structure. First is the stop bands of the propagation. In periodic structures and phononic materials, the wave has the filtering property. Elastic/acoustic waves cannot propagate freely within some frequency ranges, which are called stop bands or band gaps. In solid-state physics, a stop band, also called an energy gap, is an energy range in a solid where no electronic states can exist. In graphs of the electronic band structure of solids, the stop band generally refers to the energy difference between the top of the valence band and the bottom of the conduction band in insulators and semiconductors. It is the energy required to promote a valence electron bound to an atom to become a conduction electron, which is free to move within the crystal lattice.

For 2D periodic structures, the stop band can be complete or partial, a partial stop band is a frequency range where waves can not propagate in certain directions, the phenomenon is known also as wave beaming effect [1]. Bragg Scattering and Local Resonance are two types of stop bands in the periodic structures. Bragg scattering stop band is due to the spatial periodicity of impedance mismatch. It appears when wavelengths are on the same order as period length. In contrary, local resonance stop band depend on the properties of local resonator but not on the period length. It can lie in sub-wavelength regime whereby waves with wavelengths larger than

unit cell will be prohibited from propagation.

1.3 Existing methods to study micro-sized structures

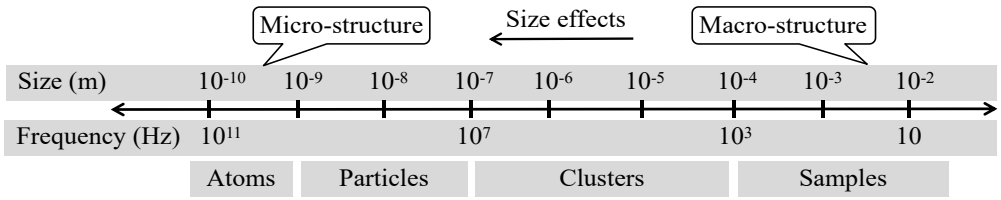

Fig. 1.4. Structures of different sizes and the size effects.

The size effect, as shown in Fig. 1.4, is a noticeable feature in micro-scale structures [3, 4]. Firstly, due to the large surface-volume ratio, micro-particles such as atoms with associated energy on the surface of the micro-structure can produce surface tension. Secondly, in addition to the macro-displacements caused by the macro-material, the micro-displacements caused by micro-material in the structure also have important influences on the structure's mechanical behavior. What is more, besides local interactions, there exist non-local or long-range interactions between micro-particles in the micro-structure. Last, the existence of characteristic length scales in the micro-structure can generate higher order deformations. CT of continuum mechanics can not describe these physical phenomena reasonably. Therefore, non-classical continuum

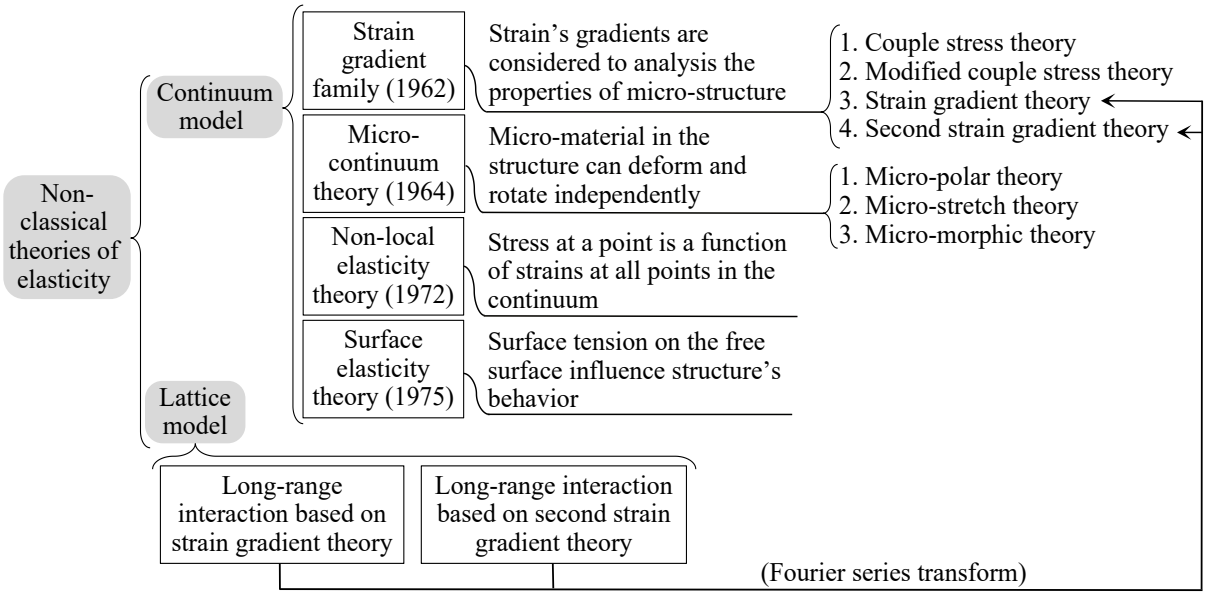

Fig. 1.5. Existing methods to study micro-sized structures.

theories of elasticity and LSM theories that can interpret the properties of micro-sized structures have been proposed. The classification of non-classical theories of elasticity is shown in Fig. 1.5 with basic concepts.

1.3.1 Non-classical continuum theories of elasticity

In order to explore the mechanism of size-dependent behaviors for micro-sized media or structures, several non-classical continuum theories of elasticity are proposed. Generally, these theories can be categorized into strain gradient family [15–17], micro-continuum theory [18, 19], non-local elasticity theory [20–22] and surface elasticity theory [23, 24].

1.3.1.1 Strain gradient family

Strain gradient family can be categorized into couple stress theory, modified couple stress theory, SG theory and SSG theory. In the couple stress theory, the non-independent gradient of rotation vector from macro-material in the structure is considered in the strain energy. By modifying the couple stress theory, the modified couple stress theory is confirmed, in which an equilibrium condition of moments is introduced to achieve the symmetrization of couple stress tensor. The SG theory considers the non-independent first gradient of strains from macro-material in the structure. The SSG theory considers both the non-independent first and second gradients of strains from macro-material in the structure.

(1) Couple stress theory

The couple stress theory was put forward by Toupin [25], in which the deformation metrics include conventional strains from macro-material and non-independent macro-rotation from macro-material in the structure. Many articles have focused on the research of couple stress theory. For example, Najafzadeh [26] introduced the torsional vibration of the porous nano-tube with an arbitrary cross-section based on couple stress theory. The novelty of his work is to present a solution by taking into account the existence of porosity. Wang [27] derived the elastic seismic wave equation through couple stress theory and compared the mathematical expression from couple stress theory with that of the conventional elastic wave equation. Fan [28] illustrated a Love wave dispersion equation by the couple stress theory for a new physical configuration. The result shows that couple stress theory solution is simple and has a great potential to be employed in the much more complex multifactor problems. By employing couple stress theory and micro-rotatory inertia, the elasto-dynamic fields of an anti-plane shear wave in nano-fiber was studied by Shodja [29]. It shows that the inclusion of micro-rotatory inertia term gives rise to the dynamic characteristic length, in addition to just the static characteristic length in the usual couple stress theory. What is more, Ghodrati [30] investigated Lamb wave propagation in a homogeneous and isotropic non-classical nano-plate. In this plate with constant thickness, the results match to CT by increasing the thickness to characteristic length ratio, and wave propagation speed in the plate is significantly increased by reducing this ratio. Nobili [31] studied the anti-plane waves which is localized at the discontinuity surface between two perfectly bonded

half-spaces. It is shown that anti-plane waves are supported under very general conditions, and this outcome stands in remarkable contrast with CT. Here, the basic concept of couple stress theory is introduced. For a continuum volume (V), the equilibrium equations is written as:

$$\begin{aligned} &\int_V \boldsymbol{f}\mathrm{d}V + \int_{\partial V} \boldsymbol{t}_n \mathrm{d}s = 0, \\ &\int_V (\boldsymbol{x} \times \boldsymbol{f} + \boldsymbol{I})\mathrm{d}V + \int_{\partial V} (\boldsymbol{x} \times \boldsymbol{t}_n + \boldsymbol{\mu}_n)\mathrm{d}s = 0, \end{aligned} \tag{1.3}$$

where $\boldsymbol{t}_n = \boldsymbol{t} \cdot \boldsymbol{n}$ is the force per unit area. $\boldsymbol{\mu}_n = \boldsymbol{\mu} \cdot \boldsymbol{n}$ is the couple vectors per unit area. The subscript n means the direction of the external normal $\boldsymbol{n}$ to the volume surface. $\boldsymbol{f}$ represents the body force and $\boldsymbol{I}$ is the body couple per unit volume of the material particles. $\boldsymbol{x}$ denotes the position vector of a material particle in the continuum.

Using divergence theorem to transform surface integrals to volume integrals, one arrives:

$$\begin{aligned} &\int_V (\boldsymbol{f} + \nabla \boldsymbol{t})\mathrm{d}V = 0, \\ &\int_V [\boldsymbol{x} \times (\boldsymbol{f} + \nabla \boldsymbol{t}) - \epsilon : \boldsymbol{t} + \nabla \boldsymbol{\mu} + \boldsymbol{I}]\mathrm{d}V = 0, \end{aligned} \tag{1.4}$$

where ϵ is the alternating tensor. Since the volume V is arbitrary, eliminating the volume dependence which leads to $\boldsymbol{f} + \nabla \boldsymbol{t} = 0$, $\nabla \boldsymbol{\mu} - \epsilon : \boldsymbol{t} + \boldsymbol{I} = 0$ which indicates that the equivalent body couple $-\epsilon : \boldsymbol{t}$ acting together with $\boldsymbol{I}$ is generated by the stress tensor $\boldsymbol{t}$. Since the couple moment should vanishes, on obtains:

$$\int_V \boldsymbol{x} \times (\boldsymbol{I} - \epsilon : \boldsymbol{t})\mathrm{d}V + \int_{\partial V} \boldsymbol{x} \times \boldsymbol{\mu}_n \mathrm{d}s = 0, \tag{1.5}$$

where $\boldsymbol{x}$ is the position vector of a material particle in the continuum. $\boldsymbol{I} - \epsilon : \boldsymbol{t}$ is the residual body couple. Using the divergence theorem, Eq.1.5 can be rewritten as:

$$\int_V [\boldsymbol{x} \times (\boldsymbol{I} + \nabla \boldsymbol{\mu} - \epsilon : \boldsymbol{t}) - \epsilon : \boldsymbol{\mu}]\mathrm{d}V = 0. \tag{1.6}$$

Introducing the symmetric part of the stress tensor ($\boldsymbol{\sigma}$) and anti-symmetric part of the stress tensor ($\boldsymbol{\tau}$), the equilibrium equation of couple stress theory can be expressed as:

$$\nabla \boldsymbol{\sigma} + \frac{1}{2}\epsilon : (\nabla^2 \boldsymbol{m} + \nabla \boldsymbol{I}) + \boldsymbol{f} = 0, \tag{1.7}$$

where $\boldsymbol{m}$ is the deviatoric couple stress tensor.

(2) Modified couple stress theory

Unlike the classical couple stress theory, the equilibrium equation in modified couple stress theory requires that the deviatoric couple stress tensor $\boldsymbol{m}$ to be symmetric. Yang et al.[17] proposed the modified couple stress theory by extracting the couple stress tensor symmetrically in which only one material length scale parameter is involved. Later, Espo [32] investigated the band gap properties of a periodic nano-beam using a modified couple stress theory. The Bloch theorem together with the transfer matrix method are employed for analyzing the nano-beam. It shows that the surface effects on the band gaps are increased when the external electrical field is increased. Liu [33] combined Legendre orthogonal polynomial method and Global matrix method with the couple stress theory to investigate the wave reflection and transmission in a couple stressed plate immersed in liquid. Increasing the frequency and decreasing the thickness can bring the incident wavelength and thickness closer to the length scale parameter, thereby leading to the effect of the couple stress more pronounced. khorshidi [34] employed modified couple stress theory with Euler–Bernoulli and Timoshenko beam theories to predict the dispersion characteristics of flexural waves in carbon nano-tubes. This study predicted the capability of carbon nano-tubes to the weakening effect in nano-scale. Soltani [35] analyzed the scale-dependent micro-inertia effect on the longitudinal dispersion by the modified couple stress theory. The higher order micro-rotations should be considered to investigate the highly nonlinear dispersion curve including an extremum/inflection point. Alizadeh [36] derived the governing equations of a noncircular micro-wire using Hamilton's principle and obtained the free torsional vibration of the noncircular micro-wire through modified couple stress theory.

(3) Strain gradient theory

Mindlin proposed the SG elasticity theory (or called First Strain Gradient) and put forward three versions of SG. For the first version, the deformation metrics include the conventional strains from macro-material and the non-independent second-order displacement gradients from macro-material. For the second version, the second-order displacement gradients are replaced by the gradient of strain. For the third version, the conventional strains, rotation gradients and symmetric part of gradient of strain are used as deformation metrics.

Many articles have focused on the study of micro-sized structures' properties through SG elasticity theory. For example, karami [37] developed a non-local SG elasticity theory to analyze wave dispersion in a doubly-curved nano-shell. The result shows that strain gradient parameters influence the wave frequencies and phase velocities. Hosseini [38] studied stress distribution in a single-walled carbon nano-tube under internal pressure and used SG theory to capture the size-dependent behavior of the nano-tube. Numerical results show that in a single-walled carbon nano-tube, as the radius is increased, the non-dimensional radial and circumferential stresses along the wall thickness increase. What is more, Eremeyev [39] studied the anti-plane surface waves in SG materials with surface stresses which indicates that the solutions

related to the surface elasticity model are more localised near the free surface. Wave propagation in Timoshenko nano-beams considering strain gradient effects was analyzed by Norouzzadeh [40]. It shows that increasing the non-local and small scale parameters has softening and hardening influences on the wave frequencies of nano-beam, respectively. Yang [41] established a dynamic Timoshenko beam model based on the new non-local SG theory and studied the wave propagation behaviors of fluid-filled carbon nano-tubes. The numerical solution indicates that the strain gradient effect leads an enhancement of stiffness when the non-local stress effect causes stiffness decrease. In the second version of SG, the strain energy density, $\overline{\mathcal{U}}$, depends on both the conventional strain and the first gradient of strain:

$$\overline{\mathcal{U}} = \overline{\mathcal{U}}(\varepsilon_{ij}, \xi_{ijk}), \tag{1.8}$$

where $\varepsilon_{ij} = sym(\nabla \mathbf{U})$ is classical infinitesimal strain, $\xi_{ijk} = \nabla\nabla\mathbf{U}$ means the first order of strain, in which $\mathbf{U}$ is the displacement vector and symbol ∇ means the gradient operator. The Cauchy stress σ_{ij} and higher-order stress τ_{ijk} are expressed as:

$$\sigma_{ij} = \frac{\partial \mathbf{U}}{\partial \varepsilon_{ij}}, \quad \tau_{ijk} = \frac{\partial \mathbf{U}}{\partial \xi_{ij}}. \tag{1.9}$$

Based on the principle of virtual work, the equilibrium equations in the body V of a solid with boundary S and sharp edge C gives as:

$$\sigma_{jk,i} - \tau_{ijk,ij} + b_k = 0, \tag{1.10}$$

with b_k is the body force per unit volume. For linear elasticity, the total strain energy density can be written as:

$$\overline{\mathcal{U}} = \frac{1}{2} C_{ijkl}\varepsilon_{ij}\varepsilon_{kl} + \frac{1}{2} F_{ijklpq}\xi_{ijk}\xi_{lpq}, \tag{1.11}$$

where C_{ijkl} means the classical fourth-order elasticity tensor and F_{ijklpq} is the sixth-order elastic tensor. For a isotropic structure, the conventional fourth-order elasticity tensor includes two $Lam\acute{e}$ constants λ and μ which will be discussed in the following section.

(4) Second strain gradient theory

As discussed in the former section, the SG in which the potential energy density composed of strain and first gradient of strain is considered, but only for micro-sized noncentro-symmetric structures [42]. In order to explore the properties of centro-symmetric structures, the SSG theory [16] was put forward, which offers a reasonable explanation for the transforming of strain or tension on a solid plane surface. For instance, Ghazavi [43] investigated the influence of length scale parameters by applying SSG theory and Euler- Bernoulli beam theory. The

linear stability analysis shows that the nano-beam becomes unstable by static divergence due to the losing stiffness. Torabi [44] reported the free vibration finite element analysis of the nano-beam and nano-plate by the SSG theory of 3D elasticity model. It is realized that the difference of the results between SSG theory and CT decreases with the increase of thickness-to-lattice parameter ratio. Khakalo [45] derived the fundamental equations for Form II of Mindlin's SSG elasticity theory for isotropic materials and proposed a simplified formulation with six and two higher-order material parameters for the strain and kinetic energy, respectively. On the other hand, Babu [46] presented a new computationally efficient nonconforming finite element formulation for the modelling of nano-plates through SSG elasticity theory. It can be concluded from the results that the effect of the positive and negative strain gradient terms is of softening and hardening nature, respectively. Delfani [47] employed Mindlin's SSG elasticity to extract an estimate of the effective shear modulus of an anti-plane mode which is a functionally graded unidirectional fibrous composite. The results indicate that, at a constant volume fraction, the shear modulus of the composite takes a higher value when the diameter of the fibers decreases. In the SSG theory, strain energy density $\overline{\mathcal{U}}$ is composed of strain $\boldsymbol{\varepsilon}$=$sym(\nabla \mathbf{U})$ from macro-material in the structure, first gradient of strain $\boldsymbol{\xi}$=$\nabla\boldsymbol{\varepsilon}$ and second gradient of strain $\boldsymbol{\zeta}$=$\nabla\nabla\boldsymbol{\varepsilon}$, as below:

$$\begin{aligned}\overline{\mathcal{U}} =& \frac{1}{2}\lambda\varepsilon_{ii}\varepsilon_{jj} + \mu\varepsilon_{ij}\varepsilon_{ij} + a_1\xi_{ijj}\xi_{ikk} + a_2\xi_{iik}\xi_{kjj} + a_3\xi_{iik}\xi_{jjk} + a_4\xi_{ijk}\xi_{ijk} + a_5\xi_{ijk}\xi_{jki} \\ &+ b_1\zeta_{iijj}\zeta_{kkll} + b_2\zeta_{ijkk}\zeta_{ijll} + b_3\zeta_{iijk}\zeta_{jkll} + b_4\zeta_{iijk}\zeta_{llkj} + b_5\zeta_{iijk}\zeta_{lljk} + b_6\zeta_{ijkl}\zeta_{ijkl} \\ &+ b_7\zeta_{ijkl}\zeta_{jkli} + c_1\varepsilon_{ii}\zeta_{jjkk} + c_2\varepsilon_{ij}\zeta_{ijkk} + c_3\varepsilon_{ij}\zeta_{kkij},\end{aligned} \tag{1.12}$$

where λ and μ represent the $Lam\acute{e}$ parameters which are related to the Young's modulus E, the Poisson's ratio ν and the shear modulus G, as μ=G=$E/2(1+\nu)$, λ=$\nu E/(1+\nu)(1-2\nu)$. a_i, b_i and c_i denote the higher order parameters [42] for SSG theory.

The components of the usual stress $\boldsymbol{\tau}_1$, and higher order stresses $\boldsymbol{\tau}_2$ and $\boldsymbol{\tau}_3$ are defined as:

$$\boldsymbol{\tau}_1 = \frac{\partial\overline{\mathcal{U}}}{\partial\boldsymbol{\varepsilon}}, \quad \boldsymbol{\tau}_2 = \frac{\partial\overline{\mathcal{U}}}{\partial\xi}, \quad \boldsymbol{\tau}_3 = \frac{\partial\overline{\mathcal{U}}}{\partial\boldsymbol{\zeta}}. \tag{1.13}$$

The potential energy density in SSG theory is a function of strain, first gradient of strain and second gradient of strain. The equilibrium equation is a high order partial differential function with classical and non-classical boundary conditions.

1.3.1.2 Micro-continuum theory

The micro-continuum theory was proposed by Eringen [48–50] including micro-polar, micro-stretch and micro-morphic theories in which micro-material in the structure can deform and rotate independently.

Currently, new researches about wave propagation characteristics through micro continuum theory have been carried out. For example, Ogam [51] studied the micro-polar behavior of materials by using a theoretical and experimental acoustic method. The micro-polar elastic behavior in the material was illustrated through the comparison between theoretical and experimental wave transmission coefficients. kalkal [52] investigated the plane waves reflection in a micro-polar medium under the effect of rotation which shows that during reflection phenomena, the sum of modulus of energy ratios is approximately equal to unity at each angle of incidence. Yadav [53] dealt with the reflection of plane waves in a micro-polar thermoelastic diffusion solid half-space. The reflection coefficients of the reflected waves are calculated for a particular material. Furthermore, Kishine [54] examined the phonon spectrum of a chiral crystal within the micro-polar elasticity theory. It shows that the polarization-dependent phonon dispersion demonstrated may lead to chirality-induced cross correlations among lattice, electronic, and magnetic degrees of freedom. Varygina [55] studied the mathematical model of multilayered cylinder shell within the framework of linear micro-polar theory of elasticity and computed the dynamic problems on the action of instant concentrated external load. The results of numerical computations of wave propagation in micro-polar cylindrical shells demonstrate qualitative difference in the wave pattern depending on the particle types.

In micro-polar mechanics in addition to classical stresses the couples tresses from independent micro-rotation of micro-material in the structure are introduced. The equations of motion of micro-polar can be expressed as [51]:

$$\begin{aligned} \rho\frac{\mathrm{d}V}{\mathrm{d}t} &= \mathrm{div}\boldsymbol{\sigma} + \rho\mathbf{f}, \\ j\frac{\mathrm{d}\omega}{\mathrm{d}t} &= \mathrm{div}\mathbf{M} - \boldsymbol{\sigma} + \rho\mathbf{m}, \end{aligned} \tag{1.14}$$

where $\boldsymbol{\sigma}$ and $\mathbf{M}$ denote the stress and independent couple stress tensors of Cauchy type, ρ is the density in the actual configuration, j means the measure of rotatory inertia of particles of micro-polar medium, $\mathbf{f}$ and $\mathbf{m}$ represent the external forces and couples, respectively.

On the other hand, Chirilua [56] studied micro-stretch elastic material with thermal and mass diffusion at the macro- and micro-level to give the plane harmonic in time wave solutions. The result shows that displacement, microrotation and microdilatation are un-damped in time waves under micro-stretch elasticity with thermal and mass diffusion. Singh [57] investigated the effect of diffusion on wave propagation and reflection in a micro-stretch solid half-space and observed the influence of diffusion parameters on the speeds and energy ratios of reflected waves. Lotfy [58] solved a model of the equations of generalized thermo-micro-stretch for an infinite space which is considered as homogeneous isotropic elastic. The presence of micro-stretch plays an important role in all the physical quantities.

The governing equations in micro-stretch elastic referred to a fixed system of rectangular

Cartesian axes are expressed as [56]:

$$\begin{aligned} &\boldsymbol{\sigma}_{ji,j} + \rho \mathbf{f}_i = \rho \ddot{\mathbf{U}}_i,\ \mathbf{h}_{k,k} + \mathbf{g} + \rho \mathbf{l} = \mathbf{J}\ddot{\phi}, \\ &\mathbf{M}_{ji,j} + \varepsilon_{irs}\boldsymbol{\sigma}_{rs} + \rho \mathbf{g}_i = \mathbf{I}_{ij}\ddot{\phi}_j,\ \dot{\mathbf{C}} = \eta_{i,i}, \end{aligned} \tag{1.15}$$

where $\boldsymbol{\sigma}$ is the components of the classical stress tensor from macro-material in the structure, $\mathbf{f}$ is the components of the body force, $\mathbf{U}$ means the components of the displacement vector field from macro-material in the structure, $\mathbf{h}$ means the independent components of the micro-stretch vector from micro-material in the structure, $\mathbf{g}$ denotes the internal body force, $\mathbf{l}$ denotes the external microstretch body load, $\mathbf{M}$ is the independent components of the couple stress tensor from micro-material in the structure, $\mathbf{C}$ is the concentration, η means the components of the flux vector of mass diffusion, ϕ is micro-dilatation function.

Furthermore, a new beam model was illustrated based on the simplified micro-morphic elasticity theory and wave propagation in an infinitely long beam was solved by Zhang [59]. Marco [60] described the dynamical behavior of a band-gap metamaterial with tetragonal symmetry micro-morphic material model. The main microscopic characteristics such as dispersion and band-gaps of the targeted metamaterial is presented. The efficient theoretical model can avoid unnecessary complexifications related as it is the case for higher gradient elasticity. Eremeyev [61] derived the conditions for acceleration waves propagation through nonlinear elastic theory of micro-morphic continuum and obtained the acoustic tensor of the micro-morphic medium and formulated the conditions of the acceleration waves existence. In order to explain the micro-morphic elasticity, the simplified strain energy density which is the fundamental function is introduced here [59]:

$$\begin{aligned} \overline{\mathcal{U}} =& \frac{1}{2}\lambda\varepsilon_{ii}\varepsilon_{jj} + \mu\varepsilon_{ij}\varepsilon_{ij} + \lambda_c\varepsilon_{ii}\xi_{jj} + 2\mu_c\varepsilon_{ij}\xi_{ij} + \frac{1}{2}\lambda_m\xi_{ii}\xi_{jj} + \mu_m\varepsilon_{ij}\xi_{ij} \\ &+ l^2(\frac{1}{2}\lambda_m\xi_{ii,k}\xi_{jj,k} + \mu_m\varepsilon_{ij,k}\xi_{ij,k}), \end{aligned} \tag{1.16}$$

in which λ and μ are classical $Lam\acute{e}$ constants from macro-material in the structure, λ_m and μ_m are independent $Lam\acute{e}$ constants from micro-material in the structure, λ_c and μ_c are independent coupling $Lam\acute{e}$ constants from micro-material in the structure, l is length scale parameter.

1.3.1.3 Non-local elasticity theory

It is well known that the stress at each point is related to the strain at the same point only in the local theory of continuum mechanics. But for micro-meter scales, the size effects become very important. In order to explain the size effects, the non-local continuum mechanics has been developed which is based on the assumption that the stress at a point is a function of strains at all points in the continuum. In the non-local elasticity theory, forces between atoms and internal length scale are considered.

The non-local elasticity theory was initially formulated by Eringen and Edelen [2, 62]. The material constant in non-local elasticity theory can be determined either from experiments or simulations. For example, Arash, Huang and Duan [63–65] evaluated the value of the material constant for the static and dynamic analysis.

The non-local models can be categorized into beam model and plate model. The non-local beam model was developed by Peddieson and Sudak [66, 67]. Peddieson applied his model to study the size effects on the bending behaviour of isotropic nano-beams. Sudak applied his model to analyze the buckling of multi-walled carbon nano-tubes. Since the early works by Peddieson and Sudak, there have been a large number of articles devoted to the modelling of nano-beams. For example, Moheimani [68] put forward the static and dynamic solutions of nano-beams under external loads using non-local theory which shows that a non-local effect could greatly affect the behaviors of nano-beam. What is more, Ghaffari [69] offered a complete solution to analyze the mechanical behavior (bending, buckling and vibration) of nano-beam under non-uniform loading. It shows that the theoretical non-local parameters can be determined to reduce the cost of experiments determining the value of non-local parameters. Bensattalah [70] employed the Differential Transform Method to predict and to analysis the non-local critical buckling loads of carbon nano-tubes with various end conditions. In order to investigate the influence of true shear stresses in non-local beam, Faghidian [71] put forward a non-local flexure beam considering the effects of true shear stresses through non-local elasticity theory. While the explicit shear force and bending moment were determined from the standard dynamic equations by Bourouina [72]. The fracture behavior is also a significant property in non-local beam. Alotta and Vantadori [73, 74] studied the fracture behavior by employing non-local theory of elasticity. Rahimi [75] governed the non-local dynamics equations of motion of Euler–Bernoulli beam to study the fracture behavior.

On the other hand, the wave propagation characteristics of non-local beam or tube have also been widely studied recently. For instance, a non-local modeling of the vibration characteristics such as wave propagation of carbon nano-tubes was introduced by Wang [76]. The numerical results show that the fluid has a significant influence on the dynamical proprieties of nano-tube, and the effect of high-speed fluid on the carbon nano-tube wall cannot be ignored. He [77] studied wave propagation in a non-local piezoelectric phononic crystal Timoshenko nano-beam. The results are helpful for the design of micro and nano-devices. Rakrak [78] analyzed the transverse wave propagating of carbon nano-tube using non-local elasticity theory. The results obtained can be used to predict the phenomenon of resonance for the forced vibration analyses of carbon nano-tubes. The bending wave propagation characteristics of a single walled carbon nano-tube was investigated by Belhadj [79] based on the theory of non-local elasticity. Different natural frequencies of single walled carbon nano-tubes of non-local parameter improve its effect on the bending vibration of simply supported carbon nano-tubes, and local natural frequencies agree well with exact results. Length and diameter of carbon nano-tubes

have a significant influence on the optical and mechanical properties. Arefi and Yayli [80, 81] presented a non-local solution for a nano-rod and evaluated the characteristics of the wave propagation in the rod structure.

One of the earliest non-local plate model was put forward by Lu [82]. This model was used to analyze the size effects on the bending and bucking behaviours of isotropic nano-plates. Recently, many articles have focused on the wave propagation in plate model through non-local theory. For example, karami [83] investigated the wave propagation of porous nano-shells using non-local theory in conjunction with a higher-order shear deformation shell theory. According to the results, it is verified that the size-dependence of the response is nearly the same to plates, beams and tubes. Opalakrishnan [84] presented the study of propagation of elastic waves in 2D nano-structures using Eringen's non-local theory. In his work, wave propagation features such as escape frequency, cut-off frequencies, phase speeds and group speeds are studied. What is more, Cherednichenko [85] investigated the uniaxial tension of a 2D plate by the non-local theory of elasticity and analyzed the demonstration of non-local effects arising in stresses. Sumelka [86] dealt with the non-local Kirchhoff–Love plates theory using fractional calculus which is a branch of mathematical analysis to study differential operators of an arbitrary order, emerged as a powerful tool for modelling complex systems. The reflection and transmission of elastic waves in non-local band-gap metamaterials are studied via the relaxed micromorphic model by Madeo [87].

In my work, in order to describe the non-local elasticity theory, an Euler–Bernoulli nano-beams (length L, width b and thickness h) is taken as an example [88], as shown in Fig.1.6. The Young's modulus E is assumed to change as arbitrary function in both axial and thickness directions, as follows:

$$E = f(x)g(z). \tag{1.17}$$

Based on Euler–Bernoulli beam theory, the displacements w and u are expressed as:

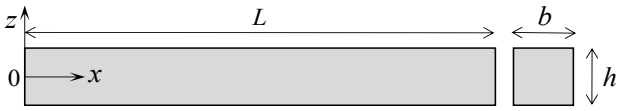

Fig. 1.6. Geometry of Euler–Bernoulli nano-beam.

$$u_1 = -z\frac{\partial w(x,t)}{\partial x}, \quad u_2 = w(x,t). \tag{1.18}$$

Here, nonzero strain is considered only:

$$\varepsilon_{11} = -z\frac{\partial^2 w(x,t)}{\partial x^2}. \tag{1.19}$$

The governing equation of the Euler–Bernoulli beam can be obtained by using the concept of minimum total potential energy principle:

$$\delta\Pi = \delta\mathcal{U} - \delta\mathcal{W} = 0, \tag{1.20}$$

in which δU and δW are variation of strain energy and variation of virtual work done by the external applied forces, respectively. The variation of strain energy is:

$$\delta\mathcal{U} = \int_V \sigma_{11}\delta\varepsilon_{11}\mathrm{d}V = \int_0^L \left(-\frac{\mathrm{d}^2 M_{11}}{\mathrm{d}x^2}\delta w\right)\mathrm{d}x, \tag{1.21}$$

where $M_{11} = \int_A z\sigma_{11}\mathrm{d}A$. The virtual work done by the external forces, f, is given:

$$\delta\mathcal{W} = \int_0^l q\delta w\mathrm{d}x. \tag{1.22}$$

Substituting Eqs.1.21 and 1.22 into Eq. 1.20, the governing equation is given as:

$$-\frac{\mathrm{d}^2 M_{11}}{\mathrm{d}x^2} + q = 0. \tag{1.23}$$

According to the non-local elasticity theory, the stress tensor at an arbitrary point x in the domain of material depends not only on the strain tensor at x but also on strain tensor at all other points in the domain. So a stress–strain relationship is written as:

$$\sigma_{ij}^{nl} = \int_V \alpha\left(|x' - x, \tau|\right)\sigma_{ij}^{l}\mathrm{d}V(x'), \tag{1.24}$$

where α is the non-local modulus, which contains the small scale effects incorporating into constitutive relations in which the non-local effects at the point x produced by local strain at the source x'. $|x - x'|$ is the distance in Euclidean form, $\tau = e_0\bar{a}/L$ denotes a material parameter that depends on internal and external characteristic length. e_0 is determined by matching the dispersion curves. σ^{nl} is the non-local stress tensor at the reference point and σ^l means the classical stress tensor at local point which is defined in the following:

$$\sigma^l = \mathcal{C} : \varepsilon, \tag{1.25}$$

where $\mathcal{C}$ is the fourth order elasticity tensor. The non-local constitutive relation given in integral form can be expressed in an equivalent differential form as:

$$(1 - \upsilon\Delta^2)\sigma^{nl} = \mathcal{C} : \varepsilon, \tag{1.26}$$

where $\upsilon = (e_0 a)^2$. For a non-local beam, the relation between the local and non-local stresses can be represented as:

$$\sigma_{11} - \upsilon \frac{\partial^2 \sigma_{11}}{\partial x^2} = E\varepsilon_{11}. \tag{1.27}$$

Then, multiplying Eq. 1.27 by z and integrating the resulting over the beam cross section area A leads to:

$$M_{11} - \upsilon \frac{\partial^2 M_{11}}{\partial x^2} = \int_A Ez \left(-z \frac{\mathrm{d}^2 w}{\mathrm{d}x^2} \right) \mathrm{d}A = -f(x) I_2 \frac{\mathrm{d}^2 w}{\mathrm{d}x^2}, \tag{1.28}$$

in which $I_2 = \int_A z^2 g(z) \mathrm{d}A$. The second derivative of Eq.1.28 which is the governing equation under non-local theory can be expressed as:

$$\frac{\partial^2 M_{11}}{\partial x^2} - \upsilon \frac{\partial^4 M_{11}}{\partial x^4} = -I_2 \left(f(x) \frac{\mathrm{d}^4 w}{\mathrm{d}x^4} + 2f'(x) \frac{\mathrm{d}^3 w}{\mathrm{d}x^3} + f''(x) \frac{\mathrm{d}^2 w}{\mathrm{d}x^2} \right). \tag{1.29}$$

1.3.1.4 Surface elasticity theory

It is well known that due to high surface-to-volume ratio in micro-sized structures, the surface tension, produced by atoms with associated energy on the free surface, has a significant influence on the structure's behavior.

The mostly used model of the surface elasticity proposed by Gurtin [89]. Recently, some researchers have focused on the exploration of surface wave properties through surface elasticity theory. For instance, Eremeyev [90] discussed the propagation of transverse surface waves along a surface of an elastic cylinder with coating. About the similarities between the generalized Young–Laplace equation and transmission conditions through a stiff interface, the presented results can be reformulated for surface shear waves propagating along such stiff interfaces. Arefi [91] evaluated the governing differential equations of the Love nano-rod model by employing the coupled stress components and surface elasticity, and discussed the characteristics of wave propagation in nano-rod. Eremeyev [92] built a new model of surface elasticity in which the surface strain energy depends on surface stretching and on changing of curvature along a preferred direction. It shows that the dispersion relation depends on the direction of wave propagation. The presented results demonstrated a influence of a surface micro-structure on surface waves.

On the other hand, the contribution of the non-local integral theory of elasticity to surface elasticity was revealed by Li [93]. In his work, a uniform and isotropic half-space medium subjected to an arbitrary uniform strain is considered. The interaction forces generated by the points within the horizon will offset against each other owing to the geometric symmetry and the symmetric distribution of attenuation functions. Xie [94] predicted the influence of surface free energy on nonlinear secondary resonance of silicon nano-beams under external hard excitations

through surface elasticity theory. It shows that due to the higher surface to volume ratio for a nano-beam, reduction in the value of beam thickness causes to enhance the difference between the classical and non-classical predictions for the nonlinear secondary resonance response.

Here, in order to introduce the surface elasticity theory, an isotropic elastic solid body V with smooth enough boundary $S = \partial V$ is considered within Gurtin–Murdoch model [89] framework. The surface stress tensor $\boldsymbol{\tau}$ is expressed as [89]:

$$\boldsymbol{\tau} = \gamma \mathbf{P} + 2(\mu_s - \gamma)\boldsymbol{\varepsilon} + (\lambda_s - \gamma)\mathbf{P}(\mathrm{tr}\boldsymbol{\varepsilon}) + \gamma \nabla_s \mathbf{U}, \tag{1.30}$$

where the surface strain tensor $\boldsymbol{\varepsilon}$ is written as:

$$\boldsymbol{\varepsilon} = \frac{1}{2}(\mathbf{P} \cdot (\nabla_s \mathbf{U}) + (\nabla_s \mathbf{U})^{\mathrm{T}} \cdot \mathbf{P}), \tag{1.31}$$

in which $\mathbf{U}$ is a displacement vector, γ means a scalar coefficient interpreted as a residual surface tension, λ_s, μ_s denote the surface $Lam\acute{e}$ constants, ∇_s is the surface nabla operator, $\mathbf{P}$ is the unit vector of outer normal to S. The proposed expression of surface stress tensor is the foundation of surface elasticity theory.

1.3.2 Lattice spring model theory

The LSM theory [95] is also a valuable approach to interpret the dynamic characteristics for micro-sized medias. In the last decade, many articles have focused on the wave propagation properties of micro-sized structures through LSM. For example, Dario [96] presented a non-local lattice model to give the micro-stiffness and micro-inertia terms a physical interpretation based on geometrical and mechanical properties of the micro-structure. The dispersion characteristics of waves propagating in nano-structure are illustrated as well. It shows that the proposed three-length-scale gradient formulation is effective to capture a range of wave dispersion characteristics arising from experiments. Nannapaneni [97] defined the strains consistently in terms of displacements in the micro-sized lattice structures, and analyzed the wave propagation proprieties using a Bloch wave theory. Liu [98] proposed a modified LSM by introducing an independent micro-rotational inertia which can indicates the scale-dependent effect. The stiffness ratio, numerical damping, lattice spacing, and micro-rotational inertia have influences on the Poisson's ratio. Also, he analyzed the dispersion relationship of elastic waves by considering the characteristic material length.

On the other hand, the dynamical properties of a lattice refined truncated nano-cube are studied by Sahmani [99], and the size-dependent non-linear large-amplitude vibrations of this structure are explored. Vila [100] analyzed the free longitudinal wave vibration in a one dimensional structured solid which is modeled as a discrete chain of masses interacting through non-linear springs, which shows that the higher the characteristic size in the underlying struc-

ture of the chain, the lower the frequencies of oscillation. Wang [101] studied wave propagation in a weakly non-linear monoatomic lattice chain with non-local interaction, and offered a way to control the wave propagation and energy transferring behaviors. Song [102] studied elastic wave propagation in non-linear periodic mass-in-mass lattice structures and discussed the band structures which can be influenced by nonlinearities of the lattice. The non-classical continuum model theory is used to capture the dynamic behavior such as dispersion and natural frequency of the lattice.

Furthermore, for the LSM based on surface elasticity theory, Hamilton [103] introduced the subject by considering embedded-atom-method calculations of the equilibrium in-plane strain for free-standing nano-sheets. Eremeyev [104] derived the dispersion relations for anti-plane surface waves using surface of lattice dynamics. The proposed model can capture material behavior related to presence of surface energy. Karlivcic [105] investigated the elastic wave propagation in lattice elastic Timoshenko beams with attached point masses. Here, a "toy-

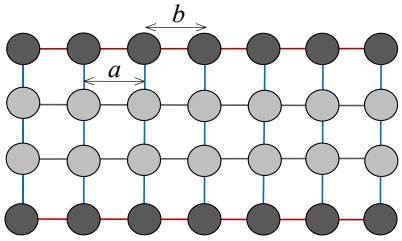

Fig. 1.7. Schematic drawing of a simple one-dimensional "toy-model". The black bonds represent bulk pair potentials with equilibrium spacing, a. The red bonds represent surface pair potentials with equilibrium spacing, b. The blue bonds are at right angles to the atomic planes and force the surface and bulk spacing to be equal.

model" [106] of LSM based on surface elasticity theory is presented. Fig.1.7 shows a simple 1D "toy-model" for surface and bulk elasticity. This is a pseudomorphic model in which the vertical black bonds force the surface layers and bulk layers with same inter-atomic separation. Here, we assume that a spring potential for the bulk layers with equilibrium length, a, and force constant, k_b. A spring potential for the two surface layers with equilibrium length, b, and force constant, k_s.

The total energy of the nano-sheet of thickness, h layers, is a function of the inter-atomic spacing, L. The energy per atom in the surface layers is $E_s = k_s(L-b)^2/2$ and the energy per atom in the bulk layers is $E_b = k_b(L-a)^2/2$. The model has two surface layers and $(h-2)$ bulk layers. The total energy per surface atom can be expressed as:

$$E_t(h) = k_s(L-b)^2 + \frac{k_b(L-a)^2(h-2)}{2}. \tag{1.32}$$

The form $E_t(h) = 2E_s + E_b(h-2)$ shows that energy of the various layers is additive and that layers can be divided into bulk and surface. The equilibrium strain (ε) for a given h is

expressed as:

$$1/\varepsilon = \left[\frac{k_b h}{2} + (k_s - k_b)\right] \frac{a}{(a-b)k_s}. \tag{1.33}$$

This model shows that the strain is a linear function of h, and that the surface layer has a residual strain whose elastic properties are different from the bulk. On the other hand, the "toy-model" can offer a quantitative prediction of surface and bulk strains.

Last, for the LSM based on long-rang interaction, Tarasov [107] proposed a LSM with nearest and next-nearest-neighbor interactions of a tension beam for the first time and confirmed the resulting dynamic equations by using Fourier series. Then, a lattice torsion beam with nearest and next-nearest interactions is proposed by Gomez [108]. The novel model proposed shows the best performance, and the governing equation being of low order can avoid the use of extra boundary conditions. Zhu [109] calculated the governing equation of a 1D tension vibration bar using a LSM with nearest, next-nearest and next-next-nearest interactions. The author [95] expounded LSMs with nearest, next-nearest and next-next-nearest interactions for bending and torsion vibration respectively, and wave dispersion relations and forced responses for bending and torsion are analyzed.

In order to explain LSM based on long-rang interaction, a LSM with the nearest-neighbor

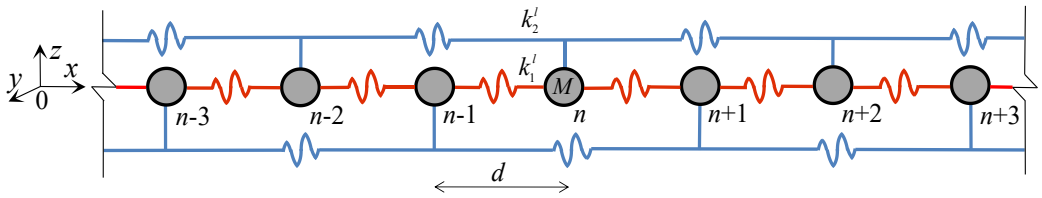

Fig. 1.8. Discrete mass-spring system with stiffness k_1^l and k_2^l, the mass M and the distance d corresponds to the lattice model with the nearest-neighbor and next-nearest-neighbor interactions.

and next-nearest-neighbor interactions is introduced within SG theory framework. The suggested LSM gives unified description of the second-gradient model. The sign in front the gradient is determined by the relation of the coupling constants of the nearest neighbor and next-nearest-neighbor interactions.

As shown in Fig.1.8, LSM for 1D tension bar can reflect the mechanical response of the continuum structure when the length between each node at small scale and P is large enough. The lattice equation of motion for node n as:

$$k_1^l(u_{n-1} - 2u_n + u_{n+1}) + k_2^l(u_{n-2} - 2u_n + u_{n+2}) - F_n = M\frac{\mathrm{d}^2 u_n(t)}{\mathrm{d}t^2}, \tag{1.34}$$

in which u_n is the displacement of mass n along x direction. Subsequently, the Fourier series transform approach [110] is used to derive a continuous equation $u(x,t)$ from the LSM $u_n(t)$.

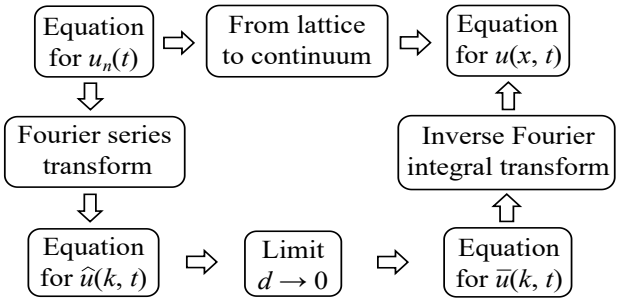

Fig. 1.9. Diagrams of sets of operations for differential equations.

The detail addressed in Fig.1.9, as a result:

$$G_2^l \frac{\partial^2 u(x,t)}{\partial x^2} + G_4^l \frac{\partial^4 u(x,t)}{\partial x^4} + o\left(G_i^l \frac{\partial^i u(x,t)}{\partial x^i}\right) - \frac{1}{\rho} f(x,t) = \frac{\mathrm{d}^2 u(x,t)}{\mathrm{d}t^2}, (i = 6, 8, ...), \tag{1.35}$$

where ρ is the mass density, $G_2^l = (k_1^l + 4k_2^l)d^2/M$, $G_4^l = \left(k_1^l + 16k_2^l\right) d^4/(12M)$.

This LSM can only be used to describe the SG theory whose continuum equation of motion contains one higher order term. But for the SSG theory, the continuum equation of motion contains two higher order terms, the LSM of nearest, next-nearest interactions is insufficient to derive this two higher order terms. So the establishment of LSM with nearest, next-nearest and next-next-nearest interactions is necessary to determine the continuum equation under SSG theory. The LSM for SSG theory is a new research topic, especially for bending and torsion vibration. If only the nearest interaction is considered, the LSM will reverse to the one by CT.

1.4 Existing methods to study periodic structures

The attentions of my work lie on the explorations of engineering periodic structures. There are many methods to study the engineering periodic structures. For instance, plane-wave expansion method [14], modified TMM [111], WFEM [95, 112], MOR technique [113] and homogenization methods [114]. These methods are mainly used in phononic materials to deal with multiple medias and assure good convergence.

1.4.1 Plane-wave expansion

The view of plane wave expansion method for continuous systems is expanding the sought-after solution field and the material properties in a Fourier series, and then invoking orthogonality of the basis functions to solve the introduced solution coefficients. Recently, a novel Fourier series expansion is proposed by Dal [115] to represent a periodic cubic lattice structure using the plane wave expansion method. Meanwhile, he discussed the flexural wave band gaps in a ternary periodic metamaterial plate by using the plane wave expansion method [116]. Riva

[117] investigated 1D wave propagation in phononic wave-guides whose non-reciprocal dispersion diagram is computed using a generalized plane wave expansion method. This new model is able to violate the mirror symmetry in the momentum space.

Furthermore, an improved fast plane wave expansion method for topology optimization of phononic crystals was put forward by Xie [118]. The properties of the unit cells affect the optimization speed as well as the overall computational time. The adaptive genetic algorithm can decrease the overall iteration time required for convergence, and improve the optimization efficiency. On the other hand, Mock [119] calculated the band structure through the plane wave expansion by considering a material constant called time-modulated permittivity. It shows how tailored time-modulation influences a directional synthetic momentum to the field causing unidirectional propagation. Here, the basic concept of plane wave expansion method is introduced. Considering a system governed by the periodic wave equation, as below:

$$\rho \frac{\partial^2 \mathbf{U}}{\partial x^2} = \frac{\partial}{\partial x}\left(\rho c^2 \frac{\partial \mathbf{U}}{\partial x}\right), \tag{1.36}$$

where $\mathbf{U}$ denotes the displacement field, ρ is the density, c means the speed of sound through the media. A lattice vector for this system can be expressed as $\mathbf{R} = n\mathbf{a} = na\hat{\mathbf{x}}$ in which $\hat{x}$ is a unit vector and n any integer. A reciprocal lattice vector can be written as $\mathbf{G}_m = m\mathbf{b} = m/a\hat{\mathbf{x}}$ where m denotes any integer. Then, the plane-wave expansion can be presented as:

$$\begin{aligned}
\mathbf{U}(x,t) &= e^{i(\kappa\cdot\mathbf{r}-\omega t)} \sum_{\mathbf{G_1}} \mathbf{U}_\kappa(\mathbf{G_1}) e^{i\mathbf{G_1}\cdot\mathbf{r}}, \\
\rho(x) &= \sum_{\mathbf{G_m}} \rho(\mathbf{G_m}) e^{i\mathbf{G_m}\cdot\mathbf{r}}, \\
\rho(x)c^2(x) &= \sum_{\mathbf{G_m}} \tau(\mathbf{G_m}) e^{i\mathbf{G_m}\cdot\mathbf{r}},
\end{aligned} \tag{1.37}$$

where $\mathbf{r} = x\hat{\mathbf{x}}$ denotes position, $\kappa = k\hat{\mathbf{x}}$ is the wave vector, $\sum_{\mathbf{G_1}}, \sum_{\mathbf{G_m}}$ are sums over all reciprocal lattice vectors. Substituting the expansions into Eq.1.36 and forming the complex inner product with $e^{i\mathbf{G_n}\cdot\mathbf{r}}$ yields:

$$\sum_{\mathbf{G_1}} \left[-\omega^2 \rho(\mathbf{G_n}\mathbf{G_m}) + (\kappa + \mathbf{G_1})\cdot(\kappa + \mathbf{G_n})\tau(\mathbf{G_n} - \mathbf{G_1})\right] \mathbf{U}_\kappa(\mathbf{G_1}) = 0. \tag{1.38}$$

For each $\mathbf{G_n}$, the nonzero terms in the inner product satisfies $\mathbf{G_1} + \mathbf{G_m} - \mathbf{G_n} = 0$. By truncating the expansion for $\mathbf{G_1}$, the eigenvalue problems leads to eigen-frequencies $\omega(\kappa)$ and eigen-vector $[\mathbf{U}_\kappa(\mathbf{G}_{-N})\mathbf{U}_\kappa(\mathbf{G}_{-N+1})...\mathbf{U}_\kappa(\mathbf{G}_N)]^{\mathrm{T}}$, while $(2N+1)$ is the number of retained terms. By solving the problems for all the wavenumbers κ in IBZ, the eigenfrequencies are obtained and they can be used to express the band structures. As in any approximation technique, a convergence criterion should be applied to determine an appropriate value for N.

1.4.2 Modified transfer matrix method

TMM with some advantages in computer implementation is a simple and accurate method for analyzing the vibration of beams and other structures. In this section, a method is presented to reduce the order of the matrix which is call modified TMM. For the modified TMM, some remarkable researches are presented here. Han [120] introduced a modified MTM to calculate the bending vibration band structure in 1D phononic crystal (PC) Euler beams. Meanwhile, a modified TMM is applied by Feyzollahzadeh [121] to study on beam vibration and the result shows that the calculation time is reduced. Yang [122] proposed the modified TMM for the Steel composite transmission shafting system based on lamination theory and layer-wise beam theory. The result shows that the modified TMM can effectively illustrate the bending vibration characteristics of the composite transmission shafting system.

Here we define a model which is divided into a series of elements with constant parameters. It leads to a differential equation with constant coefficients when using separation of variables method to solve a function $w(x)$ in which each element can be represented as follows:

$$w = \sum_{n=0}^{n=N} A_N \cosh s_n s_n + \sum_{n=0}^{n=N} B_n \sinh s_n s_n + \sum_{n=0}^{n=N} C_n \cos s_n x_n + \sum_{n=0}^{n=N} D_n \sin s_n x_n, \tag{1.39}$$

where A_n to D_n are the constant coefficients in the solution based on the problem dimension N, s_n is the eigenvalue of the differential equation. If the system response is a combination of harmonic and hyperbolic functions, A_n to D_n appear in the derivatives of the response. As a result, the state vector $\mathbf{Z}$ including the response and its derivatives can be expressed through transfer matrix function $\mathbf{T}(x)$ as follows:

$$\mathbf{Z} = \mathbf{T}(x) \cdot \mathbf{C}, \tag{1.40}$$

where $\mathbf{C}$ is the vector of constants. $\mathbf{Z}$ and $\mathbf{C}$ can be expressed as:

$$\begin{aligned} \mathbf{Z} &= [w_1, w_2, ..., w_n, \varphi_1, \varphi_2, ..., \varphi_n, M_1, M_2, ..., M_n, V_1, V_2, ..., V_n]^T, \\ \mathbf{C} &= [A_1, A_2, ..., A_n, B_1, B_2, ..., B_n, C_1, C_2, ..., C_n, D_1, D_2, ..., D_n]^T. \end{aligned} \tag{1.41}$$

In point $i-1$, x sets to zero and the state vector is expressed by $\mathbf{T}(0)$. The transfer matrix function $\mathbf{T}(x)$ at $x = 0$, is called as the "zero matrix":

$$\mathbf{Z} = \mathbf{T}(0) \cdot \mathbf{C}, \tag{1.42}$$

and vector $\mathbf{C}$ is:

$$\mathbf{C} = \mathbf{T}(0)^{-1} \mathbf{Z}_{i-1}, \tag{1.43}$$

which can be substituted into Eq.1.40 to produce the state vector:

$$\mathbf{Z}(x) = \mathbf{T}(x)\mathbf{T}(0)^{-1}\mathbf{Z}_{i-1}. \tag{1.44}$$

At same time, in point i, $x = l$ and we have:

$$\mathbf{Z}(i) = \mathbf{T}(l)\mathbf{T}(0)^{-1}\mathbf{Z}_{i-1}. \tag{1.45}$$

The system response is a combination of harmonic and hyperbolic equations. The rows of transfer matrix are derivatives of the response system. Thus, the rows of the transfer matrix will be the same every other rows and alternately, which means that in the presence of matrix $\mathbf{T}(0)$, half of the terms will be zero in each row. The idea is about the zero elements concentration and all zeros of $\mathbf{T}(0)$ are gathered on one side of matrix. The inversion of $n \times n$ matrix can be calculated instead of $2n \times 2n$ matrix.

1.4.3 Wave finite element method

The WFEM offers a numerical wave characterization of periodic structures that composed of identical unit cells coupled together. The advantage of WFEM is modeling a unit cell by the conventional finite elements, which thus complex geometries or several materials can be involved. What is more, the wave propagation of whole structure can be evaluated by analyzing a single unit cell. The size of numerical problem that related directly to the number of DOFs will be reduced, thus computational time will be saved.

Literature on WFEM is extensive and covers a vast scope of applications [123–183], ranging from damage detection, metamaterials, vibro-acoustics, inverse identification. For the investigation of 1D wave propagation characteristics in periodic structures, an enhanced WFEM was developed by Fan [141] for a reduced model with local dampers to mitigate the ill-conditioning. Free wave characteristics are analyzed by the proposed method. Hoang [145] presented a method to calculate the wave amplitudes of the moving loads applying in a periodic railway track by using the WFEM in frequency domain. Miranda [146] investigated the forced response of flexural waves propagating in a 1D phononic crystal Euler-Bernoulli beam by WFEM. The numerical band gap can match the experimental result. Guo [159] proposed a method for dynamic homogenization and vibration analysis of lattice truss core sandwich beams using WFEM. This method is used to predict wave propagating and evanescent in the periodic truss core sandwich beam. Singh [166] presented a stochastic formulation for the Bloch analysis of 1D periodic structures based on WFEM, which shows a remarkable achievement for computational cost savings. He also studied the structured uncertainties in wave characteristic of 1D periodic structures through WFEM [157]. A homogenization technique was put forward by Ahsani [172] for 1D periodic structure. In his work, the WFEM is used to retrieve the multi-modal

interface wave diffusion coefficients. What is more, Duhamel [183] proposed a WFEM to compute the dynamic response of infinite periodic structures restricted to localized time-dependent excitations. The proposed approach can predict the dynamic behavior of the periodic structure over the whole time period.

On the other hand, WFEM can also be used to calculate the 2D wave propagation characteristics in periodic structures. For example, a modeling strategy was proposed by Zergoune [140] based on WFEM to deal with the flexural vibroacoustic behavior of sandwich panels and an expression of the sound transmission loss of these sandwich panels was developed. Hong [147] presented an improved WFEM that can be used to illustrated the band-gap characteristics of stiffened shell structures. Result shows that stiffeners' geometric parameters can be selected to attenuate the out-of-plane vibration. Mencik [149] proposed a numerical method to compute the 2D wave modes of periodic structures with cyclic symmetry based on WFEM. The numerical result highlights the efficiency of the WFEM compared to FE method. Thierry [156] analyzed 2D wave propagation in highly anisotropic textile composites. In his work, the advantages of mode-based Component Mode Synthesis (CMS) and WFEM are combined. Furthermore, Errico [160] developed a WFEM to compute the sound transmission loss of any flat, curved and cylindrical, homogeneous and periodic structure. Different periodic unit cell are investigated under diffuse acoustic field excitation. A second order optimization approach was presented by Boukadia [171] based on WFEM to optimize the 2D infinite structures. The proposed method can be utilized to optimize the vibro-acoustic performances of metabeams under clamped-free boundary conditions. In addition, Guenfoud [174] dealt with multi-layer rectangular core topology systems which are built by stacking layers. The WFEM is introduced to analyze the transition frequency and to control the bending waves propagation in the structure.

According to the WFEM, only one unit cell is modeled through traditional finite elements. The dynamic equilibrium formulation of a unit cell can be written as:

$$\mathbf{K}\mathbf{u}(t) + \mathbf{C}\frac{\partial \mathbf{u}(t)}{\partial t} + \mathbf{M}\frac{\partial^2 \mathbf{u}(t)}{\partial t^2} = \mathbf{F}, \tag{1.46}$$

where $\mathbf{K}$ and $\mathbf{M}$ denote the stiffness matrix and mass matrix, respectively, $\mathbf{C} = \eta\mathbf{K}/\omega$ is identified as damping matrix considering damping lose factor η, $\mathbf{u}$ is vector of nodal displacement/rotation/torsion, $\mathbf{F}$ represents force/moment/torque. Assuming that $\mathbf{u}$ and $\mathbf{F}$ are harmonic, the dynamic stiffness matrix will be written as $\mathbf{D} = \tilde{\mathbf{K}} - \omega^2\mathbf{M}$ in frequency (ω) domain with $\tilde{\mathbf{K}} = (1+\mathrm{i}\eta)\mathbf{K}$. Eq. 1.46 can be re-expressed by dividing the DOFs into I (internal), Bd (boundary) DOFs. It should be noticed that the internal DOFs are not affected by external loads due to the coupling actions are restricted to its boundary only [184], as a result, $\mathbf{F}_{\mathrm{I}} = 0$, this yields:

$$\begin{bmatrix} \mathbf{D}_{\mathrm{BdBd}} & \mathbf{D}_{\mathrm{BdI}} \\ \mathbf{D}_{\mathrm{IBd}} & \mathbf{D}_{\mathrm{II}} \end{bmatrix} \begin{pmatrix} \hat{\mathbf{u}}_{\mathrm{Bd}} \\ \hat{\mathbf{u}}_{\mathrm{I}} \end{pmatrix} = \begin{pmatrix} \hat{\mathbf{F}}_{\mathrm{Bd}} \\ \mathbf{0} \end{pmatrix}, \tag{1.47}$$

where $\hat{\mathbf{u}}$ and $\hat{\mathbf{F}}$ are the amplitudes of $\mathbf{u}$ and $\mathbf{F}$, respectively. After dynamic condensation, the dynamic equilibrium equation will be written as:

$$\mathbb{D}\hat{\mathbf{u}}_{\mathrm{Bd}} = \hat{\mathbf{F}}_{\mathrm{Bd}}, \tag{1.48}$$

where $\mathbb{D} = \mathbf{D}_{\mathrm{BdBd}} - \mathbf{D}_{\mathrm{BdI}}\mathbf{D}_{\mathrm{II}}^{-1}\mathbf{D}_{\mathrm{IBd}}$ is the condensed form of dynamic stiffness matrix, subscript Bd represents the DOFs on the boundaries of the unit cell.

1.4.3.1 One-dimensional WFEM

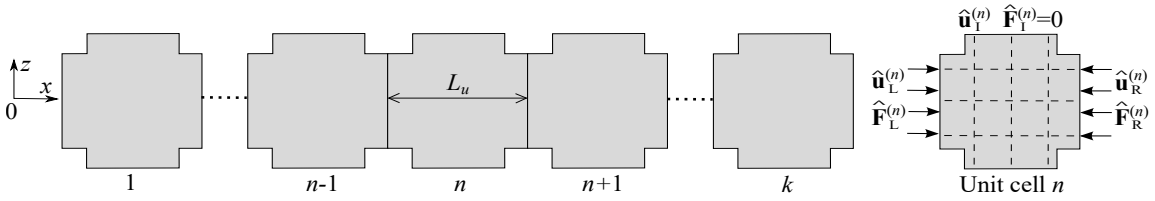

Fig. 1.10. Periodic structure constituted by k unit cell.

Considering an elastic structure with identical unit cells that arranged in x direction, as presented in Fig.1.10, the length of each unit cell is L_u, which corresponds to a small length of wave-guide or a unit length of periodic structure and only one unit cell is modeled. The left boundary and right boundary of the unit cell are meshed with same number of DOFs. There exist two forms to illustrate the wave propagation: direct form and inverse form.

(1) Direct form of WFEM1D :

Using Eq. 1.48, the vectors of nodal displacement of the right boundary of a cell related to the left boundary can be expressed, as follows:

$$\hat{\mathbf{d}}_{\mathrm{R}}^{(n)} = \mathbf{S}\hat{\mathbf{d}}_{\mathrm{L}}^{(n)}, \tag{1.49}$$

where $\hat{\mathbf{d}}_{\mathrm{L}}^{(n)} = \left[\left(\hat{\mathbf{u}}_{\mathrm{L}}^{(n)}\right)^{\mathrm{T}}\left(-\hat{\mathbf{F}}_{\mathrm{L}}^{(n)}\right)^{\mathrm{T}}\right]^{\mathrm{T}}$ and $\hat{\mathbf{d}}_{\mathrm{R}}^{(n)} = \left[\left(\hat{\mathbf{u}}_{\mathrm{R}}^{(n)}\right)^{\mathrm{T}}\left(\hat{\mathbf{F}}_{\mathrm{R}}^{(n)}\right)^{\mathrm{T}}\right]^{\mathrm{T}}$ representing the left and right state vectors for the unit cell n are $2m\times 1$ state vectors. $\mathbf{S}$ is a $2m \times 2m$ symplectic transfer matrix expressed as:

$$\mathbf{S} = \begin{bmatrix} -\mathbb{D}_{\mathrm{LR}}^{-1}\mathbb{D}_{\mathrm{LL}} & -\mathbb{D}_{\mathrm{LR}}^{-1} \\ \mathbb{D}_{\mathrm{RL}} - \mathbb{D}_{\mathrm{RR}}\mathbb{D}_{\mathrm{LR}}^{-1}\mathbb{D}_{\mathrm{LL}} & -\mathbb{D}_{\mathrm{RR}}\mathbb{D}_{\mathrm{LR}}^{-1} \end{bmatrix}. \tag{1.50}$$

Considering two consecutive cells $n-1$ and n, the coupling conditions of displacement

should be satisfied in the interface between them:

$$\hat{\mathbf{q}}_{\mathrm{R}}^{(n-1)} = \hat{\mathbf{q}}_{\mathrm{L}}^{(n)},\ \hat{\mathbf{F}}_{\mathrm{R}}^{(n-1)} + \hat{\mathbf{F}}_{\mathrm{L}}^{(n)} = 0, \tag{1.51}$$

where the superscripts $(n-1)$ and n are used to label the unit cell which the vector is referred to. The application of those relations to Eq. 1.49 allows one to establish a link between kinematic/kinetic (or mechanical) quantities on the left boundaries of unit cells $n-1$ and n as follows:

$$\hat{\mathbf{u}}_{\mathrm{L}}^{(n)} = \mathbf{S}\hat{\mathbf{u}}_{\mathrm{L}}^{(n-1)}. \tag{1.52}$$

The state vector $\hat{\mathbf{u}}^{(n)}$ can be expanded into a set of $2m$ linearly independent vectors, which can be written as:

$$\hat{\mathbf{u}}^{(n)} = \sum_{j=1}^{2m} \phi_j Q_j^{(n)}, \tag{1.53}$$

where $\{\phi_j\}_{j=1,\ldots,2m}$ and $\{Q_j\}_{j=1,\ldots,2m}$ are indexed families of vectors of wave shapes and wave amplitudes, respectively, m is a discrete index, called the band index. The wave amplitudes between two consecutive cells $n-1$ and n have a relation that pointed by Bloch's theorem for periodic structures given by:

$$Q_j^{(n)} = \lambda_j Q_j^{(n-1)}, \tag{1.54}$$

where $\lambda_j = e^{-\mathrm{i}\kappa_j L_u}$,$\kappa_j$ is the wavenumber, L_u is a cell length. Affiliated with Eq. 1.53, the state vector related to the left boundary of a cell n can be written as:

$$\mathbf{u}_{\mathrm{L}}^{(k)} = \sum_{j=1}^{2m} \phi_j e^{-\mathrm{i}\kappa_j L_u} Q_j^{(n-1)}. \tag{1.55}$$

Whereupon, substituting Eq. 1.54 into Eq. 1.55, free wave propagation characteristics are represented by solving symplectic eigenvalue problem:

$$\mathbf{S}\phi_j = \lambda_j \phi_j. \tag{1.56}$$

According to the preceding section, the solutions $\{\lambda_j \phi_j\}_{j=1,\ldots,2m}$ of the symplectic eigenvalue problems are referred to as the waves modes of the periodic structure. The eigenvalues $\{\lambda_j\}_{j=1,\ldots,2m}$ are the propagation constants which are related to the wave-numbers $\{\kappa_j\}_{j=1,\ldots,2m}$.

(2) Inverse form of WFEM1D :

Suppose a real value of wavenumber is assigned as first. The value of λ can then be derived since $\lambda = \exp(-\mathrm{i}\kappa L_u)$. According to periodic structures theory, for free wave propagation, we

have:

$$\hat{\mathbf{u}}_{\mathrm{R}}^{(n)} = \lambda \hat{\mathbf{u}}_{\mathrm{L}}^{(n)},\ \hat{\mathbf{F}}_{\mathrm{R}}^{(n)} = -\lambda \hat{\mathbf{F}}_{\mathrm{L}}^{(n)}. \tag{1.57}$$

According to the Bloch's theorem, the DOFs' relations and forces' relations can be expressed separately as:

$$\begin{pmatrix} \hat{\mathbf{u}}_{\mathrm{L}} \\ \hat{\mathbf{u}}_{\mathrm{R}} \\ \hat{\mathbf{u}}_{\mathrm{I}} \end{pmatrix} = \mathbf{\Lambda}_R \begin{pmatrix} \hat{\mathbf{u}}_{\mathrm{L}} \\ \hat{\mathbf{u}}_{\mathrm{R}} \end{pmatrix},\ \mathbf{\Lambda}_L \begin{pmatrix} \hat{\mathbf{F}}_{\mathrm{L}} \\ \hat{\mathbf{F}}_{\mathrm{R}} \\ \hat{\mathbf{0}} \end{pmatrix} = \mathbf{0}, \tag{1.58}$$

with

$$\mathbf{\Lambda}_R = \begin{bmatrix} \mathbf{I}_s & \mathbf{0} \\ \lambda \mathbf{I}_s & \mathbf{0} \\ \mathbf{0} & \mathbf{I}_I \end{bmatrix},\ \mathbf{\Lambda}_L = \begin{bmatrix} \mathbf{I}_s & \lambda^{-1}\mathbf{I}_s & \mathbf{0} \\ \mathbf{0} & \mathbf{0} & \mathbf{I}_I \end{bmatrix}, \tag{1.59}$$

where $\mathbf{I}_s$ and $\mathbf{I}_I$ denote the identity matrices of size s and I. Substituting Eq. 1.58 into Eq. 1.47 yields:

$$\mathbf{\Lambda}_L(\tilde{\mathbf{K}} - \omega^2 \mathbf{M})\mathbf{\Lambda}_R \begin{pmatrix} \hat{\mathbf{u}}_{\mathrm{L}} \\ \hat{\mathbf{u}}_{\mathrm{I}} \end{pmatrix} = \mathbf{0}. \tag{1.60}$$

Since κ is supposed to be real, the equation deduced above will become a standard and linear eigen-problem of ω^2. The size of problem is the sum of the size of $\hat{\mathbf{u}}_{\mathrm{L}}$ and $\hat{\mathbf{u}}_{\mathrm{I}}$. No numerical issue will appear in this case, however here should be noted that the attenuation of waves can not be predicted by WFEM inverse form.

1.4.3.2 Two-dimensional WFEM

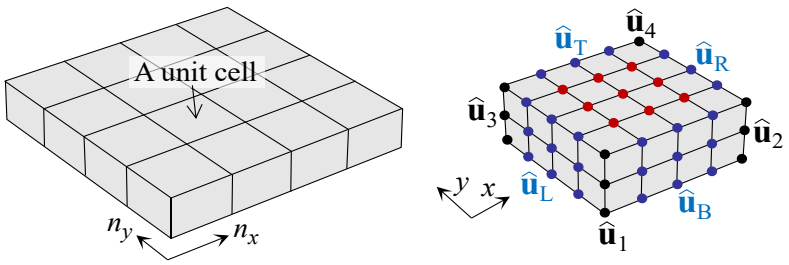

(a) 2D periodic structure (b) DOFs in a unit cell

Fig. 1.11. 2D periodic structure and its unit cells.

A scheme for 2D periodic structure and its unit cell is given in Fig.1.11. The nodes in the unit cell are divided into six parts DOFs: four corners, left, bottom, right, top and internal DOFs. They are classified by the amplitudes of nodal displacements: $[\hat{\mathbf{u}}_{\mathrm{Bd}}\ \hat{\mathbf{u}}_{\mathrm{I}}] = [\hat{\mathbf{u}}_1\ \hat{\mathbf{u}}_2\ \hat{\mathbf{u}}_3\ \hat{\mathbf{u}}_4\ \hat{\mathbf{u}}_{\mathrm{L}}\ \hat{\mathbf{u}}_{\mathrm{B}}\ \hat{\mathbf{u}}_{\mathrm{R}}\ \hat{\mathbf{u}}_{\mathrm{T}}\ \hat{\mathbf{u}}_{\mathrm{I}}]$. It should be pointed that the nodal forces are classified in the same way.

According to the periodic structures theory, the nodal DOFs are related through propagation

constants λ_x and λ_y:

$$\hat{\mathbf{u}}_2 = \lambda_x \hat{\mathbf{u}}_1,\ \hat{\mathbf{u}}_3 = \lambda_y \hat{\mathbf{u}}_1,\ \hat{\mathbf{u}}_4 = \lambda_x \lambda_y \hat{\mathbf{u}}_1,\ \hat{\mathbf{u}}_{\mathrm{R}} = \lambda_x \hat{\mathbf{u}}_{\mathrm{L}},\ \hat{\mathbf{u}}_{\mathrm{T}} = \lambda_y \hat{\mathbf{u}}_{\mathrm{B}}. \tag{1.61}$$

In addition, for free wave propagation, the sum of nodal forces of all the elements connected to nodes 1, L, B is zero, one arrives:

$$\begin{aligned} &\hat{\mathbf{F}}_1 + \hat{\mathbf{F}}_2 \lambda_x^{-1} + \hat{\mathbf{F}}_3 \lambda_y^{-1} + \hat{\mathbf{F}}_4 \lambda_x^{-1} \lambda_y^{-1} = 0, \\ &\hat{\mathbf{F}}_{\mathrm{L}} + \hat{\mathbf{F}}_{\mathrm{R}} \lambda_x^{-1} = 0, \\ &\hat{\mathbf{F}}_{\mathrm{B}} + \hat{\mathbf{F}}_{\mathrm{T}} \lambda_y^{-1} = 0. \end{aligned} \tag{1.62}$$

(1) Direct form of WFEM2D :

The internal DOFs of the unit cell are condensed. For the boundary nodes:

$$\hat{\mathbf{u}}_{\mathrm{Bd}} = \hat{\mathbf{\Lambda}}_R \begin{pmatrix} \hat{\mathbf{u}}_1 \\ \hat{\mathbf{u}}_{\mathrm{L}} \\ \hat{\mathbf{u}}_{\mathrm{B}} \end{pmatrix}, \tag{1.63}$$

with

$$\hat{\mathbf{\Lambda}}_R = \begin{bmatrix} \mathbf{I}_s & \mathbf{0} & \mathbf{0} \\ \lambda_x \mathbf{I}_s & \mathbf{0} & \mathbf{0} \\ \lambda_y \mathbf{I}_s & \mathbf{0} & \mathbf{0} \\ \lambda_x \lambda_y \mathbf{I}_s & \mathbf{0} & \mathbf{0} \\ \mathbf{0} & \mathbf{I}_{sm} & \mathbf{0} \\ \mathbf{0} & \mathbf{0} & \mathbf{I}_{sn} \\ \mathbf{0} & \lambda_x \mathbf{I}_{sm} & \mathbf{0} \\ \mathbf{0} & \mathbf{0} & \lambda_y \mathbf{I}_{sn} \end{bmatrix}. \tag{1.64}$$

Similar for the nodal forces:

$$\hat{\mathbf{\Lambda}}_L \hat{\mathbf{F}}_{\mathrm{Bd}} = \mathbf{0}, \tag{1.65}$$

with

$$\hat{\mathbf{\Lambda}}_L = \begin{bmatrix} \mathbf{I}_s & \lambda_x^{-1}\mathbf{I}_s & \lambda_y^{-1}\mathbf{I}_s & \lambda_x^{-1}\lambda_y^{-1}\mathbf{I}_s & \mathbf{0} & \mathbf{0} & \mathbf{0} & \mathbf{0} \\ \mathbf{0} & \mathbf{0} & \mathbf{0} & \mathbf{0} & \mathbf{I}_{sm} & \mathbf{0} & \lambda_x^{-1}\mathbf{I}_{sm} & \mathbf{0} \\ \mathbf{0} & \mathbf{0} & \mathbf{0} & \mathbf{0} & \mathbf{0} & \mathbf{I}_{sn} & \mathbf{0} & \lambda_y^{-1}\mathbf{I}_{sn} \end{bmatrix}, \tag{1.66}$$

where $\mathbf{I}_s$, $\mathbf{I}_{sn}$ and $\mathbf{I}_{sm}$ represent the identity matrix of size s, sn, sm respectively. So the equation

of motion Eq.1.48 becomes:

$$\hat{\mathbf{\Lambda}}_L \mathbb{D} \hat{\mathbf{\Lambda}}_R \begin{pmatrix} \hat{\mathbf{u}}_1 \\ \hat{\mathbf{u}}_\mathrm{L} \\ \hat{\mathbf{u}}_\mathrm{B} \end{pmatrix} = \mathbf{0}. \tag{1.67}$$

Suppose one of (λ_x, λ_y) is given, for example λ_y. Eq.1.67 then becomes a quadratic eigenvalue problem in λ_x as follows:

$$\frac{1}{\lambda_x} \left(\lambda_x^2 \begin{bmatrix} \mathbf{A}_{11} & \mathbf{A}_{1\mathrm{L}} & \mathbf{A}_{1\mathrm{B}} \\ \mathbf{A}_{\mathrm{L}1} & \mathbf{A}_{\mathrm{LL}} & \mathbf{A}_{\mathrm{LB}} \\ \mathbf{A}_{\mathrm{B}1} & \mathbf{A}_{\mathrm{BL}} & \mathbf{A}_{\mathrm{BB}} \end{bmatrix} + \lambda_x \begin{bmatrix} \mathbf{B}_{11} & \mathbf{B}_{1\mathrm{L}} & \mathbf{B}_{1\mathrm{B}} \\ \mathbf{B}_{\mathrm{L}1} & \mathbf{B}_{\mathrm{LL}} & \mathbf{B}_{\mathrm{LB}} \\ \mathbf{B}_{\mathrm{B}1} & \mathbf{B}_{\mathrm{BL}} & \mathbf{B}_{\mathrm{BB}} \end{bmatrix} + \begin{bmatrix} \mathbf{C}_{11} & \mathbf{C}_{1\mathrm{L}} & \mathbf{C}_{1\mathrm{B}} \\ \mathbf{C}_{\mathrm{L}1} & \mathbf{C}_{\mathrm{LL}} & \mathbf{C}_{\mathrm{LB}} \\ \mathbf{C}_{\mathrm{B}1} & \mathbf{C}_{\mathrm{BL}} & \mathbf{C}_{\mathrm{BB}} \end{bmatrix} \right) \hat{\mathbf{u}}_b = \mathbf{0}, \tag{1.68}$$

where $\hat{\mathbf{u}}_b$=$[(\hat{\mathbf{u}}_1)^\mathrm{T}\ (\hat{\mathbf{u}}_\mathrm{L})^\mathrm{T}\ (\hat{\mathbf{u}}_\mathrm{B})^\mathrm{T}]^\mathrm{T}$. The quadratic eigenvalue problem can be solved by using the polyeig function. The $\mathbf{A}$, $\mathbf{B}$ and $\mathbf{C}$ are addressed in Appendix A.

(2) Inverse form of WFEM2D :

For inverse form, the internal nodes are conserved since the dynamic condensation can not be performed, as a result:

$$\begin{pmatrix} \hat{\mathbf{u}}_\mathrm{Bd} \\ \hat{\mathbf{u}}_\mathrm{I} \end{pmatrix} = \mathbf{\Lambda}'_R \begin{pmatrix} \hat{\mathbf{u}}_1 \\ \hat{\mathbf{u}}_\mathrm{L} \\ \hat{\mathbf{u}}_\mathrm{B} \\ \hat{\mathbf{u}}_\mathrm{I} \end{pmatrix}, \tag{1.69}$$

with

$$\mathbf{\Lambda}'_R = \begin{bmatrix} \hat{\mathbf{\Lambda}}_R & \mathbf{0} \\ \mathbf{0} & \mathbf{I}_I \end{bmatrix}. \tag{1.70}$$

Similar for the nodal forces:

$$\mathbf{\Lambda}'_L \begin{pmatrix} \hat{\mathbf{F}}_\mathrm{Bd} \\ \mathbf{0} \end{pmatrix} = \mathbf{0}, \tag{1.71}$$

with

$$\mathbf{\Lambda}'_L = \begin{bmatrix} \hat{\mathbf{\Lambda}}_L & \mathbf{0} \\ \mathbf{0} & \mathbf{I}_I \end{bmatrix}. \tag{1.72}$$

Then, the Eq.1.47 becomes:

$$\mathbf{\Lambda}'_L (\tilde{\mathbf{K}} - \omega^2 \mathbf{M}) \mathbf{\Lambda}'_R \begin{pmatrix} \hat{\mathbf{u}}_1 \\ \hat{\mathbf{u}}_\mathrm{L} \\ \hat{\mathbf{u}}_\mathrm{B} \\ \hat{\mathbf{u}}_\mathrm{I} \end{pmatrix} = \mathbf{0}, \tag{1.73}$$

which becomes the following standard, linear eigenvalue problem in ω^2:

$$[\mathbf{K}^*(\lambda_x, \lambda_y) - \omega^2 \mathbf{M}^*(\lambda_x, \lambda_y)] \begin{pmatrix} \hat{\mathbf{u}}_1 \\ \hat{\mathbf{u}}_\mathrm{L} \\ \hat{\mathbf{u}}_\mathrm{B} \\ \hat{\mathbf{u}}_\mathrm{I} \end{pmatrix} = \mathbf{0}. \tag{1.74}$$

If we consider about the un-damped structure, $\mathbf{K}^*$ and $\mathbf{M}^*$ are positive definite Hermitian matrices. The eigvalues ω^2 for free wave propagation is real and positive. The size of the eigen-problem is the same as $[\hat{\mathbf{u}}_1^\mathrm{T}, \hat{\mathbf{u}}_\mathrm{L}^\mathrm{T}, \hat{\mathbf{u}}_\mathrm{B}^\mathrm{T}, \hat{\mathbf{u}}_\mathrm{I}^\mathrm{T}]^\mathrm{T}$.

1.4.4 Model order reduction technique

The MOR based on component mode methods are now described. The main one of these, known as Component Mode Synthesis (CMS) [113], contains two variants: the fixed interface method and the free interface method. Xie [185] presented an adaptive MOR strategy to reduce the number of DOFs. The associated computational cost is largely alleviated. Pereyra [186] discussed the application of MOR to problems in seismic petroleum exploration. The proposed method significantly reduced calculation time. What is more, an experimental research is made by Thierry [187] to compare with a numerical method based on CMS which can be applied to analyze vibro-acoustic and ultrasonic wave propagation in complex woven composites. Li [188] proposed a new gap element to illustrated the coupling properties of incompatible interface through CMS method. The natural frequencies and modal shapes obtained from proposed method match well with the ones obtained from full FE model.

In our work, the fixed interface method called Craig-Bampton method, conserving the physical DOFs of the boundary nodes, is combined with WFEM. It is easy to implement to WFEM formulation since wavenumbers are confirmed from relation between physical DOFs at different boundaries of unit cell. The inner DOFs $\hat{\mathbf{u}}_\mathrm{I}$ and boundary DOFs $\hat{\mathbf{u}}_\mathrm{Bd}$ can be expressed as:

$$\hat{\mathbf{u}} = [(\hat{\mathbf{u}}_\mathrm{Bd})^\mathrm{T},\ (\hat{\mathbf{u}}_\mathrm{I})^\mathrm{T}]^\mathrm{T}. \tag{1.75}$$

A reduced set of DOFs $\hat{\mathbf{p}}$ is defined as:

$$\hat{\mathbf{p}} = [(\hat{\mathbf{u}}_\mathrm{Bd})^\mathrm{T},\ (\hat{\mathbf{P}}_\mathrm{C})^\mathrm{T}]^\mathrm{T}, \tag{1.76}$$

in which $\hat{\mathbf{u}}$ is related to $\hat{\mathbf{p}}$ by the transfer matrix $\mathbf{B}$:

$$\begin{pmatrix} \hat{\mathbf{u}}_\mathrm{Bd} \\ \hat{\mathbf{u}}_\mathrm{I} \end{pmatrix} = \begin{bmatrix} \mathbf{I}_n & \mathbf{0} \\ \mathbf{\Phi}_\mathrm{Bd} & \mathbf{\Phi}_\mathrm{C} \end{bmatrix} \begin{pmatrix} \hat{\mathbf{u}}_\mathrm{Bd} \\ \hat{\mathbf{P}}_\mathrm{C} \end{pmatrix} = \mathbf{B} \begin{pmatrix} \hat{\mathbf{u}}_\mathrm{Bd} \\ \hat{\mathbf{P}}_\mathrm{C} \end{pmatrix}, \tag{1.77}$$

where

$$\mathbf{\Phi}_{\mathrm{Bd}} = -\tilde{\mathbf{K}}_{\mathrm{II}}^{-1}\tilde{\mathbf{K}}_{\mathrm{IBd}}. \tag{1.78}$$

The component modes $\mathbf{\Phi}_{\mathrm{C}}$ are selected among the eigenvectors $\mathbf{\Phi}_{\mathrm{I}}$:

$$(\tilde{\mathbf{K}}_{\mathrm{II}} - \omega_0^2\mathbf{M}_{\mathrm{II}})\mathbf{\Phi}_{\mathrm{I}} = 0. \tag{1.79}$$

$\mathbf{\Phi}_{\mathrm{C}}$ can choose modes into the frequency range [0, $2\omega_{max}$], where ω_{max} is the maximum frequency of interest for the wave dispersion analysis. The reduced mass and stiffness matrices are expressed as:

$$\overline{\mathbf{K}} = \mathbf{B}^{\mathrm{T}}\tilde{\mathbf{K}}\mathbf{B},\ \overline{\mathbf{M}} = \mathbf{B}^{\mathrm{T}}\mathbf{M}\mathbf{B}. \tag{1.80}$$

1.4.5 Homogenization methods

Numerous homogenization methods have been developed to study the heterogeneous materials or periodic structures. Homogenization methods can be categorized into equivalent strain energy method, mode-based method, wave-based method and asymptotic homogenization method.

The equivalent strain energy method was proposed initially by Nemat [114] to analyze periodically distributed inclusions and cylindrical geometries. Recently, Liu [189] developed a novel equivalent dynamic model based on equivalent strain energy principle to enhance the design capacity of vibration controllers. Results indicate that the equivalent beam model has accuracy for studying the dynamic properties of antenna truss. Neves [190] applied equivalent strain energy to design the periodic micro-structure of cellular materials for optimal elastic properties. A new strain energy-based method for homogenization cellular materials is developed by Gad [191]. The results agree well with those provided by a FE model. Suttakul [192] determined the bending response of 2D-lattice plates with unit cells based on equivalent strain energy. The obtained results show how the bending response can be adjusted by varying their unit-cell geometries.

According to equivalent strain energy method, an equivalent homogenized model with the same volume can replace the periodic structure with the following conditions: the stress and the strain tensors of the homogeneous structure are equivalent to the average stress and strain of the unit cell with:

$$\frac{1}{V}\int \boldsymbol{\sigma}\mathrm{d}V = \overline{\boldsymbol{\sigma}},\ \frac{1}{V}\int \boldsymbol{\varepsilon}\mathrm{d}V = \overline{\boldsymbol{\varepsilon}}, \tag{1.81}$$

where V is the volume of the unit cell. The average stress and strain of the homogenized model follow the Hooke's law:

$$\overline{\boldsymbol{\sigma}} = \mathbf{D}^{\mathrm{H}}\overline{\boldsymbol{\varepsilon}}, \tag{1.82}$$

where $\mathbf{D}$ is the effective elastic tensor of the material.

On the other hand, Jhung [193] put forward the mode-based method for determining equivalent Young's Modulus of solid plate to match the frequencies of the perforated plate. In his research, four steps are conducted:

i. Develop a FE model for homogeneous solid plate and perforated plate.

ii. Analysis the modal of perforated plate and the solid plate with original properties.

iii. Determine the frequencies ratio for the perforated plate to homogeneous solid plate.

iv. Calculate the multipliers of Young's modulus in homogeneous solid plate to match the frequencies of the perforated plate with original properties.

Furthermore, the wave-based method was proposed by Chronopoulos [194] to confirm a dynamic stiffness matrix for the modeled laminate. The advantage of the wave-based method are: (1) the global matrix can be easy to construct; (2) different boundary conditions can be conveniently adjusted; (3) high computational efficiency. Recently, the stochastic response of periodic flat and axial-symmetric structures was analysed by Errico [195] based on wave-based method. The proposed method shows the flexibility of linking the structural and fluid meshes to offer the possibility of applying a single unit cell to analyse different test-cases. Wang [196] used a piezoelectric ceramic to detect the damage of the concrete interface through the wave-based method. It shows the clear process of damage development. Liu [197] analyzed the free vibration proprieties of functionally graded material cylindrical shell with arbitrary boundary conditions by wave based method. The natural frequencies of functionally graded shell can be effected by geometric parameters, ratio of thickness to radius and ratio of length to the radius. Ling [198] used the wave based method to illustrate a general formulation of plate bending problems. The proposed method can save simulation time and help the deterministic numerical approach to be practical at a higher frequency range. Here, in order to derive the expressions for the equivalent dynamic mechanical characteristics. The classical laminated plate theory is used to give following expressions [194]:

$$D_{eq,i} = \frac{\omega^2 \rho_s}{\kappa_{f,i}^4},\ B_{eq,i} = \frac{\omega^2 \rho_s}{\kappa_{s,i}^4}, \tag{1.83}$$

in which ρ_s is the mass per unit of area, $D_{eq,i}$ is the equivalent flexural stiffness of the structure towards direction i, $B_{eq,i}$ means the equivalent shear stiffness.

Last, the asymptotic homogenization method proposed by Kalamkarov [199] is introduced here. The asymptotic homogenization method is used to develop a comprehensive micro-mechanical model with an embedded periodic grid of generally orthotropic reinforcements. Later on, a multifield asymptotic homogenization method for periodic elastic materials is established by Fantoni [200] to analyse the wave propagation. The result shows that the solution of the heterogeneous problem will have a better estimation when the order of approximation increase. Preve [201] introduced a multi-scale variational-asymptotic homogenization technol-

ogy for periodic micro-structures. The dispersion relation confirmed from the proposed method are compared with the one from Floquet-Bloch theory. Andrianov [202] studied a higher order asymptotic homogenization for dynamical problems and investigated the influence of the boundary conditions and system parameters on the structure's vibration proprieties. Bacigalupo [203] proposed a micro-polar-based asymptotic homogenization method to analyze the composite periodic micro-structures. The capabilities of the proposed method in predicting the periodic structures' behaviors are evaluated through some examples. In order to built the asymptotic homogenization model, there are three main steps as follow [199]:

i. Define the fast or microscopic variables in the domain of the unit cell.

ii. Consider the asymptotic expansions in terms of the small parameter ε.

iii. Modelling development of the homogeniztion procedure to confirm the resulting expression of the unit cell.

1.5 Conclusions

The literature survey presented in this chapter was guided on three aspects: The first is investigations on micro-sized periodic structure including engineering micro-sized periodic structures and free wave propagation characteristics in periodic structures. The second part is about existing methods to study micro-sized structures including continuum model and LSM. For continuum model, the non-local elasticity theory, micro-continuum theory, surface elasticity theory and strain gradient family theories are introduced.

The third part of this chapter described the periodic structures. A historical review of the studies on periodic structures was given in this chapter. Numerous methods have been developed during these studies. Among them, the plane-wave expansion method, modified TMM, WFEM and homogenization methods were explained. As one of the MOR techniques, the fixed interface method called Craig-Bampton method was introduced in detail.

Chapter 2

Wave motion analysis of second strain gradient elasticity through a wave finite element approach for one-dimensional structures

Chapter contents

2.1 Introduction 39
2.2 Bending vibration analysis for Euler-Bernoulli beam 40
2.2.1 Continuum model by second strain gradient elasticity 40
2.2.2 Lattice spring model by second strain gradient elasticity 44
2.3 Torsional vibration analysis for a bar 46
2.3.1 Continuum model by second strain gradient elasticity 46
2.3.2 Lattice spring model by second strain gradient elasticity 49
2.4 One-dimensional wave propagation characteristics 50
2.5 Numerical applications and discussions 51
2.5.1 Bending vibration of Euler-Bernoulli beam 51
2.5.2 Torsional vibration of a bar 55
2.6 Conclusions 58

2.1 Introduction

In this chapter, the SSG theory proposed by Mindlin is used within a WFEM framework for dynamic analysis of 1D Euler-Bernoulli bending beam and torsional bar. Firstly, strong forms

of continuum models including governing equations and boundary conditions for bending and torsion cases, respectively, are derived using Hamilton's principle. New "non-local" LSM are expounded, giving unified description of the SSG models for bending and torsion. These LSM can be regarded as a discrete micro-structural description of SSG continuum models and the resulting dynamic equations are transformed using Fourier series. Weak forms for both bending and torsion are established based on SSG theory. Subsequently, the WFEM is used to formulate the spectral problem and compute wave dispersion characteristics from one-dimensional unit-cell structures. Finally, dispersion relations and forced responses for bending and torsion are calculated by SSG and CT, and some useful conclusions are discussed.

2.2 Bending vibration analysis for Euler-Bernoulli beam

2.2.1 Continuum model by second strain gradient elasticity

Based on the SSG theory formulated by Mindlin [16], the strain energy density $\overline{\mathcal{U}}$ for an isotropic linearly elastic material is established as shown in Eq. 1.12. It should be pointed out that there is no mature experimental method to determine the higher order parameters. Some researchers [42] defined the parameters mentioned above in face centered cubic (fcc) materials by the Sutton-Chen potential atom method. The higher order parameters for Aluminum (Al),

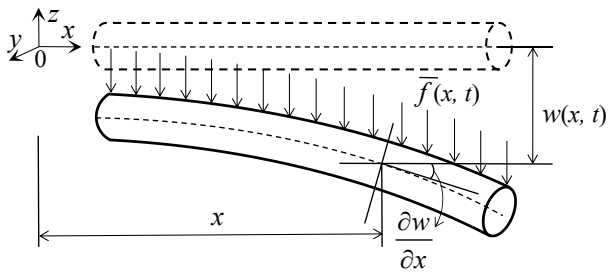

Fig. 2.1. A Euler-Bernoulli beam under Lateral distributed force.

Table 2.1. Higher order material parameters a_i (eV/Å), c_i (eV/Å).

Material	a_1	a_2	a_3	a_4	a_5	c_1	c_2	c_3
Al	0.1407	0.0027	-0.0083	0.0966	0.2584	0.5041	0.3569	0.1782
Cu	0.1833	0.0103	0.0010	0.0717	0.1891	0.8448	0.5732	0.3465
Pb	0.1039	0.0260	0.0126	0.0154	0.460	1.0991	0.6043	0.5106

Copper (Cu) and Lead (Pb) are shown in Tab. 2.1 and Tab. 2.2. In order to calculate the governing equation of a micro-sized Euler-Bernoulli bending beam, the variational principle is applied. Considering a beam on which acting a lateral distributed force $\overline{f}(x,t)$. The beam length is L as shown in Fig. 2.1. Assuming that the symmetry axis of the cross section coincides with the

Table 2.2. Higher order material parameters b_i (eV·Å).

Material	b_1	b_2	b_3	b_4	b_5	b_6	b_7
Al	0.7927	0.0644	-0.1943	-0.0009	0.0009	16.1566	48.5291
Cu	0.6612	0.0663	0.2062	0.0015	0.0015	12.6254	37.9402
Pb	0.2503	0.0154	0.0595	0.0007	0.007	2.7886	8.3842

neutral axis. According to the kinematic hypothesis, the displacement fields are as follows:

$$u_1^b = -z\frac{\partial w(x,t)}{\partial x},\ u_2^b\ = 0,\ u_3^b = w(x,t), \tag{2.1}$$

where u_1^b, u_2^b, and u_3^b mean the displacement components along x, y and z directions, respectively, superscript b of u represents bending case, $w(x,t)$ is the vertical displacement along z direction. Only nonzero components of displacement tensors are shown as:

$$\begin{aligned}
&\varepsilon_{11} = -z\frac{\partial^2 w(x,t)}{\partial x^2},\ \xi_{111} = -z\frac{\partial^3 w(x,t)}{\partial x^3},\ \xi_{311} = \xi_{131} = -\frac{\partial^2 w(x,t)}{\partial x^2},\\
&\zeta_{1111} = -z\frac{\partial^4 w(x,t)}{\partial x^4},\ \zeta_{3111} = \zeta_{1311} = \zeta_{1131} = -\frac{\partial^3 w(x,t)}{\partial x^3},\ \zeta_{1113} = \frac{\partial^3 w(x,t)}{\partial x^3}.
\end{aligned} \tag{2.2}$$

Integrating the strain energy density over its volume to obtain the beam strain potential energy as:

$$\mathcal{U} = \int_0^L \int_A \overline{\mathcal{U}} \mathrm{d}A\mathrm{d}x. \tag{2.3}$$

Whereupon, the beam strain potential energy for SSG theory can be obtained by substitution of Eq. 1.12 and Eq. 2.2 into Eq. 2.3:

$$\begin{aligned}
\mathcal{U} =& \frac{1}{2}\int_0^L \left[C_1^b \left(\frac{\partial^2 w(x,t)}{\partial x^2} \right)^2 + C_2^b \left(\frac{\partial^3 w(x,t)}{\partial x^3} \right)^2 + C_3^b \left(\frac{\partial^4 w(x,t)}{\partial x^4} \right)^2 \right.\\
&\left. + C_4^b \frac{\partial^2 w(x,t)}{\partial x^2} \frac{\partial^4 w(x,t)}{\partial x^4} \right] \mathrm{d}x,
\end{aligned} \tag{2.4}$$

where $C_1^b = 2(a_1 - a_2 + a_3 + 3a_4 - a_5)A + EI$, $C_2^b = 2(a_1 + a_2 + a_3 + a_4 + a_5)I + 4(b_2 - b_4 + b_5 + 2b_6)A$, $C_3^b = 2(b_1 + b_2 + b_3 + b_4 + b_5 + b_6 + b_7)I$, $C_4^b = 3(c_1 + c_2 + c_3)I$, A is the area of cross section, I means the moment of inertia. On the other hand, the beam kinetic energy including classical part and non-classical part is expressed as [204]:

$$\mathcal{T} = \frac{1}{2}\rho \int_\Omega \left(\dot{\mathbf{U}} \cdot \dot{\mathbf{U}} + l_1^2 \nabla\dot{\mathbf{U}} : \nabla\dot{\mathbf{U}} + l_2^4 \nabla\nabla\dot{\mathbf{U}} \vdots \nabla\nabla\dot{\mathbf{U}} \right) \mathrm{d}\Omega, \tag{2.5}$$

where l_1 and l_2 are higher-order length-scale parameters. In our work, the form of kinetic energy is simplified to consider the classical part only, whose applications can be found in

[107, 205, 206]. As a result, the beam kinetic energy will be simplified as:

$$\mathcal{T} = \frac{1}{2}\int_0^L \rho A \left(\frac{\partial w(x,t)}{\partial t}\right)^2 \mathrm{d}x, \tag{2.6}$$

where ρ denotes the linear mass density.

The work done by external classical force and higher-order forces, $\mathcal{W}$, can be established in the variation form as:

$$\begin{aligned}\delta\mathcal{W} = \int_0^L \overline{f}(x,t)\delta w(x,t)\mathrm{d}x + f_0\delta w(x,t)|_{x=0}^{L} + f_1\delta\left(\frac{\partial w(x,t)}{\partial x}\right)\Big|_{x=0}^{L} \\ + f_2\delta\left(\frac{\partial^2 w(x,t)}{\partial x^2}\right)\Big|_{x=0}^{L} + f_3\delta\left(\frac{\partial^3 w(x,t)}{\partial x^3}\right)\Big|_{x=0}^{L},\end{aligned} \tag{2.7}$$

where $\overline{f}$, and f_0 denote the classical forces, $f_{1,2,3}$ are the higher order forces of the micro-beam.

Next, the Hamilton's principle is used to calculate the strong forms of the Euler-Bernoulli beam for SSG theory as follows:

$$\int_{t_1}^{t_2}(\delta\mathcal{U} - \delta\mathcal{W} - \delta\mathcal{T})\mathrm{d}t = 0, \tag{2.8}$$

where $\delta\mathcal{U}$ is the variational form of strain energy, $\delta\mathcal{T}$ means the variational form of kinetic energy. Then doing mathematical calculations according to the variation method by substituting equations Eq. 2.4, 2.6, and 2.7 into Eq. 2.8, one obtains:

$$C_1^b\frac{\partial^4 w(x,t)}{\partial x^4} + (C_4^b - C_2^b)\frac{\partial^6 w(x,t)}{\partial x^6} + C_3^b\frac{\partial^8 w(x,t)}{\partial x^8} - \overline{f}(x,t) = \rho A\frac{\partial^2 w(x,t)}{\partial t^2}. \tag{2.9}$$

Additionally, the boundary conditions at the ends of Euler-Bernoulli beam are extracted:

$$\begin{aligned}
&-C_1^b\frac{\partial^3 w(x,t)}{\partial x^3} - (C_4^b - C_2^b)\frac{\partial^5 w(x,t)}{\partial x^5} - C_3^b\frac{\partial^7 w(x,t)}{\partial x^7} = f_0 \text{ or } \delta w(x,t) = 0, \text{ on } \Omega = \{0, L\};\\
&-C_1^b\frac{\partial^2 w(x,t)}{\partial x^2} - (C_4^b - C_2^b)\frac{\partial^4 w(x,t)}{\partial x^4} + C_3^b\frac{\partial^6 w(x,t)}{\partial x^6} = f_1 \text{ or } \delta\frac{\partial w(x,t)}{\partial x} = 0, \text{ on } \partial\Omega;\\
&-(\frac{1}{2}C_4^b - C_2^b)\frac{\partial^3 w(x,t)}{\partial x^3} + C_3^b\frac{\partial^5 w(x,t)}{\partial x^5} = f_2 \text{ or } \delta\frac{\partial^2 w(x,t)}{\partial x^2} = 0, \text{ on } \partial\Omega;\\
&\frac{1}{2}C_4^b\frac{\partial^2 w(x,t)}{\partial x^2} + C_3^b\frac{\partial^4 w(x,t)}{\partial x^4} = f_3 \text{ or } \delta\frac{\partial^3 w(x,t)}{\partial x^3} = 0, \text{ on } \partial\Omega.
\end{aligned} \tag{2.10}$$

Then, transforming strong form into weak form. In the FEM, the displacement $w(x,t)$ inside of an element at point $x \in R^2$ could be expressed by providing the values $\mathbf{u}^{(e)b}$ of nodal

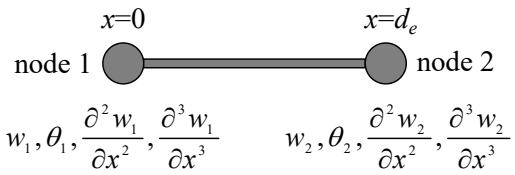

Fig. 2.2. Definition of nodal DOFs, nodal numbers and coordinate for 1D.

degree of freedoms (DOFs) vector and shape function $\mathbf{N}^b(x)$, as follows:

$$w(x,t) = \mathbf{N}^b(x)\mathbf{u}^{(e)b}(t), \tag{2.11}$$

where the sizes of $\mathbf{u}^{(e)b}$ and $\mathbf{N}^b$ are $p \times 1$ and $1 \times p$, respectively, and p means the DOFs number. In Eq. 2.11, the form of the interpolation function determines $\mathbf{u}^{(e)b}$, $\mathbf{N}^b$ and p. The C^3 continuum Hermite interpolation function that guarantees the higher-order strain field and displacement field smooth and continuous is used in Eq. 2.11. The nodal DOFs, nodal numbers and coordinate of 1D Hermite element are presented in Fig. 2.2. For 1D C^3 continuum Hermite element (element length is d_e), there are four DOFs, $w_i, \theta_i, \frac{\partial^2 w_i}{\partial x^2}, \frac{\partial^3 w_i}{\partial x^3}, i = 1, 2$, on each node. The Hermite shape functions corresponding to the eight DOFs of the 1D element can be expressed as:

$$\begin{aligned}
&\mathrm{N}_1^0 = 1 - 35\frac{x^4}{d_e^4} + 84\frac{x^5}{d_e^5} - 70\frac{x^6}{d_e^6} + 20\frac{x^7}{d_e^7}, \ \mathrm{N}_2^0 = 35\frac{x^4}{d_e^4} - 84\frac{x^5}{d_e^5} + 70\frac{x^6}{d_e^6} - 20\frac{x^7}{d_e^7},\\
&\mathrm{N}_1^1 = x - 20\frac{x^4}{d_e^3} + 45\frac{x^5}{d_e^4} - 36\frac{x^6}{d_e^5} + 10\frac{x^7}{d_e^6}, \ \mathrm{N}_2^1 = -15\frac{x^4}{d_e^3} + 39\frac{x^5}{d_e^4} - 34\frac{x^6}{d_e^5} + 10\frac{x^7}{d_e^6},\\
&\mathrm{N}_1^2 = \frac{x^2}{2} - 5\frac{x^4}{d_e^2} + 10\frac{x^5}{d_e^3} - 15\frac{x^6}{d_e^4} + 2\frac{x^7}{d_e^5}, \quad \mathrm{N}_2^2 = 5\frac{x^4}{d_e^2} - 7\frac{x^5}{d_e^3} + 13\frac{x^6}{d_e^4} - 2\frac{x^7}{d_e^5},\\
&\mathrm{N}_1^3 = \frac{x^3}{6} - 2\frac{x^4}{3d_e} + \frac{x^5}{d_e^2} - 2\frac{x^6}{3d_e^3} + \frac{x^7}{6d_e^4}, \qquad \mathrm{N}_2^3 = -\frac{x^4}{6d_e} + \frac{x^5}{2d_e^2} - \frac{x^6}{2d_e^3} + \frac{x^7}{6d_e^4},
\end{aligned} \tag{2.12}$$

where the subscript and superscript of $\mathbf{N}$ in Eq. 2.12 denote the nodal numbers and the order of the derivative with respect to coordinate $x \in [0, d_e]$, respectively. Substituting Eq. 2.11 into equilibrium equation Eq. 2.9, then doing integration to the resulting formula by the Galerkin's approach leads to:

$$\begin{aligned}
&\left[\int_0^{d_e} (\mathbf{N}^b)^{\mathrm{T}} \left(C_1^b \frac{\mathrm{d}^4 \mathbf{N}^b}{\mathrm{d}x^4} + (C_4^b - C_2^b)\frac{\mathrm{d}^6 \mathbf{N}^b}{\mathrm{d}x^6} + C_3^b \frac{\mathrm{d}^8 \mathbf{N}^b}{\mathrm{d}x^8} \right) \mathrm{d}x \right] \mathbf{u}^{(e)b} - \int_0^{d_e} (\mathbf{N}^b)^{\mathrm{T}} \overline{f}(x,t) \mathrm{d}x \\
&= \left(\int_0^{d_e} (\mathbf{N}^b)^{\mathrm{T}} \rho A \mathbf{N}^b \mathrm{d}x \right) \ddot{\mathbf{u}}^{(e)b},
\end{aligned} \tag{2.13}$$

in which the dot symbol over $\mathbf{u}^{(e)b}$ indicates the second derivative with respect to the time. In order to illustrate the weak form of Eq. 2.9, the part-by-part integration is used and the result

can be obtained as follows:

$$\mathbf{K}^{(e)b}\mathbf{u}^{(e)b} - \mathbf{F}^{(e)b} = \mathbf{M}^{(e)b}\ddot{\mathbf{u}}^{(e)b}, \tag{2.14}$$

where $\mathbf{K}^{(e)b}$ and $\mathbf{M}^{(e)b}$ represent the element stiffness matrix and mass matrix, respectively, $\mathbf{F}^{(e)b}$ denotes the element force vector for bending. Finally, the aforementioned matrices and vector are derived as:

$$\begin{aligned}
\mathbf{M}^{(e)b} &= \rho A \int_0^{d_e} (\mathbf{N}^b)^{\mathrm{T}} \mathbf{N}^b \mathrm{d}x, \\
\mathbf{K}^{(e)b} &= \int_0^{d_e} \left[C_1^b \left((\mathbf{N}^b)'' \right)^{\mathrm{T}} (\mathbf{N}^b)'' + (C_2^b - C_4^b) \left((\mathbf{N}^b)''' \right)^{\mathrm{T}} (\mathbf{N}^b)''' + C_3^b \left((\mathbf{N}^b)'''' \right)^{\mathrm{T}} (\mathbf{N}^b)'''' \right] \mathrm{d}x, \\
\mathbf{F}^{(e)b} &= \int_0^{d_e} (\mathbf{N}^b)^{\mathrm{T}} \overline{f}(x,t) \mathrm{d}x + f_0 \mathbf{N}^b|_{\partial\Omega_{f_0}} + f_1 (\mathbf{N}^b)'|_{\partial\Omega_{f_1}} + f_2 (\mathbf{N}^b)''|_{\partial\Omega_{f_2}} + f_3 (\mathbf{N}^b)'''|_{\partial\Omega_{f_3}},
\end{aligned} \tag{2.15}$$

where superscript $(')$ is partial derivative with respect to x. It is noted that ensuring the correctness of correspondent relations between the local numbering and global numbering of DOFs is a prerequisite, especially owing to the strict regularity of basis functions.

2.2.2 Lattice spring model by second strain gradient elasticity

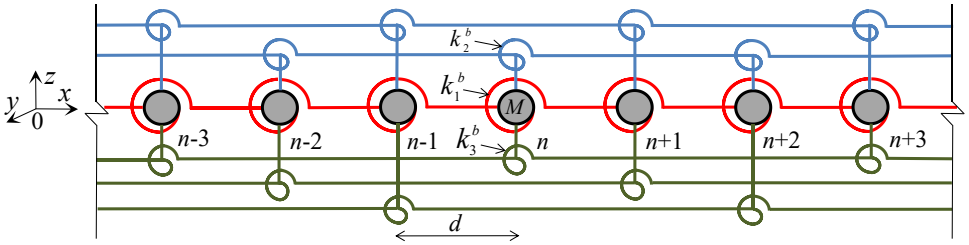

(a) LSM from Euler beam with bending coupling constants k_1^b (red line: nearest neighbor interaction), k_2^b (blue line: next-nearest neighbor interaction) and k_3^b (green line: next-next-nearest neighbor interaction) and the distance d and the mass $M = \rho A d$.

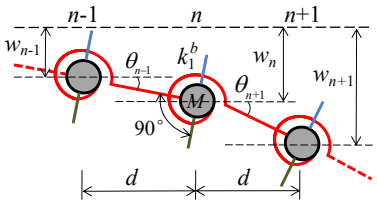

(b) The schematic deformed shape of nodes $n-1$, n and $n+1$.

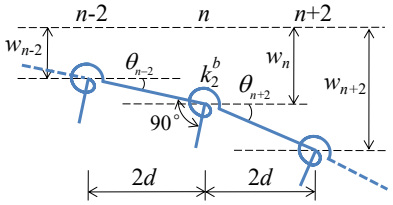

(c) The schematic deformed shape of nodes $n-2$, n and $n+2$.

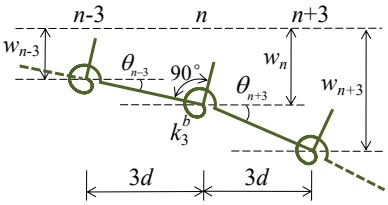

(d) The schematic deformed shape of nodes $n-3$, n and $n+3$.

Fig. 2.3. Sketch of a LSM beam.

In this part, the fundamentals of Euler–Bernoulli theory and "non-local" LSM are used to discretize the beam into a series of identical elements, as shown in Fig. 2.3, P is the total number

of lattice nodes. This LSM can reflect the mechanical response of the continuum structure when the length between each node at small scale and P is large enough. The DOFs on each node are displacement in z direction and rotation angle in $x0y$ plane. From Fig. 2.3(b), 2.3(c), 2.3(d), the total rotation angle of node n can be presented by displacement components as:

$$\Delta\theta_i = \frac{w_{n+i} - w_n}{id} - \frac{w_n - w_{n-i}}{id}, (i = 1, 2, 3). \tag{2.16}$$

The governing equation of motion at node n for a LSM of Euler beam can be illustrated by applying Lagrange equation [207] in z direction as:

$$\frac{\partial \mathcal{L}}{\partial w_n} - f_n = \frac{\mathrm{d}}{\mathrm{d}t}\left(\frac{\partial \mathcal{L}}{\partial \dot{w}_n}\right), \tag{2.17}$$

where f_n is an externally load applied at node n in z direction. $\mathcal{L}$=$\mathcal{T}$-$\mathcal{U}$ means the lagrangian that composed of the kinetic energy ($\mathcal{T}$) and potential energy ($\mathcal{U}$), where,

$$\begin{aligned} \mathcal{T} &= \frac{1}{2}M\sum_{n=1}^{P}\dot{w}_n^2, \\ \mathcal{U} &= \frac{1}{2}k_1^b\sum_{n=1}^{P}(\Delta\theta_1)^2 + \frac{1}{2}k_2^b\sum_{n=1}^{P}(\Delta\theta_2)^2 + \frac{1}{2}k_3^b\sum_{n=1}^{P}(\Delta\theta_3)^2. \end{aligned} \tag{2.18}$$

The lattice equation of motion for node n can be calculated by replacing Eq. 2.16 and Eq. 2.18 into Eq. 2.17 as:

$$\begin{aligned} &\frac{k_1^b}{d^3}\left(w_{n-2} - 4w_{n-1} + 6w_n - 4w_{n+1} + w_{n+2}\right) + \frac{k_2^b}{(2d)^3}\left(w_{n-4} - 4w_{n-2} + 6w_n - 4w_{n+2}\right. \\ &\left.+w_{n+4}\right) + \frac{k_3^b}{(3d)^3}\left(w_{n-6} - 4w_{n-3} + 6w_n - 4w_{n+3} + w_{n+6}\right) - f_n = M\frac{\mathrm{d}^2 w_n(t)}{\mathrm{d}t^2}. \end{aligned} \tag{2.19}$$

Subsequently, the Fourier series transform approach is used to derive a continuous equation $w(x,t)$ from the LSM $w_n(t)$. The process from a LSM to a continuum model was defined as [110]:

(1) Assuming $w_n(t)$ is the Fourier coefficient of field $\widehat{w}(\kappa,t)$, and defining $\mathfrak{F}_\Delta$ as the Fourier series transform:

$$\widehat{w}(\kappa,t) = \sum_{n=-\infty}^{+\infty} w_n(t)e^{-i\kappa x_n} = \mathfrak{F}_\Delta\left(w_n(t)\right). \tag{2.20}$$

(2) Using Taylor series expansion for sine function by limiting $d \to 0$:

$$\widetilde{w}(\kappa,t) = \lim_{d\to 0}\widehat{w}(\kappa,t). \tag{2.21}$$

(3) The inverse Fourier transform $\mathfrak{F}^{-1}$:

$$w(x,t)=\frac{1}{2\pi}\int_{-\infty}^{+\infty}\widetilde{w}(x,t)e^{\mathrm{i}\kappa x}\mathrm{d}\kappa=\mathfrak{F}^{-1}\left(\widetilde{w}(x,t)\right), \tag{2.22}$$

where $x_n = dn$, κ is defined as wavenumber which will be discussed later. These three steps aforementioned was proved in [110, 208]. And the detail for calculating dynamic continuum equation $w(x,t)$ from LSM addressed in Appendix B, as a result:

$$\begin{aligned}&L_4^b\frac{\partial^4 w(x,t)}{\partial x^4}+L_6^b\frac{\partial^6 w(x,t)}{\partial x^6}+L_8^b\frac{\partial^8 w(x,t)}{\partial x^8}+o\left(L_i^b\frac{\partial^i w(x,t)}{\partial x^i}\right)-\overline{f}(x,t)\\ =&\rho A\frac{\partial^2 w(x,t)}{\partial t^2},(i=10,12,...),\end{aligned} \tag{2.23}$$

with $L_4^b = k_1+2k_2^b+3k_3^b$, $L_6^b = -\left(\frac{k_1^b}{6}+\frac{4k_2^b}{3}+\frac{9k_3^b}{2}\right)d^2$, $L_8^b = \left(\frac{k_1^b}{80}+\frac{2k_2^b}{5}+\frac{243k_3^b}{80}\right)d^4$, $L_{10}^b = -\left(\frac{17k_1^b}{30240}+\frac{68k_2^b}{945}+\frac{1377k_3^b}{1120}\right)d^6$,.... The convergence condition for Eq. 2.23 is defined as:

$$\left|L_{10}^b\frac{\partial^{10}w(x,t)}{\partial x^{10}}\middle/L_8^b\frac{\partial^8 w(x,t)}{\partial x^8}\right|<1. \tag{2.24}$$

For the continuum model of Eq. 2.23, the displacement solution is $w(x,t) = w_0 e^{i(\omega t-\kappa x)}$ [209], where w_0 is amplitude, ω means angular frequency. Replacing this solution into Eq. 2.24, as a result: the Eq. 2.24 holds when the node number $P \geq \pi+1$ (here P should be infinite or large enough), then ignore higher order part, Eq. 2.23 will be written as:

$$L_4^b\frac{\partial^4 w(x,t)}{\partial x^4}+L_6^b\frac{\partial^6 w(x,t)}{\partial x^6}+L_8^b\frac{\partial^8 w(x,t)}{\partial x^8}-\overline{f}(x,t)=\rho A\frac{\partial^2 w(x,t)}{\partial t^2}. \tag{2.25}$$

Compare Eq. 2.25 with Eq. 2.9, the first 3 parts should be:

$$L_4^b = C_1^b,\ L_6^b = C_4^b - C_2^b,\ L_8^b = C_3^b, \tag{2.26}$$

with $k_1^b = \frac{3C_1^b}{2}+\frac{13(C_4^b-C_2^b)}{4d^2}+\frac{10C_3^b}{3d^4}$, $k_2^b = -\frac{3C_1^b}{10}-\frac{2(C_4^b-C_2^b)}{d^2}-\frac{8C_3^b}{3d^4}$, $k_3^b = \frac{C_1^b}{30}+\frac{(C_4^b-C_2^b)}{4d^2}+\frac{2C_3^b}{3d^4}$. Then, replacing Eq. 2.26 into Eq. 2.15, the weak formulations from LSM will be derived.

2.3 Torsional vibration analysis for a bar

2.3.1 Continuum model by second strain gradient elasticity

In order to derive the governing or differential equation of torsional problem associated with a micro-bar. The variational principal in the context of SSG theory is applied. Consider a bar of length L with distributed torque $\overline{\Gamma}(x,t)$ acting as shown in Fig. 2.4. Suppose that the

neutral axis coincides with the axis of symmetry of the cross-section. The components of the displacements are expressed as:

$$u_1^t = 0,\ u_2^t = -z\varphi(x,t),\ u_3^t = y\varphi(x,t), \tag{2.27}$$

where u_1^t, u_2^t, and u_3^t denote the torsional angle components of the torsional bar particles along x, y, and z directions of the coordinate system, respectively. Therefore, the only nonzero com-

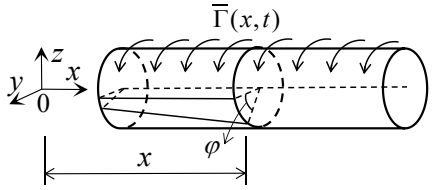

Fig. 2.4. A torsional bar under torque.

ponents of torsional angle tensors are as follows:

$$\begin{aligned}
&\varepsilon_{12} = \varepsilon_{21} = -\frac{1}{2}z\frac{\partial\varphi(x,t)}{\partial x}, \varepsilon_{13} = \varepsilon_{31} = \frac{1}{2}y\frac{\partial\varphi(x,t)}{\partial x}, \xi_{112} = -z\frac{\partial^2\varphi(x,t)}{\partial x^2}, \xi_{113} = y\frac{\partial^2\varphi(x,t)}{\partial x^2},\\
&\xi_{123} = \xi_{213} = \frac{\partial\varphi(x,t)}{\partial x}, \xi_{132} = \xi_{312} = \frac{\partial\varphi(x,t)}{\partial x}, \zeta_{1112} = -z\frac{\partial^3\varphi(x,t)}{\partial x^3}, \zeta_{1113} = y\frac{\partial^3\varphi(x,t)}{\partial x^3},\\
&\zeta_{3112} = \zeta_{1312} = \zeta_{1132} = -\frac{\partial^2\varphi(x,t)}{\partial x^2}, \zeta_{2113} = \zeta_{1213} = \zeta_{1123} = \frac{\partial^2\varphi(x,t)}{\partial x^2}.
\end{aligned} \tag{2.28}$$

In this step, the Hamilton principle is utilized to derive the governing equation and boundary conditions of a torsional bar. The detail addressed in Appendix C, one arrives:

$$C_1^t\frac{\partial^2\varphi(x,t)}{\partial x^2} + (C_4^t - C_2^t)\frac{\partial^4\varphi(x,t)}{\partial x^4} + C_3^t\frac{\partial^6\varphi(x,t)}{\partial x^6} - \overline{\Gamma}(x,t) = \rho J\frac{\partial^2\varphi}{\partial t^2}, \tag{2.29}$$

where $C_1^t = GJ+2A(4a_4-a_5)$, $C_2^t = J(a_3+a_4)/2-2A(b_4+2b_5-6b_6+2b_7)$, $C_3^t = 2J(b_5+b_6)$, $C_4^t = Jc_3$, J means torsion of inertia within plane $y0z$. Additionally, the associated boundary conditions of the bar ends (i.e. $x = 0,\ L$) for SSG theory as:

$$\begin{aligned}
&C_1^t\frac{\partial\varphi(x,t)}{\partial x} + (C_4^t - C_2^t)\frac{\partial^3\varphi(x,t)}{\partial x^3} + C_3^t\frac{\partial^5\varphi(x,t)}{\partial x^5} = \Gamma_0 \text{ or } \delta\varphi = 0,\ \text{on } \Omega = \{0, L\};\\
&(C_2^t - \frac{1}{2}C_4^t)\frac{\partial^2\varphi(x,t)}{\partial x^2} + C_3^t\frac{\partial^4\varphi(x,t)}{\partial x^4} = \Gamma_1 \text{ or } \delta\frac{\partial\varphi(x,t)}{\partial x} = 0,\ \text{on } \partial\Omega;\\
&\frac{1}{2}C_4^t\frac{\partial\varphi(x,t)}{\partial x} + C_3^t\frac{\partial^3\varphi(x,t)}{\partial x^3} = \Gamma_2 \text{ or } \delta\frac{\partial^2\varphi(x,t)}{\partial x^2} = 0,\ \text{on } \partial\Omega,
\end{aligned} \tag{2.30}$$

where Γ_0 and $\Gamma_{1,2}$ denote the classical and higher-order end-sectional loads.

In the FEM, given the vector of nodal DOFs values $\mathbf{u}^{(e)t}$ and the shape function $\mathbf{N}^t(x)$, the

torsional angle $\varphi(x,t)$ of point at $\boldsymbol{x} \in R^2$ inside of one element could be expressed as:

$$\varphi(x,t) = \mathbf{N}^t(x)\mathbf{u}^{(e)t}(t), \tag{2.31}$$

where $\mathbf{u}^{(e)t}$ is of size $r \times 1$, $\mathbf{N}^t(x)$ is a row vector of size $1 \times r$, and r is the number of nodal degrees of freedom (DOFs). In Eq. 2.31, $\mathbf{u}^{(e)t}$, $\mathbf{N}^t(x)$ and r are determined by the specific form of the interpolation function. To ensure higher displacement continuity than traditional elements, we use the C^2 continuous Hermite interpolation function for Eq. 2.31 to guarantee the continuity and smoothness of both displacement field and strain field. The definition of node numbering, nodal DOFs and coordinate for 1D Hermite elements are shown in Fig. 2.5. For

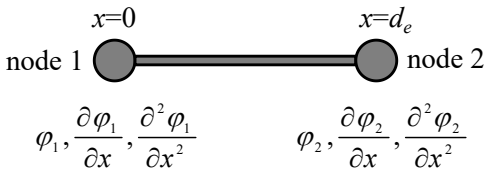

Fig. 2.5. Definition of node numbering, nodal DOFs and coordinate for 1D

1D C^2 continuous Hermite element (element length is d_e), three DOFs, φ_i, $\frac{\partial \varphi_i}{\partial x}$, $\frac{\partial^2 \varphi_i}{\partial x^2}$, $i = 1, 2$, are associated with each node. The connecting elements have these three common DOFs which ensuring continuity of slope and higher derivatives up to the second order between the elements. The Hermite polynomial shape functions corresponding to the six DOFs of 1D element are:

$$\begin{aligned}
\mathrm{N}_1^0 &= 1 - 10\frac{x^3}{d_e^3} + 15\frac{x^4}{d_e^4} - 6\frac{x^5}{d_e^5}, \quad \mathrm{N}_2^0 = 10\frac{x^3}{d_e^3} - 15\frac{x^4}{d_e^4} + 6\frac{x^5}{d_e^5}, \\
\mathrm{N}_1^1 &= \frac{x}{d_e} - 6\frac{x^3}{d_e^3} + 8\frac{x^4}{d_e^4} - 3\frac{x^5}{d_e^5}, \quad \mathrm{N}_2^1 = -4\frac{x^3}{d_e^3} + 7\frac{x^4}{d_e^4} - 3\frac{x^5}{d_e^5}, \\
\mathrm{N}_1^2 &= \frac{x^2}{2d_e^2} - 3\frac{x^3}{2d_e^3} + 3\frac{x^4}{2d_e^4} - \frac{x^5}{2d_e^5}, \; \mathrm{N}_2^2 = \frac{x^3}{2d_e^3} - \frac{x^4}{d_e^4} + \frac{x^5}{2d_e^5}.
\end{aligned} \tag{2.32}$$

According to Galerkin's method, doing the same calculating progress as shown in bending case, the element stiffness $\mathbf{K}^{(e)t}$, mass matrices $\mathbf{M}^{(e)t}$ and force vector $\mathbf{F}^{(e)t}$ are derived as:

$$\begin{aligned}
\mathbf{M}^{(e)t} &= \rho J \int_0^{d_e} (\mathbf{N}^t)^{\mathrm{T}} \mathbf{N}^t \mathrm{d}x, \\
\mathbf{K}^{(e)t} &= \int_0^{d_e} \left[C_1^t \left((\mathbf{N}^t)' \right)^{\mathrm{T}} (\mathbf{N}^t)' + (C_4^t - C_2^t) \left((\mathbf{N}^t)'' \right)^{\mathrm{T}} (\mathbf{N}^t)'' + C_3^t \left((\mathbf{N}^t)''' \right)^{\mathrm{T}} (\mathbf{N}^t)''' \right] \mathrm{d}x, \\
\mathbf{F}^{(e)t} &= \int_0^{d_e} \overline{\Gamma} \mathbf{N}^t \mathrm{d}x + \Gamma_0 \mathbf{N}^t|_{\partial\Omega_{\Gamma_0}} + \Gamma_1 (\mathbf{N}^t)'|_{\partial\Omega_{\Gamma_1}} + \Gamma_2 (\mathbf{N}^t)''|_{\partial\Omega_{\Gamma_2}}.
\end{aligned} \tag{2.33}$$

2.3.2 Lattice spring model by second strain gradient elasticity

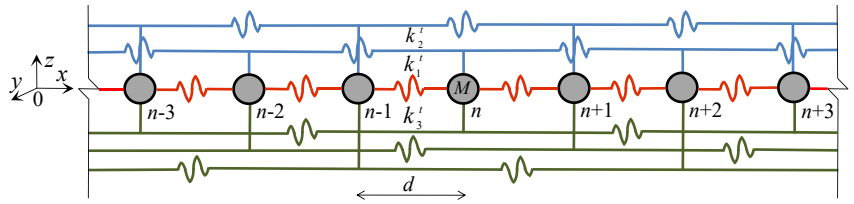

Fig. 2.6. LSM for a torsional bar with torsional coupling constants k_1^t (red line: nearest-neighbor interaction), k_2^t (blue line: next-nearest-neighbor interaction) and k_3^t (green line: next-next-nearest-neighbor interaction).

In this part, the fundamentals of "non-local" LSM for torsion is introduced to discretise the bar into a chain of identical elements, as demonstrated in Fig. 2.6. The total number of lattice nodes is N (they are numbered as $1, 2, ..., n, ...N$). As same as bending case, this chain is a lattice representation of the continuum where the interaction between each node at small scale can reproduce the mechanical response of the continuum structure at large scale (theoretically when N tends to infinity or large enough). The lattice equation of motion for particle n is:

$$\begin{aligned} &k_1^t(\varphi_{n-1} - 2\varphi_n + \varphi_{n+1}) + k_2^t(\varphi_{n-2} - 2\varphi_n + \varphi_{n+2}) + k_3^t(\varphi_{n-3} - 2\varphi_n - \varphi_{n+3}) - \Gamma_n \\ =&\frac{mJ}{A}\frac{\mathrm{d}^2\varphi_n(t)}{\mathrm{d}t^2}. \end{aligned} \tag{2.34}$$

Subsequently, the Fourier series transform approach [110] is utilized to derive a continuous equation $\varphi(x,t)$ from the LSM $\varphi_n(t)$. The detail addressed Appendix in D, as a result:

$$\begin{aligned} &L_2^t\frac{\partial^2\varphi(x,t)}{\partial x^2} + L_4^t\frac{\partial^4\varphi(x,t)}{\partial x^4} + L_6^t\frac{\partial^6\varphi(x,t)}{\partial x^6} + o\left(L_i^t\frac{\partial^i\varphi(x,t)}{\partial x^i}\right) - \overline{\Gamma}(x,t) \\ =&\rho J\frac{\mathrm{d}^2\varphi_n(t)}{\mathrm{d}t^2}, (i = 8, 10, ...), \end{aligned} \tag{2.35}$$

with $L_2^t = (k_1^t + 4k_2^t + 9k_3^t)d$, $L_4^t = \left(\frac{k_1^t}{12} + \frac{4k_2^t}{3} + \frac{27k_3^t}{4}\right)d^3$, $L_6^t = \left(\frac{k_1^t}{360} + \frac{8k_2^t}{54} + \frac{81k_3^t}{40}\right)d^5$, $L_8^t = \left(\frac{7k_1^t}{20160} + \frac{4k_2^t}{315} + \frac{729k_3^t}{2240}\right)d^7$,... Here, the convergence condition is same as bending case: $N \geq \pi + 1$. Ignore higher order part, Eq. 2.35 will be written:

$$L_2^t\frac{\partial^2\varphi(x,t)}{\partial x^2} + L_4^t\frac{\partial^4\varphi(x,t)}{\partial x^4} + L_6^t\frac{\partial^6\varphi(x,t)}{\partial x^6} - \overline{\Gamma} = \rho J\frac{\mathrm{d}^2\varphi_n(t)}{\mathrm{d}t^2}, \tag{2.36}$$

where $\overline{\Gamma}(x,t)$ is assumed as a constant $\overline{\Gamma}$. Compare Eq. 2.36 with the equation of motion for torsion from Mindlin's theory (Eq. 2.29), the first 3 parts should be same:

$$L_2^t = C_1^t, \quad L_4^t = C_4^t - C_2^t, \quad L_6^t = C_3^t, \tag{2.37}$$

with $k_1^t = \frac{3C_1^t}{2d} + \frac{13(C_2^t - C_4^t)}{2d^3} + \frac{15C_3^t}{d^5}$, $k_2^t = -\frac{3C_1^t}{20d} - \frac{2(C_2^t - C_4^t)}{d^3} - \frac{6C_3^t}{d^5}$, $k_3^t = \frac{C_1^t}{90} + \frac{(C_2^t - C_4^t)}{6d^3} + \frac{C_3^t}{d^5}$. Replacing Eq. 2.36 into Eq. 2.33, the weak formulations from LSM will be derived finally.

2.4 One-dimensional wave propagation characteristics

The unit cell stiffness matrix ($\mathbf{K}^{(b/t)}$) and mass matrix ($\mathbf{M}^{(b/t)}$) can be assembled by element stiffness and mass matrices ($\mathbf{K}^{e(b/t)}$), $\mathbf{M}^{e(b/t)}$). According to the WFEM, only one unit cell is modeled through traditional finite elements, as indicated in Fig. 1.10, The left boundary and right boundary of the unit cell are meshed with same number of DOFs. The dynamic equilibrium formulation of a unit cell can be re-expressed by dividing the DOFs into I (internal), L (left boundary) and R (right boundary) DOFs, this yields:

$$\begin{bmatrix} \mathbf{D}_{\mathrm{LL}}^{b/t} & \mathbf{D}_{\mathrm{LI}}^{b/t} & \mathbf{D}_{\mathrm{LR}}^{b/t} \\ \mathbf{D}_{\mathrm{IL}}^{b/t} & \mathbf{D}_{\mathrm{II}}^{b/t} & \mathbf{D}_{\mathrm{IR}}^{b/t} \\ \mathbf{D}_{\mathrm{RL}}^{b/t} & \mathbf{D}_{\mathrm{RI}}^{b/t} & \mathbf{D}_{\mathrm{RR}}^{b/t} \end{bmatrix} \begin{pmatrix} \hat{\mathbf{u}}_{\mathrm{L}}^{b/t} \\ \hat{\mathbf{u}}_{\mathrm{I}}^{b/t} \\ \hat{\mathbf{u}}_{\mathrm{R}}^{b/t} \end{pmatrix} = \begin{pmatrix} \hat{\mathbf{F}}_{\mathrm{L}}^{b/t} \\ \hat{\mathbf{F}}_{\mathrm{I}}^{b/t} \\ \hat{\mathbf{F}}_{\mathrm{R}}^{b/t} \end{pmatrix}, \tag{2.38}$$

where $\hat{\mathbf{u}}^{b/t}$ and $\hat{\mathbf{F}}^{b/t}$ are the amplitudes of $\mathbf{u}^{b/t}$ and $\mathbf{F}^{b/t}$, respectively. It should be noticed that the internal DOFs are not affected by external loads due to the coupling actions are restricted to its left boundary and right boundary only [184], as a result, $\hat{\mathbf{F}}_{\mathrm{I}}^{b/t} = 0$. The dynamic equilibrium equation, considering left boundary and right boundary in $\mathbf{D}^{b/t}$ only, will be written as:

$$\begin{bmatrix} \mathbb{D}_{\mathrm{LL}}^{b/t} & \mathbb{D}_{\mathrm{LR}}^{b/t} \\ \mathbb{D}_{\mathrm{RL}}^{b/t} & \mathbb{D}_{\mathrm{RR}}^{b/t} \end{bmatrix} \begin{pmatrix} \hat{\mathbf{u}}_{\mathrm{L}}^{b/t} \\ \hat{\mathbf{u}}_{\mathrm{R}}^{b/t} \end{pmatrix} = \begin{pmatrix} \hat{\mathbf{F}}_{\mathrm{L}}^{b/t} \\ \hat{\mathbf{F}}_{\mathrm{R}}^{b/t} \end{pmatrix}, \tag{2.39}$$

where $\mathbb{D}^{b/t} = \mathbf{D}_{\mathrm{BdBd}}^{b/t} - \mathbf{D}_{\mathrm{BdI}}^{b/t} (\mathbf{D}_{\mathrm{II}}^{b/t})^{-1} \mathbf{D}_{\mathrm{IBd}}^{b/t}$ is the condensed form of dynamic stiffness matrix, subscript Bd represents the DOFs on the boundaries of the unit cell. Note that this is a typical issue for WFEM [135] and a modal reduction can be applied to reduce the computational cost of the dynamic condensation. Eq. 2.39 is the starting point for the WFEM analysis that relates the displacement/rotation/torsion and force/moment/torque on the two sides of the unit cell. For the solution of propagation constants $\mathbf{\Lambda}^{b/t}$ and eigenvectors $\mathbf{\Phi}_u^{b/t}$, one can solve the direct Bloch formulation [210–212] as:

$$\left[\mathbb{D}_{\mathrm{RL}}^{b/t}(\omega) (\mathbf{\Lambda}^{b/t})^{-1} + (\mathbb{D}_{\mathrm{RR}}^{b/t}(\omega) + (\mathbb{D}_{\mathrm{LL}}^{b/t}(\omega)) + \mathbb{D}_{\mathrm{LR}}^{b/t}(\omega) \mathbf{\Lambda}^{b/t} \right] \mathbf{\Phi}_u^{b/t} = 0, \tag{2.40}$$

where $\mathbf{\Lambda}^{b/t}$ =diag$\{\lambda_j\}_{j=1,\ldots,2m}$, $\mathbf{\Phi}_u^{b/t} = \{\phi_j\}_{j=1,\ldots,2m}$. The $2m$ eigenvalues in Eq. 2.40 can be divided into (λ_j, ϕ_j^+) and $(1/\lambda_j, \phi_j^-)$. The waves propagate to the positive direction if $|1/\lambda_j|$ <1. And the waves propagate to the negative direction if $|\lambda_j|$ >1. Here, λ_j take the form $\lambda_j = exp(-\mathrm{i}\kappa_j L_u)$. The direction of wave propagation can be defined utilizing $\Re(\kappa_j)$ when $|\lambda_j| = 1$ in the passing bands, which representing the real part of the wave-number. $\Re(\kappa_j)$

>0 means that the waves propagate to the positive direction. On the other hand, $\Re(\kappa_j)$ <0 represents that the waves propagate to the negative direction.

2.5 Numerical applications and discussions

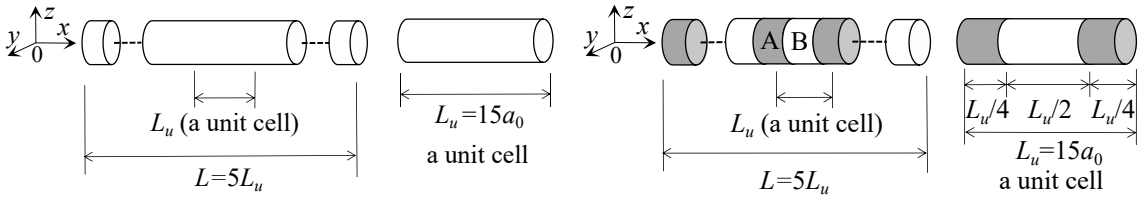

(a) Single material structure. (b) Binary periodic structure.

Fig. 2.7. One-dimensional structures' configurations.

In this section, the WFEM is applied to study bending and torsional vibration based on SSG theory. Two different structures are considered for each: one is a single material structure with 5 unit cells, each unit cell's length L_u is $15a_0$ (a_0 is the lattice parameter) as shown in Fig. 2.7(a). The other one is a binary periodic structure with 5 unit cells, each unit cell has a length $L_u = 15a_0$ and consists of parts A and B as shown in Fig. 2.7(b). Both structures have a circular cross section with radius $r = 3a_0$ and loss factor $\eta = 1 \times 10^{-4}$.

2.5.1 Bending vibration of Euler-Bernoulli beam

The bending vibration for single material and binary periodic structures are discussed. Aluminium (Al) is used for single material structure with linear mass density $\rho = 2.7\ \mathrm{g/cm^3}$ and Young's modulus $E = 70$ GPa, and each unit cell is divided into 100 elements. Al and Pb (Lead: linear mass density $\rho = 11.34\ \mathrm{g/cm^3}$, Young's modulus $E = 16$ GPa) are respectively used for part A with 50 elements and part B with 50 elements in binary periodic structure.

2.5.1.1 Euler-Bernoulli beam with single material

Firstly, the dispersion relation of a unit cell for single material Euler-Bernoulli beam is calculated by WFEM. The real part $\Re(\kappa_j)$ of wavenumber is the phase shift per unit length and the imaginary part $\Im(\kappa_j)$ means the attenuation per unit length. Only the positive waves with real and imaginary parts are illustrated due to the wavenumbers of the negative waves and positive waves are symmetric with respect to x-axis. The dimensionless wavenumbers in frequency range [0, $30\omega_{\mathrm{b1}}$], where $\omega_{\mathrm{b1}} = 3.516\sqrt{EI/\rho AL^4}$ [213] assumed as clamped-free boundary conditions, are presented in Fig. 2.8. There are four waves (κ_1, κ_2, κ_3, κ_4) predicted by SSG theory, in which κ_1 is non-classical bending wave propagating in a dispersive manner, κ_2 is the non-classical shear wave, κ_3 and κ_4 are the evanescent waves which exist exclusively in SSG

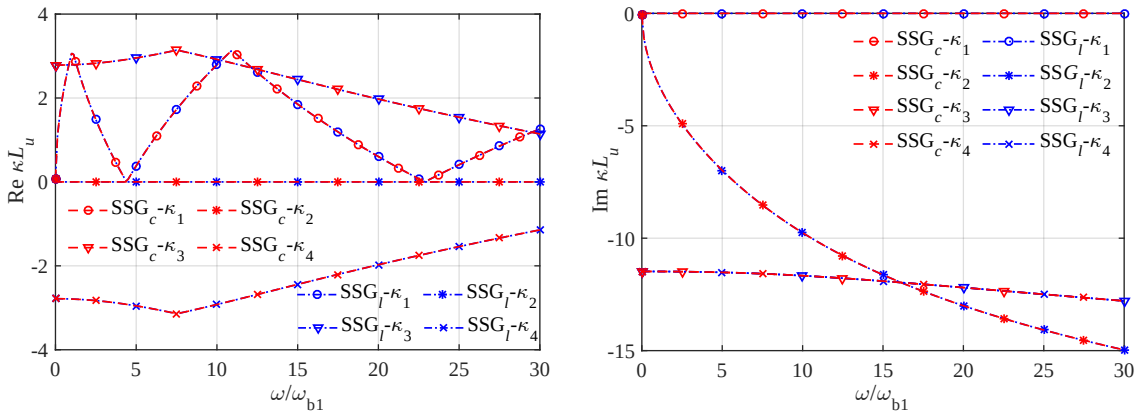

(a) Real part of positive waves. (b) Imaginary part of positive waves.

Fig. 2.8. Dispersion relation for single material Euler-Bernoulli beam by SSG (ω_{b1} is the first nature frequency, subscript c of SSG means continuum model, l is lattice model).

theory.

In order to verify the WFEM results, an analytical method is used. Replacing displacement

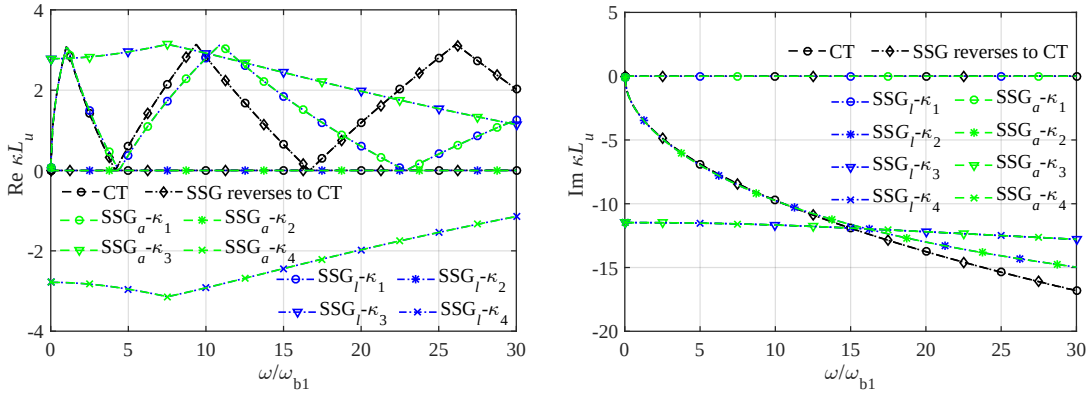

(a) Real part of positive waves. (b) Imaginary part of positive waves.

Fig. 2.9. Comparison of dispersion relation between SSG and CT and reverse SSG to CT (subscript a of SSG means analytical method, l is lattice model).

$w(x,t) = w_0 e^{i(\omega t - \kappa x)}$ into Eq. 2.9 assuming $\overline{f}(x,t) = 0$, the analytical dynamical formulation of Euler-Bernoulli beam by SSG theory becomes: $C_1^b\kappa^4 + (C_4^b - C_2^b)\kappa^6 + C_3^b\kappa^8 = \rho A\omega^2$. The results by analytical method and WFEM via LSM are shown in Fig. 2.9. The dispersion relation by WFEM is in good accordance with the analytical method. On anther hand, at low frequency, κ_1 from SSG and CT are close, but a discrepancy appears at higher frequency. Note that without higher order material contributions (i.e. a_i, b_i and c_i equal 0), SSG becomes identical to CT.

Next, the forced response for single material Euler-Bernoulli beam is discussed, as presented in Fig. 2.7(a), the beam consists of 5 unit cells. One side is clamped and another side is free and subjected to a harmonic force $\overline{f}(x,t) = e^{\mathbf{i}\omega t}$ on free end of the beam. The amplitude

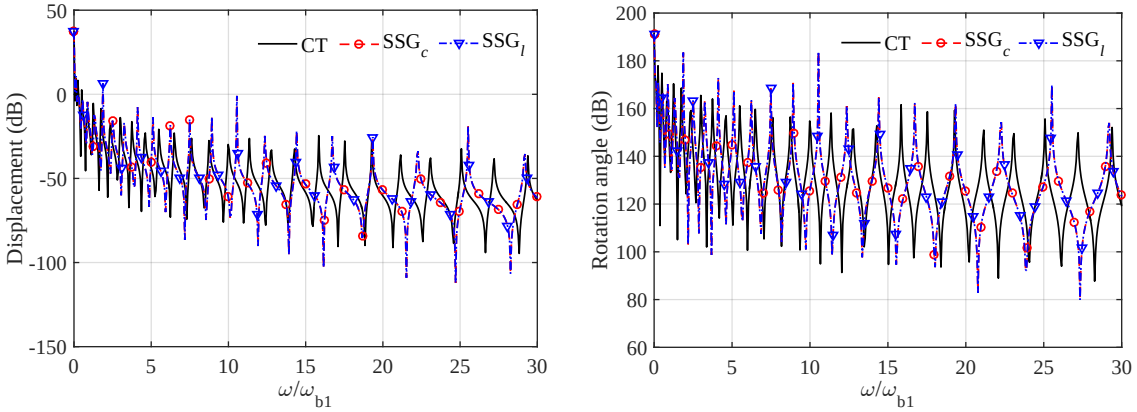

(a) Forced response of displacement along z direction.

(b) Forced response of rotation angle in $y0z$ plane.

Fig. 2.10. Forced response for single material Euler-Bernoulli beam by CT and SSG (subscript c means continuum model, l is lattice model).

at free end is calculated out on each frequency according to Eq. 1.46. The forced response is shown in Fig. 2.10 by SSG theory and CT. It can be noticed that resonances are well predicted in both theories. Same as for the dispersion curves, the results show that discrepancies between CT and SSG FRF increase with frequency. Wave propagation is significantly affected by the micro-sized structure interactions. The input vibration energy can be transferred both by propagating waves and other evanescent waves, which decay rapidly in the near field of the excitation.

2.5.1.2 Euler-Bernoulli beam with binary periodic materials

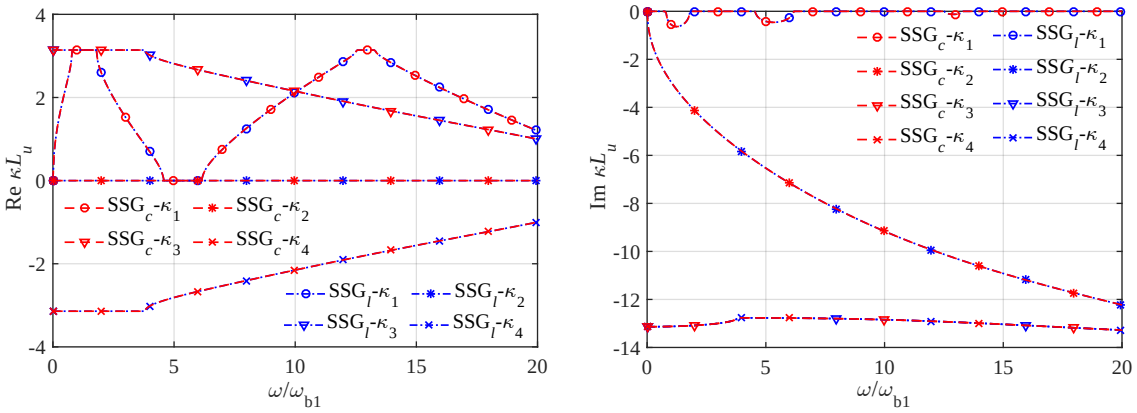

(a) Real part of positive waves.

(b) Imaginary part of positive waves.

Fig. 2.11. Dispersion relation for periodic Euler-Bernoulli beam by SSG (subscript c of SSG means continuum model, l is lattice model).

The dispersion relation with positive-going waves of a unit cell for periodic Euler-Bernoulli

beam is calculated by WFEM. The dimensionless wavenumbers with real and imaginary parts of the waves $[0, 20\omega_{\mathrm{b1}}]$ are presented in Fig. 2.11. The difference with single material structures lies in the existence of stop bands (visible here on κ_1). For the bending wave in micro-sized periodic structure we have $\Re(\kappa_1) = 0$ within pass bands and $\Im(\kappa_1) \neq 0$ within stop bands, which is a typical behavior of evanescent waves. When $\Re(\kappa_1) = 0$, the waves decay exponentially with the stop bands frequencies bounded with $\lambda = 1$. The stop bands frequencies are bounded with $\lambda = -1$ which indicates a single wavelength when $\Re(\kappa_1) = \pm\pi/L_u$.

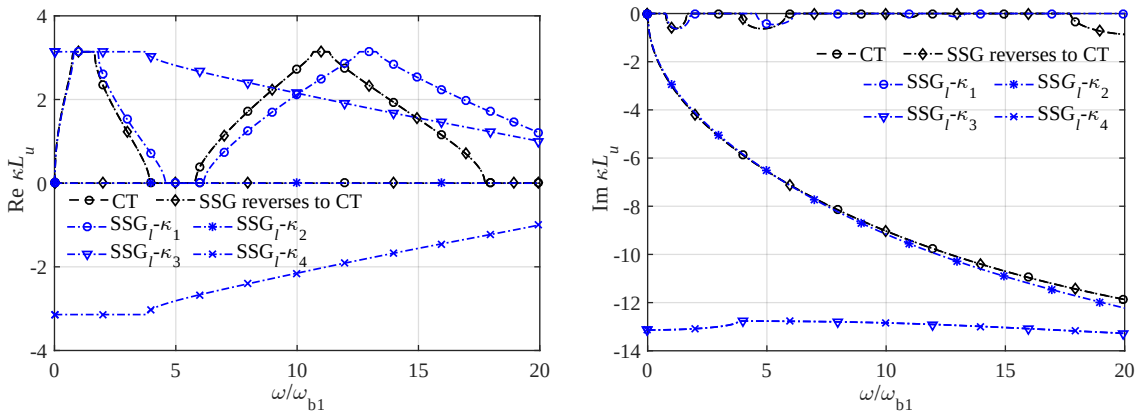

(a) Real part of positive waves. (b) Imaginary part of positive waves.

Fig. 2.12. Comparison of dispersion relation between SSG and CT and reverse SSG to CT (subscript l of SSG means lattice model).

Next, the comparison between SSG theory and CT is shown in Fig. 2.12. It is noticed that

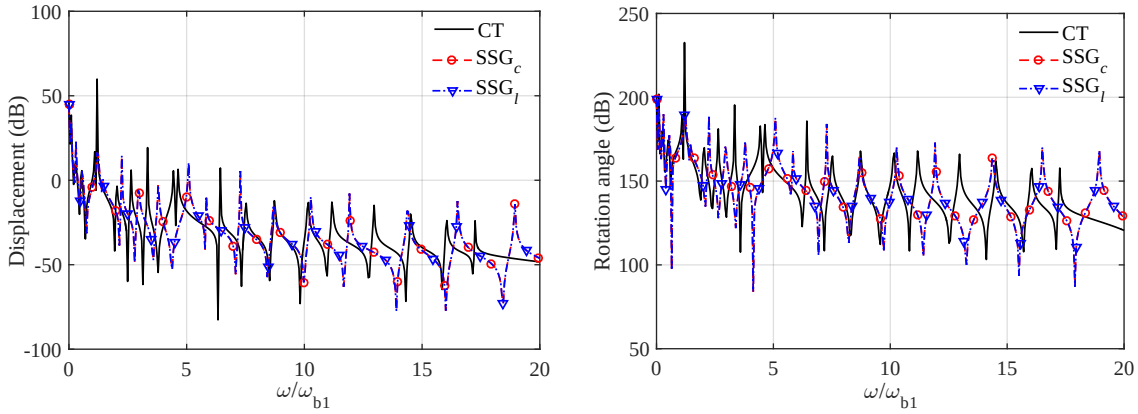

(a) Forced response of displacement. (b) Forced response of rotation angle.

Fig. 2.13. Forced response for periodic Euler-Bernoulli beam by CT and SSG (subscript c of SSG means continuum model, l denotes lattice model).

at low frequency, the first wave by SSG confirms to CT well, but the difference is bigger when frequency increase. When higher order material parameters a_i, b_i and c_i are 0, SSG will reverse

to CT.

The forced response for periodic Euler-Bernoulli beam is discussed, as presented in Fig. 2.7(b), the beam is composed of 5 unit cells, each unit cell includes two parts with A and B. The boundary condition and external force are same as bending case of single material structure. The forced response of displacement and rotation angle is shown in Fig. 2.13 by SSG theory and CT. The resonances are predicted well by both theories. The results by these two theories close to each other at lower frequency range, but the values are different in higher frequency. The frequency ranges in the stop bands indicate that there is no resonance.

2.5.2 Torsional vibration of a bar

Material Al with shear modulus $G = 26$ GPa is used for single material torsional bar with 100 elements in each unit cell. Al and Cu (shear modulus $G = 48$ GPa, linear mass density $\rho = 8.96\ \mathrm{g/cm^3}$) are used for part A with 50 elements and part B with 50 elements in binary periodic bar, respectively.

2.5.2.1 Torsional bar with single material

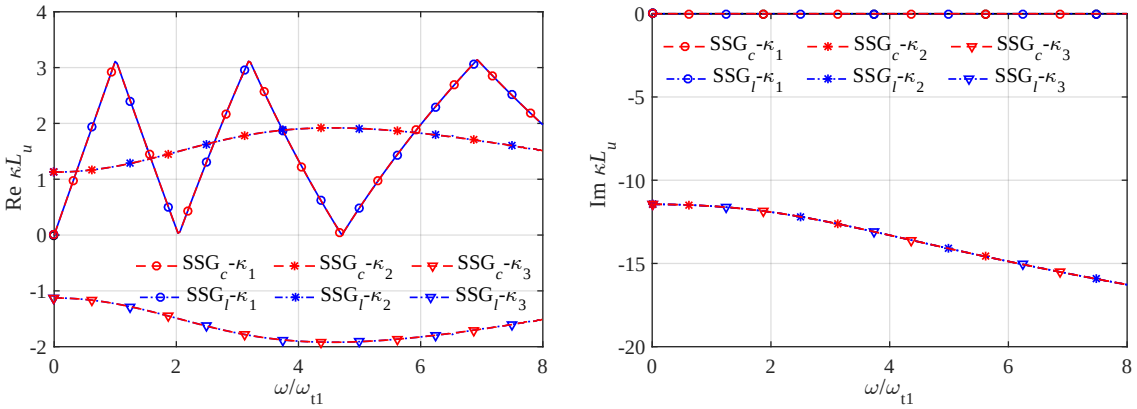

(a) Real part of positive waves.

(b) Imaginary part of positive waves.

Fig. 2.14. Dispersion relation for single material torsional bar by SSG ($\omega_{t1} = \pi\sqrt{G/4\rho L^2}$ [214] is the first nature frequency, subscript c of SSG means continuum model, l is lattice model).

Firstly, the dispersion relation of a unit cell for single material torsional bar is calculated by WFEM. The positive-going waves are shown in Fig. 2.14. Then, the WFEM is compared with the analytical method which expressed as $C_1^t\kappa^2 + (C_4^t - C_2^t)\kappa^4 + C_3^t\kappa^6 = \rho J\omega^2$. As shown in Fig. 2.15, the results indicate that there are three waves (κ_1, κ_2, κ_3) predicted by SSG theory, in which κ_1 is a dispersive non-classical torsional wave. The evanescent waves κ_2 and κ_3 exist only in SSG theory model. Next, the forced response is illustrated in Fig. 2.16 by SSG and CT. The boundary conditions are same as bending case of single material structure and a harmonic

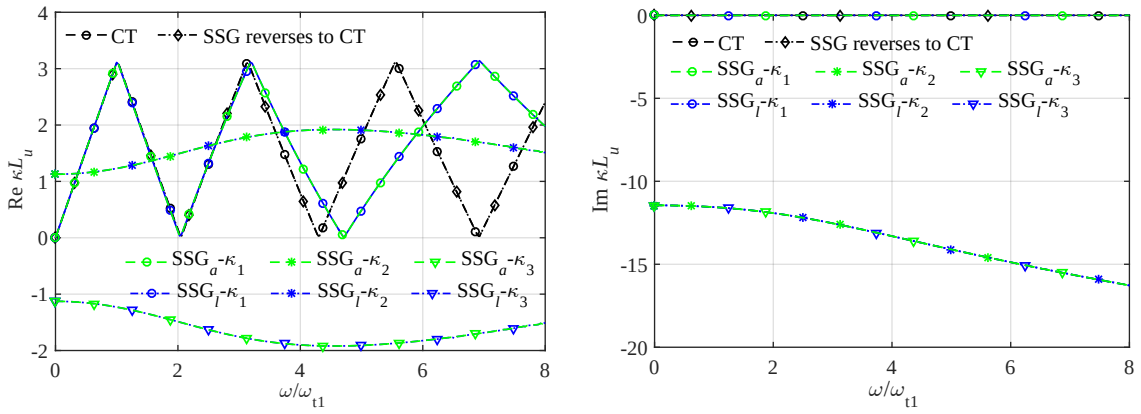

(a) Real part of positive waves.

(b) Imaginary part of positive waves.

Fig. 2.15. Comparison of dispersion relation between SSG and CT and reverse SSG to CT (subscript a means analytical method and l is lattice model).

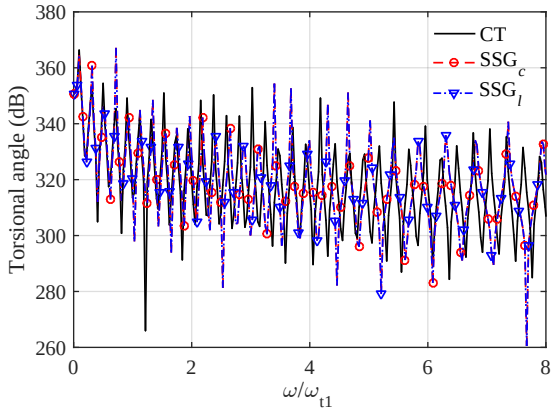

Fig. 2.16. Forced response of single material torsional bar by CT and SSG (subscript c and l of SSG denote continuum model and lattice model, respectively).

force $\overline{\Gamma}(x,t) = e^{\mathbf{i}\omega t}$ is applied on free boundary. The properties of forced responses referred in bending case of single material structure are observed in the torsional ones as well.

2.5.2.2 Torsional bar with binary periodic materials

As presented in Fig. 2.17, the dispersion relation of a unit cell for periodic torsional bar is calculated by WFEM. And the comparison between SSG theory and CT is shown in Fig. 2.18. As we can see, the wave κ_1 of SSG confirms the wave of CT well when the frequency range is in the first pass band and stop band. But as the frequency increases, the difference between this two waves is getting bigger. This phenomena shows that the micro-sized structure's characteristics can be reflected by non-local theory at high frequency range. And when higher order material parameters a_i, b_i and c_i are 0, SSG will reverse to CT. Next, the forced response for periodic torsional bar is discussed by SSG theory and CT, as shown in Fig. 2.19. The boundary conditions and external force are same as single material structure of torsional bar. The fre-

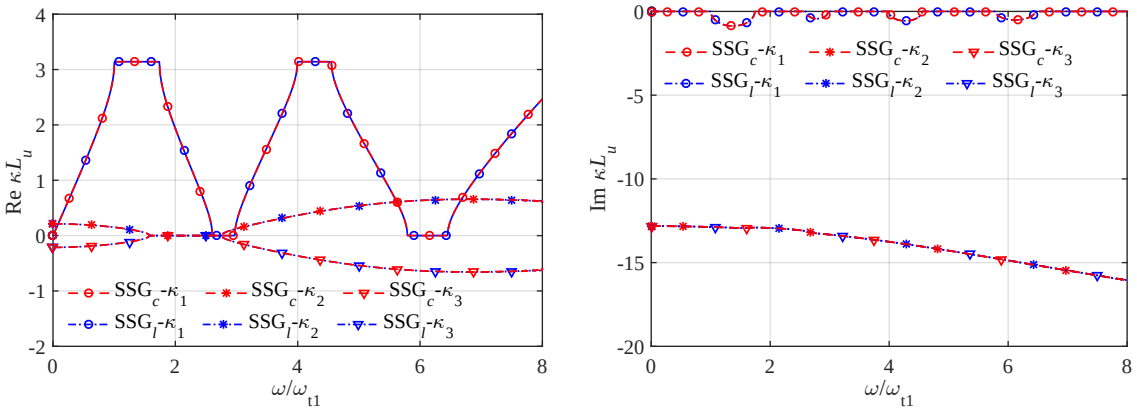

(a) Real part of positive waves. (b) Imaginary part of positive waves.

Fig. 2.17. Dispersion relation for periodic torsional bar by SSG (subscript c is continuum model, l is lattice model).

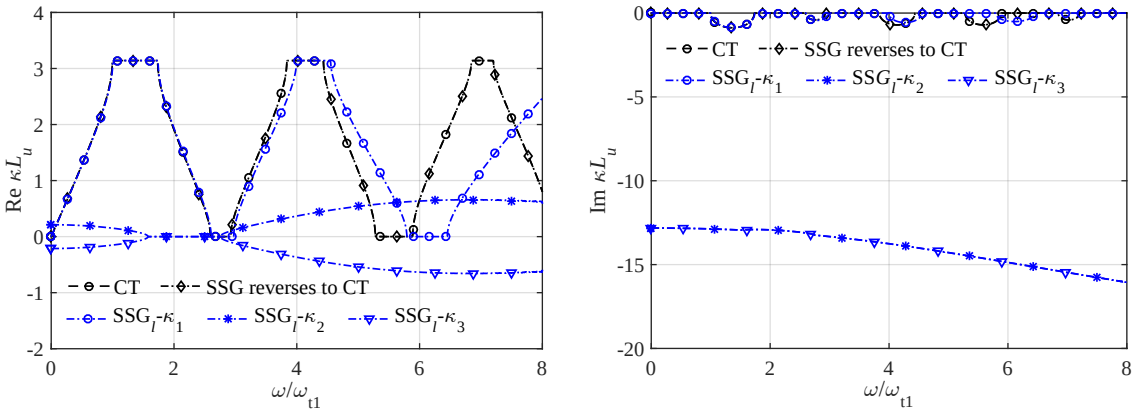

(a) Real part of positive waves. (b) Imaginary part of positive waves.

Fig. 2.18. Comparison of dispersion relation between SSG and CT and reverse SSG to CT (subscript l of SSG means lattice model).

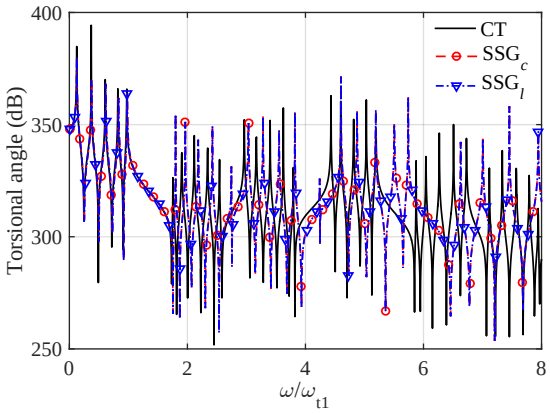

Fig. 2.19. Forced response by CT and SSG (subscript c means continuum model and l is lattice model).

quency range can be divided into two parts, namely the stop bands frequency and pass bands

frequency, and there is no resonances in stop bands. The results by these two theories match to each other just in the first pass and stop band frequency range.

2.6 Conclusions

In this chapter, we used WFEM to study the dynamic behavior and wave propagation features of complex 1D micro-sized structures. The SSG theory is used to analyze the structural characteristics. The main contributions of the work are drawn as follows:

(i) The governing equations and boundary conditions of 1D Euler Bernoulli bending beam and torsional bar are derived from continuum models based on SSG theory. Then, two "nonlocal" LSM for bending and torsion are introduced, and the dynamic equations from LSM are calculated respectively. Weak forms by SSG theory for bending and torsion are established finally. WFEM for one-dimensional structures is discussed. Free wave propagation characteristics are expressed by solving eigenvalue problems.

(ii) Bending and torsional dispersion relations for single material and binary periodic structures are presented by WFEM, respectively. For bending, there are four waves (κ_1, κ_2, κ_3, κ_4) predicted by SSG theory, in which κ_1 is non-classical bending wave propagating in a dispersive manner, κ_2 is non-classical shear wave, κ_3 and κ_4 are the evanescent waves which exist exclusively in SSG theory model. For torsion, there are three waves (κ_1, κ_2, κ_3) predicted by SSG theory, in which κ_1 is non-classical torsional wave propagating in a dispersive manner, κ_2 and κ_3 are the evanescent waves. Significant stop bands are observable for both bending and torsion modes in SSG periodic structures.

(iii) For the forced response of bending and torsion, wave propagation is significantly affected by the micro-structure interactions. The input vibration energy can be transferred both by propagating waves and other evanescent waves which decay rapidly in the near field of the excitation.

Chapter 3

Multi-scale modelling based on second strain gradient elasticity for a two-dimensional beam grid

Chapter contents

3.1 Introduction 59
3.2 Strong formulas for out-of plane vibration 60
3.2.1 Continuum model by second strain gradient elasticity 60
3.2.2 Lattice spring model by second strain gradient elasticity 61
3.3 Wave finite element method for 2D structures 62
3.3.1 Finite element procedure 62
3.3.2 2D wave propagation analysis 64
3.4 Numerical examples and discussions 65
3.4.1 Band structure 66
3.4.2 Slowness surfaces 67
3.4.3 Energy flow vector fields 68
3.4.4 Wave beaming effects 70
3.4.5 Wave shapes 74
3.5 Conclusions 75

3.1 Introduction

In chapter 2, the author used SSG theory within WFEM framework to study 1D wave propagation characteristic of Euler-Bernoulli bending beam and torsional bar. However, the prop-

agation of waves in realistic periodic structures is very complicated. The potential dynamic properties of complex structures cannot be obtained by studying 1D waves only. So, the exploration of 2D waves in complex structures is of great significance.

In this chapter, the SSG theory is used for the dynamic analysis of a 2D micro-sized beam grid which is restricted to out-of plane vibration. Firstly, the dynamic continuum equations of continuum model and LSM are derived respectively. Subsequently, weak formulas are established within the framework of SSG theory and the global dynamic stiffness matrix of a unit cell is assembled. The WFEM2D is applied for the vibrational analysis of 2D periodic wave-guides. Finally, the band structure and slowness surfaces are studied in frequency spectrum. In addition, the energy flow vector fields and wave beaming effects are analyzed through SSG theory and CT. The results show that the proposed approach is of significant potential in investigating the 2D wave propagation characteristics of complex micro-sized periodic structures.

3.2 Strong formulas for out-of plane vibration

3.2.1 Continuum model by second strain gradient elasticity

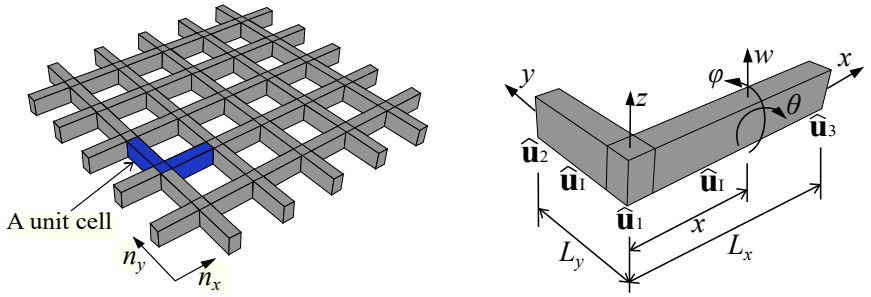

(a) A beam grid. (b) A unit cell of the beam grid.

Fig. 3.1. Sketch of 2D beam grid and displacements at position x on a branch of the unit cell (displacement w along z direction, angle θ in $x0z$ plane and angle φ in $y0z$ plane, $\hat{\mathbf{u}}_{1,2,3}$ is corner DOFs, $\hat{\mathbf{u}}_{\mathrm{I}}$ is internal DOFs).

As shown in Fig. 3.1(a), a beam grid is presented as a 2D periodic structure. The dynamical properties of whole beam grid can be reflected through the spectral analysis of a unit cell in framework of WFEM [215]. Starting with the dynamical analysis of the beam along x direction in the unit cell as shown in Fig. 3.1(b). According to the out-of plane vibration analysis [216], the vibration of beam is restricted to bending and torsion. The calculating process of strong formulas for continuum model is shown in Fig. 3.2. All the details for illustrating the governing equations and boundary conditions of bending and torsion cases can be found in the author's paper [95] and main derivation results are cited in this work. Here should be pointed that the beam kinetic energy consists of two parts: the classical part and the non-classical part. In our work, the form of kinetic energy is simplified to consider the classical part only, whose applications can be found in [107, 205, 206].

Firstly, the beam along x direction in the unit cell is regarded as a Euler-Bernoulli micro-

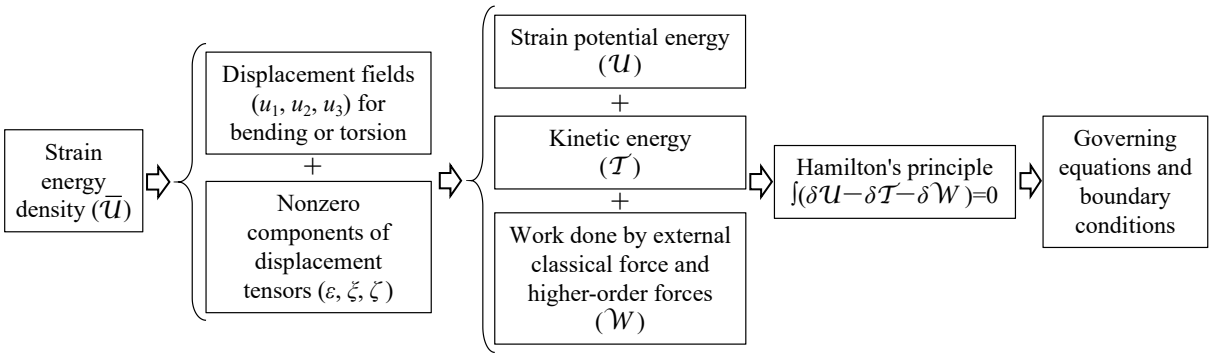

Fig. 3.2. Graphical representation for analysing continuum model vibration.

sized bending beam with displacements w along z direction and angle θ in $x0z$ plane. The variational principle is applied to derive the governing equation. Consider a lateral distributed force $\overline{f}(x,t)$ along z direction acting on the beam. According to the calculating process in Fig. 3.2, the governing equation and boundary conditions for bending can be deduced by SSG theory, which are shown in Eq.2.9 and Eq.2.10.

Next, the beam is regarded as a torsional beam with angle φ in $y0z$ plane. A distributed torque $\overline{\Gamma}(x,t)$ around x axis is considered. In order to derive the strong formulas of torsional vibration, the variational principle is used as well. The governing equation and boundary conditions for torsion can be calculated, which are shown in Eq.2.29 and Eq.2.30 respectively.

3.2.2 Lattice spring model by second strain gradient elasticity

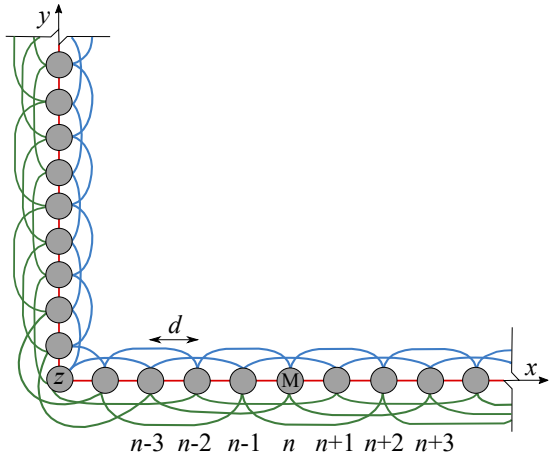

Fig. 3.3. A unit cell by LSM with coupling relations. Red line denotes the nearest neighbor interaction, blue line means the next-nearest neighbor interaction and green line represents the next-next-nearest neighbor interaction. d is the distance between two nodes and the mass $M = \rho Ad$. z axis is perpendicular to $x0y$ plane.

As shown in Fig. 3.3, the discrete structure, formed by interactions of nearest, next-nearest and next-next-nearest neighbors, is a valuable presentation for SSG model. The distance d is a

numerical parameter which is used for the convergence study [107]. The process of dynamic analysis for bending and torsion is presented in Fig. 3.4. The lattice equation of motion for displacement field on node n is illustrated from the LSM method. After Fourier series transform [110], the dynamic continuum equations for bending and torsion will be derived separately.

Starting with the bending analysis within the LSM framework, the branch of the unit cell

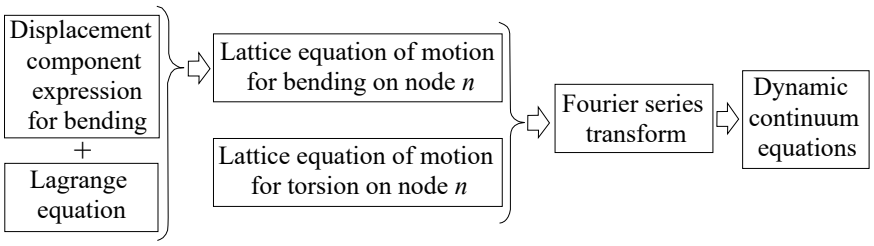

Fig. 3.4. Graphical representation for analyzing LSM vibration.

along x direction, as shown in Fig. 3.3, is regarded as a discrete form of Euler–Bernoulli beam based on SSG theory. The coupling constants from nearest (red line), next-nearest (blue line) and next-next-nearest (green line) neighbors interactions can be expressed by k_1^b, k_2^b and k_3^b which are called bending stiffness. The Degree of Freedoms (DOFs) on node n are displacement w along z direction and angle of rotation θ in $x0z$ plane. The governing equation can be illustrated based on Fourier series transform approach as shown in Eq.2.23. Ignore the higher order infinitesimal part o in Eq.2.23, the continuum equation for micro-sized Euler–Bernoulli lattice bending beam can be confirmed.

Next, the branch of the unit cell along x direction is regarded as a lattice torsional beam, as shown in Fig. 3.3, the three coupling parameters from the interactions of nearest, next-nearest and next-next-nearest neighbors are represented by torsional stiffness k_1^t, k_2^t and k_3^t. The expression of $\varphi(x,t)$ from the torsional LSM can be obtained, as presented in Eq.2.35. Remove the higher order infinitesimal part o, the continuum equation of torsional beam by LSM can be confirmed and the relations between the torsional stiffness and higher order parameters can be derived finally.

3.3 Wave finite element method for 2D structures

3.3.1 Finite element procedure

In this part, the weak formulas for out-of plane vibration are transformed from strong formulas. As shown in Fig. 3.5, nodal displacement field for an element is:

$$\mathbf{u}^{(e)}(t) = \left[w_1, \varphi_1, \theta_1, \frac{\partial \varphi_1}{\partial x}, \frac{\partial^2 w_1}{\partial x^2}, \frac{\partial^2 \varphi_1}{\partial x^2}, \frac{\partial^3 w_1}{\partial x^3}, w_2, \varphi_2, \theta_2, \frac{\partial \varphi_2}{\partial x}, \frac{\partial^2 w_2}{\partial x^2}, \frac{\partial^2 \varphi_2}{\partial x^2}, \frac{\partial^3 w_2}{\partial x^3} \right]^{\mathrm{T}}, \tag{3.1}$$

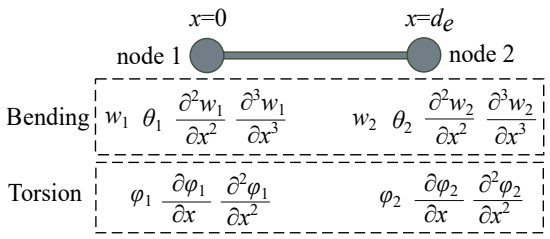

Fig. 3.5. Two nodes fourteen DOFs in an element.

in which the four DOFs, $w_i, \theta_i, \frac{\partial^2 w_i}{\partial x^2}, \frac{\partial^3 w_i}{\partial x^3}, i = 1, 2$, belong to bending on each node and the three DOFs, $\varphi_i, \frac{\partial \varphi_i}{\partial x}, \frac{\partial^2 \varphi_i}{\partial x^2}, i = 1, 2$, belong to torsion on each node. Then, defining bending displacement $w(x,t)$ and torsion displacement $\varphi(x,t)$ on point $x \in \mathbb{R}^2$ inside an element:

$$\begin{aligned} \begin{pmatrix} w(x,t) \\ \varphi(x,t) \end{pmatrix} &= \begin{pmatrix} \mathbf{N}^b(x) \\ \mathbf{N}^t(x) \end{pmatrix} \mathbf{u}^{(e)}(t) \\ &= \begin{bmatrix} \mathrm{N}_1^{b0},\ 0,\ \mathrm{N}_1^{b1},\ 0,\ \mathrm{N}_1^{b2},\ 0,\ \mathrm{N}_1^{b3},\ \mathrm{N}_2^{b0},\ 0,\ \mathrm{N}_2^{b1},\ 0,\ \mathrm{N}_2^{b2},\ 0,\ \mathrm{N}_2^{b3} \\ 0,\ \mathrm{N}_1^{t0},\ 0,\ \mathrm{N}_1^{t1},\ 0,\ \mathrm{N}_1^{t2},\ 0,\ 0,\ \mathrm{N}_2^{t0},\ 0,\ \mathrm{N}_2^{t1},\ 0,\ \mathrm{N}_2^{t2},\ 0 \end{bmatrix} \mathbf{u}^{(e)}(t), \end{aligned} \tag{3.2}$$

where the size of $\mathbf{N}^b$ is $1 \times p$ in which p is the number of DOFs for bending. $\mathbf{N}^t$ has the size of $1 \times r$ in which r is the number of DOFs for torsion.

In order to obtain the shape functions $\mathbf{N}^b$ for bending and $\mathbf{N}^t$ for torsion, the C^3 and C^2 continuum Hermite interpolation functions [95, 217, 218] guaranteeing the displacement and strain fields continuous and smooth at higher-order level are utilized in Eq. 3.2, as expressed:

$$\begin{aligned}
\mathrm{N}_1^{b0} &= 1 - 35\frac{x^4}{d_e^4} + 84\frac{x^5}{d_e^5} - 70\frac{x^6}{d_e^6} + 20\frac{x^7}{d_e^7}, & \mathrm{N}_2^{b0} &= 35\frac{x^4}{d_e^4} - 84\frac{x^5}{d_e^5} + 70\frac{x^6}{d_e^6} - 20\frac{x^7}{d_e^7}, \\
\mathrm{N}_1^{b1} &= x - 20\frac{x^4}{d_e^3} + 45\frac{x^5}{d_e^4} - 36\frac{x^6}{d_e^5} + 10\frac{x^7}{d_e^6}, & \mathrm{N}_2^{b1} &= -15\frac{x^4}{d_e^3} + 39\frac{x^5}{d_e^4} - 34\frac{x^6}{d_e^5} + 10\frac{x^7}{d_e^6}, \\
\mathrm{N}_1^{b2} &= \frac{x^2}{2} - 5\frac{x^4}{d_e^2} + 10\frac{x^5}{d_e^3} - 15\frac{x^6}{d_e^4} + 2\frac{x^7}{d_e^5}, & \mathrm{N}_2^{b2} &= 5\frac{x^4}{d_e^2} - 7\frac{x^5}{d_e^3} + 13\frac{x^6}{d_e^4} - 2\frac{x^7}{d_e^5}, \\
\mathrm{N}_1^{b3} &= \frac{x^3}{6} - 2\frac{x^4}{3d_e} + \frac{x^5}{d_e^2} - 2\frac{x^6}{3d_e^3} + \frac{x^7}{6d_e^4}, & \mathrm{N}_2^{b3} &= -\frac{x^4}{6d_e} + \frac{x^5}{2d_e^2} - \frac{x^6}{2d_e^3} + \frac{x^7}{6d_e^4}, \\
\mathrm{N}_1^{t0} &= 1 - 10\frac{x^3}{d_e^3} + 15\frac{x^4}{d_e^4} - 6\frac{x^5}{d_e^5}, & \mathrm{N}_2^{t0} &= 10\frac{x^3}{d_e^3} - 15\frac{x^4}{d_e^4} + 6\frac{x^5}{d_e^5}, \\
\mathrm{N}_1^{t1} &= \frac{x}{d_e} - 6\frac{x^3}{d_e^3} + 8\frac{x^4}{d_e^4} - 3\frac{x^5}{d_e^5}, & \mathrm{N}_2^{t1} &= -4\frac{x^3}{d_e^3} + 7\frac{x^4}{d_e^4} - 3\frac{x^5}{d_e^5}, \\
\mathrm{N}_1^{t2} &= \frac{x^2}{2d_e^2} - 3\frac{x^3}{2d_e^3} + 3\frac{x^4}{2d_e^4} - \frac{x^5}{2d_e^5}, & \mathrm{N}_2^{t2} &= \frac{x^3}{2d_e^3} - \frac{x^4}{d_e^4} + \frac{x^5}{2d_e^5},
\end{aligned} \tag{3.3}$$

where the subscript number of $\mathbf{N}$ denotes the node number, superscript number means the derivative order with respect to $x \in [0, d_e]$ coordinate.

Submitting $w(x,t)$ and $\varphi(x,t)$ from Eq. 3.2 into equilibrium equation Eq. 2.9 and Eq. 2.29 respectively. Doing the integration according to Galerkin's approach and part-by-part integration to the resulting function. The weak forms can be derived and the element mass matrices $\mathbf{M}^{(e)b}$ and $\mathbf{M}^{(e)t}$, stiffness matrices $\mathbf{K}^{(e)b}$ and $\mathbf{K}^{(e)t}$, force vectors $\mathbf{F}^{(e)b}$ and $\mathbf{F}^{(e)t}$ for bending and torsion are extracted separately as:

$$
\begin{aligned}
\mathbf{M}^{(e)b} &= \rho A \int_0^{d_e} (\mathbf{N}^b)^{\mathrm{T}} \mathbf{N}^b \mathrm{d}x, \\
\mathbf{M}^{(e)t} &= \rho J \int_0^{d_e} (\mathbf{N}^t)^{\mathrm{T}} \mathbf{N}^t \mathrm{d}x, \\
\mathbf{K}^{(e)b} &= \int_0^{d_e} \left[C_1^b \left((\mathbf{N}^b)'' \right)^{\mathrm{T}} (\mathbf{N}^b)'' + (C_2^b - C_4^b) \left((\mathbf{N}^b)''' \right)^{\mathrm{T}} (\mathbf{N}^b)''' + C_3^b \left((\mathbf{N}^b)'''' \right)^{\mathrm{T}} (\mathbf{N}^b)'''' \right] \mathrm{d}x, \\
\mathbf{K}^{(e)t} &= \int_0^{d_e} \left[C_1^t \left((\mathbf{N}^t)' \right)^{\mathrm{T}} (\mathbf{N}^t)' + (C_2^t - C_4^t) \left((\mathbf{N}^t)'' \right)^{\mathrm{T}} (\mathbf{N}^t)'' + C_3^t \left((\mathbf{N}^t)''' \right)^{\mathrm{T}} (\mathbf{N}^t)''' \right] \mathrm{d}x, \\
\mathbf{F}^{(e)b} &= \int_0^{d_e} \overline{f}(x,t) \mathbf{N}^b \mathrm{d}x + f_0 \mathbf{N}^b|_{\partial\Omega_{f_0}} + f_1 (\mathbf{N}^b)'|_{\partial\Omega_{f_1}} + f_2 (\mathbf{N}^b)''|_{\partial\Omega_{f_2}} + f_3 (\mathbf{N}^b)'''|_{\partial\Omega_{f_3}}, \\
\mathbf{F}^{(e)t} &= \int_0^{d_e} \overline{\Gamma}(x,t) \mathbf{N}^t \mathrm{d}x + \Gamma_0 \mathbf{N}^t|_{\partial\Omega_{\Gamma_0}} + \Gamma_1 (\mathbf{N}^t)'|_{\partial\Omega_{\Gamma_1}} + \Gamma_2 (\mathbf{N}^t)''|_{\partial\Omega_{\Gamma_2}},
\end{aligned}
\tag{3.4}
$$

where superscript $(')$ means partial derivative with respect to coordinate x. The matrices and vector for an element are illustrated by adding bending and torsion cases together:

$$
\mathbf{M}^{(e)} = \mathbf{M}^{(e)b} + \mathbf{M}^{(e)t},\ \mathbf{K}^{(e)} = \mathbf{K}^{(e)b} + \mathbf{K}^{(e)t},\ \mathbf{F}^{(e)} = \mathbf{F}^{(e)b} + \mathbf{F}^{(e)t}. \tag{3.5}
$$

3.3.2 2D wave propagation analysis

The global mass matrix $\mathbf{M}$ and stiffness matrix $\mathbf{K}$ of a unit cell can be assembled by the element mass matrix $\mathbf{M}^{(e)}$ and stiffness matrix $\mathbf{K}^{(e)}$ separately. Defining that $\hat{\mathbf{u}}$ and $\hat{\mathbf{F}}$ are the amplitudes of nodal harmonic displacement $\mathbf{u}$ and force $\mathbf{F}$ of a unit cell, respectively. As presented in Fig. 3.1(b), the nodal DOFs ($\hat{\mathbf{u}}$) are divided into corners DOFs ($\hat{\mathbf{u}}_1$, $\hat{\mathbf{u}}_2$, $\hat{\mathbf{u}}_3$) and internal DOFs ($\hat{\mathbf{u}}_{\mathrm{I}}$). The vectors of corners forces are represented by $\hat{\mathbf{F}}_1$, $\hat{\mathbf{F}}_2$ and $\hat{\mathbf{F}}_3$. Assuming that there are no external forces on the internal DOFs: $\hat{\mathbf{F}}_{\mathrm{I}} = \mathbf{0}$. The unit cell's dynamical equilibrium equation [219] is:

$$
(\tilde{\mathbf{K}} - \omega^2 \mathbf{M}) \hat{\mathbf{u}} = \hat{\mathbf{F}}, \tag{3.6}
$$

where $\hat{\mathbf{u}} = [(\hat{\mathbf{u}}_1)^{\mathrm{T}}, (\hat{\mathbf{u}}_2)^{\mathrm{T}}, (\hat{\mathbf{u}}_3)^{\mathrm{T}}, (\hat{\mathbf{u}}_{\mathrm{I}})^{\mathrm{T}}]^{\mathrm{T}}$, $\hat{\mathbf{F}} = [(\hat{\mathbf{F}}_1)^{\mathrm{T}}, (\hat{\mathbf{F}}_2)^{\mathrm{T}}, (\hat{\mathbf{F}}_3)^{\mathrm{T}}, \mathbf{0}^{\mathrm{T}}]^{\mathrm{T}}$. According to the Bloch's theorem, the DOFs' relations and forces' relations can be expressed separately as [220]:

$$
\hat{\mathbf{u}} = \mathbf{\Lambda}_R \begin{pmatrix} \hat{\mathbf{u}}_1 \\ \hat{\mathbf{u}}_{\mathrm{I}} \end{pmatrix},\ \mathbf{\Lambda}_L \hat{\mathbf{F}} = \mathbf{0}, \tag{3.7}
$$

with

$$\mathbf{\Lambda}_R = \begin{bmatrix} \mathbf{I}_s & \mathbf{0} \\ \lambda_y \mathbf{I}_s & \mathbf{0} \\ \lambda_x \mathbf{I}_s & \mathbf{0} \\ \mathbf{0} & \mathbf{I}_I \end{bmatrix}, \ \mathbf{\Lambda}_L = \begin{bmatrix} \mathbf{I}_s & \lambda_y^{-1}\mathbf{I}_s & \lambda_x^{-1}\mathbf{I}_s & \mathbf{0} \\ \mathbf{0} & \mathbf{0} & \mathbf{0} & \mathbf{I}_I \end{bmatrix}, \tag{3.8}$$

where λ_x and λ_y are related to wave-numbers κ_x and κ_y by $\lambda_x = \exp(-\mathrm{i}\kappa_x L_x)$ and $\lambda_y = \exp(-\mathrm{i}\kappa_y L_y)$ respectively, $\mathbf{I}_s$ and $\mathbf{I}_I$ denote the identity matrices of size s and I. Substituting Eq. 3.7 into Eq. 3.6 yields:

$$\mathbf{\Lambda}_L(\tilde{\mathbf{K}} - \omega^2\mathbf{M})\mathbf{\Lambda}_R \begin{pmatrix} \hat{\mathbf{u}}_1 \\ \hat{\mathbf{u}}_\mathrm{I} \end{pmatrix} = \mathbf{0}. \tag{3.9}$$

Eq. 3.9 provides a way to analyze the wave propagation in 2D periodic structures. There exist two different forms to solve this equation: the first one is fixing frequency (ω) and λ_y, all possible solutions for λ_x are sought which correspond to evanescent or propagation waves. The second one is fixing λ_x and λ_y, the values of ω are calculated. In our work, the second form which is called inverse form is used. As shown in Fig. 1.3(b), the wave-numbers κ_x and κ_y change within the first Brillouin zone $[-\pi/L_x, \pi/L_x]$ and $[-\pi/L_y, \pi/L_y]$ and are discretised into (κ_x^i, κ_y^j), with κ_x^i being the i-th term, κ_y^j being the j-th term. The corresponding frequencies (ω) are sorted in the ascending order $\omega^{i,j}_{1,2,3,\ldots k,\ldots n}$. The k-th slowness surface is formed by $\omega_k^{i,j}$. The Poynting vector (i.e., energy flow vector) at any point (κ_x, κ_y) is same as the gradient of slowness surface [221]. For the iso-frequency contour of the slowness surface, Poynting vector is normal to the contour curves. This character can be used to determine the direction of wave propagation and non-propagation which is known as the wave beaming effect.

In addition, a convenient 2D representation of the slowness surface is the band structure, which is obtained by plotting the wave-numbers along the contour O–A–B–O as shown in Fig. 1.3(b). The plane wave propagates with wave-number $\kappa_{\theta'}$ in angle θ' as shown in Fig. 1.3(c). The band structure can be used to explore the frequency ranges of stop bands and the location where different slowness surfaces touch each other.

3.4 Numerical examples and discussions

In this part, the inverse form of WFEM is applied to analyze the un-damped out-of plane vibration of a beam grid by SSG and CT. As presented in Fig. 3.1(b), the material of a unit cell in the beam grid is Aluminum with $15a_0$ wide and $20a_0$ high in cross-section, $L_x = 250a_0$ and $L_y = 175a_0$ ($a_0 = 4.04 \times 10^{-10}$m is the lattice parameter). The size of this unit cell is at nano-sized level and the characteristics of non-local interactions in the unit cell can be presented effectively. The Young's modulus $E = 70$ GPa, linear mass density $\rho = 2.7\ \mathrm{g/cm^3}$, and each

branch of the unit cell is meshed into 20 elements. The beam grid contains 20 unit cells along x direction and 20 unit cells along y direction. Here should be pointed that the circular frequency is normalized as ω/ω_0, in which ω_0 is the first nature circular frequency of the unit cell.

3.4.1 Band structure

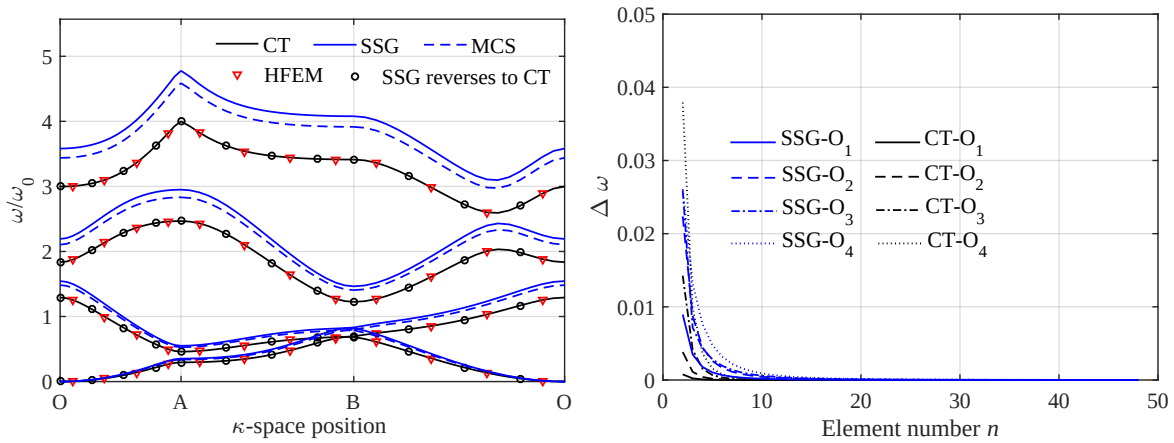

(a) Band structure by SSG and CT and validation.

(b) Convergence of band structure at boundary point O by SSG and CT.

Fig. 3.6. Band structure, validation and convergence.

Fig. 3.6(a) shows the four lowest branches of the normalized frequency spectrum along the boundary (O-A-B-O) of the irreducible first Brillouin zone for 2D beam grid. The blue lines represent the results from SSG theory and black lines denote the CT. The curve by SSG is close to the one by CT at low frequency. But the difference between SSG and CT becomes more obvious as frequency increases. The frequency value by SSG is higher than CT at same κ-space position. Due to the existence of non-classical parts containing higher-order parameters in SSG, the eigenvalue ω calculated by the dynamical equilibrium equation of SSG theory is bigger than the one of CT at same κ-space position. In order to valid the band structure by CT, a linear elastic method called Hierarchical Finite Element Method (HFEM) [222] is used, as shown in Fig. 3.6(a), the result by HFEM matches CT well. At the same time, when the higher order parameters a_i, b_i and c_i are equal to zero, SSG will reverse to CT. On the other hand, a higher-order continuum theory called Modified Couple Stress (MCS) theory [81, 223] is used to compare with SSG theory. It shows that the discrepancy between SSG and MCS becomes more obvious as frequency increases. This is because that the curvature tensor is considered in MCS theory, curvature tensor and higher order terms of strain tensor are considered in SSG theory. Fig. 3.6(b) is about the convergence of the first four frequencies at boundary point O by SSG and CT. It indicates that the variety of frequency decreases with element number increases and shows the convergence.

3.4.2 Slowness surfaces

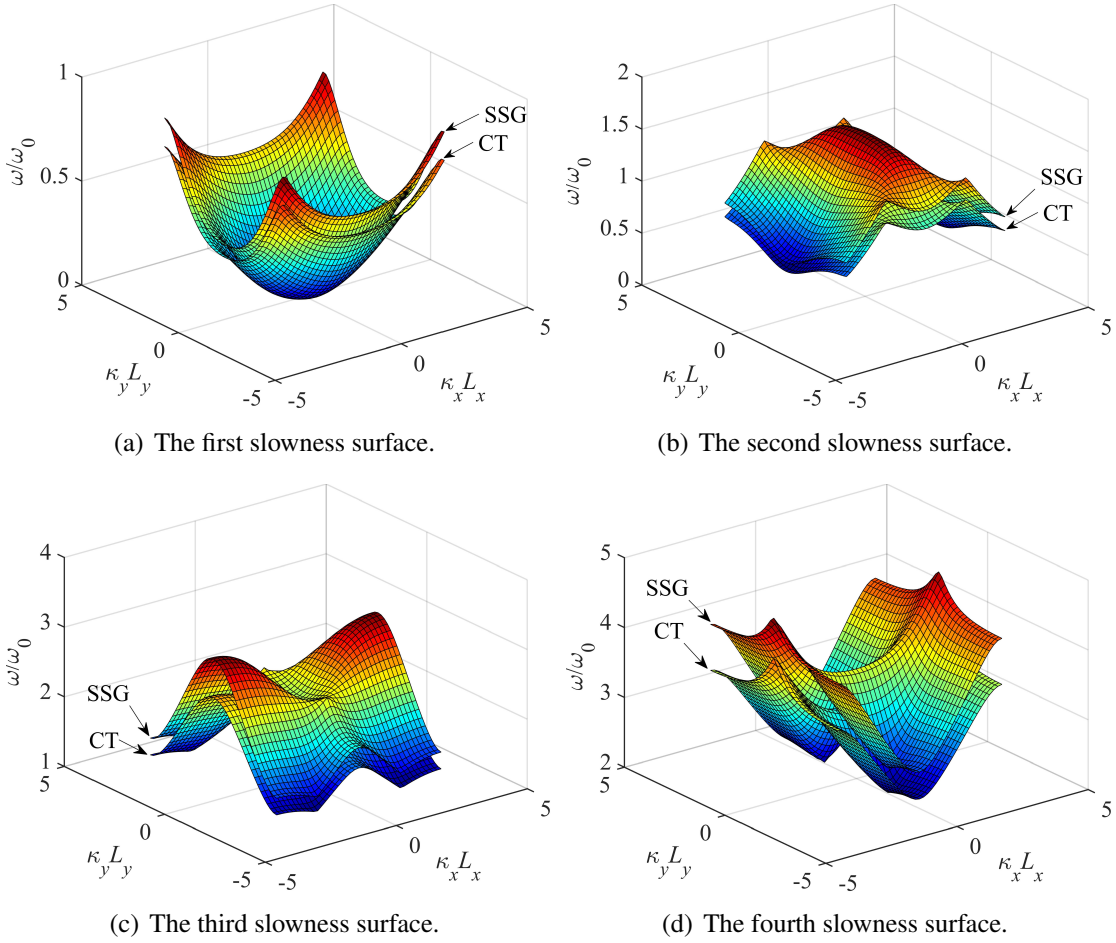

(a) The first slowness surface.

(b) The second slowness surface.

(c) The third slowness surface.

(d) The fourth slowness surface.

Fig. 3.7. The first four slowness surfaces by SSG and CT.

The first four slowness surfaces, as presented in Fig. 3.7, are studied in the frequency range based on SSG and CT. The 3D surfaces are symmetric with respect to κ_x and κ_y. The slowness surface position by SSG is higher than CT. This phenomenon can be explained by taking the bending wave as an example: assuming the lateral distributed force $\overline{f}(x,t) = 0$ and submitting bending displacement $w(x,t) = w_0 e^{i(\omega t - \kappa x)}$ into Eq. 2.9, the dynamical equation of bending wave by SSG theory becomes: $C_1^b \kappa^4 + (C_4^b - C_2^b)\kappa^6 + C_3^b \kappa^8 = \rho A \omega^2$, in which the term containing the fourth power of wave-number corresponds to CT. It can be clearly found that the frequency value by SSG is bigger than the value by CT at same κ-space position.

As shown in Fig. 3.8, in order to calculate the iso-frequency contours, the normalized frequencies are chosen at 0.008 and 0.08 on the first slowness surface, 0.9 and 1.2 on the second slowness surface, 1.9 and 2.1 on the third slowness surface, 2.5 and 2.9 on the fourth slowness surface. The direction, perpendicular to the iso-frequency line, indicates the direction of wave propagation and more details will be discussed in next section. There exists a big difference

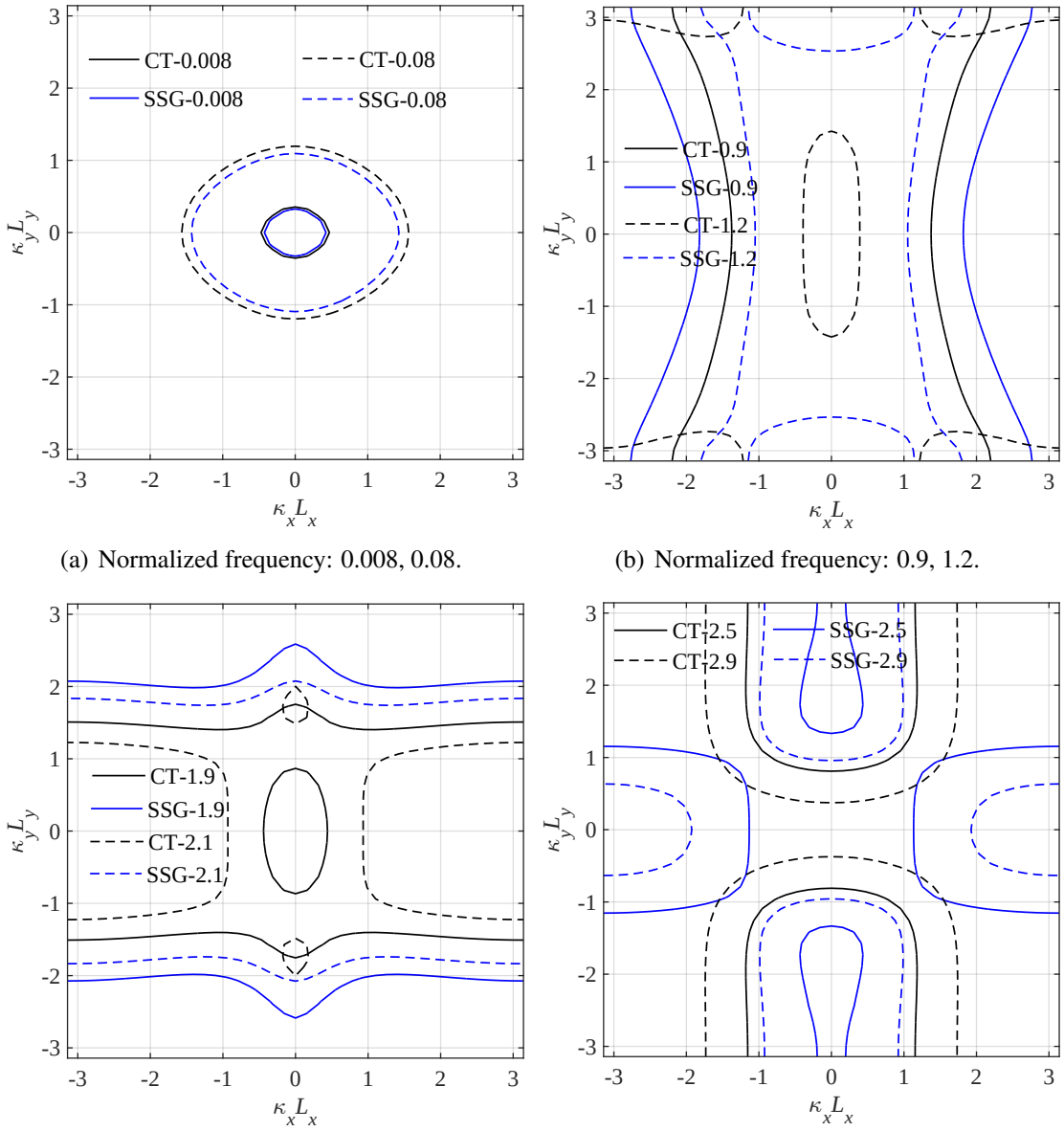

(a) Normalized frequency: 0.008, 0.08.

(b) Normalized frequency: 0.9, 1.2.

(c) Normalized frequency: 1.9, 2.1.

(d) Normalized frequency: 2.5, 2.9.

Fig. 3.8. The iso-frequency contour of first four slowness surfaces by SSG and CT.

between SSG and CT at higher frequency, which means that the high-order parameters have a significant influence on the value of iso-frequency contours at higher frequency.

3.4.3 Energy flow vector fields

The energy flow vector fields by SSG and CT on the first four slowness surfaces are studied in this part. As shown in Fig. 3.9, the direction of arrow indicates the direction of energy flow and the length of arrow means the gradient value of energy flow. The blue arrow from SSG and black arrow from CT almost overlap, which indicates that the gradient and direction of

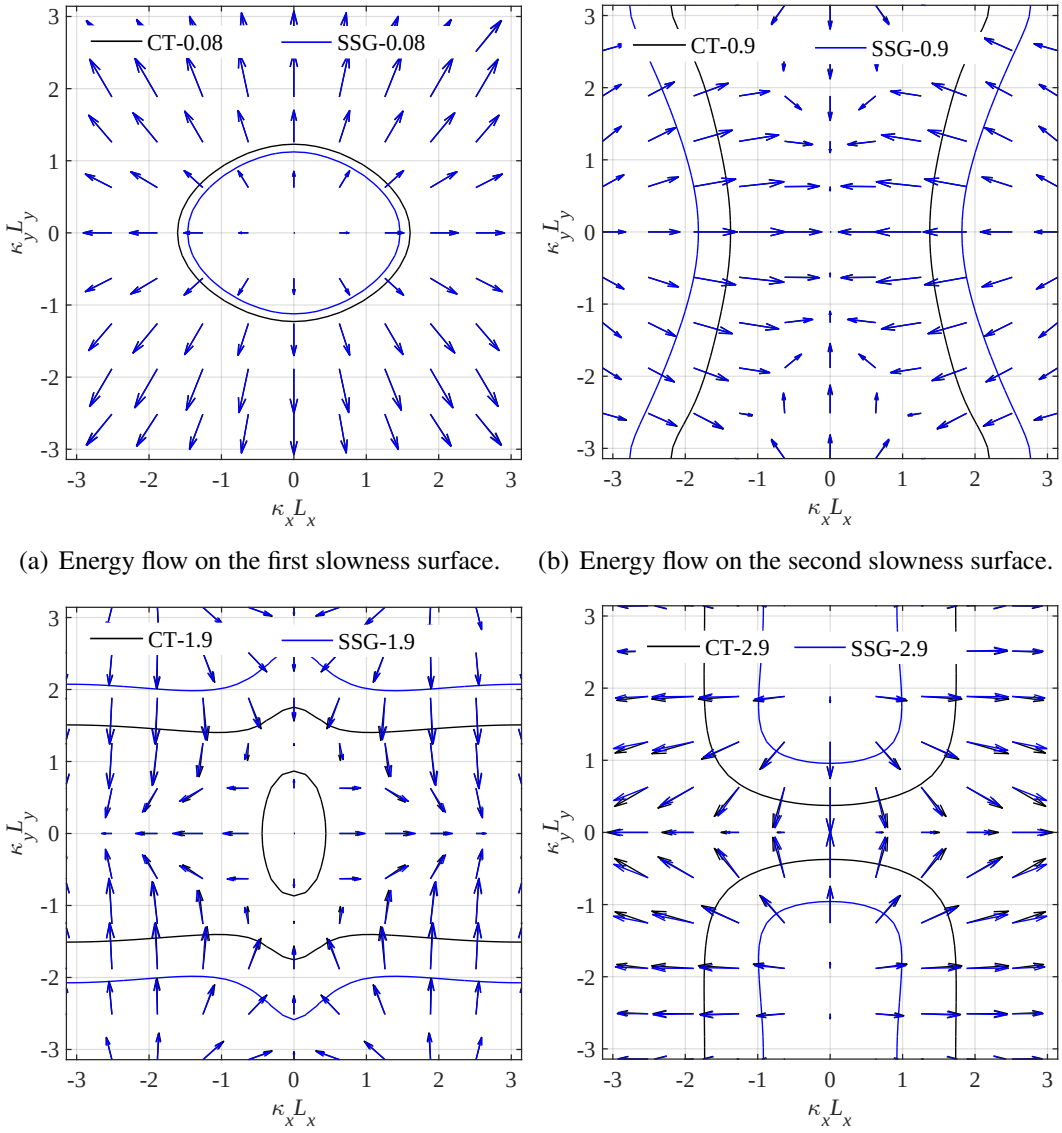

(a) Energy flow on the first slowness surface. (b) Energy flow on the second slowness surface.

(c) Energy flow on the third slowness surface. (d) Energy flow on the fourth slowness surface.

Fig. 3.9. Energy flow vector fields by SSG and CT on the first four slowness surfaces.

energy flow by SSG are basically the same as that by CT at the same κ-space position. At low frequency, as shown in Fig. 3.9(a), the behavior of beam grid is similar to an homogeneous orthotropic plate where the dynamic energy spreads in all directions and is perpendicular to the iso-frequency contour. At higher frequency such as 0.9, as shown in Fig. 3.9(b), the directions of majority energy are limited to x direction, which means that there are stop bands in y direction. When normalized frequency is 1.9 as presented in Fig. 3.9(c), the directions of majority energy are restricted to y direction and stop bands exist in x direction.

The distance from any point on the iso-frequency contour to the center point of the figure represents the wave number $\kappa_{\theta'}$ with θ' for plane wave propagation. On the first slowness

surface, the position of the iso-frequency contour from SSG is located inside the iso-frequency contour from CT, which means that $\kappa_{\theta'}$ from SSG is smaller than the one from CT at same wave propagation angle θ'. Contrast that with the second and third slowness surfaces, whose iso-frequency contour position from SSG is located outside the one from CT, which shows that $\kappa_{\theta'}$ from SSG is bigger than the one from CT.

3.4.4 Wave beaming effects

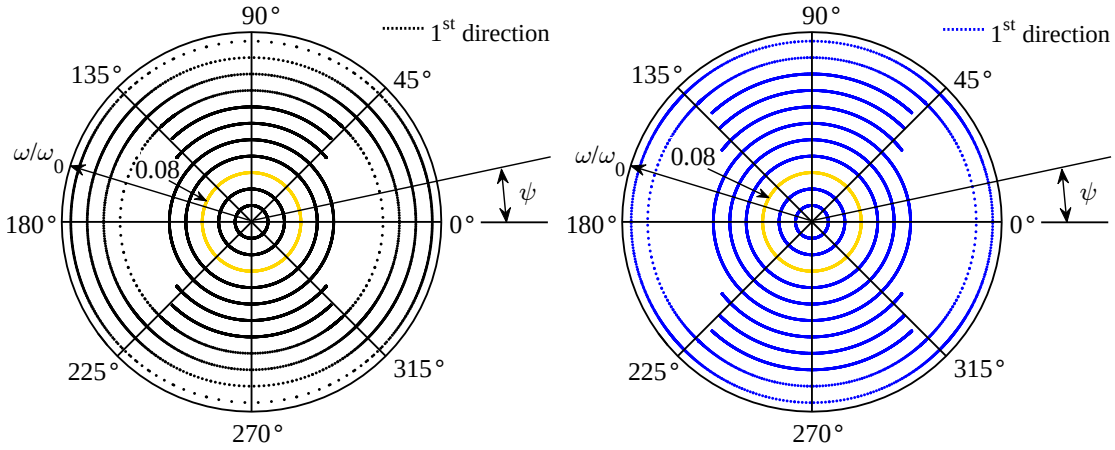

(a) CT. (b) SSG.

Fig. 3.10. Direction of wave propagation on the 1st slowness surface (ω increases from the center of the polar image to the edge, ψ is the range of free wave propagation under a considered frequency, frequency rang: 0-0.5).

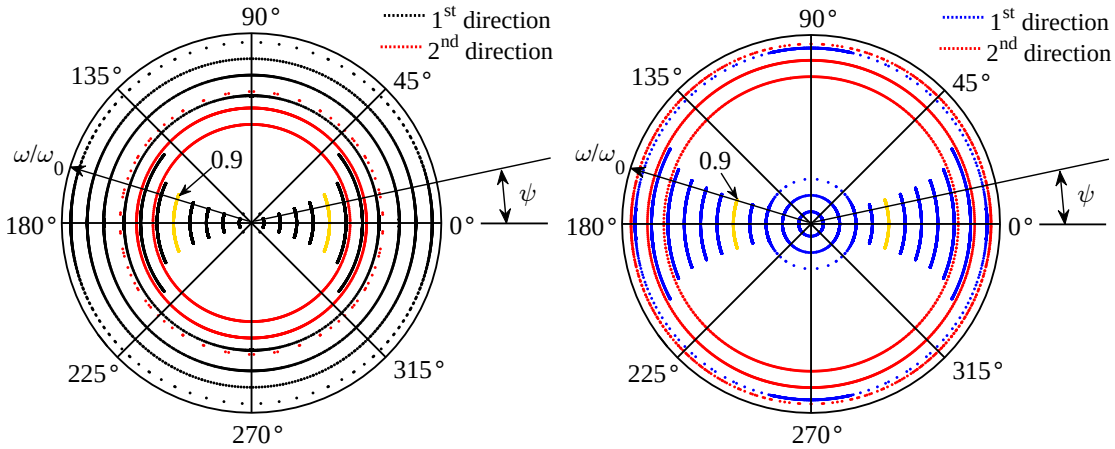

(a) CT. (b) SSG.

Fig. 3.11. Direction of wave propagation on the 2nd slowness surface (ω increases from the center of the polar image to the edge, ψ is the range of free wave propagation under a considered frequency, frequency rang: 0.5-1.5).

For further research of wave propagation directivity, the function $\kappa_y = f(\kappa_x)$ is defined for a given iso-frequency contour line in the first quadrant as shown in Fig.3.9. The wave

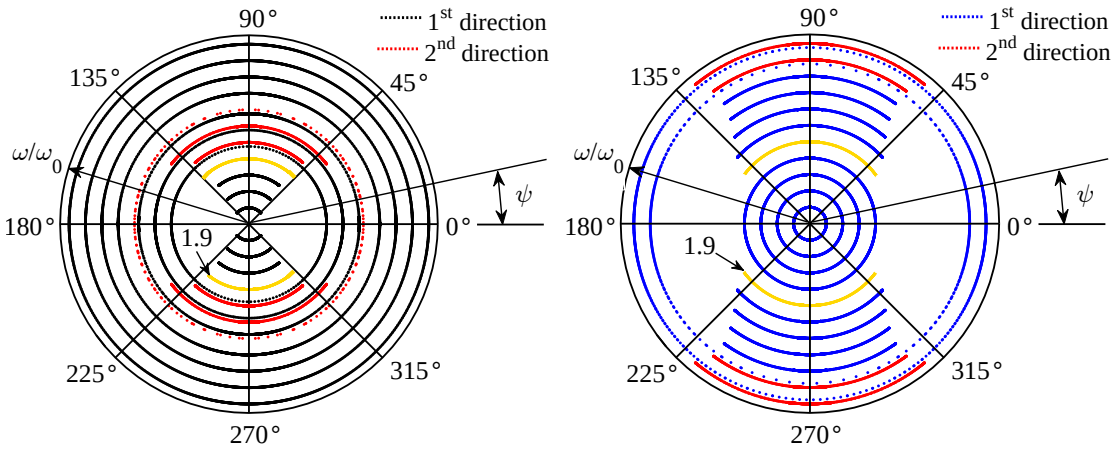

(a) CT. (b) SSG.

Fig. 3.12. Direction of wave propagation on the 3rd slowness surface (ω increases from the center of the polar image to the edge, ψ is the range of free wave propagation under a considered frequency, frequency rang: 1.5-2.5).

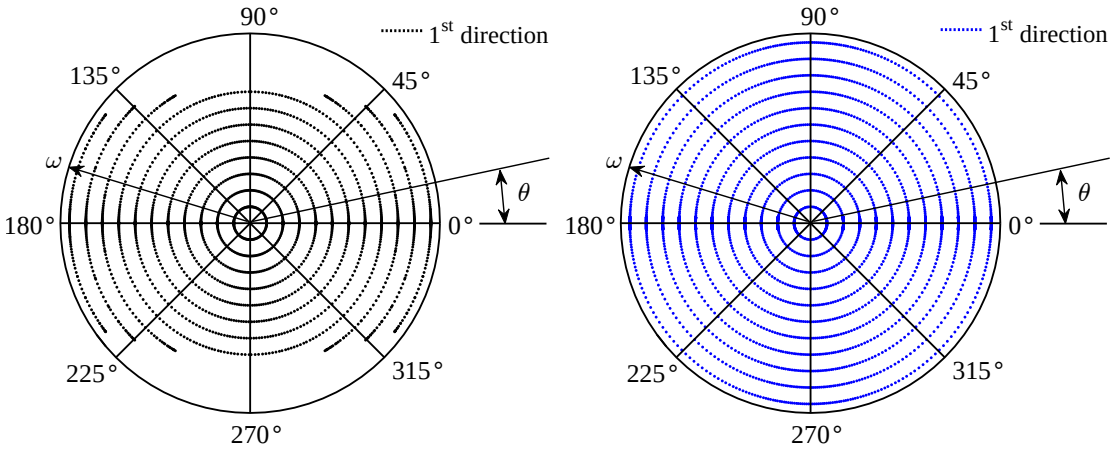

(a) CT. (b) SSG.

Fig. 3.13. Direction of wave propagation on the 4th slowness surface (ω increases from the center of the polar image to the edge, ψ is the range of free wave propagation under a considered frequency, frequency rang: 2.5-3.5).

propagation direction ψ, perpendicular to the iso-frequency contour, can be confirmed by $\psi = \arctan(\mathrm{d}\kappa_y/\mathrm{d}\kappa_x) + \pi/2$ [224]. The frequency dependent directional behavior of the beam grid by CT and SSG can be visualized through polar images as shown in Fig. 3.10 to Fig. 3.13. In the case of ω/ω_0 =0.08 on first slowness surface, wave propagation occurs in all directions which verifies the conclusion in previous section. The direction of wave propagation under other different frequencies can be predicted as well. It should be pointed out that there exist two directions of wave propagation at some frequencies as shown in Fig. 3.11 and Fig. 3.12. This is because there may be two iso-frequency contours at a certain frequency in the first quadrant, for example as shown in Fig. 3.9(c) for CT case. Two different directions of wave propagation can be generated with one being primary and another one being secondary. In this work, the

primary wave propagation directivity is studied.

In addition, the harmonic displacement fields are explored under Born-von Karman bound-

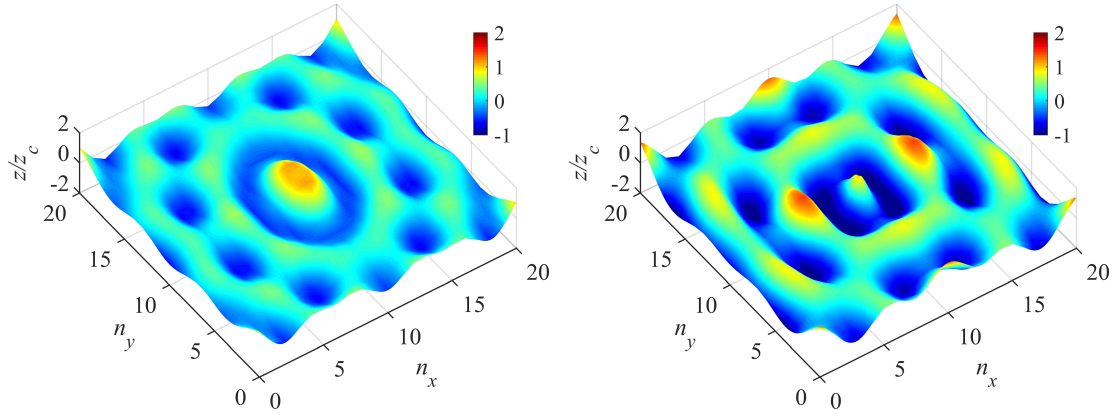

(a) CT. (b) SSG.

Fig. 3.14. Harmonic displacement field when $\omega/\omega_0 = 0.08$.

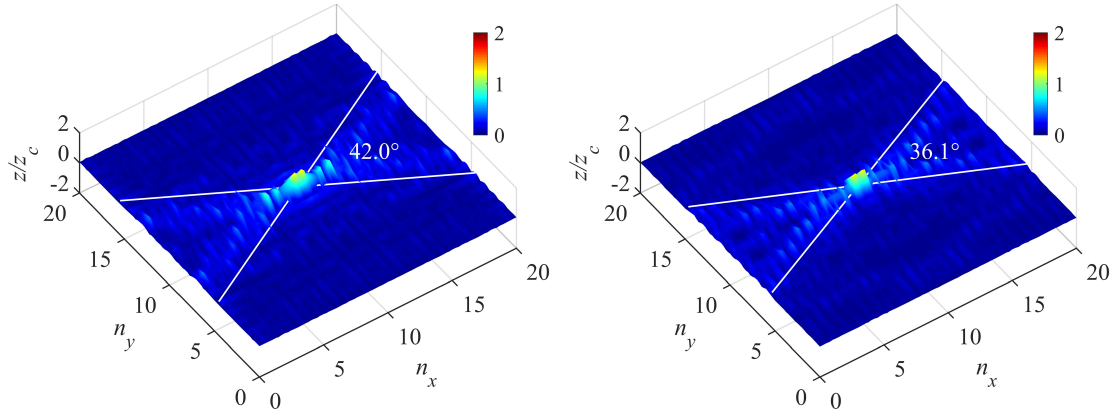

(a) CT. (b) SSG.

Fig. 3.15. Harmonic displacement field when $\omega/\omega_0 = 0.9$.

ary conditions [1, 113]: In damped systems, the response of harmonic displacement is considered approximately independent from boundary conditions. The function of harmonic displacement fields by FE method is expressed as: $[(1+\mathrm{i}\eta)\mathbf{K}' - \omega^2\mathbf{M}']\hat{\mathbf{u}}' = \hat{\mathbf{F}}'$ [1], in which $\mathbf{K}'$ and $\mathbf{M}'$ are stiffness and mass matrices of the beam grid with 20 unit cells along x direction and 20 unit cells along y direction. Due to the existence of damping loss factor η, the input power from external force rarely reaches the system boundary. So, the response by the above equation is closely approximate to the response of an infinite system. The free boundary condition was chosen for the beam grid in this work. Loss factor η is 0.05 and a harmonic force with unit amplitude is loaded at central place of the structure along z direction.

The results of displacement amplitudes along z direction, normalized with respect to the

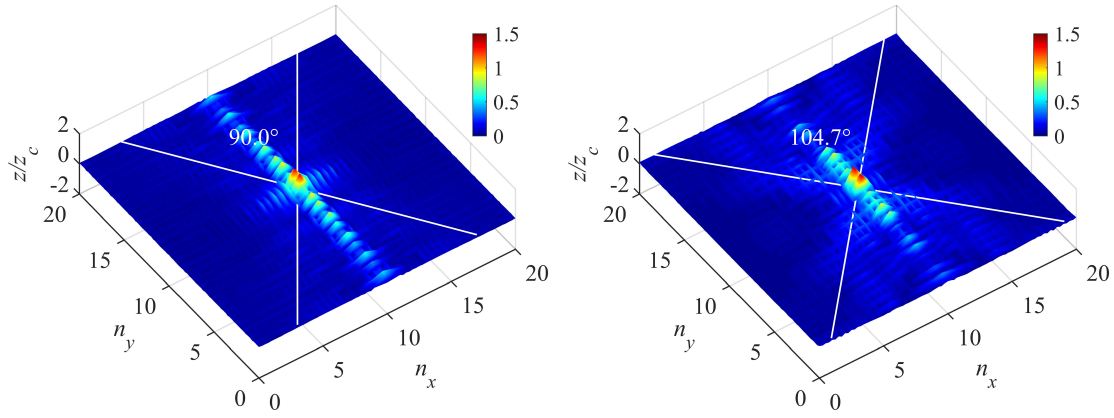

(a) CT. (b) SSG.

Fig. 3.16. Harmonic displacement field when $\omega/\omega_0 = 1.9$.

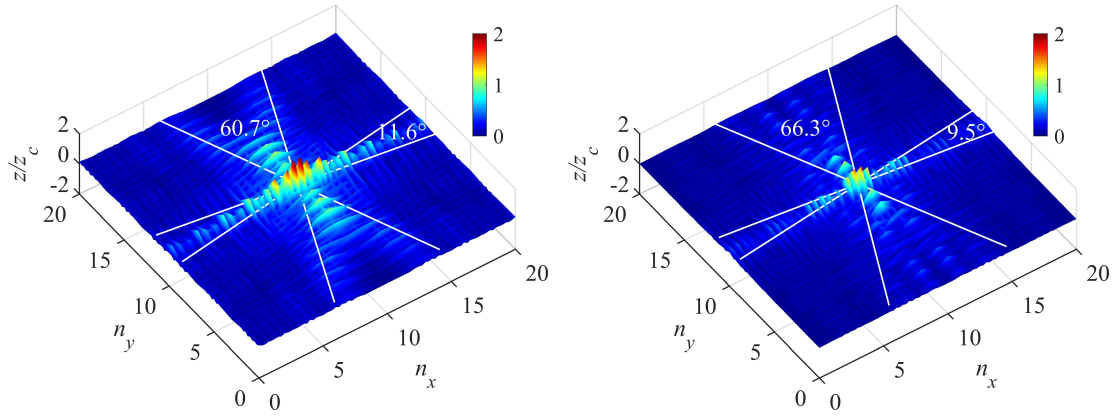

(a) CT. (b) SSG.

Fig. 3.17. Harmonic displacement field when $\omega/\omega_0 = 2.9$.

central point amplitudes (z_c), are presented in Fig. 3.14 to Fig. 3.17 by CT and SSG respectively. The continuous maps are obtained by interpolating the nodal displacements. The white lines on the harmonic displacement field images show the range of wave propagation as predicted in Fig. 3.10 to Fig. 3.13: $\psi = 360°$ by CT and SSG when normalized frequency is 0.08; $\psi = 42°$ by CT and $\psi = 36.1°$ by SSG when normalized frequency is 0.9; $\psi = 90°$ by CT and $\psi = 104.7°$ by SSG when normalized frequency is 1.9. The above results show that the directional patterns of the harmonic displacement response match the predictions from the energy flow vector fields, as well as the wave propagation directivity analysis. On the other hand, at low frequency, the wave propagation range by SSG is consistent with the one by CT. At high frequency, the wave propagation range by SSG is larger than the one by CT.

Next, the normalized forced response contours is discussed, as shown in Fig. 3.18, the iso-displacement contours are calculated at position $z/z_c = 0.1$ along z direction by SSG and CT. Here we fix the normalized frequency as 1.9. The wave spreads in y direction both by SSG and

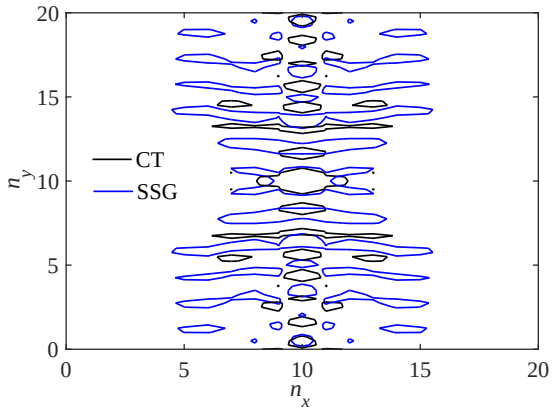

Fig. 3.18. Normalized forced response contours by SSG and CT (ω/ω_0=1.9, z/z_c=0.1).

CT. However, the range of wave propagation by SSG is bigger than the one by CT at same frequency. Furthermore, from the midpoint of the beam grid to the edge in y direction, the range of wave propagation increases first and then decreases by CT. In contrast, the range of wave propagation increases first and then remains unchanged by SSG.

3.4.5 Wave shapes

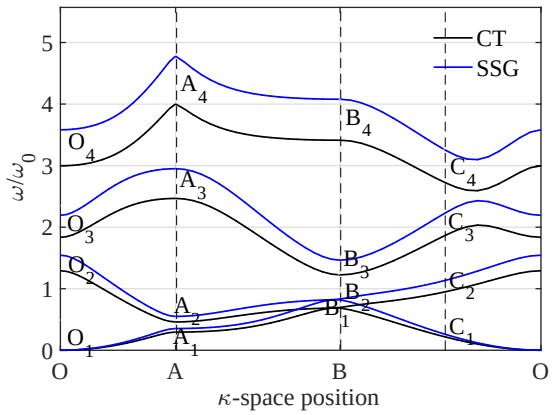

Fig. 3.19. The points on band structure for studying wave shapes.

The study of wave shapes at different κ-space position and frequency is another important part for understanding the dynamical characteristics of structure. The wave, which shows how energy travels, is the vibration of molecules or basic particles in the structure. The amplitude of wave shape is the strength of a wave's effect: the higher the amplitude, the more the particles are displaced. Different wave shapes have different harmonics. A harmonic is an additional frequency created by the wave.

In this part, the wave shapes $\mathbf{\Phi}$ for bending along z direction are studied by SSG and CT. The wave shapes illustrated from Eq 3.9 can be expressed as $\mathbf{\Phi} = [\phi_1, \phi_\mathrm{I}]$ in which corner node $\mathbf{u}_1$ and internal nodes $\mathbf{u}_\mathrm{I}$ are considered only. The global shapes can be obtained from

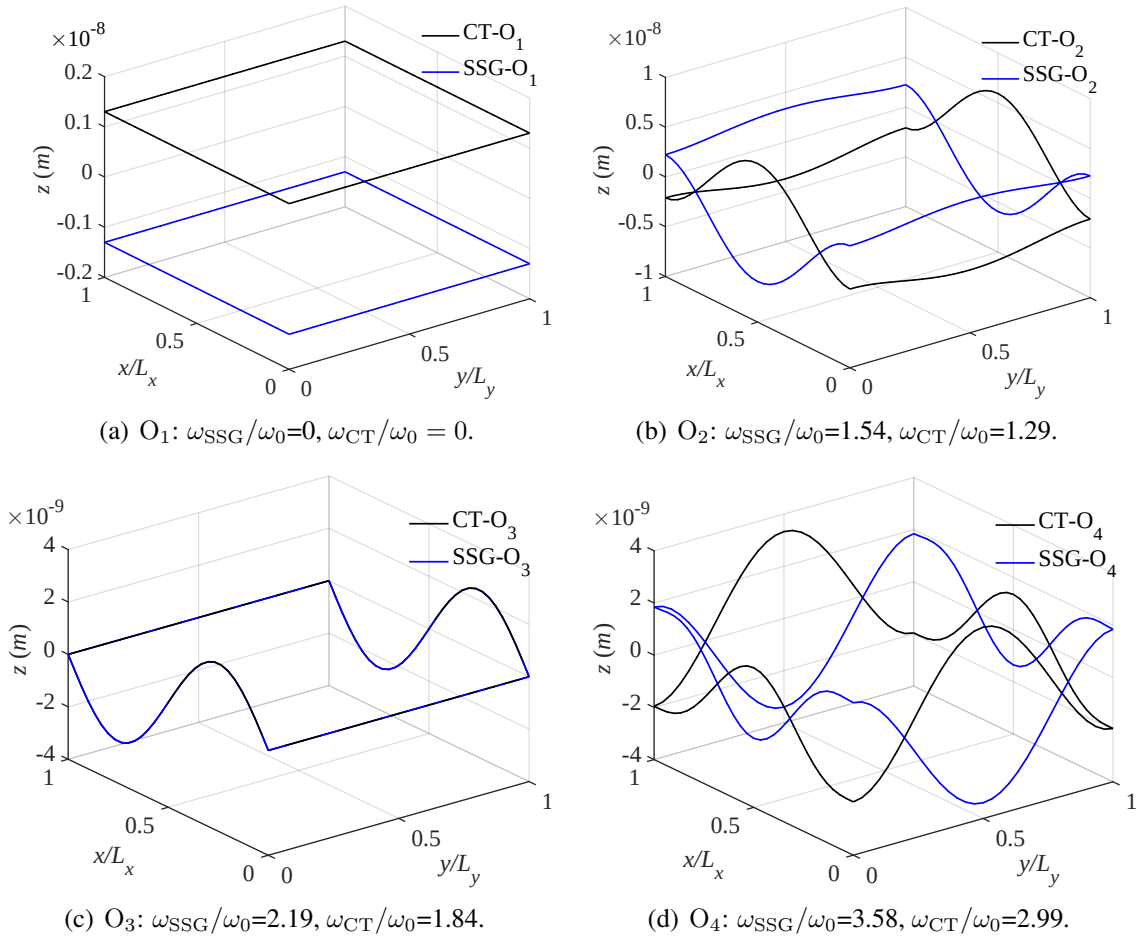

(a) O_1: ω_{SSG}/ω_0=0, $\omega_{CT}/\omega_0 = 0$. (b) O_2: ω_{SSG}/ω_0=1.54, ω_{CT}/ω_0=1.29.

(c) O_3: ω_{SSG}/ω_0=2.19, ω_{CT}/ω_0=1.84. (d) O_4: ω_{SSG}/ω_0=3.58, ω_{CT}/ω_0=2.99.

Fig. 3.20. Wave shapes on points O_1, O_2, O_3 and O_4 ($\kappa_x = 0$, $\kappa_y = 0$).

$[\phi_1, \phi_2, \phi_3, \phi_I]^{\mathcal{T}} = \mathbf{\Lambda}_R[\phi_1, \phi_I]^{T}$. The marked points O_i, A_i, B_i and C_i (i=1, 2, 3, 4) are shown in Fig. 3.19. The wave shapes at points O_1, O_2, O_3 and O_4 ($\kappa_x = 0$, $\kappa_y = 0$) are given in Fig. 3.20 which are extended in a rectangular domain from the unit cell. It can be seen that the wave shapes by SSG are similar to CT. However, the amplitudes direction of wave shapes by CT are opposite to the one by SSG at points O_1, O_2 and O_4. The wave shapes at points A_i, B_i and C_i are presented in Appendix E.

3.5 Conclusions

In this chapter, SSG theory is used for the dynamic analysis of a 2D micro-sized beam grid within the WFEM framework. Some conclusions in our work are addressed as follow:

(i) Strong formulas of continuum model for out-of plane vibration containing governing equations and boundary conditions are illustrated based on Hamilton principle. A valuable long-range LSM, formed by interactions of nearest, next-nearest and next-next-nearest neigh-

bors, is elaborated which provides a reasonable explanation for the SSG model. Weak formulas including element stiffness and mass matrices are established within the framework of SSG theory and global dynamic stiffness matrix of a unit cell is assembled. The reason for combining SSG theory and WFEM is that the characteristics of micro-sized medias can be interpreted by SSG theory and the dynamical properties of complex periodic structures can be investigated through WFEM.

(ii) The band structure for 2D beam grid is illustrated by SSG and CT. The curve by SSG is close to the one by CT at low frequency. However, the difference between SSG and CT becomes more obvious as frequency increases. This phenomenon can be explained as: the dynamical equilibrium equation is a high order partial differential function composed of classical part and non-classical part in SSG theory. Due to the existence of non-classical parts containing higher-order parameters, the eigenvalue ω calculated by the dynamical equilibrium equation from SSG theory is bigger than the one from CT at same κ-space position. The first four slowness surfaces are studied in the frequency range by SSG and CT. The 3D surfaces are symmetric with respect to κ_x and κ_y.

(iii) The direction, perpendicular to iso-frequency line, indicates the direction of wave propagation. The iso-frequency lines by SSG are close to CT at low frequency. The difference between SSG and CT lies in the higher frequency, which means that the high-order parameters have a significant influence on the value of iso-frequency contours at higher frequency. Furthermore, the energy flow vector fields by SSG and CT on the first four slowness surfaces are studied. At low frequency, the behavior of beam grid is similar to an homogeneous orthotropic plate where the dynamic energy spreads in all directions and is normal to the iso-frequency contour. At higher frequency, the directions of majority energy are limited to specific directions.

(iv) The harmonic displacement fields along z direction are studied by SSG and CT. The directional patterns of the harmonic displacement response match the predictions from the energy flow vector fields, as well as the wave propagation directivity analysis. The range of wave propagation by SSG is bigger than the one by CT at same frequency. Furthermore, from the midpoint of the beam grid to the edge, the range of wave propagation increases first and then decreases by CT. In contrast, the range of wave propagation increases first and then remains unchanged by SSG.

Chapter 4

Numerical investigation on multi-mode propagation and diffusion in a three-dimensional beam

Chapter contents

4.1 Introduction 78
4.2 Second strain gradient theory for 3D model 78
4.2.1 Calculation of constitutive relations 78
4.3 Discretization and element matrices 80
4.4 Diffusion calculation based on second strain gradient elasticity 82
4.4.1 Diffusion with simple coupling condition 83
4.4.2 Diffusion with complex coupling condition 84
4.5 Numerical applications and discussions 86
4.5.1 Dispersion relation 87
4.5.2 Effects of higher order parameters 88
4.5.3 Diffusion through a simple coupling element 91
4.5.4 Diffusion through a complex coupling element 92
4.5.5 Forced response 93
4.5.6 Wave shapes 94
4.6 Conclusions 95

4.1 Introduction

In chapter 2 and chapter 3, the SSG theory is used to analyze the single mode (e.g., bending, torsion) propagation within WFEM framework. As we all know, in the real engineering structures, there exist complex waves including high-order waves. Therefore, in recent years, the exploration for multi-mode propagation and diffusion in the complex structures has become a hot spot.

In this chapter, SSG theory is applied for the multi-mode propagation and diffusion analysis of a 3D micro-sized beam. Firstly, the constitutive relation of 3D model is introduced. The weak formulations are calculated by using the Hamilton's principle and global dynamic stiffness matrix of a unit cell is assembled. Then, free wave propagation and diffusion characteristics are expressed in the WFEM framework. The effects of higher order parameters on the dispersion curves are presented. Furthermore, the wave diffusion through a simple coupling condition and a complex coupling condition are confirmed respectively. Finally, some useful conclusions are presented.

4.2 Second strain gradient theory for 3D model

In this part, the constitutive relations of 3D micro-sized model are introduced in the SSG theory framework firstly. Then, the displacement vector is derived by employing the six quin-tic Hermite polynomial shape function. The weak formulations including element stiffness, mass matrices and force vector are calculated by using the Hamilton's principle finally.

4.2.1 Calculation of constitutive relations

The strain energy density $\overline{\mathcal{U}}$ composed of strain $\boldsymbol{\varepsilon}$=$sym(\nabla \mathbf{U})$, first gradient of strain $\boldsymbol{\xi}$=$\nabla\boldsymbol{\varepsilon}$ and second gradient of strain $\boldsymbol{\zeta}$=$\nabla\nabla\boldsymbol{\varepsilon}$ in the SSG theory framework was put forward by Mindlin, as presented in Eq. 1.12.

Based on the three-dimensional elasticity theory, the vector of displacement field defined in the Cartesian coordinate system (x, y, z) is given as:

$$\mathbf{U}(x,y,z,t) = \begin{pmatrix} u_1(x,y,z,t) \\ u_2(x,y,z,t) \\ u_3(x,y,z,t) \end{pmatrix}, \tag{4.1}$$

where u_1, u_2 and u_3 are the the displacements along x, y and z direction.

The relations between strains and displacement components can be defined by introducing

the vectors of first, second and third order derivatives of displacement components:

$$\boldsymbol{\varepsilon} = \boldsymbol{\Psi}_1 \mathbf{U},\ \boldsymbol{\xi} = \boldsymbol{\Psi}_2 \mathbf{U},\ \boldsymbol{\zeta} = \boldsymbol{\Psi}_3 \mathbf{U}, \tag{4.2}$$

where

$$\begin{aligned}
\boldsymbol{\Psi}_1 &= \begin{bmatrix} \partial_x & 0 & 0 \\ 0 & \partial_y & 0 \\ 0 & 0 & \partial_z \\ 0 & \partial_z & \partial_y \\ \partial_z & 0 & \partial_x \\ 0 & \partial_y & \partial_x \end{bmatrix}, \boldsymbol{\Psi}_2 = \begin{bmatrix} \mathbf{e}_1 & \mathbf{0} & \mathbf{0} \\ \mathbf{0} & \mathbf{e}_1 & \mathbf{0} \\ \mathbf{0} & \mathbf{0} & \mathbf{e}_1 \end{bmatrix} \otimes \begin{pmatrix} \partial_{xx} \\ \partial_{yy} \\ \partial_{zz} \\ 2\partial_{xy} \\ 2\partial_{xz} \\ 2\partial_{yz} \end{pmatrix}, \\
\boldsymbol{\Psi}_3 &= \begin{bmatrix} \mathbf{e}_2 & \mathbf{0} & \mathbf{0} \\ \mathbf{0} & \mathbf{e}_2 & \mathbf{0} \\ \mathbf{0} & \mathbf{0} & \mathbf{e}_2 \end{bmatrix} \otimes \begin{bmatrix} \partial_{xxx}, \partial_{yyy}, \partial_{zzz}, 3\partial_{xxy}, 3\partial_{xxz}, 3\partial_{yyx}, 3\partial_{yyz}, 3\partial_{zzx}, 3\partial_{zzy}, 6\partial_{xyz} \end{bmatrix}^{\mathrm{T}},
\end{aligned} \tag{4.3}$$

in which, symbol $\otimes$ stands for the Kronecker product, $\mathbf{e}_1$ with size 6×1 and $\mathbf{e}_2$ with size 10×1 are the matrices whose element value is 1. Then, the constitutive relations for 3D model by SSG theory are defined as:

$$\boldsymbol{\tau}_1 = \mathbf{L}\boldsymbol{\varepsilon} + \mathbf{C}\boldsymbol{\zeta},\ \boldsymbol{\tau}_2 = \mathbf{A}\boldsymbol{\xi},\ \boldsymbol{\tau}_3 = \mathbf{B}\boldsymbol{\zeta} + \mathbf{C}^{\mathrm{T}}\boldsymbol{\varepsilon}, \tag{4.4}$$

in which, $\mathbf{L} = \begin{bmatrix} \lambda+2\mu & \lambda & \lambda & \mathbf{0} \\ \lambda & \lambda+2\mu & \lambda & \mathbf{0} \\ \lambda & \lambda & \lambda+2\mu & \mathbf{0} \\ \mathbf{0} & \mathbf{0} & \mathbf{0} & \mu\mathbf{I} \end{bmatrix}$, $\mathbf{A} = \begin{bmatrix} \mathbf{A}_1 & \mathbf{0} & \mathbf{0} & \mathbf{0} \\ \mathbf{0} & \mathbf{A}_1 & \mathbf{0} & \mathbf{0} \\ \mathbf{0} & \mathbf{0} & \mathbf{A}_1 & \mathbf{0} \\ \mathbf{0} & \mathbf{0} & \mathbf{0} & \mathbf{A}_2 \end{bmatrix}$,

$\mathbf{B} = \begin{bmatrix} \mathbf{B}_{11} & \mathbf{B}_{12} & \mathbf{B}_{13} & \mathbf{B}_{14} & \mathbf{B}_{15} & \mathbf{B}_{16} \\ \mathbf{B}_{21} & \mathbf{B}_{22} & \mathbf{B}_{23} & \mathbf{B}_{24} & \mathbf{B}_{25} & \mathbf{B}_{26} \\ \mathbf{B}_{31} & \mathbf{B}_{32} & \mathbf{B}_{33} & \mathbf{B}_{34} & \mathbf{B}_{35} & \mathbf{B}_{36} \\ \mathbf{B}_{41} & \mathbf{B}_{42} & \mathbf{B}_{43} & \mathbf{B}_{44} & \mathbf{B}_{45} & \mathbf{B}_{46} \\ \mathbf{B}_{51} & \mathbf{B}_{52} & \mathbf{B}_{53} & \mathbf{B}_{54} & \mathbf{B}_{55} & \mathbf{B}_{56} \\ \mathbf{B}_{61} & \mathbf{B}_{62} & \mathbf{B}_{63} & \mathbf{B}_{64} & \mathbf{B}_{65} & \mathbf{B}_{66} \end{bmatrix}$, $\mathbf{C} = \begin{bmatrix} \mathbf{C}_1 & \mathbf{C}_2 & \mathbf{C}_3 & \mathbf{C}_4 & \mathbf{C}_5 & \mathbf{C}_6 \end{bmatrix}$. The details of matrices $\mathbf{A}$, $\mathbf{B}$ and $\mathbf{C}$ are presented in Appendix F. Finally, the strain energy density for SSG theory can be rewritten as the matrix form:

$$\overline{\mathcal{U}} = \frac{1}{2}\left(\boldsymbol{\varepsilon}^{\mathrm{T}}\boldsymbol{\tau}_1 + \boldsymbol{\xi}^{\mathrm{T}}\boldsymbol{\tau}_2 + \boldsymbol{\zeta}^{\mathrm{T}}\boldsymbol{\tau}_3\right). \tag{4.5}$$

Eq. 4.5 is the basic form of building the 3D model using partial differential equations (PDE) weak form in some commercial numerical simulation software (e.g., COMSOL).

4.3 Discretization and element matrices

The definition of node DOFs for 1D and 3D Hermite elements are shown in Fig.4.1. Firstly, in order to ensure the continuity of higher derivatives up to the second order between 1D elements, the six-term polynomial function is considered to interpolate the scalar field U_1=$u_1(x,t)$ inside a 1D element, as follows:

$$\mathrm{U}_1 = \left[\begin{array}{cccccc} 1 & x & x^2 & x^3 & x^4 & x^5 \end{array}\right] \left(\begin{array}{c} \mathrm{s}_0 \\ \mathrm{s}_1 \\ \mathrm{s}_2 \\ \mathrm{s}_3 \\ \mathrm{s}_4 \\ \mathrm{s}_5 \end{array}\right) = \mathbf{xs}. \tag{4.6}$$

The evaluation of the nodal displacement vector $\overline{\mathbf{u}}_1^{(e)}$, as presented in Fig.4.1(a), gives:

$$\overline{\mathbf{u}}_1^{(e)} = \left[\begin{array}{cccccc} 1 & -d_e & d_e^2 & -d_e^3 & d_e^4 & -d_e^5 \\ 0 & 1 & -2d_e & 3d_e^2 & -4d_e^3 & 5d_e^4 \\ 0 & 0 & 2 & -6d_e & 12d_e^2 & -20d_e^3 \\ 1 & d_e & d_e^2 & d_e^3 & d_e^4 & d_e^5 \\ 0 & 1 & 2d_e & 3d_e^2 & 4d_e^3 & 5d_e^4 \\ 0 & 0 & 2 & 6d_e & 12d_e^2 & 20d_e^3 \end{array}\right] \mathbf{s} = \mathbf{ds}. \tag{4.7}$$

Then, submitting Eq.4.7 into Eq.4.6, the displacement vector within the 1D element can be

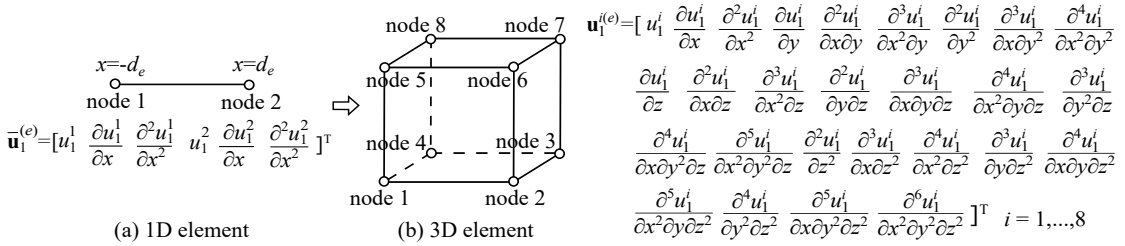

Fig. 4.1. Definition of node numbers, nodal DOFs for 1D and 3D Hermite elements with C^2 continuity.

derived by employing the six quin-tic Hermite polynomial shape function and nodal displacement vector, as follows:

$$\mathrm{U}_1 = \mathbf{xd}^{-1}\overline{\mathbf{u}}_1^{(e)} = \mathbf{N}(x)\overline{\mathbf{u}}_1^{(e)}, \tag{4.8}$$

in which the shape function $\mathbf{N}(x)$ is written as:

$$\mathbf{N}(x)=\begin{bmatrix} \mathrm{N}_1^0(x) \\ \mathrm{N}_1^1(x) \\ \mathrm{N}_1^2(x) \\ \mathrm{N}_2^0(x) \\ \mathrm{N}_2^1(x) \\ \mathrm{N}_2^2(x) \end{bmatrix}^{\mathrm{T}} = \begin{bmatrix} \frac{5x^3}{8d_e^3}-\frac{15x}{16d_e}-\frac{3x^5}{16d_e^5}+\frac{1}{2} \\ \frac{5d_e}{16}-\frac{7x}{16}-\frac{3x^2}{8d_e}+\frac{5x^3}{8d_e^2}+\frac{x^4}{16d_e^3}-\frac{3x^5}{16d_e^4} \\ \frac{d_e^2}{16}-\frac{d_e x}{16}-\frac{x^2}{8}+\frac{x^3}{8d_e}+\frac{x^4}{16d_e^2}-\frac{x^5}{16d_e^3} \\ \frac{15x}{16d_e}-\frac{5x^3}{8d_e^3}+\frac{3x^5}{16d_e^5}+\frac{1}{2} \\ \frac{3x^2}{8d_e}-\frac{7x}{16}-\frac{5d_e}{16}+\frac{5x^3}{8d_e^2}-\frac{x^4}{16d_e^3}-\frac{3x^5}{16d_e^4} \\ \frac{d_e x}{16}+\frac{d_e^2}{16}-\frac{x^2}{8}-\frac{x^3}{8d_e}+\frac{x^4}{16d_e^2}+\frac{x^5}{16d_e^3} \end{bmatrix}^{\mathrm{T}}. \tag{4.9}$$

On the other hand, according to the calculating process above, the shape functions $\mathbf{N}(y)$ = $\mathbf{N}(x)|_{x=y}$ = [$\mathrm{N}_1^0(y)$, $\mathrm{N}_1^1(y)$, $\mathrm{N}_1^2(y)$, $\mathrm{N}_2^0(y)$, $\mathrm{N}_2^1(y)$, $\mathrm{N}_2^2(y)$], $\mathbf{N}(z)$=$\mathbf{N}(x)|_{x=z}$=[$\mathrm{N}_1^0(z)$, $\mathrm{N}_1^1(z)$, $\mathrm{N}_1^2(z)$, $\mathrm{N}_2^0(z)$, $\mathrm{N}_2^1(z)$, $\mathrm{N}_2^2(z)$] can be confirmed as well. Then, the shape function of the hexahedral element, as shown in Fig.4.1, can be developed by expanding the relation of the 1D element to 3D element [217, 218], as follows:

$$\mathbb{N}(x,y,z)=\begin{bmatrix} \mathbf{N}_1\otimes\mathbf{E}_1 \\ \mathbf{N}_2\otimes\mathbf{E}_2 \\ \mathbf{N}_3\otimes\mathbf{E}_3 \end{bmatrix}. \tag{4.10}$$

The element in $\mathbf{N}_p$ and $\mathbf{E}_p$ ($p=1,2,3$) are defined as:

$$\begin{aligned} &\mathrm{N}_p^{i(j,k,l)}(x,y,z)=\mathrm{N}_{i'}^j(x)\mathrm{N}_{i''}^k(y)\mathrm{N}_{i'''}^l(z), \\ &\mathbf{E}_p=\begin{bmatrix} \epsilon_{p1} & \epsilon_{p2} & \epsilon_{p3} \end{bmatrix}, \end{aligned} \tag{4.11}$$

where $\mathrm{N}_p^{i(j,k,l)}(x,y,z)$ is associated with the DOFs $\partial^{j+k+l}u_1^i/(\partial x^j\partial y^k\partial z^l)$ of node i of the hexahedron element. $i=1,...,8$. $j,k,l=0,1,2$. $i',i'',i'''=1,2$ relate to the node number in the corresponding 1D element and they take values of 1 or 2 if the coordinate value of node i is $-d_e$ or d_e. For example, $\mathrm{N}_1^{2(1,2,2)}(x,y,z)$=$\mathrm{N}_2^1(x)\mathrm{N}_1^2(y)\mathrm{N}_1^2(z)$. $\epsilon_{pq}=1$ for $p=q$. $\epsilon_{pq}=0$ for $p\neq q$ ($q=1,2,3$). The displacement vector $\mathbf{U}(x,y,z)$ within 3D element can be presented by employing the 3D shape function $\mathbb{N}(x,y,z)$ and nodal displacement vector $\mathbf{u}^{(e)}$, one obtains:

$$\mathbf{U}(x,y,z,t)=\mathbb{N}(x,y,z)\mathbf{u}^{(e)}(t), \tag{4.12}$$

where $\mathbf{u}^{(e)}$=$[(\mathbf{u}_1^{(e)})^{\mathrm{T}}, (\mathbf{u}_2^{(e)})^{\mathrm{T}}, (\mathbf{u}_3^{(e)})^{\mathrm{T}}]^{\mathrm{T}}$, $(\mathbf{u}_p^{(e)})^{\mathrm{T}}$=$[(\mathbf{u}_p^{1(e)})^{\mathrm{T}}, (\mathbf{u}_p^{2(e)})^{\mathrm{T}}, ..., (\mathbf{u}_p^{8(e)})^{\mathrm{T}}]^{\mathrm{T}}$ $(p = 1, 2, 3)$. Then, integrating the strain energy density over its volume to obtain the strain potential energy:

$$\mathcal{U} = \int_V \overline{\mathcal{U}} \mathrm{d}V = \frac{1}{2} \mathbf{u}^{(e)\mathrm{T}} \mathbf{K}^{(e)} \mathbf{u}^{(e)}. \tag{4.13}$$

Meanwhile, the simplified kinetic energy $\mathcal{T}$ and work done $\delta\mathcal{W}$ by external force are:

$$\begin{aligned} \mathcal{T} =& \frac{1}{2} \int_V \left(\frac{\partial \mathbf{U}}{\partial t} \right)^{\mathrm{T}} \rho \left(\frac{\partial \mathbf{U}}{\partial t} \right) \mathrm{d}V = \frac{1}{2} \left(\frac{\partial \mathbf{u}^{(e)}}{\partial t} \right)^{\mathrm{T}} \mathbf{M} \left(\frac{\partial \mathbf{u}^{(e)}}{\partial t} \right), \\ \delta\mathcal{W} =& \int_V \delta \mathbf{U}^{\mathrm{T}} \mathbf{f}_V \mathrm{d}V + \int_S \delta \mathbf{U}^{\mathrm{T}} \mathbf{f}_S \mathrm{d}S = \delta \mathbf{u}^{(\mathrm{e})\mathrm{T}} \mathbf{F}^{(e)}, \end{aligned} \tag{4.14}$$

where ρ denotes the linear mass density, $\mathbf{f}_V$ is the volume force, $\mathbf{f}_S$ means the face force. By introducing 3D element stiffness, mass matrices and force vector:

$$\begin{aligned} \mathbf{K}^{(e)} &= \int_V \left(\mathbb{N}^{\mathrm{T}} \boldsymbol{\Psi}_1^{\mathrm{T}} \mathbf{L} \boldsymbol{\Psi}_1 \mathbb{N} + \mathbb{N}^{\mathrm{T}} \boldsymbol{\Psi}_2^{\mathrm{T}} \mathbf{A} \boldsymbol{\Psi}_2 \mathbb{N} + \mathbb{N}^{\mathrm{T}} \boldsymbol{\Psi}_3^{\mathrm{T}} \mathbf{B} \boldsymbol{\Psi}_3 \mathbb{N} + 2\mathbb{N}^{\mathrm{T}} \boldsymbol{\Psi}_3^{\mathrm{T}} \mathbf{C} \boldsymbol{\Psi}_1 \mathbb{N} \right) \mathrm{d}V, \\ \mathbf{M}^{(e)} &= \int_V \left(\mathbb{N}^{\mathrm{T}} \rho \mathbb{N} \right) \mathrm{d}V, \\ \mathbf{F}^{(e)} &= \int_V \left(\mathbb{N}^{\mathrm{T}} \mathbf{f}_V \right) \mathrm{d}V + \int_S \left(\mathbb{N}^{\mathrm{T}} \mathbf{f}_S \right) \mathrm{d}S, \end{aligned} \tag{4.15}$$

the Hamilton's principle in time domain leads to:

$$\int_{t_1}^{t_2} (\delta\mathcal{U} - \delta\mathcal{W} - \delta\mathcal{T}) \, \mathrm{d}t = \int_{t_1}^{t_2} \left[\delta \mathbf{u}^{(e)\mathrm{T}} \left(\mathbf{M}^{(e)} \frac{\partial^2 \mathbf{u}^{(e)}}{\partial t^2} + \mathbf{K}^{(e)} \mathbf{u}^{(\mathrm{e})} - \mathbf{F}^{(e)} \right) \right] \mathrm{d}t = 0. \tag{4.16}$$

4.4 Diffusion calculation based on second strain gradient elasticity

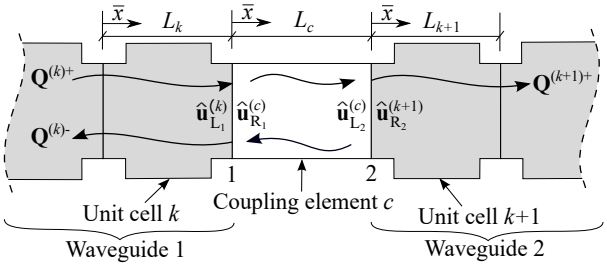

Fig. 4.2. Two coupled waveguides through a coupling element.

This section is concerned with the characterization of coupling conditions between two semi-infinite periodic waveguides which are connected through an elastic coupling element at surfaces 1 and 2 as shown in Fig.4.2. Here should be noted that the coupling element is only

subject to the coupling actions, which means there is no force inside the element. The reflection coefficients ($\mathbf{R}$) and transmission coefficients ($\mathbf{T}$) are confirmed through two different coupling conditions. Simple coupling condition: wave modes calculation in waveguides and coupling element are based on the same theory (SSG-SSG). Complex coupling condition: wave modes calculation in waveguides is based on the CT but SSG theory in coupling element (CT-SSG).

4.4.1 Diffusion with simple coupling condition

In order to illustrate the wave diffusion, the wave propagation characteristics should be introduced firstly. Our study focuses on the description of wave propagating along x direction in a slender waveguide, as shown in Fig.1.10, which is composed of identical unit cells coupled together. The dynamics of the system is formulated by using WFEM which offers a numerical wave characterization of periodic structures. The dynamic equilibrium equation of unit cell k with length L_k is expressed in Eq.1.46, where $\mathbf{K}$ and $\mathbf{M}$ denote the unit cell stiffness and mass matrices assembled by element stiffness and mass matrices ($\mathbf{K}^{(e)}$, $\mathbf{M}^{(e)}$), $\mathbf{C} = \eta\mathbf{K}/\omega$ is defined as damping matrix considering damping lose factor η, $\mathbf{u}$ is nodal displacement vector, $\mathbf{F}$ represents nodal force vector. Assuming that $\mathbf{u}$ and $\mathbf{F}$ are harmonic, the dynamic stiffness matrix will be written as $\mathbf{D}$=$\tilde{\mathbf{K}}-\mathrm{M}\omega^2$ in frequency domain with $\tilde{\mathbf{K}} = (1+\mathrm{i}\eta)\mathbf{K}$. Then, Eq. 1.46 can be re-expressed by dividing the DOFs into left boundary (L), internal (I) and right boundary (R) DOFs, as described in Fig. 1.10, this yields:

$$\begin{bmatrix} \mathbf{D}_{\mathrm{LL}} & \mathbf{D}_{\mathrm{LI}} & \mathbf{D}_{\mathrm{LR}} \\ \mathbf{D}_{\mathrm{IL}} & \mathbf{D}_{\mathrm{II}} & \mathbf{D}_{\mathrm{IR}} \\ \mathbf{D}_{\mathrm{RL}} & \mathbf{D}_{\mathrm{RI}} & \mathbf{D}_{\mathrm{RR}} \end{bmatrix} \begin{pmatrix} \hat{\mathbf{u}}_{\mathrm{L}} \\ \hat{\mathbf{u}}_{\mathrm{I}} \\ \hat{\mathbf{u}}_{\mathrm{R}} \end{pmatrix} = \begin{pmatrix} \hat{\mathbf{F}}_{\mathrm{L}} \\ \hat{\mathbf{F}}_{\mathrm{I}} \\ \hat{\mathbf{F}}_{\mathrm{R}} \end{pmatrix}, \tag{4.17}$$

in which $\hat{\mathbf{u}}$ and $\hat{\mathbf{F}}$ are the amplitudes of $\mathbf{u}$ and $\mathbf{F}$, respectively. Assuming that $\hat{\mathbf{F}}_{\mathrm{I}} = 0$ [184]. The dynamic equilibrium equation will be re-written as:

$$\begin{bmatrix} \mathbb{D}_{\mathrm{LL}} & \mathbb{D}_{\mathrm{LR}} \\ \mathbb{D}_{\mathrm{RL}} & \mathbb{D}_{\mathrm{RR}} \end{bmatrix} \begin{pmatrix} \hat{\mathbf{u}}_{\mathrm{L}} \\ \hat{\mathbf{u}}_{\mathrm{R}} \end{pmatrix} = \begin{pmatrix} \hat{\mathbf{F}}_{\mathrm{L}} \\ \hat{\mathbf{F}}_{\mathrm{R}} \end{pmatrix}, \tag{4.18}$$

where $\mathbb{D}$=$\mathbf{D}_{\mathrm{BdBd}}-\mathbf{D}_{\mathrm{BdI}}\mathbf{D}_{\mathrm{II}}^{-1}\mathbf{D}_{\mathrm{IBd}}$ is the condensed form of dynamic stiffness matrix, subscript Bd represents the DOFs on the unit cell boundaries. Eq. 4.18 is the expression of the WFEM analysis that relates the displacement and force on the left and right boundaries of unit cell. For the solution of propagation constants $\mathbf{\Lambda}$ and eigenvectors $\mathbf{\Phi}_{\mathrm{u}}$, one can solve the direct Bloch formulation [95, 210] as:

$$\left[\mathbb{D}_{\mathrm{RL}}(\omega)\mathbf{\Lambda}^{-1} + (\mathbb{D}_{\mathrm{RR}}(\omega) + (\mathbb{D}_{\mathrm{LL}}(\omega)) + \mathbb{D}_{\mathrm{LR}}(\omega)\mathbf{\Lambda}\right]\mathbf{\Phi}_{\mathrm{u}} = 0, \tag{4.19}$$

where $\mathbf{\Lambda}$=diag $\{\lambda_j\}_{j=1,\ldots,2p}$, $\mathbf{\Phi}_{\mathrm{u}}$=$\{\phi_j\}_{j=1,\ldots,2p}$ which can be divided into $\mathbf{\Phi}_{\mathrm{u}}^{+}$=$\left\{\phi_j^{+}\right\}_{j=1,\ldots,p}$ and $\mathbf{\Phi}_{\mathrm{u}}^{-}$=$\left\{\phi_j^{-}\right\}_{j=p+1,\ldots,2p}$, in which p=m for SSG, p=n for CT. The propagation constants $\mathbf{\Lambda}$ relating the displacements between two consecutive unit cells can be used to define the positive, negative, propagating and evanescent waves. The waves propagate to the positive direction when $|1/\lambda_j|$ <1. The waves propagate to the negative direction when $|\lambda_j|$ >1. Here, λ_j take the form λ_j=exp$(-\mathrm{i}\kappa_j L_{(q)})$, subscript q=c for coupling element, q=k, k+1 for unit cells. It should be noted that the spectral analysis method of the coupling element and unit cell k+1 is the same as that of the unit cell k.

Then, the reflection coefficients ($\mathbf{R}$) and transmission coefficients ($\mathbf{T}$) can be calculated through a simple coupling element. Assuming that the incident waves come from the infinity of waveguide 1 and there is no reflection from the end of waveguide 2. The initial boundary of waveguide 1 is also non-reflecting. The local dynamic equilibrium can be written using the state vectors expansion on the positive-going wave amplitudes $\mathbf{Q}^{(k)+}$ at surface 1, $\mathbf{Q}^{(k+1)+}$ at surface 2 and negative-going wave amplitudes $\mathbf{Q}^{(k)-}$ at surface 1, as shown in Fig.4.2. Defining $\mathbf{Q}^{(k)+}$=$\mathbf{I}$, $\mathbf{Q}^{(k)-}$=$\mathbf{R}$, $\mathbf{Q}^{(k+1)+}$=$\mathbf{T}$. As a result, the $\mathbf{R}$ and $\mathbf{T}$ coefficients are expressed as [225]:

$$\begin{aligned}\begin{pmatrix}\mathbf{R}\\ \mathbf{T}\end{pmatrix} = &\begin{bmatrix}\mathbb{D}_{\mathrm{RL}}^{(k)}\mathbf{\Phi}_{\mathrm{u}}^{(k)-}\mathbf{\Lambda}^{(k)}+\left(\mathbb{D}_{\mathrm{RR}}^{(k)}+\mathbb{D}_{\mathrm{LL}}^{(c)}\right)\mathbf{\Phi}_{\mathrm{u}}^{(k)-}, & \mathbb{D}_{\mathrm{LR}}^{(c)}\mathbf{\Phi}_{\mathrm{u}}^{(k)+}\\ \mathbb{D}_{\mathrm{RL}}^{(c)}\mathbf{\Phi}_{\mathrm{u}}^{(k)-}, & \mathbb{D}_{\mathrm{LR}}^{(k+1)}\mathbf{\Phi}_{\mathrm{u}}^{(k+1)+}\mathbf{\Lambda}^{(k+1)}+\left(\mathbb{D}_{\mathrm{LL}}^{(k+1)}+\mathbb{D}_{\mathrm{RR}}^{(c)}\right)\mathbf{\Phi}_{\mathrm{u}}^{(k+1)+}\end{bmatrix}^{-1}\\ &\cdot\begin{bmatrix}-\left(\mathbb{D}_{\mathrm{RL}}^{(k)}+\mathbf{\Lambda}^{(k)}\left(\mathbb{D}_{\mathrm{RR}}^{(k)}+\mathbb{D}_{\mathrm{LL}}^{(c)}\right)\right)\mathbf{\Phi}_{\mathrm{u}}^{(k)+}\\ -\mathbf{\Lambda}^{(k)}\mathbb{D}_{\mathrm{RL}}^{(c)}\mathbf{\Phi}_{\mathrm{u}}^{(k)+}\end{bmatrix},\end{aligned} \tag{4.20}$$

where superscript k represents the unit cell, c means the coupling element. The $\mathbf{R}$ and $\mathbf{T}$ coefficients can be derived through calssical theory or SSG theory individually.

4.4.2 Diffusion with complex coupling condition

As shown in Fig.4.2, the coupling element is described by SSG theory model. The waveguides are built by CT model. The description of complex coupling condition enriches the wave propagation and diffusion features in complex system. Firstly, the displacement field of coupling element (c) and unit cells (k, k+1) can be represented by the superposition of the eigenmodes:

$$\hat{\mathbf{u}}^{(q)\pm} = \mathbf{\Phi}_{\mathrm{u}}^{(q)\pm}\boldsymbol{\upsilon}^{(q)\pm}\mathbf{Q}^{(q)\pm}, \tag{4.21}$$

where $\mathbf{Q}^{(q)\pm}$ is the amplitudes of wave modes. $\boldsymbol{\upsilon}^{(q)\pm}$=diag $\left\{\exp\left(\mp\mathrm{i}\kappa_j^{(q)}\overline{x}\right)\right\}$ $(0 \le \overline{x} \le L_{(q)})$. On the other hand, the force components of coupling element (c) and unit cells (k, k+1) can be expressed as:

$$\hat{\mathbf{F}}^{(q)\pm} = \mathbf{\Phi}_{\mathrm{F}}^{(q)\pm}\boldsymbol{\upsilon}^{(q)\pm}\mathbf{Q}^{(q)\pm}, \tag{4.22}$$

in which $\mathbf{\Phi}_{\mathrm{F}}^{(q)\pm}$=$\mathbb{D}_{\mathrm{LL}}^{(q)}\mathbf{\Phi}_{\mathrm{u}}^{(q)\pm}$+$\mathbb{D}_{\mathrm{LR}}^{(q)}\mathbf{\Phi}_{\mathrm{u}}^{(q)\pm}\mathrm{diag}\left\{\exp\left(\mp\mathrm{i}\kappa_j^{(q)}L_{(q)}\right)\right\}$ according to Eq.4.18. The eigen-solutions will be same when waveguides 1 and 2 have the same cross-section and material.

The state vector on the right side of surface 1, represented by R_1, is expressed as:

$$\left(\begin{array}{c}\hat{\mathbf{u}}_{\mathrm{R}_1}^{(c)}\\ \hat{\mathbf{F}}_{\mathrm{R}_1}^{(c)}\end{array}\right)=\left[\begin{array}{c}\hat{\mathbf{u}}_{\mathrm{R}_1}^{(c)+}+\hat{\mathbf{u}}_{\mathrm{R}_1}^{(c)-}\\ \hat{\mathbf{F}}_{\mathrm{R}_1}^{(c)+}+\hat{\mathbf{F}}_{\mathrm{R}_1}^{(c)-}\end{array}\right]=\left[\begin{array}{cc}\mathbf{\Phi}_{\mathrm{u}}^{(c)+} & \mathbf{\Phi}_{\mathrm{u}}^{(c)-}\\ \mathbf{\Phi}_{\mathrm{F}}^{(c)+} & \mathbf{\Phi}_{\mathrm{F}}^{(c)-}\end{array}\right]\left[\begin{array}{c}\boldsymbol{\upsilon}^{(c)+}\mathbf{Q}^{(c)+}\\ \boldsymbol{\upsilon}^{(c)-}\mathbf{Q}^{(c)-}\end{array}\right]. \tag{4.23}$$

In addition, the state vector on the left side of surface 2, represented by L_2, is written as:

$$\begin{aligned}&\left(\begin{array}{c}\hat{\mathbf{u}}_{\mathrm{L}_2}^{(c)}\\ \hat{\mathbf{F}}_{\mathrm{L}_2}^{(c)}\end{array}\right)=\left[\begin{array}{c}\hat{\mathbf{u}}_{\mathrm{L}_2}^{(c)+}+\hat{\mathbf{u}}_{\mathrm{L}_2}^{(c)-}\\ \hat{\mathbf{F}}_{\mathrm{L}_2}^{(c)+}+\hat{\mathbf{F}}_{\mathrm{L}_2}^{(c)-}\end{array}\right]\\ =&\left[\begin{array}{cc}\mathbf{\Phi}_{\mathrm{u}}^{(c)+} & \mathbf{\Phi}_{\mathrm{u}}^{(c)-}\\ \mathbf{\Phi}_{\mathrm{F}}^{(c)+} & \mathbf{\Phi}_{\mathrm{F}}^{(c)-}\end{array}\right]\left[\begin{array}{cc}\boldsymbol{\upsilon}^{(c)+}|_{\overline{x}=L_c} & \mathbf{0}\\ \mathbf{0} & \boldsymbol{\upsilon}^{(c)-}|_{\overline{x}=L_c}\end{array}\right]\left[\begin{array}{c}\boldsymbol{\upsilon}^{(c)+}\mathbf{Q}^{(c)+}\\ \boldsymbol{\upsilon}^{(c)-}\mathbf{Q}^{(c)-}\end{array}\right].\end{aligned} \tag{4.24}$$

Combining Eq.4.23 and Eq.4.24, the relation between state vector on left and right side of coupling element will be conformed:

$$\left(\begin{array}{c}\hat{\mathbf{u}}_{\mathrm{L}_2}^{(c)}\\ \hat{\mathbf{F}}_{\mathrm{L}_2}^{(c)}\end{array}\right)=\mathbf{S}^{(c)}\left(\begin{array}{c}\hat{\mathbf{u}}_{\mathrm{R}_1}^{(c)}\\ \hat{\mathbf{F}}_{\mathrm{R}_1}^{(c)}\end{array}\right), \tag{4.25}$$

with

$$\mathbf{S}^{(c)}=\left[\begin{array}{cc}\mathbf{\Phi}_{\mathrm{u}}^{(c)+} & \mathbf{\Phi}_{\mathrm{u}}^{(c)-}\\ \mathbf{\Phi}_{\mathrm{F}}^{(c)+} & \mathbf{\Phi}_{\mathrm{F}}^{(c)-}\end{array}\right]\left[\begin{array}{cc}\boldsymbol{\upsilon}^{(c)+}|_{\overline{x}=L_c} & \mathbf{0}\\ \mathbf{0} & \boldsymbol{\upsilon}^{(c)-}|_{\overline{x}=L_c}\end{array}\right]\left[\begin{array}{cc}\mathbf{\Phi}_{\mathrm{u}}^{(c)+} & \mathbf{\Phi}_{\mathrm{u}}^{(c)-}\\ \mathbf{\Phi}_{\mathrm{F}}^{(c)+} & \mathbf{\Phi}_{\mathrm{F}}^{(c)-}\end{array}\right]^{-1}. \tag{4.26}$$

Next, Assuming that the incident waves come from the infinity of waveguide 1 and there is no reflection from the end of waveguide 2. The initial boundary of waveguide 1 is also non-reflecting. The state vector on the left side of surface 1, represented by L_1, is expressed as:

$$\left(\begin{array}{c}\hat{\mathbf{u}}_{\mathrm{L}_1}^{(k)}\\ \hat{\mathbf{F}}_{\mathrm{L}_1}^{(k)}\end{array}\right)=\left[\begin{array}{c}\hat{\mathbf{u}}_{\mathrm{L}_1}^{(k)+}+\hat{\mathbf{u}}_{\mathrm{L}_1}^{(k)-}\\ \hat{\mathbf{F}}_{\mathrm{L}_1}^{(k)+}+\hat{\mathbf{F}}_{\mathrm{L}_1}^{(k)-}\end{array}\right]=\left[\begin{array}{cc}\mathbf{\Phi}_{\mathrm{u}}^{(k)+} & \mathbf{\Phi}_{\mathrm{u}}^{(k)-}\\ \mathbf{\Phi}_{\mathrm{F}}^{(k)+} & \mathbf{\Phi}_{\mathrm{F}}^{(k)-}\end{array}\right]\left[\begin{array}{c}\boldsymbol{\upsilon}^{(k)+}|_{\overline{x}=L_k}\mathbf{Q}^{(k)+}\\ \boldsymbol{\upsilon}^{(k)-}|_{\overline{x}=L_k}\mathbf{Q}^{(k)-}\end{array}\right]. \tag{4.27}$$

The state vector on the right side of surface 2, represented by R_2, is written as:

$$\left(\begin{array}{c}\hat{\mathbf{u}}_{\mathrm{R}_2}^{(k+1)}\\ \hat{\mathbf{F}}_{\mathrm{R}_2}^{(k+1)}\end{array}\right)=\left(\begin{array}{c}\hat{\mathbf{u}}_{\mathrm{R}_2}^{(k+1)+}\\ \hat{\mathbf{F}}_{\mathrm{R}_2}^{(k+1)+}\end{array}\right)=\left[\begin{array}{c}\mathbf{\Phi}_{\mathrm{u}}^{(k+1)+}\boldsymbol{\upsilon}^{(k+1)+}|_{\overline{x}=0}\mathbf{Q}^{(k+1)+}\\ \mathbf{\Phi}_{\mathrm{F}}^{(k+1)+}\boldsymbol{\upsilon}^{(k+1)+}|_{\overline{x}=0}\mathbf{Q}^{(k+1)+}\end{array}\right]. \tag{4.28}$$

Here should be noted that the size of state vector for coupling element is $2m\times 1$, but $2n\times 1$ for unit cells k and k+1. The higher order parts in state vector for coupling element is $2(m-n)\times 1$. In order to ensure the continuity on surfaces 1 and 2, defining new state vectors

including higher order parts $(2(m-n)\times 1)$ for unit cells k and k+1:

$$\begin{pmatrix} \hat{\mathbf{u}}^{*(k)}_{\mathrm{L}_1} \\ \hat{\mathbf{F}}^{*(k)}_{\mathrm{L}_1} \end{pmatrix} = \begin{pmatrix} \hat{\mathbf{u}}^{(k)}_{\mathrm{L}_1} \\ \hat{\mathbf{u}}^{\prime(k)}_{\mathrm{L}_1} \\ \hat{\mathbf{F}}^{(k)}_{\mathrm{L}_1} \\ \hat{\mathbf{F}}^{\prime(k)}_{\mathrm{L}_1} \end{pmatrix}, \begin{pmatrix} \hat{\mathbf{u}}^{*(k+1)}_{\mathrm{R}_2} \\ \hat{\mathbf{F}}^{*(k+1)}_{\mathrm{R}_2} \end{pmatrix} = \begin{pmatrix} \hat{\mathbf{u}}^{(k+1)}_{\mathrm{R}_2} \\ \hat{\mathbf{u}}^{\prime(k+1)}_{\mathrm{R}_2} \\ \hat{\mathbf{F}}^{(k+1)}_{\mathrm{R}_2} \\ \hat{\mathbf{F}}^{\prime(k+1)}_{\mathrm{R}_2} \end{pmatrix}, \tag{4.29}$$

where $\hat{\mathbf{u}}^{\prime(k)}_{\mathrm{L}_1}$, $\hat{\mathbf{F}}^{\prime(k)}_{\mathrm{L}_1}$ are unknown higher order displacements and forces vectors for unit cell k. $\hat{\mathbf{u}}^{\prime(k+1)}_{\mathrm{L}_1}$, $\hat{\mathbf{F}}^{\prime(k+1)}_{\mathrm{L}_1}$ are unknown higher order displacements and forces vectors for unit cell k+1. The continuity on surfaces 1 and 2 is:

$$\begin{pmatrix} \hat{\mathbf{u}}^{(c)}_{\mathrm{R}_1} \\ \hat{\mathbf{F}}^{(c)}_{\mathrm{R}_1} \end{pmatrix} = \begin{pmatrix} \hat{\mathbf{u}}^{*(k)}_{\mathrm{L}_1} \\ \hat{\mathbf{F}}^{*(k)}_{\mathrm{L}_1} \end{pmatrix}, \begin{pmatrix} \hat{\mathbf{u}}^{(c)}_{\mathrm{L}_2} \\ \hat{\mathbf{F}}^{(c)}_{\mathrm{L}_2} \end{pmatrix} = \begin{pmatrix} \hat{\mathbf{u}}^{*(k+1)}_{\mathrm{R}_2} \\ \hat{\mathbf{F}}^{*(k+1)}_{\mathrm{R}_2} \end{pmatrix}. \tag{4.30}$$

Combining Eq.4.25, Eq.4.29 and Eq.4.30, assume that higher order forces vectors for unit cell k and k+1 are $\mathbf{0}$. Define $\mathbf{Q}^{(k)+}$=$\mathbf{I}$, $\mathbf{Q}^{(k)-}$=$\mathbf{R}$, $\mathbf{Q}^{(k+1)+}$=$\mathbf{T}$, the $\mathbf{R}$ and $\mathbf{T}$ coefficients for complex coupling condition can be conformed as:

$$\begin{bmatrix} \boldsymbol{\Phi}^{(k+1)+}_{\mathrm{u}} \boldsymbol{\upsilon}^{(k+1)+}|_{\overline{x}=0}\mathbf{T} \\ \hat{\mathbf{u}}^{(k+1)}_{\mathrm{R}_2} \\ \boldsymbol{\Phi}^{(k+1)+}_{\mathrm{F}} \boldsymbol{\upsilon}^{(k+1)+}|_{\overline{x}=0}\mathbf{T} \\ \mathbf{0} \end{bmatrix} = \mathbf{S}^{(c)} \begin{bmatrix} \boldsymbol{\Phi}^{(k)+}_{\mathrm{u}} \boldsymbol{\upsilon}^{(k)+}|_{\overline{x}=L_k}\mathbf{I} + \boldsymbol{\Phi}^{(k)-}_{\mathrm{u}} \boldsymbol{\upsilon}^{(k)-}|_{\overline{x}=L_k}\mathbf{R} \\ \hat{\mathbf{u}}^{(k)}_{\mathrm{L}_1} \\ \boldsymbol{\Phi}^{(k)+}_{\mathrm{F}} \boldsymbol{\upsilon}^{(k)+}|_{\overline{x}=L_k}\mathbf{I} + \boldsymbol{\Phi}^{(k)-}_{\mathrm{F}} \boldsymbol{\upsilon}^{(k)-}|_{\overline{x}=L_k}\mathbf{R} \\ \mathbf{0} \end{bmatrix}. \tag{4.31}$$

4.5 Numerical applications and discussions

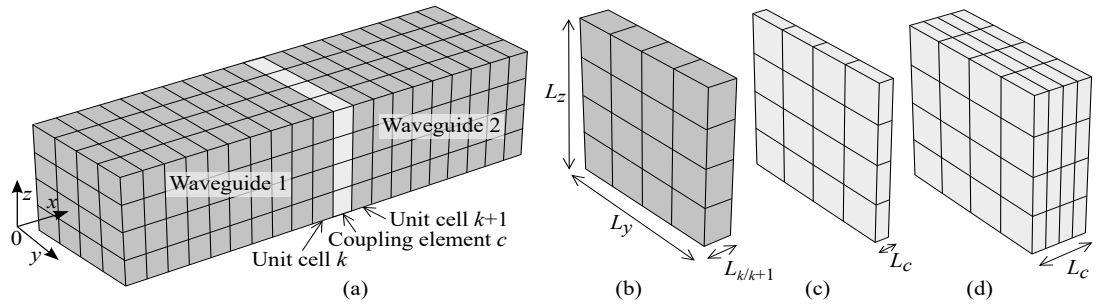

Fig. 4.3. Finite element model. (a): two waveguides coupled by a coupling element, (b): a unit cell k/k+1, (c): a simple coupling element, (d): a complex coupling element.

In this part, the WFEM is applied to analyze the multi-mode propagation and diffusion. The unit cells k and k+1 with $L_{k/k+1} = 50a_0$, $L_y = 300a_0$ and $L_z = 300a_0$ (a_0 is the lattice parameter) as presented in Fig.4.3(b). The coupling element with $L_c = 25a_0$ for simple coupling condition as shown in Fig.4.3(c) and $L_c = 100a_0$ for complex coupling condition as shown in

Fig.4.3(d). Materials Aluminum (Al) and Copper (Cu) are used here. The Young's modulus E is 70 GPa for Al and 110 GPa for Cu, linear mass density ρ is 2.7 $\mathrm{g/cm^3}$ for Al and 8.96 $\mathrm{g/cm^3}$ for Cu. The damping lose factor η=$1e^{-4}$. Unit cells k and k+1 are meshed into 16 3D elements respectively, coupling element for simple coupling condition is meshed into 16 3D elements but 64 3D elements for complex coupling condition.

4.5.1 Dispersion relation

The dispersion relation of unit cell k is calculated by WFEM as shown in Fig.4.4. The real part $\Re(\kappa_j)$ of wavenumber is the phase shift per unit length and the imaginary part $\Im(\kappa_j)$ means the attenuation per unit length. Only the positive waves with real and imaginary parts are illustrated due to the wavenumbers of the negative waves and positive waves are symmetric with respect to x-axis. The frequency is normalized as ω/ω_0, in which ω_0 is the first nature frequency of the unit cell. The blue lines represent the results from SSG theory and black lines denote the CT. The curve by SSG is close to the one by CT at low frequency. But the difference between

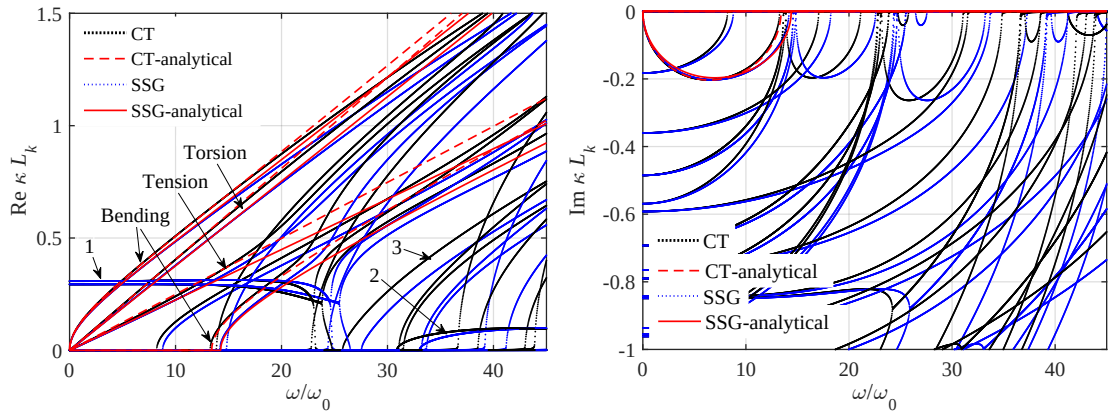

(a) Real part of positive waves.

(b) Imaginary part of positive waves.

Fig. 4.4. Dispersion relation of unit cell k by SSG and CT.

SSG and CT becomes more obvious as frequency increases. On the other hand, the value of wavenumber κ by SSG is smaller than CT at same frequency, especially for bending, tension and torsion modes. This phenomenon can be explained as: the potential energy density in SSG theory is a function of strain, first gradient of strain and second gradient of strain, which leads to the dynamical equilibrium equation being a high order partial differential function composed of classical part and non-classical part. Due to the existence of non-classical parts containing higher-order parameters, the interactions between microscopic particles within the structure are non-local or long-range, which hardened the stiffness of the material and caused the wavenumber value to decrease.

In order to verify the WFEM results, the analytical methods referring to the tension, torsion

and Timoshenko bending vibration [226] are used. The results from analytical methods match the ones from WFEM, but the difference between them becomes more obvious as frequency increases. Besides the tension, torsion and bending modes, there are high-order modes that analytical methods can not predict. Note that the normalized cut-on frequency for the complex thickness contractional wave 1 [210] is 23 by CT, instead of 26 by SSG, and the second-order bending wave cuts-on at 13 by CT but 15 by SSG. Other waves such as 2 and 3 are more complex, which lead to confusions in the wave modes classification.

Here, the aliasing effects should be introduced. The practical implementation of the proposed method arises two main problems. The first one is choice of unit cell's size whose value cannot be arbitrary. The second one is the pertinent frequency band under consideration. Along the propagation direction, the chosen finite element must then correctly represent a part of propagating wave along the propagation axis. So, based on a kind of Shannon space theorem, pertinent wavelengths or wavenumbers κ_j should be connected to the propagation distance: $\mathrm{Re}(\kappa_j(\omega)) < \pi/L_k$. However, it should be pointed that this value is too far removed from practical applications. Practically, wavenumbers prediction should start at around 6 to 10 elements per wavelength. As a result, errors and deviations are expected to appear around $\mathrm{Re}(\kappa_j(\omega)) < \pi/3L_k$ or $\mathrm{Re}(\kappa_j(\omega)) < \pi/6L_k$. large values of L_k will limit the wavenumber validity domain, and consequently the given frequency band leading to aliasing. Small values of the propagation distance L_k will lead to two difficulties. The first one is connected to the nature of the employed finite elements. Depending on the cross section shape, L_k should respect the strain and stress intrinsic limitations. The second problem is mainly numerical. Small propagation distances will lead to eigenvalues close to unity.

4.5.2 Effects of higher order parameters

As mentioned in previous section, the dispersion relations are influenced by the higher-order parameters $a_i (i = 1, ..., 5)$, $b_j (j = 1, ..., 7)$ and $c_k (k = 1, ..., 3)$ in the SSG framework. In order to study the effects of these parameters on the results, each parameter is multiplied by a ratio ($\delta_a a_i$, $\delta_b b_j$, $\delta_c c_k$) and the influence of these parameters on the results will be analysed by changing the value of δ_a, δ_b, δ_c as -100, -10, -1, -0.5, 0, 0.5, 1, 10, 100. In this work, four different cases are presented. Case 1: δ_a, δ_b, δ_c change at the same time. Case 2: δ_a changes only. Case 3: δ_b changes only and in case 4: δ_c changes only.

The joint effects of a_i, b_j and c_k on the bending and tension dispersion relations including real part and imaginary part are presented in Fig.4.5(a) and Fig.4.6(a) respectively. When δ_a= δ_b= δ_c=-100, the value of wavenumber is the largest in real part but smallest in imaginary part. When δ_a= δ_b= δ_c=100, the value of wavenumber is the smallest in real part but largest in imaginary part. On the other hand, as the ratio increases, the value of the real part decreases but the imaginary value increases. What is more, the individual effects of a_i, b_j and c_k on the

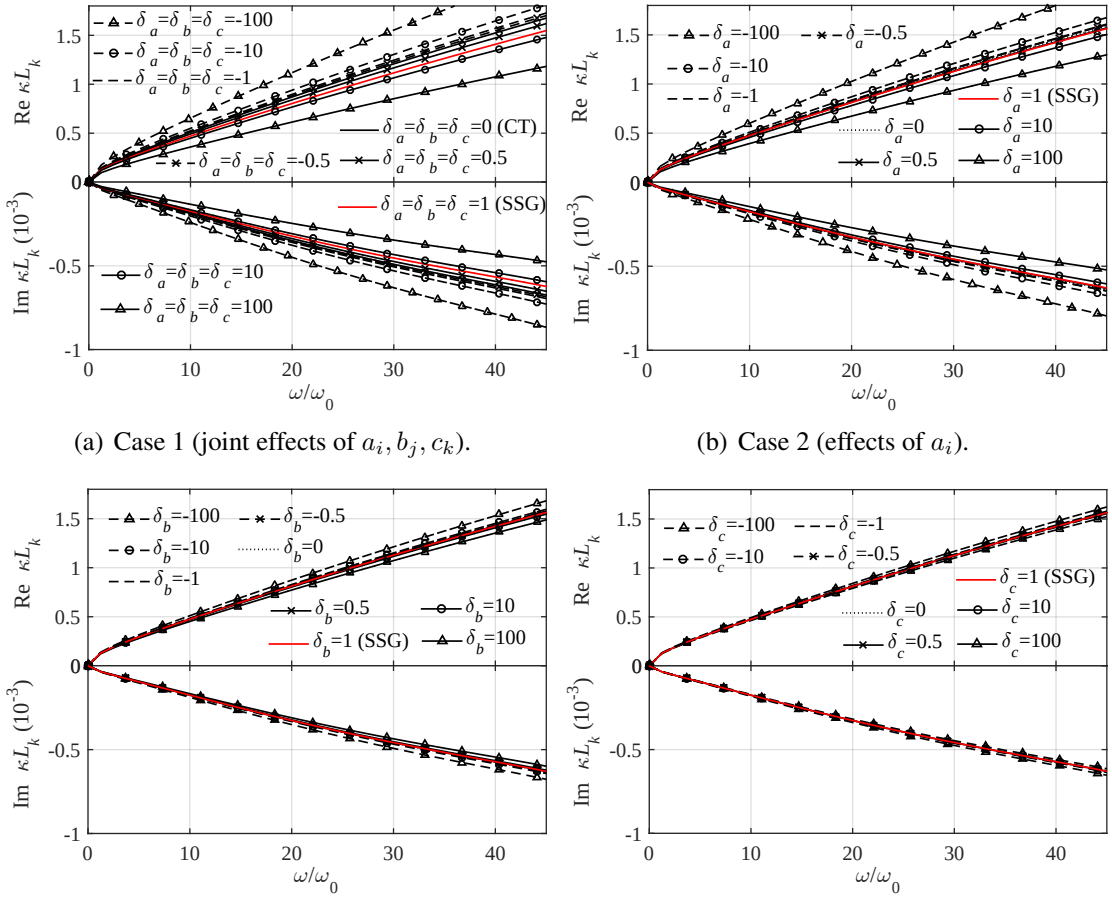

(a) Case 1 (joint effects of a_i, b_j, c_k). (b) Case 2 (effects of a_i).

(c) Case 3 (effects of b_j). (d) Case 4 (effects of c_k).

Fig. 4.5. Effects of higher order parameters for bending.

value of wavenumber are shown in Fig.4.5(b), Fig.4.5(c), Fig.4.5(d) and Fig.4.6(b), Fig.4.6(c), Fig.4.6(d). It can be clearly seen that each parameter has an impact similar to that of case 1, that is, the value of the real part decreases but the imaginary value increases as the ratio increases. However, the difference between these three cases is that parameters a_i have the biggest impact on the results but parameters c_k have the smallest impact on the results.

In order to specifically discuss the influence of the parameters on the results, a rate of

Table 4.1. Effects of higher order parameters to real and imaginary part of bending (ω/ω_0=30).

$\delta_{a/b/c}$	-100	-10	-1	-0.5	0	0.5	1(SSG)	10	100
$\Delta\kappa(\delta_a, \delta_b, \delta_c)$	35.87	9.69	3.92	3.42	1.94(CT)	0.48	0	-5.24	-23.19
$\Delta\kappa(\delta_a, \delta_b{=}\delta_c{=}1)$	24.54	6.63	2.68	2.34	1.33	0.33	0	-3.59	-15.87
$\Delta\kappa(\delta_b, \delta_a{=}\delta_c{=}1)$	5.66	1.53	0.62	0.54	0.31	0.08	0	-0.83	-3.66
$\Delta\kappa(\delta_c, \delta_a{=}\delta_b{=}1)$	1.89	0.51	0.21	0.18	0.10	0.03	0	-0.28	-1.22

change for wavenumber is defined as: $\Delta\kappa = (\kappa - \kappa_{\mathrm{SSG}})/\kappa_{\mathrm{SSG}} \times 100\%$, in which κ is the value of wavenumber under different parameter ratio, κ_{SSG} is the value of wavenumber by SSG the-

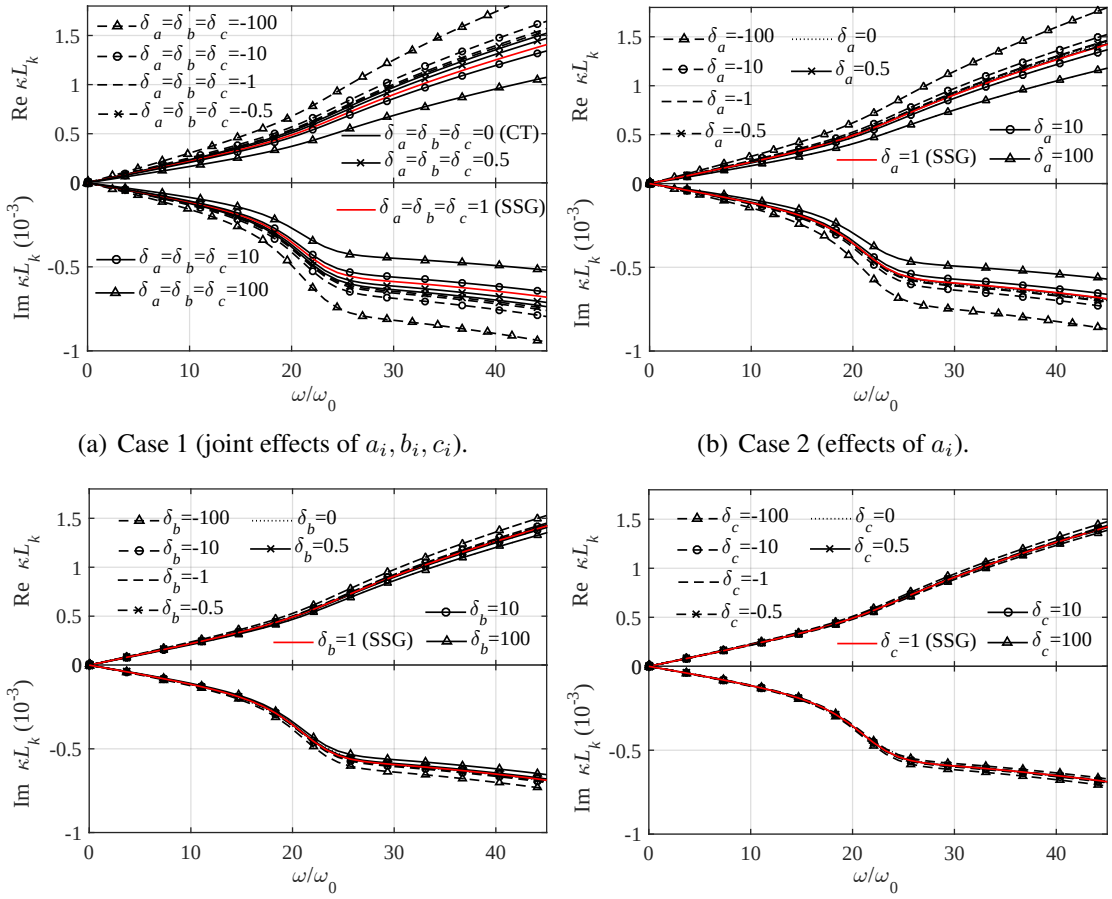

(a) Case 1 (joint effects of a_i, b_i, c_i). (b) Case 2 (effects of a_i).

(c) Case 3 (effects of b_i). (d) Case 4 (effects of c_i).

Fig. 4.6. Effects of higher order parameters for tension.

Table 4.2. Effects of higher order parameters to real and imaginary part of tension (ω/ω_0=30).

$\delta_{a/b/c}$	-100	-10	-1	-0.5	0	0.5	1(SSG)	10	100
$\Delta\kappa(\delta_a, \delta_b, \delta_c)$	37.75	10.20	4.12	3.59	2.04(CT)	0.51	0	-5.12	-24.41
$\Delta\kappa(\delta_a, \delta_b{=}\delta_c{=}1)$	26.43	7.14	2.89	2.52	1.43	0.36	0	-3.86	-17.09
$\Delta\kappa(\delta_b, \delta_a{=}\delta_c{=}1)$	7.55	2.04	0.82	0.72	0.41	0.10	0	-1.10	-4.88
$\Delta\kappa(\delta_c, \delta_a{=}\delta_b{=}1)$	3.78	1.02	0.41	0.36	0.20	0.05	0	-0.55	-2.44

ory (δ_a= δ_b= δ_c=1). $\Delta\kappa$ is then calculated when normalized frequency is chosen as 30 under different parameter ratio. As shown in Tab. 4.1 for bending and Tab. 4.2 for tension, with the ratio of parameters increases, the value of $\Delta\kappa$ decreases. At the same ratio of parameter, δ_a, δ_b and δ_c together have a bigger impact on the results than their respective effect on the results. For example, $\Delta\kappa$=35.87 for bending and $\Delta\kappa$=37.75 for tension when δ_a=δ_b=δ_c=-100; $\Delta\kappa$=24.54 for bending and $\Delta\kappa$=26.43 for tension when δ_a=-100, δ_b=δ_c=1; $\Delta\kappa$=5.66 for bending and $\Delta\kappa$=7.55 for tension when δ_b=-100, δ_a=δ_c=1; $\Delta\kappa$=1.89 for bending and $\Delta\kappa$=3.78 for tension when δ_c=-100, δ_a=δ_b=1. On the other hand, the sum of the value $\Delta\kappa(\delta_a, \delta_b{=}\delta_c{=}1)$, $\Delta\kappa(\delta_b, \delta_a{=}\delta_c{=}1)$ and

$\Delta\kappa(\delta_c, \delta_a{=}\delta_b{=}1)$ is approximately equal to the combined value $\Delta\kappa(\delta_a, \delta_b, \delta_c)$. What is more, When $\delta_a = \delta_b = \delta_c$=0, the result belongs to the CT. When $\delta_a = \delta_b = \delta_c$=1, the result belongs to the SSG.

4.5.3 Diffusion through a simple coupling element

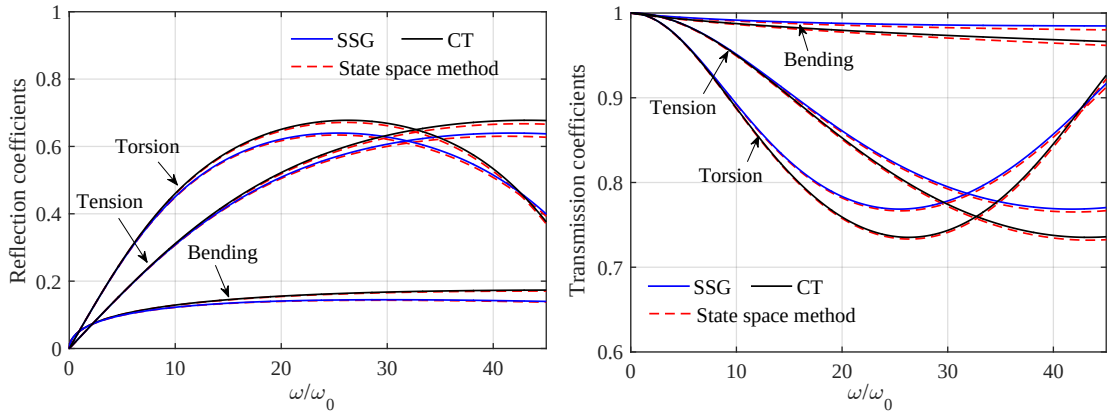

(a) Reflection coefficients (R). (b) Transmission coefficients (T).

Fig. 4.7. Absolute values of diffusion coefficients by SSG and CT (the material of coupling element is Cu, unit cell k and k+1 are Al).

In this part, the diffusion is discussed through a simple coupling element which is shown in Fig.4.3(c), firstly, when the material of coupling element is same as the waveguides, the incident waves will be fully transmitted without reflection. The value of transmission coefficient is 1 and the value of reflection coefficient is 0. Secondly, when the material of coupling element is Cu and the material of waveguides are Al, there exist wave reflection and transmission. The resulting $\mathbf{R}$ and $\mathbf{T}$ coefficients can be illustrated by Eq. 4.20. As shown in Fig.4.7, the diffusion coefficients including bending, tension and torsion modes are presented by CT and SSG theory. The blue lines represent the results from SSG theory and black lines denote the CT. The curve by SSG is close to the one by CT at low frequency. The difference between SSG and CT becomes more obvious as frequency increases. For bending, tension and torsion modes, the value of reflection coefficient by CT is bigger than the one by SSG but the value of transmission coefficient by CT is smaller than the one by SSG. The difference between SSG and CT diffusion coefficients is due to the size effect, which is caused by the non-local interactions in the micro-sized structures. Higher order parameters exert stiffness-hardening mechanisms especially at high frequency. In order to verify the WFEM results, a state space method [227] is used and the results from two different methods match each other well.

4.5.4 Diffusion through a complex coupling element

In order to study the wave diffusion under a complex coupling condition, as shown in Fig.4.3(d), first of all, defining the the materials of coupling element, unit cell k and k+1 are Al, the diffusion model of coupling element is built by SSG theory with higher-order parameters, the diffusion models of unit cell k and k+1 are built by CT. The $\mathbf{R}$ and $\mathbf{T}$ coefficients can be calculated from Eq. 4.31 including bending, tension and torsion modes. As shown in

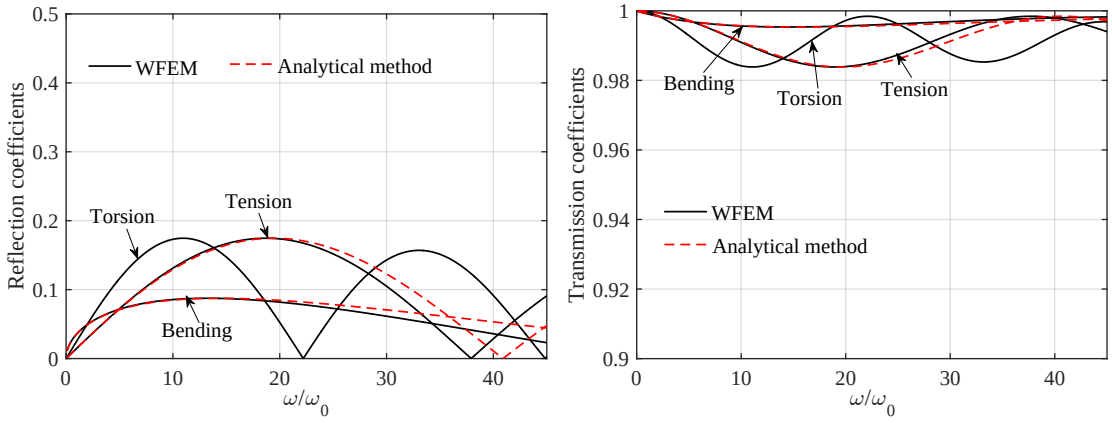

(a) Reflection coefficients (R). (b) Transmission coefficients (T).

Fig. 4.8. Absolute values of diffusion coefficients (the materials of coupling element, unit cell k and k+1 are Al).

Fig. 4.8, The black lines denote the WFEM results. As a result, the value of $\mathbf{R}$ representing the non-classical part of reflection is no longer 0, and the value of $\mathbf{T}$ representing the non-classical part of transmission is no longer 1. The influence of non-local interactions caused by higher-order parameters can be reflected by this model. On the other hand, an analytical method [228], shown by the red lines, is used to valid the WFEM results for bending and tension. As we can see, for the reflection coefficient, the result obtained by WFEM is very close to the one by the analytical method at low frequency, but the results are different at high frequencies. For the transmission coefficient, the results by WFEM matches the results by analytical method well.

In addition, the joint influence of classical parameters (i.e., Young's modulus, Poisson's ratio and mass density) and higher-order parameters of material on diffusion is also a very meaningful study. Defining the material of coupling element is Cu, unit cell k and k+1 are Al, the diffusion model of coupling element is built by SSG theory with higher-order parameters, the diffusion models of unit cell k and k+1 are built by CT. The $\mathbf{R}$ and $\mathbf{T}$ coefficients including bending, tension and torsion modes can be illustrated by Eq. 4.31 as well. As shown in Fig.4.9, the black lines denote the WFEM results and the red lines represent the results from an analytical method [228]. The diffusion is different from the case presented in Fig.4.8. This shows that the impedance mismatch is not only due to the non-local interactions caused by higher order parameters but also the local interactions caused by classical parameters.

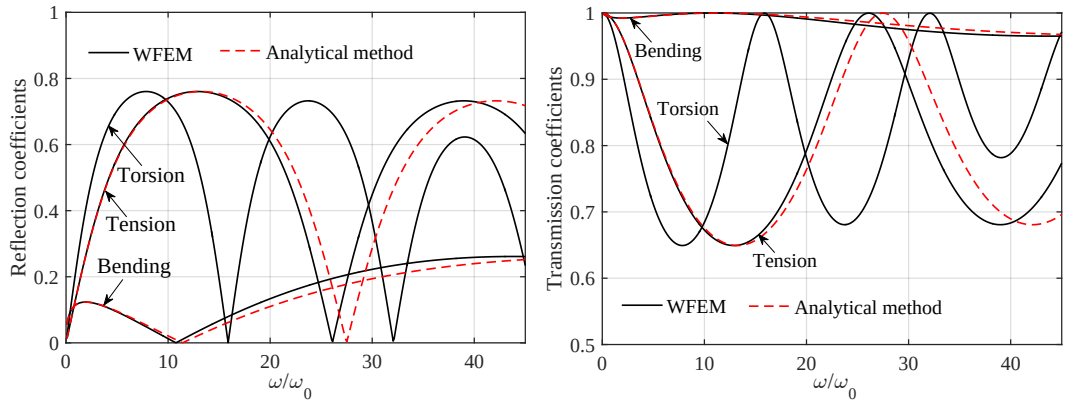

(a) Reflection coefficients (R). (b) Transmission coefficients (T).

Fig. 4.9. Absolute values of diffusion coefficients (coupling element is Cu, unit cell k and k+1 are Al).

4.5.5 Forced response

In this part, the forced response for waveguide 1 is discussed, as presented in Fig. 4.3(a), the waveguide 1 consists of 10 unit cells. There are two boundary conditions in this study: One is that left end of waveguide 1 is clamped, right end of waveguide 1 is free (C-F), another is that left and right ends of waveguide 1 are free (F-F). A harmonic force with a unit amplitude is loaded at center point of right end along z direction. Then, the amplitude of displacement at center point of right end is calculated out on each frequency according to $\mathbf{D}'\mathbf{u}'=\mathbf{F}'$, in which $\mathbf{D}'$ is the global dynamical stiffness matrix of waveguide assambled from a unit cell dynamical stiffness matrix $\mathbf{D}$.

The forced responses for C-F and F-F doundary conditions are shown in Fig. 4.10(a) and

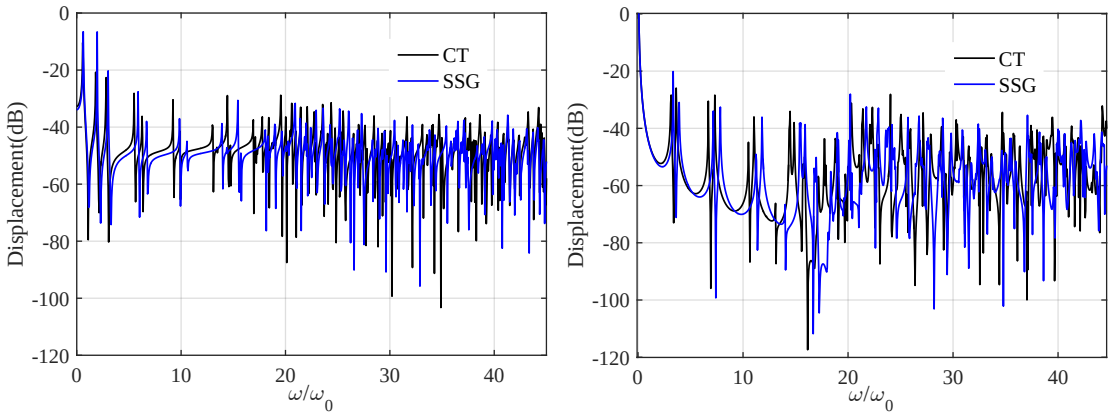

(a) C-F boundary condition. (b) F-F boundary condition.

Fig. 4.10. Forced response of waveguide 1 by SSG and CT.

Fig. 4.10(b) respectively by SSG theory and CT. It can be noticed that resonances are well predicted in both theories. The comparison between SSG theory and CT shows that at low fre-

quency, the forced response by SSG confirms to CT well. On the other hand, the discrepancies of forced responses between CT and SSG increase with frequency increases. Wave propagation is significantly affected by the long-range interactions in micro-sized structure. The input vibration energy can be transferred both by propagating waves and other evanescent waves, which decay rapidly in the near field of the excitation.

4.5.6 Wave shapes

The study of wave shapes at different frequency is another important part for understanding the dynamical characteristics of structures. In this part, the wave shapes for bending (see in Fig.4.11) and tension (see in Fig.4.12) are discussed by SSG and CT.

As shown in Fig.4.11, the real part of bending modes by SSG and CT are presented. At

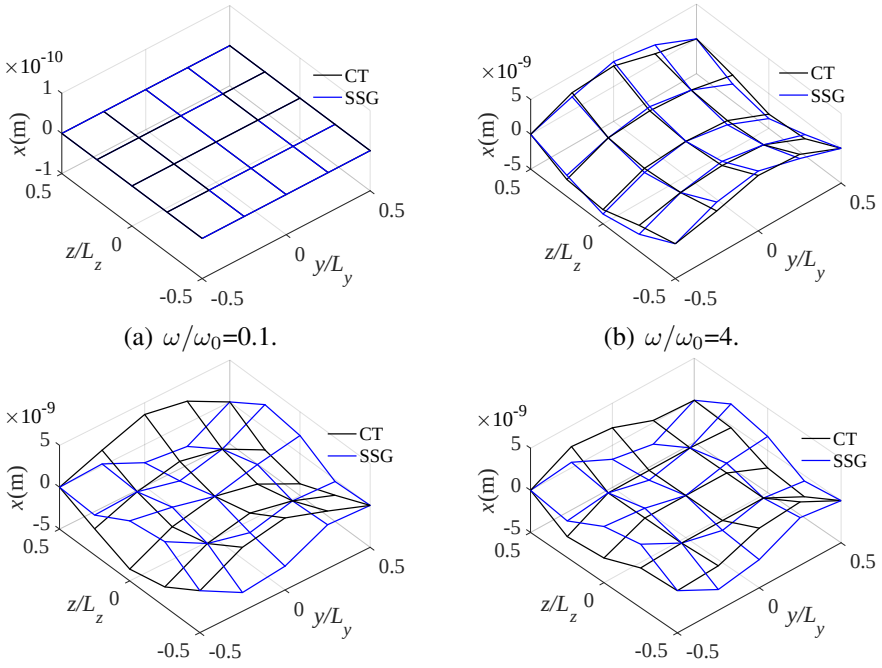

(a) ω/ω_0=0.1. (b) ω/ω_0=4.

(c) ω/ω_0=12. (d) ω/ω_0=20.

Fig. 4.11. Bending modes (real part) by SSG and CT.

low frequency such as ω/ω_0=0.1, the wave shape by CT is nearly the same as the one by SSG. However, with the frequency increase, the difference of wave shape between CT and SSG is more oblivious. For instance, the amplitude direction of wave shape by CT is opposite to the one by SSG when ω/ω_0=12.

On the other hand, the real part of tension modes by SSG and CT are shown in Fig.4.12. As we can see, at low frequency such as ω/ω_0=0.1, the wave shape by CT is also nearly the same as the one by SSG. When ω/ω_0=4, the amplitude direction of wave shape by CT is opposite to the one by SSG, and the value of wave shape amplitude by CT is bigger than the one by SSG.

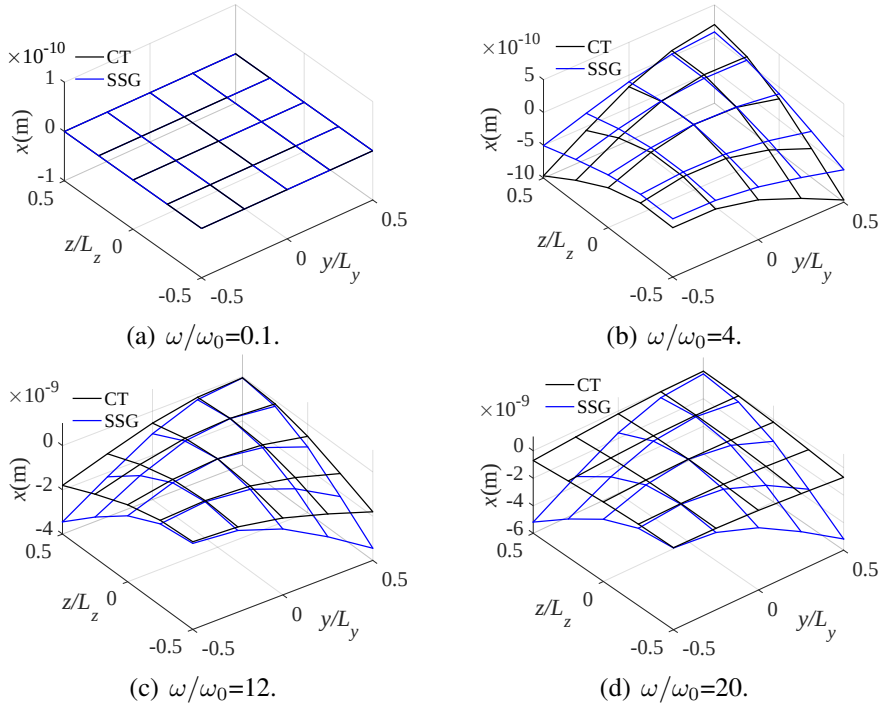

Fig. 4.12. Tension modes (real part) by SSG and CT.

What is more, when ω/ω_0=12 or 20, the amplitude value by CT is smaller than the one by SSG.

4.6 Conclusions

In this chapter, SSG theory is used for the multi-mode propagation and diffusion analysis within the WFEM framework. Some conclusions in our work are addressed as follow:

(i) The constitutive relations of 3D micro-sized model are introduced in the SSG theory framework. The displacement vector is derived by employing the six quin-tic Hermite polynomial shape function. The weak formulations including element stiffness, mass matrices and force vector are calculated by using the Hamilton's principle and global dynamic stiffness matrix of a unit cell is assembled. The reason for combining SSG theory and WFEM is that the characteristics of micro-sized medias can be interpreted by SSG theory and the dynamical properties of complex periodic structures can be investigated through WFEM.

(ii) Free wave propagation characteristics are expressed by solving eigenvalue problems through WFEM. The dispersion relation for a 3D beam is illustrated by SSG and CT. The curve by SSG is close to the one by CT at low frequency. But the difference between SSG and CT becomes more obvious as frequency increases. On the other hand, the κ value by SSG is smaller than CT at same frequency, especially for bending, tension and torsion modes. This

phenomenon can be explained as: the potential energy density in SSG theory is a function of strain, first gradient of strain and second gradient of strain, which leads to the dynamical equilibrium equation being a high order partial differential function composed of classical part and non-classical part. Due to the existence of non-classical parts containing higher-order parameters, the interactions between microscopic particles within the structure are non-local or long-range, which hardened the stiffness of the material and caused the wavenumber value to decrease.

(iii) The joint effects of a_i, b_j and c_k on the bending and tension dispersion relations are presented. What is more, the individual effects of a_i, b_j and c_k on the dispersion relations are studied as well. The effect of a_i on the result is biggest and the effect of c_i on the result is smallest. The forced responses including two boundary conditions for waveguide are discussed. The comparison between SSG theory and CT shows that at low frequency, the forced response by SSG confirms to CT well. On the other hand, the discrepancies of forced responses between CT and SSG increase with frequency increases. Wave propagation is significantly affected by the long-range interactions in micro-sized structure.

(iv) The diffusion including R and T coefficients is confirmed through three different cases. First: the material of coupling element is different to the waveguides, but the wave modes calculation in waveguides and coupling element are based on the same theory (classical or SSG). Second: the material of coupling element is same as the waveguides, the wave modes calculation in waveguides is based on the classical theory but SSG theory for coupling element. Third: the material of coupling element is different to the waveguides, the wave modes calculation in waveguides is based on the classical theory but SSG theory for coupling element. For the first case, the diffusion curve by SSG is close to the one by CT at low frequency. However, the difference between SSG and CT becomes more obvious as frequency increases. For the second case, the value of $\mathbf{R}$ representing the non-classical part of reflection is no longer 0, and the value of $\mathbf{T}$ representing the non-classical part of transmission is no longer 1. The influence of non-local interactions caused by higher-order parameters can be reflected by this model. For the third case, the impedance mismatch is not only due to the non-local interactions caused by higher order parameters in the SSG theory model but also the local interactions caused by Young's modulus and mass density.

Chapter 5

Dynamic and sensitivity analysis of a two-dimensional full plate

Chapter contents

5.1 Introduction 97
5.2 2D wave propagation analysis 98
5.2.1 Inverse form of 2D wave finite element method 98
5.2.2 Direct form of 2D wave finite element method 98
5.2.3 Sound transmission by second strain gradient elasticity 101
5.2.4 Numerical simulations of a 2D full plate 103
5.3 Sensitivity analysis of higher order parameters 109
5.3.1 Fourier amplitude sensitivity test formulation 109
5.3.2 Numerical applications of sensitivity analysis 111
5.4 Conclusions 117

5.1 Introduction

In chapter 4, SSG theory is applied for the multi-mode propagation and diffusion analysis of a micro-sized beam. The wave propagation analysis is based on the WFEM1D. Meanwhile, a large number of 2D full plate structures are wildly used in engineering. The propagation of 2D waves in these 2D full plates is more in line with the real situation. So, the exploration of 2D waves in 2D full plate structures is of great significance.

In this chapter, SSG theory is applied for a 2D full plate within WFEM2D framework. Firstly, the CI method is applied to illustrate the NEP and conform the band structure and iso-frequency contours. Then, a SA method is introduced for this 2D full plate to investigate the

effects of higher order parameters on dispersion. Finally, some useful conclusions are discussed.

5.2 2D wave propagation analysis

A scheme for 2D periodic structure and its unit cell is given in Fig.1.11. The DOFs in the unit cell are classified by the amplitudes of nodal displacements: $[\hat{\mathbf{u}}_{\mathrm{Bd}}\ \hat{\mathbf{u}}_{\mathrm{I}}]$ = $[\hat{\mathbf{u}}_1\ \ \hat{\mathbf{u}}_2\ \ \hat{\mathbf{u}}_3\ \ \hat{\mathbf{u}}_4\ \ \hat{\mathbf{u}}_{\mathrm{L}}\ \ \hat{\mathbf{u}}_{\mathrm{B}}\ \ \hat{\mathbf{u}}_{\mathrm{R}}\ \ \hat{\mathbf{u}}_{\mathrm{T}}\ \ \hat{\mathbf{u}}_{\mathrm{I}}]$. The nodal forces are classified in the same way. There are two ways to illustrate the wave propagation: Inverse form and direct form.

5.2.1 Inverse form of 2D wave finite element method

For the inverse form, the internal nodes are conserved since the dynamic condensation can not be performed. the dynamical equation of motion is:

$$[\mathbf{K}^*(\lambda_x,\lambda_y)-\omega^2\mathbf{M}^*(\lambda_x,\lambda_y)]\begin{pmatrix}\hat{\mathbf{u}}_1\\ \hat{\mathbf{u}}_{\mathrm{L}}\\ \hat{\mathbf{u}}_{\mathrm{B}}\\ \hat{\mathbf{u}}_{\mathrm{I}}\end{pmatrix}=\mathbf{0}, \tag{5.1}$$

in which $\mathbf{K}^*$ and $\mathbf{M}^*$ are explained in Eq. 1.74. Eq. 5.1 provides a way to analyze the wave propagation in 2D periodic structures. The view of WFEM2D inverse form is fixing λ_x and λ_y, the values of ω are calculated. The corresponding frequencies (ω) are sorted in the ascending order $\omega^{i,j}_{1,2,3,\ldots k,\ldots n}$. The k-th slowness surface is formed by $\omega^{i,j}_k$. In addition, a convenient 2D representation of the slowness surface is the band structure, which is obtained by plotting the wave-numbers along the contour O–A–B–C–O as shown in Fig. 1.3(b).

5.2.2 Direct form of 2D wave finite element method

As shown in Fig.1.3(c), there exist two different situations to solve the direct form of WFEM2D: θ'=0 and $\theta' \neq$0.

5.2.2.1 Wave propagation angle θ'=0

Suppose λ_y is given, which means the wave propagates along x direction, the dynamical equation for 2D unit cell as shown in Eq.1.68 is written as:

$$\frac{1}{\lambda_x}\left(\lambda_x^2\begin{bmatrix}\mathbf{A}_{11}&\mathbf{A}_{1\mathrm{L}}&\mathbf{A}_{1\mathrm{B}}\\ \mathbf{A}_{\mathrm{L}1}&\mathbf{A}_{\mathrm{LL}}&\mathbf{A}_{\mathrm{LB}}\\ \mathbf{A}_{\mathrm{B}1}&\mathbf{A}_{\mathrm{BL}}&\mathbf{A}_{\mathrm{BB}}\end{bmatrix}+\lambda_x\begin{bmatrix}\mathbf{B}_{11}&\mathbf{B}_{1\mathrm{L}}&\mathbf{B}_{1\mathrm{B}}\\ \mathbf{B}_{\mathrm{L}1}&\mathbf{B}_{\mathrm{LL}}&\mathbf{B}_{\mathrm{LB}}\\ \mathbf{B}_{\mathrm{B}1}&\mathbf{B}_{\mathrm{BL}}&\mathbf{B}_{\mathrm{BB}}\end{bmatrix}+\begin{bmatrix}\mathbf{C}_{11}&\mathbf{C}_{1\mathrm{L}}&\mathbf{C}_{1\mathrm{B}}\\ \mathbf{C}_{\mathrm{L}1}&\mathbf{C}_{\mathrm{LL}}&\mathbf{C}_{\mathrm{LB}}\\ \mathbf{C}_{\mathrm{B}1}&\mathbf{C}_{\mathrm{BL}}&\mathbf{C}_{\mathrm{BB}}\end{bmatrix}\right)\hat{\mathbf{u}}_b=\mathbf{0}, \tag{5.2}$$

where $\hat{\mathbf{u}}_b$=$[(\hat{\mathbf{u}}_1)^{\mathrm{T}},\ (\hat{\mathbf{u}}_{\mathrm{L}})^{\mathrm{T}},\ (\hat{\mathbf{u}}_{\mathrm{B}}^{\mathrm{T}})]^{\mathrm{T}}$. The $\mathbf{A}$, $\mathbf{B}$ and $\mathbf{C}$ are addressed in Appendix A. The quadratic eigen-problem in Eq.5.2 can be solved using the following linearization:

$$\begin{bmatrix} -\mathbf{C} & \mathbf{0} \\ \mathbf{0} & \mathbf{I} \end{bmatrix} \begin{pmatrix} \hat{\mathbf{u}}_b \\ \lambda_x \hat{\mathbf{u}}_b \end{pmatrix} = \lambda_x \begin{bmatrix} \mathbf{B} & \mathbf{A} \\ \mathbf{I} & \mathbf{0} \end{bmatrix} \begin{pmatrix} \hat{\mathbf{u}}_b \\ \lambda_x \hat{\mathbf{u}}_b \end{pmatrix}. \tag{5.3}$$

In our work, assume that the wavenumber $\kappa_y = 0$, which means $\lambda_y = 1$. Then, wavenumber κ_x can be solved from Eq.5.3 under different frequency.

5.2.2.2 Wave propagation angle $\theta' \neq 0$

In this part, a solution strategy based on CI method is introduced to solve the NEP when wave propagation angle is not equal to 0. As presented in Fig.1.3(c), define the wave propagation constants λ_x, λ_y as:

$$\lambda_x = e^{-\mathrm{i}\kappa_{\theta'}\cos(\theta')L_x},\ \lambda_y = e^{-\mathrm{i}\kappa_{\theta'}\sin(\theta')L_y}. \tag{5.4}$$

In Eq.5.4, the linear dimension of the cell along x direction is referred to as L_x, θ' is heading angle of the wave propagation and $\kappa_{\theta'}$ means the wavenumber. In practice, the non-dimensional wavenumber κ' and the scaled heading angle β are introduced as:

$$\kappa' = \kappa_{\theta'}[(L_x\mathrm{cos}\beta)^2 + (L_y\mathrm{sin}\beta)^2]^{-\frac{1}{2}},\ \mathrm{tan}\beta = \frac{L_y}{L_x}\mathrm{tan}\theta'. \tag{5.5}$$

Then, the wave propagation constants can be re-expressed as:

$$\lambda_x = e^{-\mathrm{i}\kappa'\cos(\beta)},\ \lambda_y = e^{-\mathrm{i}\kappa'\sin(\beta)}. \tag{5.6}$$

Consequently, Eq.1.67 will be re-written in the following form:

$$[\hat{\mathbf{\Lambda}}_L(\kappa', \beta)\mathbb{D}(\omega)\hat{\mathbf{\Lambda}}_R(\kappa', \beta)]\hat{\mathbf{u}}_b = \mathbf{0}. \tag{5.7}$$

In our work, the frequency ω and heading β are fixed, all the eigenvalues κ' can be solved within a specific contour Γ of the complex plane corresponding to the eigen-vectors $\hat{\mathbf{u}}_b$:

$$\hat{\mathbb{D}}(\kappa')\hat{\mathbf{u}}_b = \mathbf{0}, \tag{5.8}$$

where $\hat{\mathbb{D}}(\kappa') \in \mathbb{C}^{n,n}$. The above NEP can be deduced using the contour integral method (CI) which is based on the analysis of the moments related to the matrix $\hat{\mathbb{D}}(\kappa')$, as defined:

$$\mathcal{A}_p = \frac{1}{2\pi\mathrm{i}}\int_{\Gamma}(\kappa')^p\hat{\mathbb{D}}(\kappa')^{-1}\hat{\mathcal{V}}\mathrm{d}\kappa', \tag{5.9}$$

with $p \in \mathbb{N}$. In Eq.5.9, $\hat{\mathcal{V}}(\kappa') \in \mathbb{C}^{n,l}$ is a probe matrix which can be chosen at random practically. Moments $\mathcal{A}_p$ contain the spectrum information of $\hat{\mathbb{D}}(\kappa')$ inside the contour Γ. So as to illustrated the eigenvalues and eigenvectors, $2\overline{p}$ moments are utilized to built the block Hankel matrices $\mathcal{B}_0$ and $\mathcal{B}_1 \in \mathbb{C}^{\overline{p}n,\overline{p}l}$ as follows:

$$\mathcal{B}_0 = \begin{bmatrix} \mathcal{A}_0 & \dots & \mathcal{A}_{\overline{p}-1} \\ \vdots & \ddots & \vdots \\ \mathcal{A}_{\overline{p}-1} & \dots & \mathcal{A}_{2\overline{p}-2} \end{bmatrix}, \ \mathcal{B}_1 = \begin{bmatrix} \mathcal{A}_1 & \dots & \mathcal{A}_{\overline{p}} \\ \vdots & \ddots & \vdots \\ \mathcal{A}_{\overline{p}} & \dots & \mathcal{A}_{2\overline{p}-1} \end{bmatrix}, \tag{5.10}$$

in which $\overline{p} \in \mathbb{N}$. Then, the Singular Value Decomposition (SVD) is expressed as:

$$\mathcal{B}_0 = \mathcal{V}\Sigma\mathcal{W}^{\mathrm{H}}, \tag{5.11}$$

which can be used to confirm the low rank approximation:

$$\mathcal{B}_0 \approx \mathcal{V}_0\Sigma_0\mathcal{W}_0^{\mathrm{H}}. \tag{5.12}$$

Namely, a tolerance ε_{SVD} is introduced. Only the m leading singular values, which corresponds columns of $\mathcal{V}$ and $\mathcal{W}$, are reserved according to the sorting of the singular values:

$$\sigma_1 \geq \cdots \geq \sigma_m \geq \sigma_{SVD} \geq \sigma_{m+1} \approx \cdots \approx 0. \tag{5.13}$$

After the algebraic manipulation, the eigenvalues of matrix $\hat{\mathcal{B}}$ can be calculated, which are same as the ones by the original NEP (i.e. Eq.5.8) inside the contour Γ, as follows:

$$\hat{\mathcal{B}} = \mathcal{V}_0^{\mathrm{H}}\mathcal{B}_1\mathcal{W}_0\Sigma^{-1}, \tag{5.14}$$

where $\hat{\mathcal{B}} \in \mathbb{C}^{m,m}$. Also, being $\mathbf{s}_i$ the eigenvectors of $\hat{\mathcal{B}}$, the original eigenvectors $\hat{\mathbf{u}}_{bi}$ can be retrieved from the first n rows of $\mathcal{V}_0\mathbf{s}_i$. As a result, the NEP in Eq.5.8 is reformulated in terms of a reduced sized linear eigenvalue problem with the same eigenvalues inside Γ. Here, assuming that n_{sol} is the number of eigenvalues within Γ and expecting that $m \geq n_{sol}$ after the low rank decomposition. In order to satisfy the condition above, the number of moments and columns of the probe matrix have to be chosen as $\overline{p}l \geq n_{sol}$. Here should be noted that $\overline{p} \geq 1$ is necessary only if algebraic multiplicity solutions are higher than the one are expected. As a basic rule, the maximum order of the moments $2\overline{p} - 1$ must keep small for the reasons of accuracy and stability. In practice, a numerical approximation of the integral in Eq.5.9 is necessary. Set a parametrization of the contour as:

$$\Gamma = \gamma_0 + \gamma_1(\mathrm{cos}t + \mathrm{i}\gamma_2\mathrm{sin}t), \tag{5.15}$$

where $0 \leq t \leq 2\pi$. Based on these circumstances, the integral is approximated by a N-point trapezoidal rule, which causes to the discrete approximation of Eq.5.9, one arrives:

$$\mathcal{A}_p \approx \frac{\gamma_1}{N} \sum_{j=1}^{N} (\kappa')_j^p \omega_j \mathbf{X}_j, \tag{5.16}$$

in which κ'_j is the integration point along Γ, $\omega_j = (\gamma_2 \mathrm{cos}t_j + \mathrm{i}\ \mathrm{sin}t_j)$ is the weight and $\hat{\mathcal{D}}(\kappa'_j)\mathbf{X}_j = \hat{\mathcal{V}}$ is the N linear system to be deduced. In order to ensure the numerical stability, a shift and scale transformation is utilized to the spectrum. The monomial basis $((\kappa' - \gamma_0)/\gamma_1)^p$ is appiled in Eqs.5.9 and 5.16 in place of $(\kappa')^p$. The procedure above can be used to confirm the wavenumbers of different wave propagation angles within a closed curve of the complex plane.

5.2.3 Sound transmission by second strain gradient elasticity

The transmission of sound through a 2D full plate is of interest in many applications such as aerospace and automotive. There have been a number of researches of the acoustic performance of infinite structures [229–231]. If we consider an external force vector $\mathbf{F}^e$=[$\mathbf{F}_1^e$ $\mathbf{F}_2^e$ $\mathbf{F}_3^e$ $\mathbf{F}_4^e$ $\mathbf{F}_{\mathrm{L}}^e$ $\mathbf{F}_{\mathrm{B}}^e$ $\mathbf{F}_{\mathrm{R}}^e$ $\mathbf{F}_{\mathrm{T}}^e$ $\mathbf{F}_{\mathrm{I}}^e$] imposed on the unit cell by the acoustic pressure fields, the dynamic equation Eq.1.67 will be re-written as:

$$\overline{\mathbb{D}}\hat{\mathbf{u}}_b = \mathbf{A}\hat{\mathbf{F}}_b^e, \tag{5.17}$$

where $\overline{\mathbb{D}}$=$\hat{\mathbf{\Lambda}}_L \mathbb{D} \hat{\mathbf{\Lambda}}_R$, $\mathbf{A}$=$\hat{\mathbf{\Lambda}}_L \hat{\mathbf{\Lambda}}_R$, $\hat{\mathbf{F}}_b^e$=[$(\hat{\mathbf{F}}_1^e)^{\mathrm{T}}$ $(\hat{\mathbf{F}}_{\mathrm{L}}^e)^{\mathrm{T}}$ $(\hat{\mathbf{F}}_{\mathrm{B}}^e)^{\mathrm{T}}$]$^{\mathrm{T}}$ are the external forces amplitudes on node 1 and boundaries L, B. An oblique incident plane wave impinging the plate on one side is concerned. The amplitude of this wave is p^I. The interaction between this incident wave and the plate create a reflected wave with amplitude p^R on the same side, and a transmitted wave on the other one with amplitude p^T. The sound field on the incident side is then the superposition of the incident and reflected waves:

$$P^I = p(x, y, z)|_{z>0} = p^I \mathrm{exp}(-\mathrm{i}\kappa_z^I z) + p^R \mathrm{exp}(-\mathrm{i}\kappa_z^R z), \tag{5.18}$$

where the common factor $\mathrm{exp}(\mathrm{i}(\omega t - \kappa_x x - \kappa_y y)$ has been ignored for legibility. The wavenumber components κ_x, κ_y and κ_z have the relationship, as:

$$\kappa_x^2 + \kappa_y^2 + (\kappa_z^I)^2 = \kappa^2 = (\frac{\omega}{c^I})^2, \tag{5.19}$$

in which c^I is the speed of sound in the fluid of the incident side. In the same way, the sound field on the transmission side includes only the transmitted wave propagating in the same direction as the incident wave:

$$P^T = p(x, y, z)|_{z<0} = p^T \mathrm{exp}(-\mathrm{i}\kappa_z^T z), \tag{5.20}$$

with the relation $\kappa_x^2 + \kappa_y^2 + (\kappa_z^T)^2 = (\frac{\omega}{c^T})^2$, in which c^T is the speed of sound in the fluid on the transmission side. Potential phase difference between the pressure fields leads to the amplitudes complex of p^R and p^T. κ_x and κ_y are conserved across the plate, only κ_z component change according to the nature of fluid. Assume that the fluid keep same on both sides, one arrives:

$$\rho^I = \rho^T = \rho,\ c^I = c^T = c. \tag{5.21}$$

Then, we set θ^* as the angle between the wave vector and the normal of the plate, while ϕ^* gives the azimuthal angle of its orientation in the plane. As a result:

$$\kappa_x = \kappa \mathrm{sin}\theta^* \mathrm{cos}\phi^*,\ \kappa_y = \kappa \mathrm{sin}\theta^* \mathrm{sin}\phi^*,\ \kappa_z = \kappa \mathrm{cos}\theta^*. \tag{5.22}$$

The force loaded on the nodes of the FE model of the plate can be expressed from these two pressure fields. Due to the pressure force is exerted along the normal to the plate, only non-zero terms in the external force vector related to the DOFs in z direction on the incident and transmission sides are considered, which are expressed as $\hat{\mathrm{F}}_b^{eI}$ and $\hat{\mathrm{F}}_b^{eT}$ respectively. Assume $\hat{\mathbf{u}}_b^{eO}$ and $\hat{\mathbf{F}}_b^{eO}$ are the displacement and force vectors on all other DOFs. Eq.5.17 becomes:

$$\begin{bmatrix} \overline{d}^{II} & \overline{\mathbb{D}}^{IO} & \overline{d}^{IT} \\ \overline{\mathbb{D}}^{OI} & \overline{\mathbb{D}}^{OO} & \overline{\mathbb{D}}^{OT} \\ \overline{d}^{TI} & \overline{\mathbb{D}}^{TO} & \overline{d}^{TT} \end{bmatrix} \begin{pmatrix} \hat{\mathrm{u}}_b^{eI} \\ \hat{\mathbf{u}}_b^{eO} \\ \hat{\mathrm{u}}_b^{eT} \end{pmatrix} = \begin{pmatrix} \hat{\mathrm{F}}_b^{eI} \\ \hat{\mathbf{F}}_b^{eO} \\ \hat{\mathrm{F}}_b^{eT} \end{pmatrix} = \begin{pmatrix} S(p^I + p^R) \\ \mathbf{0} \\ Sp^T \end{pmatrix}, \tag{5.23}$$

where S is the free surface of the element, which is identical on both sides. Doing condensation for Eq.5.23, one arrives:

$$\begin{bmatrix} \overline{d}_c^{II} & \overline{d}_c^{IT} \\ \overline{d}_c^{TI} & \overline{d}_c^{TT} \end{bmatrix} \begin{pmatrix} \hat{\mathrm{u}}_b^{eI} \\ \hat{\mathrm{u}}_b^{eT} \end{pmatrix} = \begin{pmatrix} S(p^I + p^R) \\ Sp^T \end{pmatrix}. \tag{5.24}$$

The interaction of fluid-structure is characterized by the continuity of normal particle velocity at the interface. For the incident side:

$$\rho\omega^2 \hat{\mathrm{u}}_b^{eI} = \frac{\partial P^I}{\partial z} = -\mathrm{i}\kappa_z (p^I - p^R). \tag{5.25}$$

What is more, for the transmission side:

$$\rho\omega^2 \hat{\mathrm{u}}_b^{eT} = \frac{\partial P^T}{\partial z} = -\mathrm{i}\kappa_z p^T. \tag{5.26}$$

Then, the acoustic admittance introduced as:

$$Y = \mathrm{cos}(\theta^*)/(\mathrm{i}\omega\rho c), \tag{5.27}$$

the displacements $\hat{\mathrm{u}}_b^{eI}$ and $\hat{\mathrm{u}}_b^{eT}$ can be expressed as:

$$\hat{\mathrm{u}}_b^{eI} = Y(p^I - p^R),\ \hat{\mathrm{u}}_b^{eT} = Yp^T. \tag{5.28}$$

$\hat{\mathrm{u}}_b^{eI}$ and $\hat{\mathrm{u}}_b^{eT}$ can be re-injected into Eq.5.24, leading to two scalar equations related to the unknowns p^R and p^T, yields:

$$\begin{bmatrix} \overline{d}_c^{II} + \dfrac{S}{Y} & -\overline{d}_c^{IT} \\ \overline{d}_c^{TI} & -\overline{d}_c^{TT} - \dfrac{S}{Y} \end{bmatrix} \begin{pmatrix} p^R \\ p^T \end{pmatrix} = p^I \begin{pmatrix} \overline{d}_c^{II} - \dfrac{S}{Y} \\ \overline{d}_c^{TI} \end{pmatrix}. \tag{5.29}$$

Solving Eq.5.29, gives the acoustic transparency and absorption coefficients, as:

$$\tau^t = \left|\frac{p^T}{p^I}\right|^2,\ \tau^a = 1 - \left|\frac{p^R}{p^I}\right|^2. \tag{5.30}$$

Finally, the transmission loss (TL) for a plane wave is expressed as:

$$\mathrm{TL} = -10\log_{10}\tau^t. \tag{5.31}$$

5.2.4 Numerical simulations of a 2D full plate

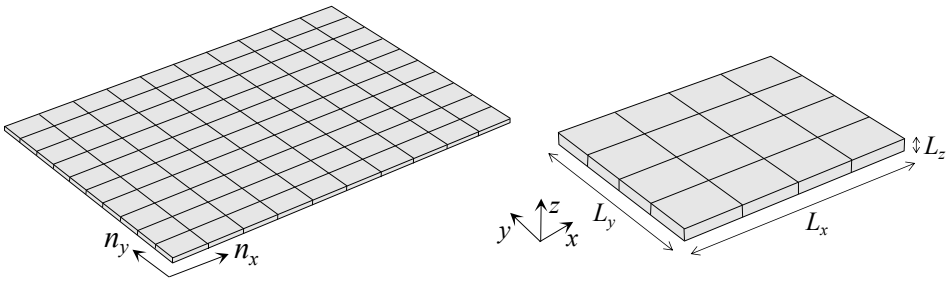

(a) A 2D full plate (b) A unit cell meshed into 16 3D elements

Fig. 5.1. A 2D full plate and its unit cells.

In this part, a 2D full plate is applied, as presented in Fig.5.1. The WFEM2D is used to analyze the 2D wave propagation. The material of a unit cell is Aluminum (Al) with $L_x = 20a_0$, $L_y = 16a_0$ and $L_z = 1a_0$ (a_0 is the lattice parameter). The Young's modulus E is 70 GPa, mass density ρ is 2.7 $\mathrm{g/cm^3}$. Damping lose factor η=$1e^{-4}$. Each unit cell is meshed into 16 elements.

5.2.4.1 Wave propagation angle θ'=0

The dispersion relation of a unit cell is calculated by WFEM2D direct form and CI method as shown in Fig.5.2. The real part $\Re(\kappa_j)$ of wavenumber is the phase shift per unit length

and the imaginary part $\Im(\kappa_j)$ means the attenuation per unit length. Only the positive waves with real and imaginary parts are illustrated due to the wavenumbers of the negative waves and positive waves are symmetric with respect to x-axis. The frequency is normalized as ω/ω_0, in which ω_0 is the first nature frequency of the unit cell. The blue lines represent the results from SSG theory and black lines denote the CT. The curve by SSG is close to the one by CT at low frequency. But the difference between SSG and CT becomes more obvious as frequency increases. CI method can predict first three modes (1: bending, 2: shearing, 3: tension) only.

In order to verify the WFEM results, the analytical methods referring to the tension, shear-

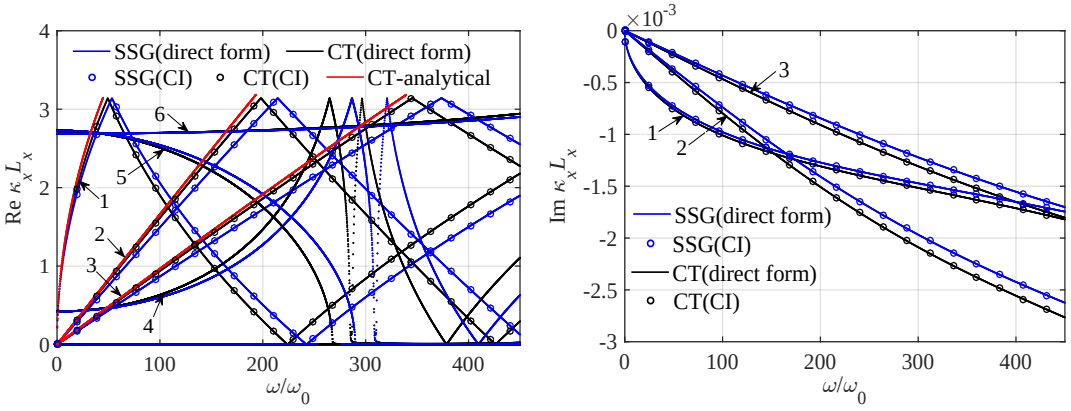

(a) Real part by CT and SSG. (b) Imaginary part by CT and SSG.

Fig. 5.2. Dispersion relation from WFEM2D direct form ($\theta' = 0$, 1: bending, 2: shearing, 3: tension).

ing and bending vibration [226] are used. The results from analytical methods match the ones from WFEM CT, but the difference between them becomes more obvious as frequency increases. Besides the tension, shearing and bending modes, there are high-order modes (e.g., modes 4, 5, 6) that analytical methods can not predict.

Next, the band structure is introduced based on WFEM2D inverse form. As presenred

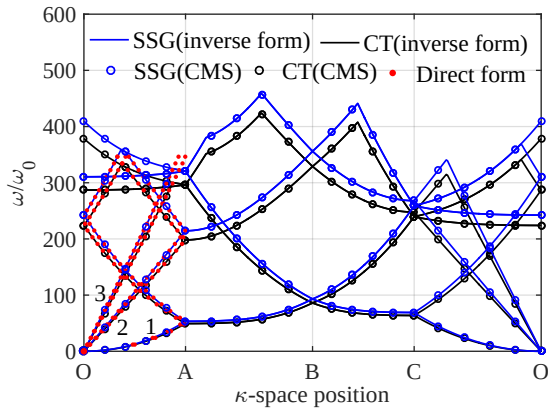

Fig. 5.3. Band structure from WFEM2D inverse form (red lines: first three modes from WFEM2D direct form, 1: bending, 2: shearing, 3: tension).

in Fig.5.3, the five lowest branches of the normalized frequency spectrum along the boundary (O-A-B-C-O) of the irreducible first Brillouin zone are calculated. The blue lines represent the results from SSG theory and black lines denote the CT. The curve by SSG is close to the one by CT at low frequency. But the difference between SSG and CT becomes more obvious as frequency increases. On the other hand, the frequency value by SSG is higher than CT at same κ-space position. This phenomenon can be explained as: the potential energy density in SSG theory is a function of strain, first gradient of strain and second gradient of strain, which leads to the dynamical equilibrium equation being a high order partial differential function composed of classical part and non-classical part. Due to the existence of non-classical parts containing higher-order parameters, the eigenvalue ω calculated by the dynamical equilibrium equation of SSG theory is bigger than the one of CT at same κ-space position. In order to valid the band structure, a Component Mode Synthesis (CMS) method [113] is used, as shown in Fig. 5.3, the result by WFEM2D inverse form matches CMS well.

5.2.4.2 Wave propagation angle $\theta' \neq 0$

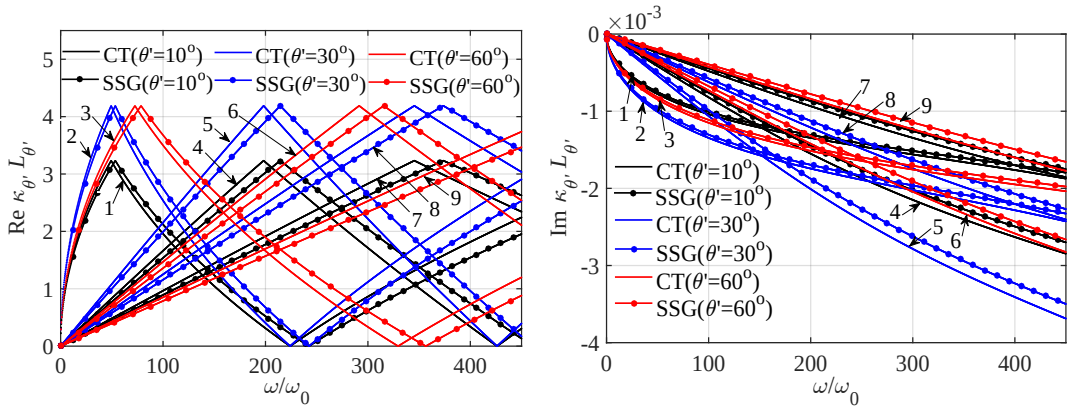

(a) Real part by CT and SSG.

(b) Imaginary part by CT and SSG.

Fig. 5.4. Dispersion relation by CI method (1: bending with $\theta' = 10°$, 2: bending with $\theta' = 30°$, 3: bending with $\theta' = 60°$, 4: shearing with $\theta' = 10°$, 5: shearing with $\theta' = 30°$, 6: shearing with $\theta' = 60°$, 7: tension with $\theta' = 10°$, 8: tension with $\theta' = 30°$, 9: tension with $\theta' = 60°$).

In this part, the situation for wave propagation angle $\theta' \neq 0$ is discussed. The dispersion relation of a unit cell is illustrated by CI method as shown in Fig.5.4. Only the positive bending, shearing and tension waves with real and imaginary parts are discussed. The frequency is normalized as ω/ω_0, in which ω_0 is the first nature frequency of the unit cell. The black lines represent the results when $\theta' = 10°$, blue lines denote the results when $\theta' = 30°$ and red lines mean the results when $\theta' = 60°$. The curve by SSG is close to the one by CT at low frequency. But the difference between SSG and CT becomes more obvious as frequency increases.

On the other hand, for the same wave, the wave frequency at which the wave reaches the

FBz boundary is different under different wave propagation angles θ'. Here we take bending (1, 2, 3) by SSG as an example, for bending 1, the wave reaches the boundary of the FBz at ω/ω_0=50, for bending 2, the wave reaches the boundary of the FBz at ω/ω_0=50, for bending 3, the wave arrives the boundary of the FBz at ω/ω_0=70.

5.2.4.3 Slowness surfaces

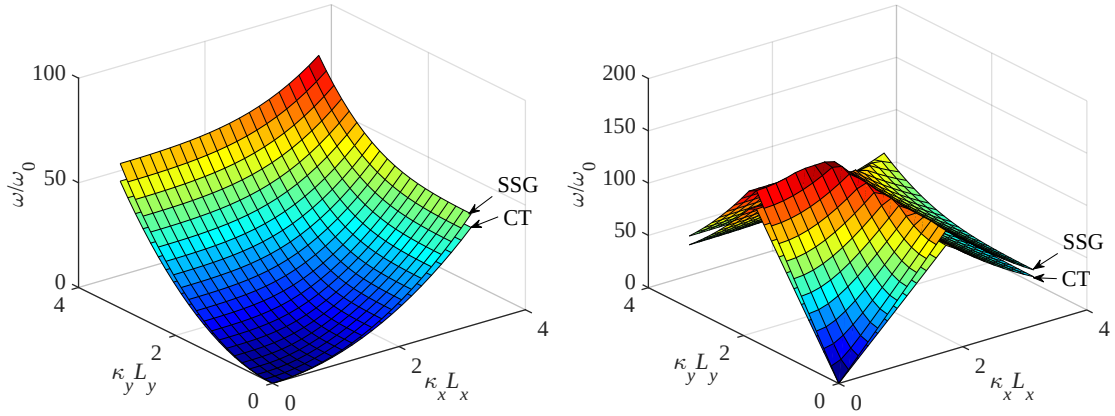

(a) The 1st slowness surface in the first quadrant. (b) The 2nd slowness surface in the first quadrant.

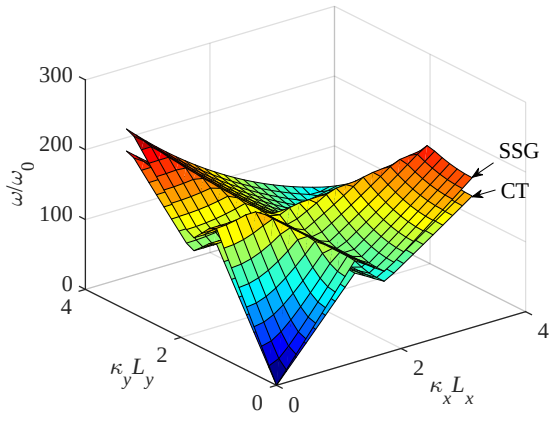

(c) The 3rd slowness surface in the first quadrant.

Fig. 5.5. The first three slowness surfaces in the first quadrant by CT and SSG.

The first three slowness surfaces in the first quadrant, as presented in Fig. 5.5, are discussed in the frequency range based on SSG and CT. The 3D surfaces are symmetric with respect to κ_x and κ_y. The slowness surface position by SSG is higher than CT. This phenomenon can be explained as: the potential energy density in SSG theory is a function of strain, first gradient of strain and second gradient of strain, which leads to the dynamical equilibrium equation being a high order partial differential function composed of classical part and non-classical part. Due to the existence of non-classical parts containing higher-order parameters, the eigenvalue ω calculated by SSG theory is bigger than the one of CT at same κ-space position.

5.2.4.4 Iso-frequency contours

As shown in Fig. 5.6, the iso-frequency contours are illustrated through CI method. In order to calculate the iso-frequency contours, the normalized frequencies are chosen at 30 and 65. The direction, perpendicular to the iso-frequency line, indicates the direction of wave propagation and more details will be discussed in next section. At low frequency, as shown in Fig. 5.6(a), the iso-frequency lines by SSG are close to CT. However, there exists a big difference between SSG and CT at higher frequency, which means that the high-order parameters have a significant influence on the value of iso-frequency contours at higher frequency. What is more, the CMS method is used for the validation, the results by CI match the results by CMS well.

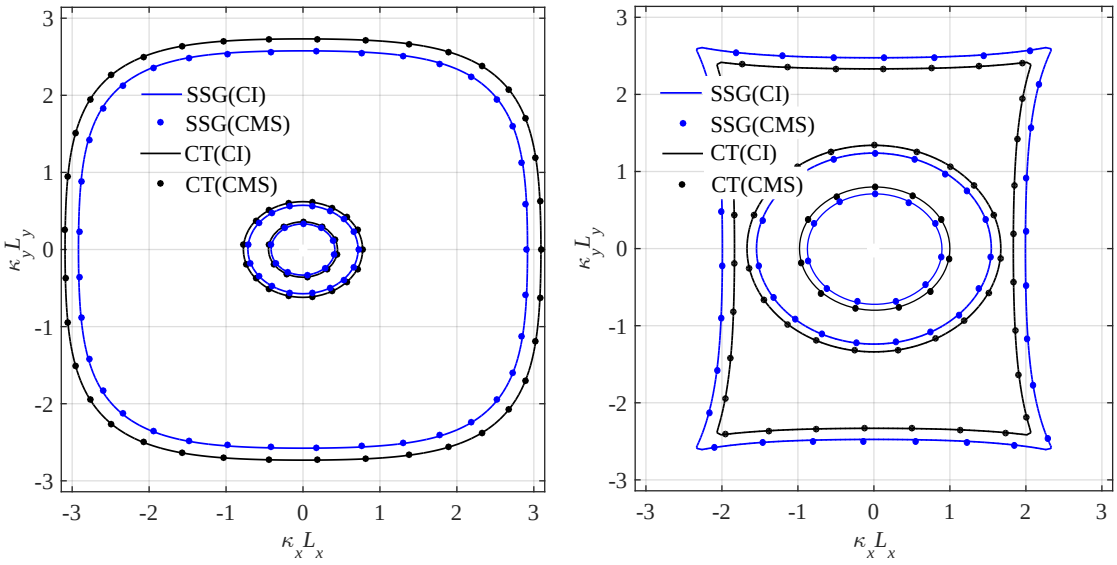

(a) $\omega/\omega_0 = 30$. (b) $\omega/\omega_0 = 65$.

Fig. 5.6. The iso-frequency contours by CT and SSG.

5.2.4.5 Energy flow vector fields

The energy flow vector fields by SSG and CT on the first two slowness surfaces are studied in this part. As shown in Fig. 5.7, the direction of arrow indicates the direction of energy flow and the length of arrow means the gradient value of energy flow. The blue arrow from SSG and black arrow from CT almost overlap, which indicates that the gradient and direction of energy flow by SSG are basically the same as that by CT at the same κ-space position. At low frequency, as shown in Fig. 5.7(a), the dynamic energy spreads in all directions and is perpendicular to the iso-frequency contour. At higher frequency such as 65, as shown in Fig. 5.7(b), in the middle part, the energy spreads outward. But at the edge, the energy spreads to the inside. The distance from any point on the iso-frequency contour to the center point of the figure represents the wave number $\kappa_{\theta'}$ with θ' for plane wave propagation. On the first slowness

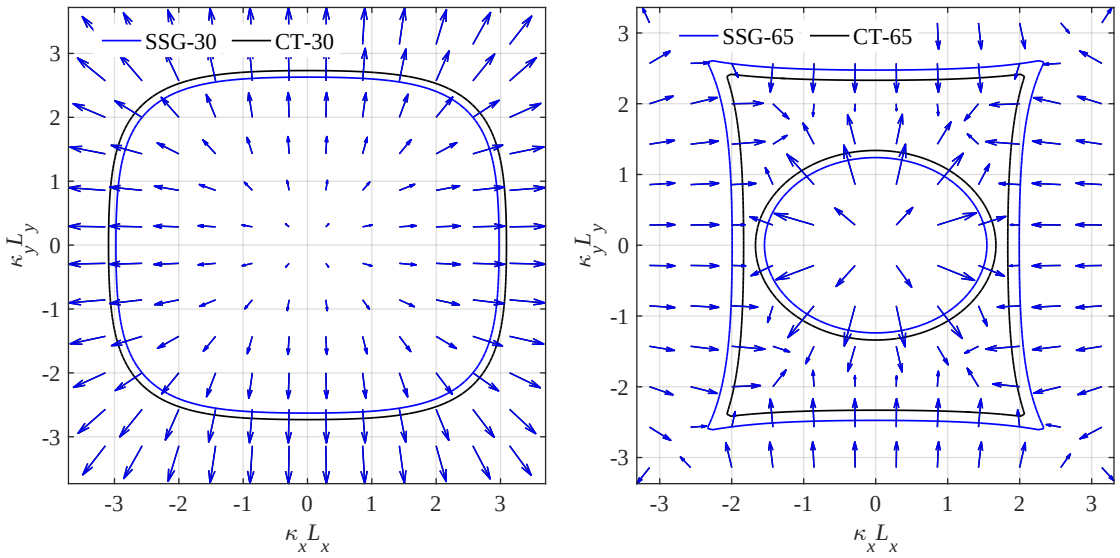

(a) The 1st slowness surface. (b) The 2nd slowness surface.

Fig. 5.7. The energy flow vector fields by CT and SSG.

surface, the position of the iso-frequency contour by SSG is located inside the one by CT, which means that $\kappa_{\theta'}$ by SSG is smaller than the one by CT at same wave propagation angle θ'. On the second slowness surface, whose iso-frequency contour position by SSG is located outside the one by CT at the edge, but inside the one by CT in the middle.

5.2.4.6 Sound transmission analysis

In this part, the transmission loss of the 2D full plate is presented by SSG and CT. Fig. 5.8 shows the oblique incidence TL for plane wave with incidence angles θ^*=45°, ϕ^*=0. At low frequencies, the TL by SSG matches the one by CT. The resonances of the wave modes have a particularly strong influence on the TL. Particularly, the dips around the first three resonances.

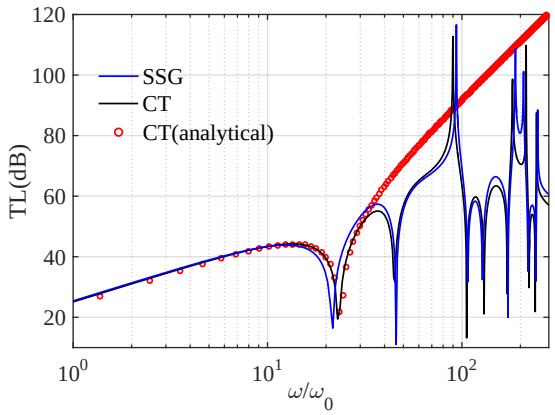

Fig. 5.8. Transmission loss of the 2D full plate ($\theta^* = 45°, \phi^* = 0$).

On the other hand, the first resonance frequency by SSG is smaller than the one by CT. But for other resonance frequencies, the ones by SSG nearly match the ones by CT. In order to valid the result from WFEM CT, a analytical method called Love-Kirchoff theory [232] is used, which shows that the agreement between the analytical and WFEM CT predictions is excellent at low frequency.

5.3 Sensitivity analysis of higher order parameters

The sensitivity analysis is based on the Fourier Amplitude Sensitivity Test (FAST)[233]. FAST is a global sensitivity analysis technology under a variance decomposition which can offer information about sensitivity covering the whole design space and can illustrate interaction effects between input parameters. It is an efficient technique that allows estimation of the "main

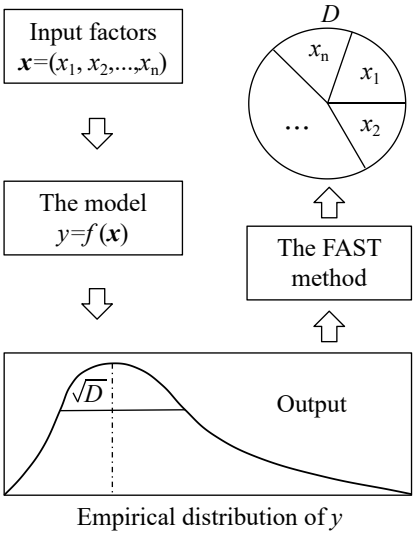

Fig. 5.9. The general scheme of SA method. The total variance of output is apportioned to the various input factors.

effect" (also named first order term) and the so-called "Total Sensitivity Index" (TSI). The general scheme of SA method is presented in Fig. 5.9.

5.3.1 Fourier amplitude sensitivity test formulation

Defining a model as a real valued function f over $K = [0,1]^n$, which can map a vector of input parameters $\mathbf{x} = (x_1, ..., x_n)$ to a scalar output $y = f(\mathbf{x})$. The unique partition of f is expressed as:

$$\begin{aligned} y = f(x_1, x_2, ..., x_n) &= \sum_{U \in [1,n]} f_U(x|_U) \mathrm{d}x|_U \\ &= f_0 + \sum_{i=1}^{n} f_i(x_i) + \sum_{1 \le i < j \le n} f_{ij}(x_i, x_j) + ... + f_{1,...,n}(x_1, ..., x_n), \end{aligned} \tag{5.32}$$

which provides that each function f_U has zero mean over its range of variation $K|_U$, which means the subspace of K spanned by the dimensions contained in subset U. This writes:

$$\int_{K|_U} f_U(x_U)\mathrm{d}x_U = 0. \tag{5.33}$$

The decomposition offered by Eq.5.32 is called the high order model representation (HDMR) [234] or Hoeffding decomposition.

For a given set of indices U=($i_1, ..., i_k$), the partial variance is therefore the variance of f_U:

$$D_U = \int_{K|_U} f_U(x_U)^2\mathrm{d}x_U. \tag{5.34}$$

The sensitivity index, which is represented as the ratio of the variance of the function f_U to the total variance of the model, is relative to the set U :

$$\mathrm{SI}(U) = \frac{D_U}{D}. \tag{5.35}$$

The calculation of all the 2^n sensitivity indices is needed to fully represent the model, which requires long computational time. However, most information of a parameter's influence can be obtained in the first-order sensitivity index and the total sensitivity index, which can be deduced more efficiently with the FAST method.

FAST method can be used to avoid the evaluation of the multidimensional integrals needed to compute the f_i functions by introducing a single 1D integral along a space-filling curve in the design space. This curve is defined to be periodic with different periods relative to each parameter. The sampling function given by [235]:

$$x_i = \frac{1}{2} + \frac{1}{\pi}\arcsin(\sin(\omega_i s + \vartheta_i)). \tag{5.36}$$

The frequencies ω_i are integers chosen to minimize interference between parameters [236]. ϑ_i are chosen real numbers with random in the interval $[0, 2\pi]$. The integer set frequencies $\{\omega_i\}$ is interference free up to order M under the condition of all linear combinations:

$$\sum_{i=1}^{n} v_i\omega_i \neq 0, \tag{5.37}$$

where $v_i \in \mathbb{Z}$ and $\sum_{i=1}^{n} |v_i| < M$, M denotes a parameter at the investigator disposition. Due to all the frequencies are integers, the resulting function shows 2π-periodic characteristics with respect to variable s. Then, a sampling is illustrated by utilizing $N > 2\omega_n + 1$ samples in the $[0, 2\pi]$ interval. The discrete Fourier transform $\hat{y}_k$ can be easily confirmed via the model output $y_k = f(x_k)$ on each sample.

The values of the frequencies ω_i for M=4 and less than 19 parameters have been given by

Table 5.1. Set of integer frequencies ω_i for 14, 15 and 16 parameters with M=4 (n is parameters number).

n	Frequency set
14	{87, 133, 195, 251, 277, 315, 355, 387, 409, 429, 439, 445, 453, 457}
15	{67, 143, 189, 251, 307, 333, 371, 411, 443, 465, 485, 495, 501, 509, 513}
16	{73, 169, 245, 291, 353, 409, 435, 473, 513, 545, 567, 587, 597, 603, 611, 615}

[233] in Tab. 5.1. The total variance of the function in the design space is calculated through Parseval's theorem as:

$$D = \int_K \left(f^2(x) - f_0^2\right) \mathrm{d}x \approx \sum_{k=1}^{N} y_k^2 = \sum_{k=1}^{N} \hat{y}_k^2. \tag{5.38}$$

The sensitivity contribution of parameter i is then approximated by summing the coefficients indexed under the M lowest multiples of ω_i:

$$D_i = \sum_{k=1}^{M} \hat{y}_{k\omega_i}^2. \tag{5.39}$$

The main effect is confirmed as:

$$\mathrm{ME}(i) = \frac{D_i}{D}. \tag{5.40}$$

On the other hand, the total sensitivity index of parameter i is then given as:

$$\mathrm{TSI}(i) = 1 - \frac{D_{\sim i}}{D}, \tag{5.41}$$

where $D_{\sim i}$ is the partial variance relative to all parameters but i.

5.3.2 Numerical applications of sensitivity analysis

Table 5.2. Sampling bounds for inputs.

Input factors	Lower bound	Upper bound	Samples
$a_i (i = 1, ..., 5)$	$-100a_i$	$100a_i$	5000
$b_i (i = 1, ..., 7)$	$-100b_i$	$100b_i$	5000
$c_i (i = 1, ..., 3)$	$-100c_i$	$100c_i$	5000

In this part, the FAST method is used to analysis the sensitivity effects of 15 higher order parameters for the dispersion relation including bending, shearing and tension modes, as shown in Fig.5.2. The sampling bounds for inputs are given in Tab.5.2.

5.3.2.1 Statistics of the output set with inputs for dispersion relation

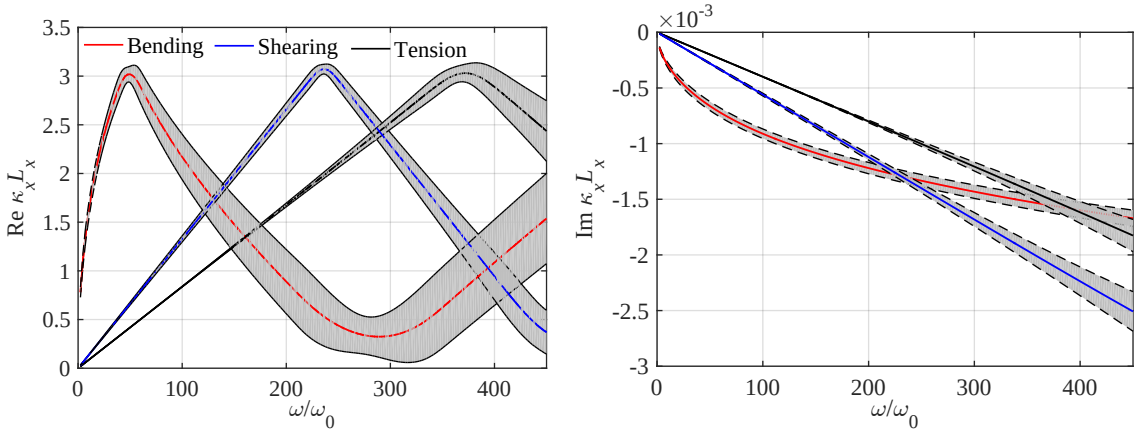

(a) Real part. (b) Imaginary part.

Fig. 5.10. Mean value ± standard deviation.

Firstly, the statistics of the output set with inputs (a_i, b_i, c_i) for dispersion relation (bending, shearing and tension) are discussed. As shown in Fig.5.10, several frequency zones can be identified. For real part of bending wave, mean absorption as well as standard deviations increase steeply up to 50, then decrease till to 280 and increase after 280 again. For real parts of shearing and tension waves, mean absorption and standard deviations increase up to 230 and 370 respectively and then decrease. On the other hand, for all the modes (bending, shearing and tension), as frequency increase, the range between $+$standard deviation and $-$standard deviation increase continuously.The 15 higher order parameters has the greatest impact on bending wave.

Then, the Normalized Standard Deviation (NSD) is shown in Fig.5.11. For real part of

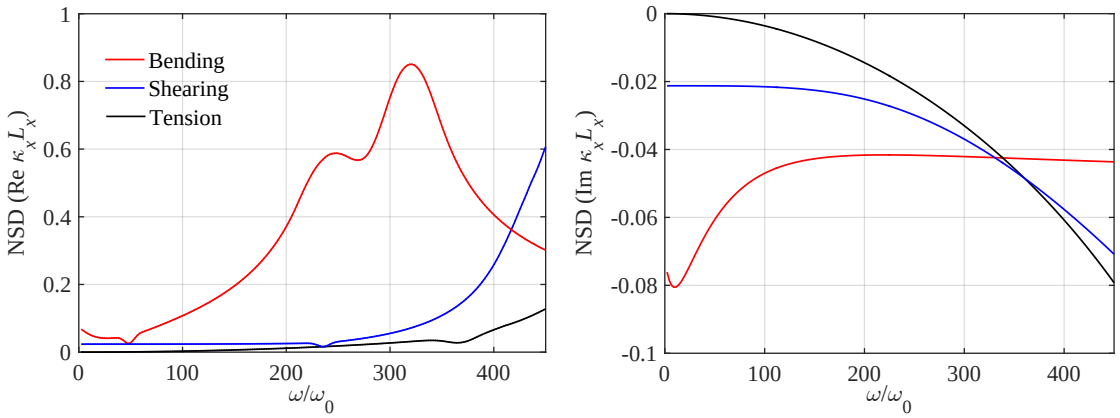

(a) Real part. (b) Imaginary part.

Fig. 5.11. NSD (ratio of standard deviation to mean value).

bending mode, the maximum value of NSD lies between 300 and 350 Hz, with a moderate and

increasing mean value of κ_x. It imposes a focus on sensitivity indexes around 350. However, for real parts of shearing and tension modes, the values of NSD increase with the frequency increase.

5.3.2.2 Sensitivity analysis for dispersion relation

In this part, SA with 15 higher order parameters is discussed. The influence of each input parameter on the result including bending, tension and shearing modes are illustrated.

Bending mode :

Starting with the SA for bending mode firstly. The influences of a_i on the result are shown in

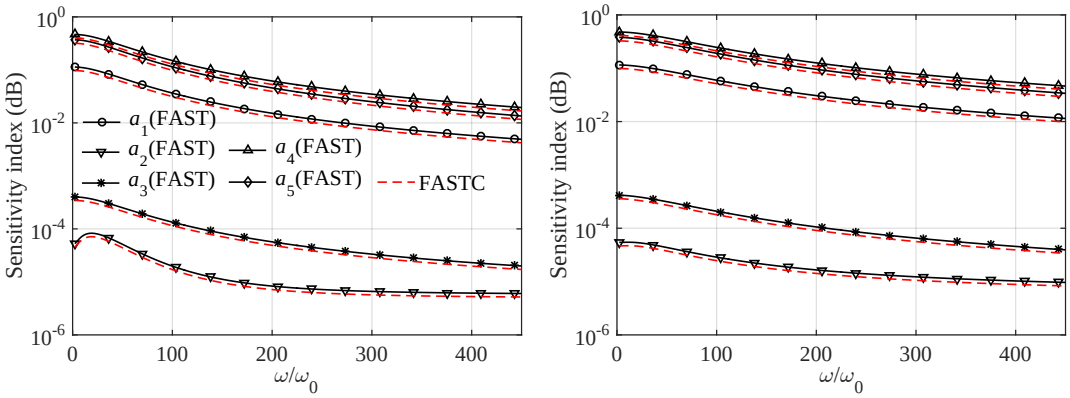

(a) Real part. (b) Imaginary part.

Fig. 5.12. Sensitivity analysis of a_i for bending.

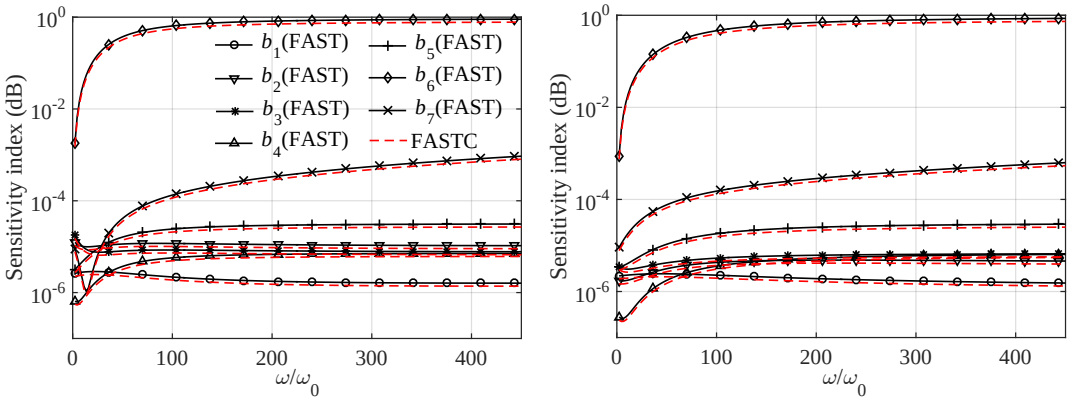

(a) Real part. (b) Imaginary part.

Fig. 5.13. Sensitivity analysis of b_i for bending.

Fig.5.12, the sensitivity index for a_2 increases first and then decreases with frequency increases for the real part. The sensitivity indexes for a_1, a_3, a_4, a_5 decrease with the frequency increases

for both real and imaginary parts. The parameter a_4 has the biggest influence to the result.

The influences of b_i on the result are shown in Fig.5.13, the sensitivity index for b_7 decreases first and then increases with the frequency increases for the real part. The sensitivity indexes for b_1, b_2, b_3, b_4, b_5 and b_6 increase with the frequency increases for both real and imaginary parts. Furthermore, the parameter b_6 has the biggest influence to the result.

The influences of c_i on the result are shown in Fig.5.14, the sensitivity index for c_1 and c_3

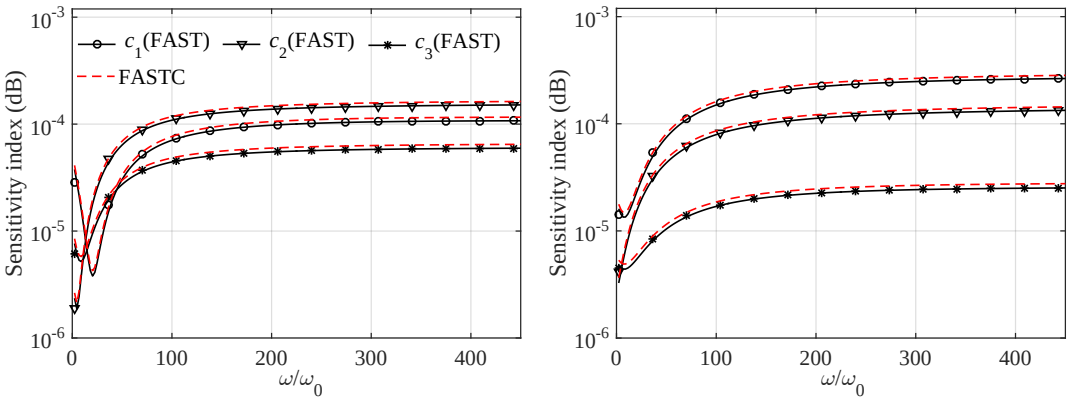

(a) Real part. (b) Imaginary part.

Fig. 5.14. Sensitivity analysis of c_i for bending.

decrease first and then increase with the frequency increases for both real and imaginary parts. The sensitivity index for c_2 increases with the frequency increases for both real and imaginary parts. On the other hand, the parameter c_1 has the biggest influence to the result at low frequency but c_2 has the biggest influence to the result at higher frequency.

Tension mode :

Then, the SA for tension mode is discussed. The influences of a_i on the result are shown

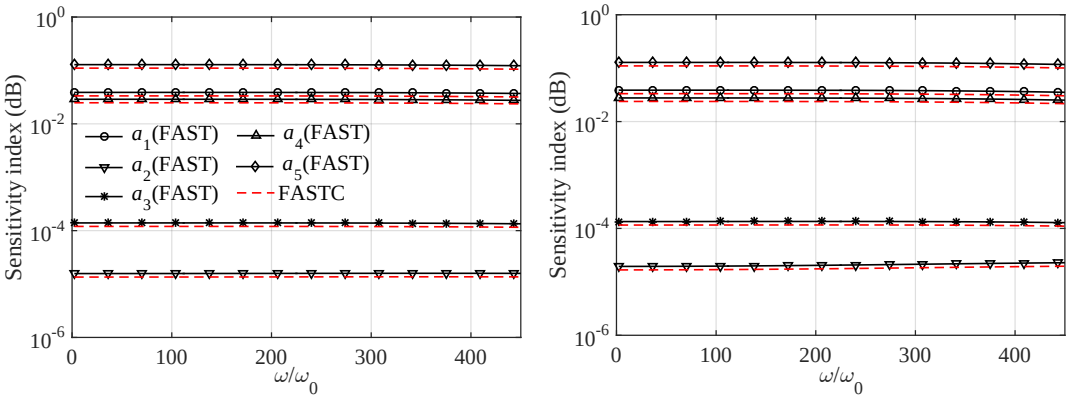

(a) Real part. (b) Imaginary part.

Fig. 5.15. Sensitivity analysis of a_i for tension.

in Fig.5.15, the sensitivity index for each a_i nearly keep a constant value with the frequency increases for both real and imaginary parts, which indicates that the effect each a_i on the result is continuous. On the other hand, the parameter a_5 has the biggest influence to the result.

The influences of b_i on the result are shown in Fig.5.16, the sensitivity indexes for b_6 and b_7

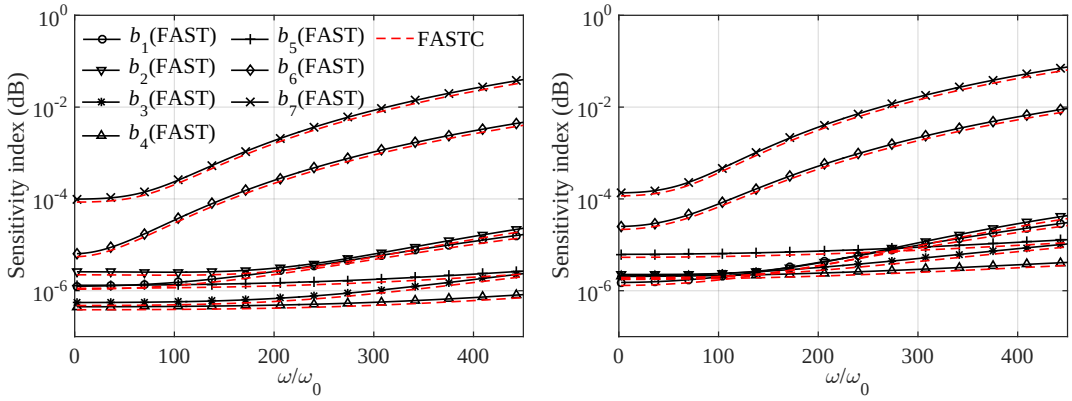

(a) Real part. (b) Imaginary part.

Fig. 5.16. Sensitivity analysis of b_i for tension.

increase with the frequency increases for the real and imaginary parts. The sensitivity indexes for b_1, b_2, b_3, b_4 and b_5 stay the same first and then increase with the frequency increases for both real and imaginary parts. Furthermore, the parameter b_7 has the biggest influence to the result.

The influences of c_i on the result are shown in Fig.5.17, the sensitivity indexes for c_1, c_2

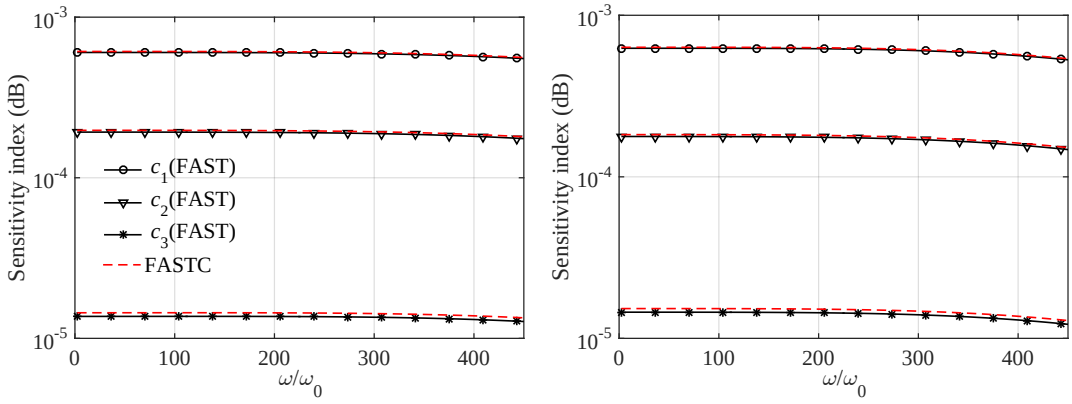

(a) Real part. (b) Imaginary part.

Fig. 5.17. Sensitivity analysis of c_i for tension.

and c_3 decrease with the frequency increases for both real and imaginary parts. However, the reduction is very slow. On the other hand, the parameter c_1 has the biggest influence to the result.

Shearing mode :

Last, the SA for shearing mode is presented. The influences of a_i on the result are addressed

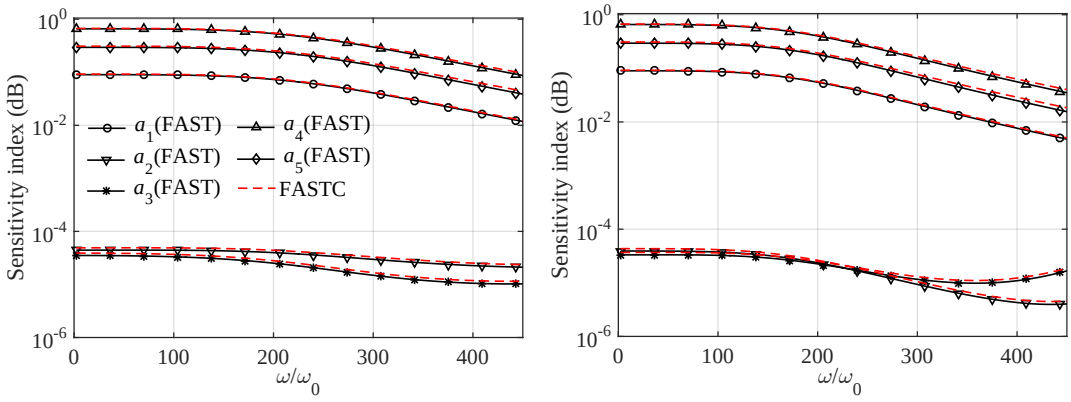

(a) Real part. (b) Imaginary part.

Fig. 5.18. Sensitivity analysis of a_i for shearing.

in Fig.5.18, the sensitivity index for each a_i decrease with the frequency increases for real part. But the influence of a_3 on the result decreases first and then increases for the imaginary part. On the other hand, the parameter a_4 has the biggest influence to the result.

The influences of b_i on the result are shown in Fig.5.19, the sensitivity indexes for b_6 and

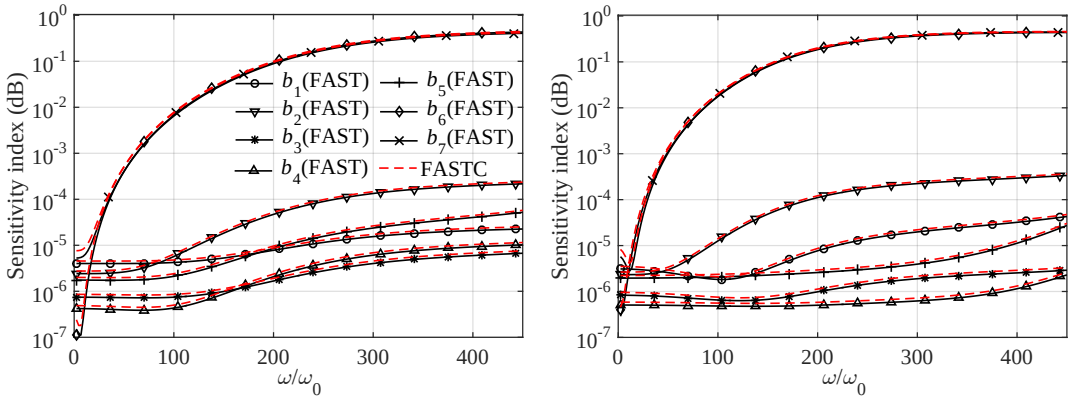

(a) Real part. (b) Imaginary part.

Fig. 5.19. Sensitivity analysis of b_i for shearing.

b_7 increase with the frequency increases for the real and imaginary parts. On the other hand, the sensitivity indexes for b_1, b_2, b_3, b_4 and b_5 keep the same at low frequency and then increase at high frequency for both real and imaginary parts. Furthermore, the parameter b_6 and b_7 have the biggest influences to the result.

The influences of c_i on the result are shown in Fig.5.20, the sensitivity index for c_1, c_2 and c_3 increase with the frequency increases for both real part. However, the sensitivity indexes for

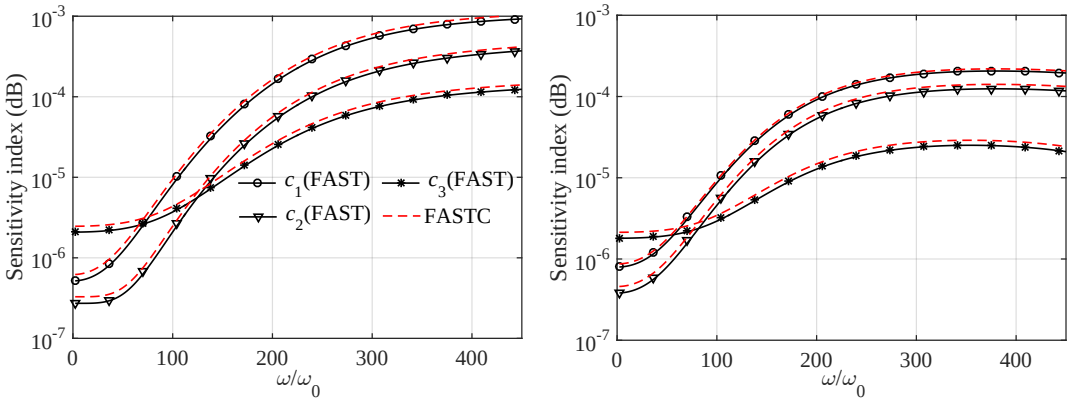

(a) Real part. (b) Imaginary part.

Fig. 5.20. Sensitivity analysis of c_i for shearing.

c_1, c_2 and c_3 increase first and then decline slowly with the frequency increase. On the other hand, the parameter c_3 has the biggest influence to the result at low frequency but parameter c_1 has the biggest influence to the result at high frequency. In order to valid the results from FAST, a method called Fourier Amplitude Sensitivity Test with Correlation (FASTC) [237] is used for bending, shearing and tension modes. As we can see, the results from FAST match the ones from FASTC well.

5.4 Conclusions

In this chapter, SSG theory is used for the exploration of 2D waves in a 2D full plate within the WFEM framework. Some conclusions in our work are addressed as follow:

(i) 2D wave propagation are analyzed including direct and inverse forms. Two different situations are discussed to solve the direct form of WFEM2D. The first one is wave propagation angle θ'=0, the second one is wave propagation angle $\theta' \neq$0. In order to study the second situation, a solution strategy based on the CI method is introduced to solve the NEP within the WFEM2D framework. What is more, the transmission of sound through a 2D full plate is introduced by SSG theory.

(ii) The dispersion relation of a unit cell is calculated by WFEM2D direct form and CI method, and the band structure is introduced based on WFEM2D inverse form. The curve by SSG is close to the one by CT at low frequency. But the difference between SSG and CT becomes more obvious as frequency increases. The result by WFEM2D inverse form matches CMS and WFEM2D direct form well.

(iii) The dispersion relation by CI method under different wave propagation angles are discussed. The first three slowness surfaces in the first quadrant are presented. The iso-frequency contours are illustrated through CI method. Then, energy flow vector fields by SSG and CT on the first two slowness surfaces are studied which shows that the dynamic energy spreads in all directions and is perpendicular to the iso-frequency contour at low frequency. however, at higher frequency, the energy spreads outward in the middle part but spreads to the inside at the edge.

(iv) The SA based on the FAST is introduced. The statistics of the output set with inputs (a_i, b_i, c_i) for dispersion relation (bending, shearing and tension) are discussed. As the frequency increase, the range between $+$standard deviation and $-$standard deviation increase continuously. The 15 higher order parameters have the greatest impact on bending wave. The NSD is illustrated. Furthermore, SA for dispersion relation is introduced.

Chapter 6

Conclusions and perspectives

Chapter contents

6.1 Conclusions 119
6.2 Perspectives 120

6.1 Conclusions

The main findings and contributions of the conducted work are summarized below:

(i) Chapter 1 presents the results of the conducted literature survey. The survey concerns the review of previous researches on periodic structure, of existing methods on the studying of micro-sized medias. The existing methods for studying micro-sized structures including continuum model and LSM are introduced. What is more, the plane wave expansion, modified TMM, WFEM, homogenization methods and MOR method are discussed for the research of periodic structures.

(ii) Chapter 2 provides a method which combines SSG theory with WFEM to analyse the dynamic behavior of 1D micro-sized structures. A continuum model for Euler-Bernoulli bending beam and torsional bar by SSG are introduced. The strong forms including governing equations and boundary conditions are illustrated by applying the variation method. The LSM of a micro-sized Euler-Bernoulli bending beam and torsional bar are discussed. After Fourier series transforming, the continuous governing equations of motion are determined and the variational, or weak, formulations are then calculated. The dispersion relations and forced responses for bending and torsion in micro-sized structures are calculated by SSG.

(iii) Chapter 3 illustrates the dynamical behaviors of a 2D beam grid within the WFEM framework. The analysis is restricted to out-of plane vibration including bending and torsion. The weak formulas of an element are illustrated and the global dynamic stiffness matrix of a unit cell is assembled. WFEM inverse form for 2D periodic systems is introduced. Dynamic behaviors of the beam grid such as band structure, slowness surfaces, energy flow vector fields and wave beaming effects are discussed.

(iv) Chapter 4 investigates the dynamical behaviors of a 3D slender beam. The constitutive relations of 3D micro-sized model are introduced in the SSG theory framework and the weak formulations including element stiffness, mass matrices and force vector are calculated. Afterwards, free wave propagation characteristics are expressed by solving eigenvalue problems in the direct WFEM framework, diffusion matrix for a simple coupling condition and a complex coupling condition are confirmed. Wave dispersion and diffusion, effects of higher order parameters and forced response are introduced.

(v) Chapter 5 predicts the wave propagation characteristics in a micro-sized 2D full plate under SSG theory. An eigenvalue solving approach called CI method is applied to illustrate the NEP and conform the band structure and iso-frequency contours. SA is introduced for this 2D full plate to investigate the effects of higher order parameters on the dispersion relation.

6.2 Perspectives

Micro-sized periodic structures have been studied widely. WFEM based on SSG theory is an available method which offers a range of applications over different kinds of micro-sized periodic structures. The author attempts to foresee some probable perspective works as follows:

(i) Some researchers [42] defined the higher order parameters a_i, b_i and c_i emerging in SSG theory for face centered cubic (fcc) materials by the Sutton-Chen potential atom method. It should be pointed out that there is no mature experimental method to determine the higher order parameters. So, the use of experimental methods to obtain the physical meaning of these higher-order parameters is of great value for a better understanding of SSG theory.

(ii) LSM theory [95] is a valuable approach to interpret the dynamic characteristics for micro-sized medias. One of its applications is the investigation of wave propagation within linear strain-gradient elasticity for 1D lattice structures. The continuum equation of motion with derivatives can be determined by long-range interactions in LSM. The LSM formed by nearest, next-nearest and next-next-nearest interactions between different mass nodes can be used to describe the SSG theory whose continuum equation of motion contains two higher order term

for 1D longitudinal or bending model. But for the 2D or 3D lattice structures, confirming the LSM formed by nearest, next-nearest and next-next-nearest interactions between different mass nodes is a new research topic.

(iii) On the other hand, the governing equation can be deduced for the LSM. But it is difficult to obtain the analytical solution of boundary conditions for LSM. For instance, a new "non-local" LSM are expounded in Chapter 2, giving unified description of the SSG models for bending and torsion. The governing equations for bending and torsion are illustrated using Fourier series. However, there is still no effective way to establish boundary conditions.

(iv) WFEM is based on the spectral study of a single unit cell to reflect the dynamic characteristics of the entire periodic structure [238]. The resulting mass and stiffness matrices are post-processed to establish the dynamic stiffness matrix of the unit cell. The advantage of WFEM is modeling a unit cell by the conventional finite elements, which thus complex geometries or several materials can be involved. What is more, the wave propagation of whole structure can be evaluated by analyzing a single unit cell. The size of numerical problem that related directly to the number of DOFs will be reduced, thus computational time will be saved. But for a unit cell based on SSG theory, take a 3D model as an example, the DOFs on each node is 27, which is much more than the one based on CT with only 3 DOFs on each node. Therefore, the computing time based on the SSG theory is long. How to effectively reduce computing costs will be the next step of my research.

(v) Due to the unavoidable existence of damping in the structure, it is important to investigate the damping effect in periodic structures in the further. In my work, the effect of damping is identified as damping lose factor η which is caused by internal friction within the material or at the joints. It is of simple treatment and also seems to be more closely related to the problem cases treated in this work. But for the viscous damping or other linear damping models, the effect of damping could be considered by means of the damping matrix $\mathbf{C}$. What is more, the higher order parameters, which reflect the non-local behavior of micro-sized structures, should also be considered in the damping matrix in the SSG theory framework.

(vi) In Chapter 5, SSG theory is applied for a 2D full plate within WFEM2D framework. An eigenvalue solving approach called CI method is applied to illustrate the NEP and conformed the band structure and iso-frequency contours. However, using CI method to solve NEP requires a lot of computational time.

Appendix A

Expressions of the coefficients A, B and C in Eq.1.68

$$\mathbf{A}_{11} = \mathbb{D}_{12} + \mathbb{D}_{34} + \mathbb{D}_{32}\lambda_y^{-1} + \mathbb{D}_{14}\lambda_y \tag{A.1}$$

$$\mathbf{A}_{1\mathrm{L}} = \mathbb{D}_{1\mathrm{R}} + \mathbb{D}_{3\mathrm{R}}\lambda_y^{-1} \tag{A.2}$$

$$\mathbf{A}_{1\mathrm{B}} = \mathbf{0} \tag{A.3}$$

$$\mathbf{A}_{\mathrm{L}1} = \mathbb{D}_{\mathrm{L}2} + \mathbb{D}_{\mathrm{L}4}\lambda_y \tag{A.4}$$

$$\mathbf{A}_{\mathrm{LL}} = \mathbf{A}_{\mathrm{LR}} \tag{A.5}$$

$$\mathbf{A}_{\mathrm{LB}} = \mathbf{0} \tag{A.6}$$

$$\mathbf{A}_{\mathrm{B}1} = \mathbb{D}_{\mathrm{B}2} + \mathbb{D}_{\mathrm{T}4} + \mathbb{D}_{\mathrm{T}2}\lambda_y^{-1} + \mathbb{D}_{\mathrm{B}4}\lambda_y \tag{A.7}$$

$$\mathbf{A}_{\mathrm{BL}} = \mathbb{D}_{\mathrm{BR}} + \mathbb{D}_{\mathrm{TR}}\lambda_y^{-1} \tag{A.8}$$

$$\mathbf{A}_{\mathrm{BB}} = \mathbf{0} \tag{A.9}$$

$$\mathbf{B}_{11} = \mathbb{D}_{11} + \mathbb{D}_{22} + \mathbb{D}_{33} + \mathbb{D}_{44} + (\mathbb{D}_{31} + \mathbb{D}_{42})\lambda_y^{-1} + (\mathbb{D}_{13} + \mathbb{D}_{24})\lambda_y \tag{A.10}$$

$$\mathbf{B}_{1\mathrm{L}} = \mathbb{D}_{1\mathrm{L}} + \mathbb{D}_{2\mathrm{R}} + (\mathbb{D}_{3\mathrm{L}} + \mathbb{D}_{4\mathrm{R}})\lambda_y^{-1} \tag{A.11}$$

$$\mathbf{B}_{1\mathrm{B}} = \mathbb{D}_{1\mathrm{B}} + \mathbb{D}_{3\mathrm{T}} + \mathbb{D}_{3\mathrm{B}}\lambda_y^{-1} + \mathbb{D}_{1\mathrm{T}}\lambda_y \tag{A.12}$$

$$\mathbf{B}_{\mathrm{L}1} = \mathbb{D}_{\mathrm{L}1} + \mathbb{D}_{\mathrm{R}2} + \mathbb{D}_{\mathrm{L}3}\lambda_y^{-1} + \mathbb{D}_{\mathrm{R}4}\lambda_y \tag{A.13}$$

$$\mathbf{B}_{\mathrm{LL}} = \mathbb{D}_{\mathrm{LL}} + \mathbb{D}_{\mathrm{RR}} \tag{A.14}$$

$$\mathbf{B}_{\mathrm{LB}} = \mathbb{D}_{\mathrm{LB}} + \mathbb{D}_{\mathrm{LT}}\lambda_y \tag{A.15}$$

$$\mathbf{B}_{\mathrm{B}1} = \mathbb{D}_{\mathrm{B}1} + \mathbb{D}_{\mathrm{T}3} + \mathbb{D}_{\mathrm{T}1}\lambda_y^{-1} + \mathbb{D}_{\mathrm{B}3}\lambda_y \tag{A.16}$$

$$\mathbf{B}_{\mathrm{BL}} = \mathbb{D}_{\mathrm{BL}} + \mathbb{D}_{\mathrm{TL}}\lambda_y^{-1} \tag{A.17}$$

$$\mathbf{B}_{\mathrm{BB}} = \mathbb{D}_{\mathrm{BB}} + \mathbb{D}_{\mathrm{TT}} + \mathbb{D}_{\mathrm{TB}}\lambda_y^{-1} + \mathbb{D}_{\mathrm{BT}}\lambda_y \tag{A.18}$$

$$\mathbf{C}_{11} = \mathbb{D}_{21} + \mathbb{D}_{43} + \mathbb{D}_{41}\lambda_y^{-1} + \mathbb{D}_{23}\lambda_y \tag{A.19}$$

$$\mathbf{C}_{1\mathrm{L}} = \mathbb{D}_{2\mathrm{L}} + \mathbb{D}_{4\mathrm{L}}\lambda_y^{-1} \tag{A.20}$$

$$\mathbf{C}_{1\mathrm{B}} = \mathbb{D}_{2\mathrm{B}} + \mathbb{D}_{4\mathrm{T}} + \mathbb{D}_{4\mathrm{B}}\lambda_y^{-1} + \mathbb{D}_{2\mathrm{T}}\lambda_y \tag{A.21}$$

$$\mathbf{C}_{\mathrm{L}1} = \mathbb{D}_{\mathrm{R}1} + \mathbb{D}_{\mathrm{R}3}\lambda_y \tag{A.22}$$

$$\mathbf{C}_{\mathrm{LL}} = \mathbb{D}_{\mathrm{RL}} \tag{A.23}$$

$$\mathbf{C}_{\mathrm{LB}} = \mathbb{D}_{\mathrm{RB}} + \mathbb{D}_{\mathrm{RT}}\lambda_y \tag{A.24}$$

$$\mathbf{C}_{\mathrm{B}1} = \mathbf{0} \tag{A.25}$$

$$\mathbf{C}_{\mathrm{BL}} = \mathbf{0} \tag{A.26}$$

$$\mathbf{C}_{\mathrm{BB}} = \mathbf{0} \tag{A.27}$$

Appendix B

Transform the bending LSM to continuum model

The lattice function of motion on node n will be derived by submitting Eq. 2.16 and Eq. 2.18 into Eq. 2.17 as:

$$\begin{aligned}
&\frac{k_1^b}{d^3}\left(w_{n-2}-4w_{n-1}+6w_n-4w_{n+1}+w_{n+2}\right)\\
&+\frac{k_2^b}{(2d)^3}\left(w_{n-4}-4w_{n-2}+6w_n-4w_{n+2}+w_{n+4}\right)\\
&+\frac{k_3^b}{(3d)^3}\left(w_{n-6}-4w_{n-3}+6w_n-4w_{n+3}+w_{n+6}\right)\\
&-f_n=M\frac{\mathrm{d}^2w_n(t)}{\mathrm{d}t^2}.
\end{aligned} \tag{B.1}$$

Multiplying Eq. (B.1) by $e^{-i\kappa nd}$, and n changes from $-\infty$ to $+\infty$. Afterwards, Eq. (B.1) can be expressed as:

$$\begin{aligned}
&\frac{k_1^b}{d^3}\sum_{n=-\infty}^{+\infty}e^{-i\kappa nd}\left(w_{n-2}-4w_{n-1}+6w_n-4w_{n+1}+w_{n+2}\right)\\
&+\frac{k_2^b}{(2d)^3}\sum_{n=-\infty}^{+\infty}e^{-i\kappa nd}\left(w_{n-4}-4w_{n-2}+6w_n-4w_{n+2}+w_{n+4}\right)\\
&+\frac{k_3^b}{(3d)^3}\sum_{n=-\infty}^{+\infty}e^{-i\kappa nd}\left(w_{n-6}-4w_{n-3}+6w_n-4w_{n+3}+w_{n+6}\right)\\
&-\sum_{n=-\infty}^{+\infty}e^{-i\kappa nd}f_n\\
=&M\sum_{n=-\infty}^{+\infty}e^{-i\kappa nd}\frac{\mathrm{d}^2w_n(t)}{\mathrm{d}t^2}.
\end{aligned} \tag{B.2}$$

Then, the first three parts in the left side of the equation above are presented as:

$$\begin{aligned}
&\frac{k_1^b}{d^3}\Bigg[e^{-2i\kappa d}\sum_{m=-\infty}^{+\infty}e^{-i\kappa md}w_m-4e^{-i\kappa d}\sum_{j=-\infty}^{+\infty}e^{-i\kappa jd}w_j+6\sum_{n=-\infty}^{+\infty}e^{-i\kappa nd}w_n-4e^{i\kappa d}\sum_{p=-\infty}^{+\infty}e^{-i\kappa pd}w_p\\
&+e^{2i\kappa d}\sum_{q=-\infty}^{+\infty}e^{-i\kappa qd}w_q\Bigg]+\frac{k_1^b}{(2d)^3}\Bigg[e^{-4i\kappa d}\sum_{m=-\infty}^{+\infty}e^{-i\kappa md}w_m-4e^{-2i\kappa d}\sum_{j=-\infty}^{+\infty}e^{-i\kappa jd}w_j+6\sum_{n=-\infty}^{+\infty}e^{-i\kappa nd}w_n\\
&-4e^{2i\kappa d}\sum_{p=-\infty}^{+\infty}e^{-i\kappa pd}w_p+e^{4i\kappa d}\sum_{q=-\infty}^{+\infty}e^{-i\kappa qd}w_q\Bigg]+\frac{k_1^b}{(3d)^3}\Bigg[e^{-6i\kappa d}\sum_{m=-\infty}^{+\infty}e^{-i\kappa md}w_m\\
&-4e^{-3i\kappa d}\sum_{j=-\infty}^{+\infty}e^{-i\kappa jd}w_j+6\sum_{n=-\infty}^{+\infty}e^{-i\kappa nd}w_n-4e^{3i\kappa d}\sum_{p=-\infty}^{+\infty}e^{-i\kappa pd}w_p+e^{6i\kappa d}\sum_{q=-\infty}^{+\infty}e^{-i\kappa qd}w_q\Bigg].
\end{aligned}\tag{B.3}$$

The definition in Eq. (2.20) is used here, and Eq. (B.3) can be shown as:

$$\begin{aligned}
&\frac{4k_1^b}{d^3}\left[-2\sin^2\left(\frac{\kappa d}{2}\right)\right]^2\hat{w}(\kappa,t)+\frac{4k_2^b}{(2d)^3}\left[-8\sin^2\left(\frac{\kappa d}{2}\right)+8\sin^4\left(\frac{\kappa d}{2}\right)\right]^2\hat{w}(\kappa,t)\\
&+\frac{4k_3^b}{(3d)^3}\left[-18\sin^2\left(\frac{\kappa d}{2}\right)+48\sin^4\left(\frac{\kappa d}{2}\right)-32\sin^6\left(\frac{\kappa d}{2}\right)\right]^2\hat{w}(\kappa,t).
\end{aligned}\tag{B.4}$$

Next, step 2 in Eq. (2.21) is utilized in sine function form at the point 0. Submitting Eq. (B.4) into Eq. (B.2), one arrives:

$$\begin{aligned}
&L_4^b\kappa^4\tilde{w}(\kappa,t)-L_6^b\kappa^6\tilde{w}(\kappa,t)+L_8^b\kappa^8\tilde{w}(\kappa,t)-o(L_j^b\kappa^j\tilde{w}(\kappa,t))-\mathcal{F}\left(\overline{f}(x,t)\right)\\
=&\rho A\frac{\partial^2\tilde{w}(\kappa,t)}{\partial t^2},(j=10,12,...),
\end{aligned}\tag{B.5}$$

where L_4^b, L_6^b, L_8^b, L_j^b are expressed in Chapter 2. Eq. (B.5) will be re-expressed based on step 3 in Eq. (2.22):

$$\begin{aligned}
&L_4^b\mathcal{F}^{-1}(\kappa^4\tilde{w}(\kappa,t))-L_6^b\mathcal{F}^{-1}(\kappa^6\tilde{w}(\kappa,t))+L_8^b\mathcal{F}^{-1}(\kappa^8\tilde{w}(\kappa,t))-o\left(L_j^b\mathfrak{F}^{-1}(\kappa^j\tilde{w}(\kappa,t))\right)\\
&-\overline{f}(x,t)=\rho A\frac{\partial^2\mathcal{F}^{-1}(\tilde{w}(\kappa,t))}{\partial t^2},
\end{aligned}\tag{B.6}$$

in which: $\mathcal{F}^{-1}(\kappa^4\tilde{w}(\kappa,t))=\frac{\partial^4w(x,t)}{\partial x^4}$, $\mathcal{F}^{-1}(\kappa^6\tilde{w}(\kappa,t))=-\frac{\partial^6w(x,t)}{\partial x^6}$, $\mathcal{F}^{-1}(\kappa^8\tilde{w}(\kappa,t))=\frac{\partial^8w(x,t)}{\partial x^8}$. Finally, the dynamic continuum function $w(x,t)$ will be written as:

$$L_4^b\frac{\partial^4w(x,t)}{\partial x^4}+L_6^b\frac{\partial^6w(x,t)}{\partial x^6}+L_8^b\frac{\partial^8w(x,t)}{\partial x^8}+o\left(L_i^b\frac{\partial^jw(x,t)}{\partial x^j}\right)-\overline{f}(x,t)=\rho A\frac{\partial^2w(x,t)}{\partial t^2}.\tag{B.7}$$

Appendix C

Governing equation and associated boundary conditions of a torsional bar by SSG theory

Based on Eq. 2.27 and Eq. 2.28, $\overline{\mathcal{U}}$ (the strain energy density) of a torsional bar by SSG theory is expressed as:

$$\begin{aligned}\overline{\mathcal{U}} =&\mu(\varepsilon_{21}^2+\varepsilon_{12}^2+\varepsilon_{13}^2+\varepsilon_{31}^2)+a_3(\xi_{112}^2+\xi_{113}^2)+a_4(\xi_{112}^2+\xi_{113}^2+\xi_{123}^2+\xi_{213}^2+\xi_{132}^2\\&+\xi_{312}^2)+a_5\xi_{213}\xi_{312}+b_4\zeta_{1132}\zeta_{1123}+b_5(\zeta_{1132}^2+\zeta_{1123}^2+\zeta_{1112}^2+\zeta_{1113}^2)+b_6(\zeta_{3112}^2\\&+\zeta_{1312}^2+\zeta_{1132}^2+\zeta_{2113}^2+\zeta_{1213}^2+\zeta_{1123}^2+\zeta_{1112}^2+\zeta_{1113}^2)+b_7(\zeta_{3112}\zeta_{1123}+\zeta_{2113}\zeta_{1132})\\&+c_3(\varepsilon_{12}\zeta_{1112}+\varepsilon_{13}\zeta_{1113}).\end{aligned} \tag{C.1}$$

Integrating strain energy density over its volume, the strain energy of the bar will be calculated as:

$$\mathcal{U}=\int_0^L\int_A\overline{\mathcal{U}}\mathrm{d}A\mathrm{d}x^{'}. \tag{C.2}$$

By substitution of Eq. 2.28 and Eq. C.1 into Eq. C.2, the strain energy of the torsional bar by SSG theory is expressed as:

$$\begin{aligned}\mathcal{U}=&\frac{1}{2}\int_0^L\left[C_1^t\left(\frac{\partial\varphi(x,t)}{\partial x}\right)^2+C_2^t\left(\frac{\partial^2\varphi(x,t)}{\partial x^2}\right)^2+C_3^t\left(\frac{\partial^3\varphi(x,t)}{\partial x^3}\right)^2\right.\\&\left.+C_4^t\frac{\partial\varphi(x,t)}{\partial x}\frac{\partial^3\varphi(x,t)}{\partial x^3}\right]\mathrm{d}x,\end{aligned} \tag{C.3}$$

where $C_1^t=GJ+2A(4a_4-a_5)$, $C_2^t=J(a_3+a_4)/2-2A(b_4+2b_5-6b_6+2b_7)$, $C_3^t=2J(b_5+b_6)$, $C_4^t=Jc_3$, J means torsion of inertia within plane $y0z$.

The kinetic energy of the bar is presented as:

$$\mathcal{T} = \frac{1}{2}\int_0^L \rho J \left(\frac{\partial \varphi(x,t)}{\partial t}\right)^2 \mathrm{d}x. \tag{C.4}$$

The work done by external classical force and higher-order forces, W, can be established in the variation form as:

$$\delta\mathcal{W} = \int_0^L \overline{\Gamma}(x,t)\delta\varphi \mathrm{d}x + \Gamma_0 \delta\varphi(x,t)|_{x=0}^{L} + \Gamma_1 \delta\left(\frac{\partial \varphi(x,t)}{\partial x}\right)\Big|_{x=0}^{L} + \Gamma_2 \delta\left(\frac{\partial^2 \varphi(x,t)}{\partial x}\right)\Big|_{x=0}^{L}, \tag{C.5}$$

where $\overline{\Gamma}(x,t)$ means the distributed torque within plane $y0z$, Γ_0 denotes the classical torque, $\Gamma_{1,2}$ are higher-order end-sectional torques of the micro-bar.

In this step, the Hamilton principle is used to calculate the strong forms of the bar for SSG theory as follows:

$$\int_{t_1}^{t_2} (\delta\mathcal{U} - \delta\mathcal{W} - \delta\mathcal{T})\mathrm{d}t = 0, \tag{C.6}$$

where $\delta\mathcal{U}$ and $\delta\mathcal{T}$ are the variation form of strain energy and kinetic energy, respectively. Then doing mathematical calculations according to the variation method by substituting equations Eq. C.3, Eq. C.4, and Eq. C.5 into Eq. C.6, one arrives at:

$$C_1^t \frac{\partial^2 \varphi(x,t)}{\partial x^2} + (C_4^t - C_2^t)\frac{\partial^4 \varphi(x,t)}{\partial x^4} + C_3^t \frac{\partial^6 \varphi(x,t)}{\partial x^6} - \overline{\Gamma}(x,t) = \rho J \frac{\partial^2 \varphi(x,t)}{\partial t^2}. \tag{C.7}$$

Additionally, the associated boundary conditions for a torsional bar written as:

$$\begin{aligned}
&C_1^t \frac{\partial \varphi(x,t)}{\partial x} + (C_4^t - C_2^x)\frac{\partial^3 \varphi(x,t)}{\partial x^3} + C_3^t \frac{\partial^5 \varphi(x,t)}{\partial x^5} = \Gamma_0 \text{ or } \delta\varphi(x,t) = 0, \text{ on } \Omega = \{0, L\}; \\
&(C_2^t - \frac{1}{2}C_4^t)\frac{\partial^2 \varphi(x,t)}{\partial x^2} + C_3^t \frac{\partial^4 \varphi(x,t)}{\partial x^4} = \Gamma_1 \text{ or } \delta\frac{\partial \varphi(x,t)}{\partial x} = 0, \text{ on } \partial\Omega; \\
&\frac{1}{2}C_4^t \frac{\partial \varphi(x,t)}{\partial x} + C_3^t \frac{\partial^3 \varphi(x,t)}{\partial x^3} = \Gamma_2 \text{ or } \delta\frac{\partial^2 \varphi(x,t)}{\partial x^2} = 0, \text{ on } \partial\Omega.
\end{aligned} \tag{C.8}$$

Appendix D

LSM vibration analysis for torsion

The torsional lattice function of motion $\varphi_n(t)$ on node n is expressed as:

$$k_1^t(\varphi_{n-1}-2\varphi_n+\varphi_{n+1})+k_2^t(\varphi_{n-2}-2\varphi_n+\varphi_{n+2})+k_3^t(\varphi_{n-3}-2\varphi_n-\varphi_{n+3})-\Gamma_n=\frac{MJ}{A}\frac{\mathrm{d}^2\varphi_n(t)}{\mathrm{d}t^2}. \tag{D.1}$$

In order to obtain the dynamic continuum function $\varphi(x,t)$, the same method is used as shown in Appendix in B. Multiplying Eq. (D.1) by $e^{-i\kappa nd}$ with n from $-\infty$ to $+\infty$, Eq. (D.1) will be expressed as:

$$\begin{aligned}&k_1^t\sum_{n=-\infty}^{+\infty}e^{-i\kappa nd}(\varphi_{n-1}-2\varphi_n+\varphi_{n+1})+k_2^t\sum_{n=-\infty}^{+\infty}e^{-i\kappa nd}(\varphi_{n-2}-2\varphi_n+\varphi_{n+2})\\&+k_3^t\sum_{n=-\infty}^{+\infty}e^{-i\kappa nd}(\varphi_{n-3}-2\varphi_n+\varphi_{n+3})-\sum_{n=-\infty}^{+\infty}e^{-i\kappa nd}\Gamma_n=\frac{MJ}{A}\sum_{n=-\infty}^{+\infty}e^{-i\kappa nd}\frac{\mathrm{d}^2\varphi_n(t)}{\mathrm{d}t^2}.\end{aligned} \tag{D.2}$$

Employing the same mathematical calculations and Fourier series transform approach as explained in Appendix B: (1) Defining an assumption that $\varphi_n(t)$ is the Fourier constant of $\widehat{\varphi}(\kappa,t)$, (2) The expansion of Taylor series is used based on the limitation of $d\to 0$, (3) Defining $\mathcal{F}^{-1}$ as inverse Fourier transform. Then, the dynamic continuum function $\varphi(x,t)$ is illustrated as:

$$\begin{aligned}&L_2^t\frac{\partial^2\varphi(x,t)}{\partial x^2}+L_4^t\frac{\partial^4\varphi(x,t)}{\partial x^4}+L_6^t\frac{\partial^6\varphi(x,t)}{\partial x^6}+o\left(L_j^t\frac{\partial^j\varphi(x,t)}{\partial x^i}\right)-\overline{\Gamma}(x,t)\\&=\rho J\frac{\mathrm{d}^2\varphi(x,t)}{\mathrm{d}t^2},(j=8,10,...),\end{aligned} \tag{D.3}$$

with L_2^t, L_4^t, L_6^t, L_j^t are shown in Chapter 2.

Appendix E

The wave shapes in Chapter 3

The wave shapes at points A_1, A_2, A_3, A_4 B_1, B_2, B_3, B_4 C_1, C_2, C_3, C_4 are given:

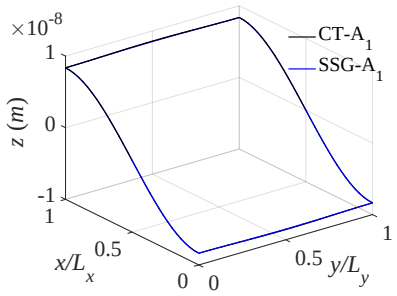

(a) A_1

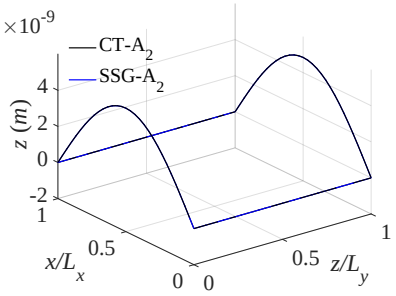

(b) A_2

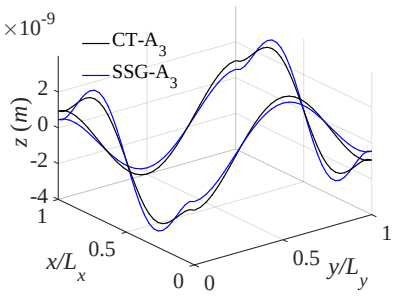

(c) A_3

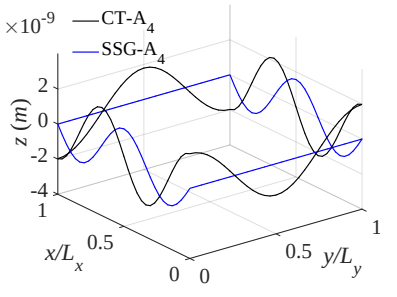

(d) A_4

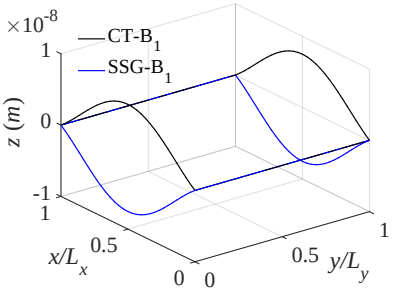

(e) B_1

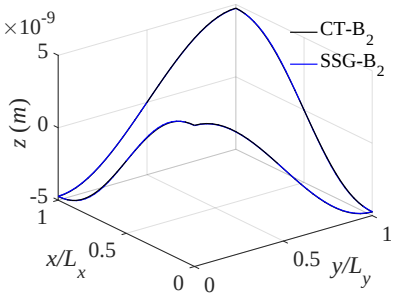

(f) B_2

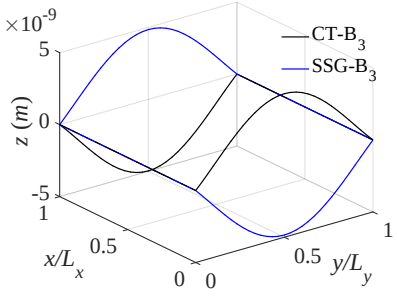

(g) B_3

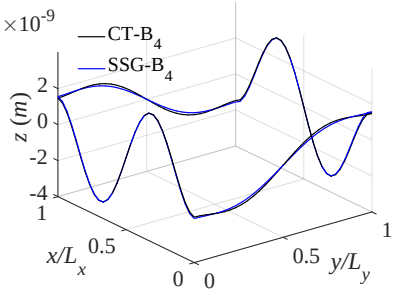

(h) B_4

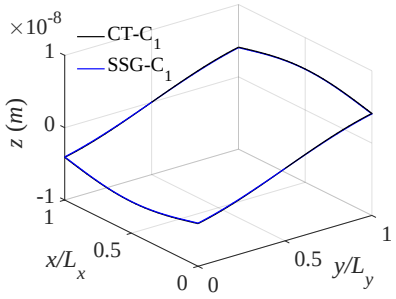

(i) C_1

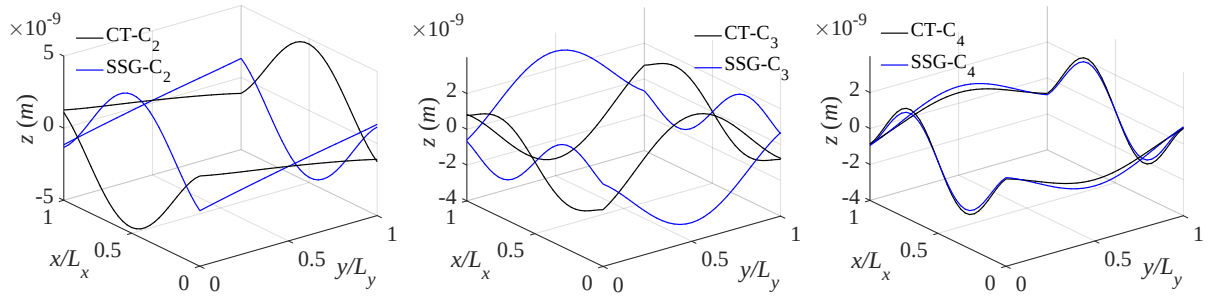

(j) C_2 (k) C_3 (l) C_4

Fig. E.1. Wave shapes on points A_i, B_i, and C_i (i=1,...,4). A_1 : $\omega_{SSG}/\omega_0 = 0.35$, $\omega_{CT}/\omega_0 = 0.34$. A_2 : $\omega_{SSG}/\omega_0 = 0.55$, $\omega_{CT}/\omega_0 = 0.46$. A_3 : $\omega_{SSG}/\omega_0 = 2.95$, $\omega_{CT}/\omega_0 = 2.47$. A_4 : $\omega_{SSG}/\omega_0 = 4.78$, $\omega_{CT}/\omega_0 = 4.00$. B_1 : $\omega_{SSG}/\omega_0 = 0.79$, $\omega_{CT}/\omega_0 = 0.69$. B_2 : $\omega_{SSG}/\omega_0 = 0.83$, $\omega_{CT}/\omega_0 = 0.69$. B_3 : $\omega_{SSG}/\omega_0 = 1.46$, $\omega_{CT}/\omega_0 = 1.23$. B_4 : $\omega_{SSG}/\omega_0 = 4.08$, $\omega_{CT}/\omega_0 = 3.41$. C_1 : $\omega_{SSG}/\omega_0 = 0.25$, $\omega_{CT}/\omega_0 = 0.21$. C_2 : $\omega_{SSG}/\omega_0 = 1.14$, $\omega_{CT}/\omega_0 = 0.95$. C_3 : $\omega_{SSG}/\omega_0 = 2.24$, $\omega_{CT}/\omega_0 = 1.87$. C_4 : $\omega_{SSG}/\omega_0 = 3.25$, $\omega_{CT}/\omega_0 = 2.72$.

Appendix F

Definition of matrices A, B and C in Chapter 4

The details of matrices $\mathbf{A}$, $\mathbf{B}$ and $\mathbf{C}$ are presented as:

$$\mathbf{A}_1 = \begin{bmatrix} \overline{a}_1 & \overline{a}_2 & \overline{a}_2 & \overline{a}_1 & \overline{a}_3 \\ \overline{a}_2 & \overline{a}_4 & 2a_3 & \overline{a}_5 & \frac{a_2}{2} \\ \overline{a}_2 & 2a_2 & \overline{a}_4 & \frac{a_2}{2} & \overline{a}_5 \\ \overline{a}_3 & \overline{a}_5 & \frac{a_2}{2} & \overline{a}_6 & \frac{a_1}{2} \\ \overline{a}_3 & \frac{a_2}{2} & \overline{a}_5 & \frac{a_1}{2} & \overline{a}_6 \end{bmatrix}, \mathbf{A}_2 = \begin{bmatrix} a_4 & \frac{a_5}{2} & \frac{a_5}{2} \\ \frac{a_5}{2} & a_4 & \frac{a_5}{2} \\ \frac{a_5}{2} & \frac{a_5}{2} & a_4 \end{bmatrix}, \mathbf{B}_{11} = \begin{bmatrix} \overline{b}_1 & 0 & 0 & 0 & 0 \\ 0 & \overline{b}_4 & 0 & \overline{b}_7 & 0 \\ 0 & 0 & \overline{b}_4 & 0 & \overline{b}_7 \\ 0 & \overline{b}_7 & 0 & \overline{b}_2 & 0 \\ 0 & 0 & \overline{b}_7 & 0 & \overline{b}_2 \end{bmatrix},$$

$$\mathbf{B}_{12} = \mathbf{B}_{21}^{\mathrm{T}} = \begin{bmatrix} \overline{b}_6 & 0 & \overline{b}_6 & 0 & 0 \\ 0 & 0 & 0 & \frac{2}{3}b_5 & 0 \\ 0 & \frac{2}{3}b_5 & 0 & 0 & 0 \\ 0 & 0 & 0 & \frac{\overline{b}_7}{3} & 0 \\ 0 & \frac{\overline{b}_7}{3} & 0 & 0 & 0 \end{bmatrix}, \mathbf{B}_{22} = \begin{bmatrix} \overline{b}_9 + \overline{b}_{11} & 0 & \overline{b}_{11} & 0 & 0 \\ 0 & \overline{b}_5 & 0 & 0 & 0 \\ \overline{b}_{11} & 0 & \overline{b}_9 + \overline{b}_{11} & 0 & 0 \\ 0 & 0 & 0 & \overline{b}_5 & 0 \\ 0 & 0 & 0 & 0 & \frac{\overline{b}_9}{2} \end{bmatrix},$$

$$\mathbf{B}_{33} = \begin{bmatrix} \overline{b}_4 & 0 & 0 & 0 & 0 \\ 0 & \overline{b}_1 & 0 & \frac{\overline{b}_6}{3} & 0 \\ 0 & 0 & \overline{b}_4 & 0 & \frac{2}{3}b_5 \\ 0 & \overline{b}_6 & 0 & \overline{b}_9 + \overline{b}_{11} & 0 \\ 0 & 0 & \frac{2}{3}b_5 & 0 & \overline{b}_5 \end{bmatrix},$$

$$\mathbf{B}_{34}=\mathbf{B}_{43}^{\mathrm{T}}=\begin{bmatrix} \overline{b}_7 & 0 & \frac{2}{3}b_5 & 0 & 0 \\ 0 & 0 & 0 & \frac{\overline{b}_6}{3} & 0 \\ 0 & \overline{b}_7 & 0 & 0 & 0 \\ 0 & 0 & 0 & \overline{b}_{11} & 0 \\ 0 & \frac{\overline{b}_7}{3} & 0 & 0 & 0 \end{bmatrix},\ \mathbf{B}_{44}=\begin{bmatrix} \overline{b}_2 & 0 & \frac{\overline{b}_7}{3} & 0 & 0 \\ 0 & \overline{b}_2 & 0 & 0 & 0 \\ \frac{\overline{b}_7}{3} & 0 & \overline{b}_1 & 0 & 0 \\ 0 & 0 & 0 & \overline{b}_9+\overline{b}_{11} & 0 \\ 0 & 0 & 0 & 0 & \frac{\overline{b}_9}{3} \end{bmatrix},$$

$$\mathbf{B}_{55}=\begin{bmatrix} \overline{b}_4 & 0 & 0 & 0 & 0 \\ 0 & \overline{b}_1 & 0 & \frac{2}{3}b_5 & 0 \\ 0 & 0 & \overline{b}_1 & 0 & \overline{b}_6 \\ 0 & \frac{2}{3}b_5 & 0 & \overline{b}_5 & 0 \\ 0 & 0 & \overline{b}_6 & 0 & \overline{b}_9+\overline{b}_{11} \end{bmatrix},\ \mathbf{B}_{66}=\begin{bmatrix} \overline{b}_5 & 0 & \frac{\overline{b}_7}{3} & 0 & 0 \\ 0 & \overline{b}_9+\overline{b}_{11} & 0 & 0 & 0 \\ \frac{\overline{b}_7}{3} & 0 & \overline{b}_2 & 0 & 0 \\ 0 & 0 & 0 & \overline{b}_2 & 0 \\ 0 & 0 & 0 & 0 & \frac{\overline{b}_9}{3} \end{bmatrix},$$

$$\mathbf{B}_{56}=\mathbf{B}_{65}^{\mathrm{T}}=\begin{bmatrix} \frac{2}{3}b_5 & 0 & \overline{b}_7 & 0 & 0 \\ 0 & 0 & 0 & \overline{b}_7 & 0 \\ 0 & \frac{\overline{b}_6}{3} & 0 & 0 & 0 \\ 0 & 0 & 0 & \frac{\overline{b}_7}{3} & 0 \\ 0 & \overline{b}_{11} & 0 & 0 & 0 \end{bmatrix},\ \mathbf{B}_{13}=\mathbf{B}_{31}^{\mathrm{T}}=\begin{bmatrix} 0 & 2b_1 & 0 & \overline{b}_{13} & 0 \\ 2b_4 & 0 & 0 & 0 & 0 \\ 0 & 0 & 0 & 0 & 0 \\ \overline{b}_{12} & 0 & 0 & 0 & 0 \\ 0 & 0 & 0 & 0 & 0 \end{bmatrix},$$

$$\mathbf{B}_{14}=\mathbf{B}_{41}^{\mathrm{T}}=\begin{bmatrix} 0 & 0 & 0 & \frac{2}{3}b_1 & 0 \\ \overline{b}_{12} & 0 & \frac{2}{3}b_4 & 0 & 0 \\ 0 & 0 & 0 & 0 & \frac{b_3}{6} \\ \overline{b}_{10} & 0 & \overline{b}_{17} & 0 & 0 \\ 0 & 0 & 0 & 0 & \overline{b}_{15} \end{bmatrix},\ \mathbf{B}_{23}=\mathbf{B}_{32}^{\mathrm{T}}=\begin{bmatrix} 0 & \overline{b}_{13} & 0 & \overline{b}_3 & 0 \\ 0 & 0 & 0 & 0 & 0 \\ 0 & \frac{2}{3}b_1 & 0 & \overline{b}_{16} & 0 \\ \frac{2}{3}b_4 & 0 & 0 & 0 & 0 \\ 0 & 0 & \frac{b_3}{6} & 0 & \overline{b}_{18} \end{bmatrix},$$

$$\mathbf{B}_{24}=\mathbf{B}_{42}^{\mathrm{T}}=\begin{bmatrix} 0 & 0 & 0 & \overline{b}_{16} & 0 \\ 0 & 0 & 0 & 0 & \overline{b}_{18} \\ 0 & 0 & 0 & \overline{b}_{19} & 0 \\ \overline{b}_{17} & 0 & \overline{b}_{14} & 0 & 0 \\ 0 & \overline{b}_{15} & 0 & 0 & 0 \end{bmatrix},\ \mathbf{B}_{15}=\mathbf{B}_{51}^{\mathrm{T}}=\begin{bmatrix} 0 & 0 & 2b_1 & 0 & \overline{b}_{13} \\ 0 & 0 & 0 & 0 & 0 \\ 2b_4 & 0 & 0 & 0 & 0 \\ 0 & 0 & 0 & 0 & 0 \\ \overline{b}_{12} & 0 & 0 & 0 & 0 \end{bmatrix},$$

$$\mathbf{B}_{16}=\mathbf{B}_{61}^{\mathrm{T}}=\begin{bmatrix} 0 & \frac{2}{3}b_1 & 0 & 0 & 0 \\ 0 & 0 & 0 & 0 & \frac{b_3}{6} \\ \frac{2}{3}b_4 & 0 & \overline{b}_{12} & 0 & 0 \\ 0 & 0 & 0 & 0 & \overline{b}_{15} \\ \overline{b}_{17} & 0 & \overline{b}_{10} & 0 & 0 \end{bmatrix},\ \mathbf{B}_{25}=\mathbf{B}_{52}^{\mathrm{T}}=\begin{bmatrix} 0 & 0 & \frac{2}{3}b_1 & 0 & \overline{b}_{16} \\ \frac{2}{3}b_4 & 0 & 0 & 0 & 0 \\ 0 & 0 & \overline{b}_{13} & 0 & \overline{b}_3 \\ 0 & 0 & 0 & 0 & 0 \\ 0 & \frac{b_3}{6} & 0 & \overline{b}_{18} & 0 \end{bmatrix},$$

$$\mathbf{B}_{26}=\mathbf{B}_{62}^{\mathrm{T}}=\begin{bmatrix} 0 & \overline{b}_{19} & 0 & 0 & 0 \\ \overline{b}_{14} & 0 & \overline{b}_{17} & 0 & 0 \\ 0 & \overline{b}_{16} & 0 & 0 & 0 \\ 0 & 0 & 0 & 0 & \overline{b}_{18} \\ 0 & 0 & 0 & \overline{b}_{15} & 0 \end{bmatrix},\ \mathbf{B}_{35}=\mathbf{B}_{53}^{\mathrm{T}}=\begin{bmatrix} 0 & 0 & 0 & 0 & 0 \\ 0 & 0 & 2b_1 & 0 & \frac{2}{3}b_1 \\ 0 & 2b_4 & 0 & \frac{2}{3}b_4 & 0 \\ 0 & 0 & \frac{4}{3}b_1 & 0 & \overline{b}_{19} \\ 0 & \frac{2}{3}b_4 & 0 & \overline{b}_{14} & 0 \end{bmatrix},$$

$$\mathbf{B}_{36}=\mathbf{B}_{63}^{\mathrm{T}}=\begin{bmatrix} 0 & 0 & 0 & 0 & \frac{b_3}{6} \\ 0 & \overline{b}_{13} & 0 & 0 & 0 \\ 0 & 0 & 0 & \overline{b}_{12} & 0 \\ 0 & \overline{b}_{16} & 0 & 0 & 0 \\ 0 & 0 & 0 & \overline{b}_{17} & 0 \end{bmatrix},\ \mathbf{B}_{45}=\mathbf{B}_{54}^{\mathrm{T}}=\begin{bmatrix} 0 & 0 & 0 & 0 & 0 \\ 0 & \overline{b}_{12} & 0 & \overline{b}_{17} & 0 \\ 0 & 0 & 0 & 0 & 0 \\ 0 & 0 & \overline{b}_{13} & 0 & \overline{b}_{16} \\ \frac{b_3}{6} & 0 & 0 & 0 & 0 \end{bmatrix},$$

$$\mathbf{B}_{45}=\mathbf{B}_{54}^{\mathrm{T}}=\begin{bmatrix} 0 & 0 & 0 & 0 & \overline{b}_{15} \\ 0 & 0 & 0 & \overline{b}_{10} & 0 \\ 0 & 0 & 0 & 0 & \overline{b}_{18} \\ 0 & \overline{b}_3 & 0 & 0 & 0 \\ \overline{b}_{18} & 0 & \overline{b}_{15} & 0 & 0 \end{bmatrix},\ \mathbf{C}_1=\begin{bmatrix} \overline{c}_1 & 0 & 0 & 0 & 0 \\ c_1 & 0 & 0 & 0 & 0 \\ c_1 & 0 & 0 & 0 & 0 \\ 0 & 0 & 0 & 0 & 0 \\ 0 & 0 & \frac{c_3}{2} & 0 & \overline{c}_3 \\ 0 & \frac{c_3}{2} & 0 & \overline{c}_3 & 0 \end{bmatrix},$$

$$\mathbf{C}_2=\begin{bmatrix} \overline{c}_2 & 0 & \overline{c}_2 & 0 & 0 \\ \overline{c}_2 & 0 & c_1 & 0 & 0 \\ c_1 & 0 & \overline{c}_2 & 0 & 0 \\ 0 & 0 & 0 & 0 & \frac{c_2}{6} \\ 0 & \frac{c_3}{2} & 0 & 0 & 0 \\ 0 & 0 & 0 & \frac{c_3}{2} & 0 \end{bmatrix},\ \mathbf{C}_3=\begin{bmatrix} 0 & c_1 & 0 & \overline{c}_4 & 0 \\ 0 & \overline{c}_1 & 0 & \overline{c}_2 & 0 \\ 0 & c_1 & 0 & c_1 & 0 \\ 0 & 0 & \frac{c_3}{2} & 0 & \frac{c_3}{2} \\ 0 & 0 & 0 & 0 & 0 \\ \frac{c_3}{2} & 0 & 0 & 0 & 0 \end{bmatrix},$$

$$\mathbf{C}_4 = \begin{bmatrix} 0 & 0 & 0 & c_1 & 0 \\ 0 & 0 & 0 & \overline{c}_2 & 0 \\ 0 & 0 & 0 & \overline{c}_2 & 0 \\ 0 & \overline{c}_3 & 0 & 0 & 0 \\ 0 & 0 & 0 & 0 & \dfrac{c_2}{6} \\ 0 & 0 & \dfrac{c_3}{2} & 0 & 0 \end{bmatrix}, \mathbf{C}_5 = \begin{bmatrix} 0 & 0 & c_1 & 0 & \overline{c}_4 \\ 0 & 0 & c_1 & 0 & c_1 \\ 0 & 0 & \overline{c}_1 & 0 & \overline{c}_2 \\ 0 & \dfrac{c_3}{2} & 0 & \dfrac{c_3}{2} & 0 \\ \dfrac{c_3}{2} & 0 & 0 & 0 & 0 \\ 0 & 0 & 0 & 0 & 0 \end{bmatrix},$$

$$\mathbf{C}_6 = \begin{bmatrix} 0 & c_1 & 0 & 0 & 0 \\ 0 & \overline{c}_4 & 0 & 0 & 0 \\ 0 & \overline{c}_4 & 0 & 0 & 0 \\ 0 & 0 & 0 & \overline{c}_3 & 0 \\ \dfrac{c_3}{2} & 0 & \overline{c}_3 & 0 & 0 \\ 0 & 0 & 0 & 0 & \dfrac{c_2}{6} \end{bmatrix},$$

where $\overline{a}_1$=$2(a_1 + a_2 + a_3 + a_4 + a_5)$, $\overline{a}_2$=$a_2 + 2a_3$, $\overline{a}_3$=$\dfrac{2a_1 + a_2}{2}$, $\overline{a}_4$=$2(a_3 + a_4)$, $\overline{a}_5$=$\dfrac{a_2 + 2a_5}{2}$, $\overline{a}_6$=$\dfrac{a_1 + 2a_4 + a_5}{2}$, $\overline{b}_1$=$2(b_1+b_2+b_3+b_4+b_5+b_6+b_7)$, $\overline{b}_2$=$\dfrac{2}{9}(2b_2+b_3+b_5+3b_6+2b_7)$, $\overline{b}_3$=$\dfrac{2}{9}(b_1+b_3+2b_7)$, $\overline{b}_4$=$2(b_5+b_6)$, $\overline{b}_5$=$\dfrac{2}{9}(b_5+3b_6)$, $\overline{b}_6$=$(2b_1+b_3+2b_4+2b_5)/3$, $\overline{b}_7$=$\dfrac{b_3 + 2b_5}{3}$, $\overline{b}_8$=$\dfrac{2}{3}(b_1+b_2+b_3+b_4+b_5)$, $\overline{b}_9$=$\dfrac{2}{9}(b_2+3b_6+b_7)$, $\overline{b}_{10}$=$\dfrac{2}{9}(2b_2+b_3+b_4)$, $\overline{b}_{11}$=$\dfrac{2}{9}(b_1+b_4+b_5)$, $\overline{b}_{12}$=$\dfrac{b_3 + 2b_4 + 2b_7}{3}$, $\overline{b}_{13}$=$\dfrac{2b_1 + 2b_2 + b_3}{3}$, $\overline{b}_{14}$=$\dfrac{2}{9}(b_4 + b_7)$, $\overline{b}_{15}$=$\dfrac{4b_2 + b_3}{18}$, $\overline{b}_{16}$=$\dfrac{2b_1 + b_3}{9}$, $\overline{b}_{17}$=$\dfrac{b_3 + 2b_4}{9}$, $\overline{b}_{18}$=$\dfrac{b_3 + 4b_7}{18}$, $\overline{b}_{19}$=$\dfrac{2}{9}(b_1 + b_2)$, $\overline{c}_1$=$c_1 + c_2 + c_3$, $\overline{c}_2$=$\dfrac{c_1 + c_3}{3}$, $\overline{c}_3$=$\dfrac{2c_2 + c_3}{6}$, $\overline{c}_4$=$\dfrac{c_1 + c_2}{3}$.

List of Figures

1.1 Periodically positioned nano-sized Silicon resonators [5]. 6
1.2 Nano-coatings for aerospace materials [6]. 6
1.3 A unit cell in the 2D periodic structure and its first Brillouin zone. 7
1.4 Structures of different sizes and the size effects. 9
1.5 Existing methods to study micro-sized structures. 9
1.6 Geometry of Euler–Bernoulli nano-beam. 18
1.7 Schematic drawing of a simple one-dimensional "toy-model". The black bonds represent bulk pair potentials with equilibrium spacing, a. The red bonds represent surface pair potentials with equilibrium spacing, b. The blue bonds are at right angles to the atomic planes and force the surface and bulk spacing to be equal. 22
1.8 Discrete mass-spring system with stiffness k_1^l and k_2^l, the mass M and the distance d corresponds to the lattice model with the nearest-neighbor and next-nearest-neighbor interactions. 23
1.9 Diagrams of sets of operations for differential equations. 24
1.10 Periodic structure constituted by k unit cell. 29
1.11 2D periodic structure and its unit cells. 31

2.1 A Euler-Bernoulli beam under Lateral distributed force. 40
2.2 Definition of nodal DOFs, nodal numbers and coordinate for 1D. 43
2.3 Sketch of a LSM beam. 44
2.4 A torsional bar under torque. 47
2.5 Definition of node numbering, nodal DOFs and coordinate for 1D 48
2.6 LSM for a torsional bar with torsional coupling constants k_1^t (red line: nearest-neighbor interaction), k_2^t (blue line: next-nearest-neighbor interaction) and k_3^t (green line: next-next-nearest-neighbor interaction). 49
2.7 One-dimensional structures' configurations. 51
2.8 Dispersion relation for single material Euler-Bernoulli beam by SSG ($\omega_{\mathrm{b}1}$ is the first nature frequency, subscript c of SSG means continuum model, l is lattice model). 52

2.9 Comparison of dispersion relation between SSG and CT and reverse SSG to CT (subscript a of SSG means analytical method, l is lattice model). 52
2.10 Forced response for single material Euler-Bernoulli beam by CT and SSG (subscript c means continuum model, l is lattice model). 53
2.11 Dispersion relation for periodic Euler-Bernoulli beam by SSG (subscript c of SSG means continuum model, l is lattice model). 53
2.12 Comparison of dispersion relation between SSG and CT and reverse SSG to CT (subscript l of SSG means lattice model). 54
2.13 Forced response for periodic Euler-Bernoulli beam by CT and SSG (subscript c of SSG means continuum model, l denotes lattice model). 54
2.14 Dispersion relation for single material torsional bar by SSG ($\omega_{\mathrm{t}1} = \pi\sqrt{G/4\rho L^2}$ [214] is the first nature frequency, subscript c of SSG means continuum model, l is lattice model). 55
2.15 Comparison of dispersion relation between SSG and CT and reverse SSG to CT (subscript a means analytical method and l is lattice model). 56
2.16 Forced response of single material torsional bar by CT and SSG (subscript c and l of SSG denote continuum model and lattice model, respectively). 56
2.17 Dispersion relation for periodic torsional bar by SSG (subscript c is continuum model, l is lattice model). 57
2.18 Comparison of dispersion relation between SSG and CT and reverse SSG to CT (subscript l of SSG means lattice model). 57
2.19 Forced response by CT and SSG (subscript c means continuum model and l is lattice model). 57

3.1 Sketch of 2D beam grid and displacements at position x on a branch of the unit cell (displacement w along z direction, angle θ in $x0z$ plane and angle φ in $y0z$ plane, $\hat{\mathbf{u}}_{1,2,3}$ is corner DOFs, $\hat{\mathbf{u}}_{\mathrm{I}}$ is internal DOFs). 60
3.2 Graphical representation for analysing continuum model vibration. 61
3.3 A unit cell by LSM with coupling relations. Red line denotes the nearest neighbor interaction, blue line means the next-nearest neighbor interaction and green line represents the next-next-nearest neighbor interaction. d is the distance between two nodes and the mass $M = \rho Ad$. z axis is perpendicular to $x0y$ plane. 61
3.4 Graphical representation for analyzing LSM vibration. 62
3.5 Two nodes fourteen DOFs in an element. 63
3.6 Band structure, validation and convergence. 66
3.7 The first four slowness surfaces by SSG and CT. 67
3.8 The iso-frequency contour of first four slowness surfaces by SSG and CT. . . . 68
3.9 Energy flow vector fields by SSG and CT on the first four slowness surfaces. . . 69

3.10 Direction of wave propagation on the 1st slowness surface (ω increases from the center of the polar image to the edge, ψ is the range of free wave propagation under a considered frequency, frequency rang: 0-0.5). 70
3.11 Direction of wave propagation on the 2nd slowness surface (ω increases from the center of the polar image to the edge, ψ is the range of free wave propagation under a considered frequency, frequency rang: 0.5-1.5). 70
3.12 Direction of wave propagation on the 3rd slowness surface (ω increases from the center of the polar image to the edge, ψ is the range of free wave propagation under a considered frequency, frequency rang: 1.5-2.5). 71
3.13 Direction of wave propagation on the 4th slowness surface (ω increases from the center of the polar image to the edge, ψ is the range of free wave propagation under a considered frequency, frequency rang: 2.5-3.5). 71
3.14 Harmonic displacement field when $\omega/\omega_0 = 0.08$. 72
3.15 Harmonic displacement field when $\omega/\omega_0 = 0.9$. 72
3.16 Harmonic displacement field when $\omega/\omega_0 = 1.9$. 73
3.17 Harmonic displacement field when $\omega/\omega_0 = 2.9$. 73
3.18 Normalized forced response contours by SSG and CT (ω/ω_0=1.9, z/z_c=0.1). . . 74
3.19 The points on band structure for studying wave shapes. 74
3.20 Wave shapes on points O_1, O_2, O_3 and O_4 ($\kappa_x = 0$, $\kappa_y = 0$). 75

4.1 Definition of node numbers, nodal DOFs for 1D and 3D Hermite elements with C^2 continuity. 80
4.2 Two coupled waveguides through a coupling element. 82
4.3 Finite element model. (a): two waveguides coupled by a coupling element, (b): a unit cell k/k+1, (c): a simple coupling element, (d): a complex coupling element. 86
4.4 Dispersion relation of unit cell k by SSG and CT. 87
4.5 Effects of higher order parameters for bending. 89
4.6 Effects of higher order parameters for tension. 90
4.7 Absolute values of diffusion coefficients by SSG and CT (the material of coupling element is Cu, unit cell k and k+1 are Al). 91
4.8 Absolute values of diffusion coefficients (the materials of coupling element, unit cell k and k+1 are Al). 92
4.9 Absolute values of diffusion coefficients (coupling element is Cu, unit cell k and k+1 are Al). 93
4.10 Forced response of waveguide 1 by SSG and CT. 93
4.11 Bending modes (real part) by SSG and CT. 94
4.12 Tension modes (real part) by SSG and CT. 95

5.1 A 2D full plate and its unit cells. 103

5.2 Dispersion relation from WFEM2D direct form ($\theta' = 0$, 1: bending, 2: shearing, 3: tension). 104
5.3 Band structure from WFEM2D inverse form (red lines: first three modes from WFEM2D direct form, 1: bending, 2: shearing, 3: tension). 104
5.4 Dispersion relation by CI method (1: bending with $\theta'= 10°$, 2: bending with $\theta'= 30°$, 3: bending with $\theta'= 60°$, 4: shearing with $\theta'= 10°$, 5: shearing with $\theta'= 30°$, 6: shearing with $\theta'= 60°$, 7: tension with $\theta'= 10°$, 8: tension with $\theta'= 30°$, 9: tension with $\theta'= 60°$). 105
5.5 The first three slowness surfaces in the first quadrant by CT and SSG. 106
5.6 The iso-frequency contours by CT and SSG. 107
5.7 The energy flow vector fields by CT and SSG. 108
5.8 Transmission loss of the 2D full plate ($\theta^* = 45°, \phi^* = 0$). 108
5.9 The general scheme of SA method. The total variance of output is apportioned to the various input factors. 109
5.10 Mean value $\pm$ standard deviation. 112
5.11 NSD (ratio of standard deviation to mean value). 112
5.12 Sensitivity analysis of a_i for bending. 113
5.13 Sensitivity analysis of b_i for bending. 113
5.14 Sensitivity analysis of c_i for bending. 114
5.15 Sensitivity analysis of a_i for tension. 114
5.16 Sensitivity analysis of b_i for tension. 115
5.17 Sensitivity analysis of c_i for tension. 115
5.18 Sensitivity analysis of a_i for shearing. 116
5.19 Sensitivity analysis of b_i for shearing. 116
5.20 Sensitivity analysis of c_i for shearing. 117

E.1 Wave shapes on points A_i, B_i, and C_i (i=1,...,4). $A_1 : \omega_{SSG}/\omega_0 = 0.35$, $\omega_{CT}/\omega_0 = 0.34$. $A_2 : \omega_{SSG}/\omega_0 = 0.55, \omega_{CT}/\omega_0 = 0.46$. $A_3 : \omega_{SSG}/\omega_0 = 2.95$, $\omega_{CT}/\omega_0 = 2.47$. $A_4 : \omega_{SSG}/\omega_0 = 4.78, \omega_{CT}/\omega_0 = 4.00$. $B_1 : \omega_{SSG}/\omega_0 = 0.79$, $\omega_{CT}/\omega_0 = 0.69$. $B_2 : \omega_{SSG}/\omega_0 = 0.83, \omega_{CT}/\omega_0 = 0.69$. $B_3 : \omega_{SSG}/\omega_0 = 1.46$, $\omega_{CT}/\omega_0 = 1.23$. $B_4 : \omega_{SSG}/\omega_0 = 4.08, \omega_{CT}/\omega_0 = 3.41$. $C_1 : \omega_{SSG}/\omega_0 = 0.25$, $\omega_{CT}/\omega_0 = 0.21$. $C_2 : \omega_{SSG}/\omega_0 = 1.14, \omega_{CT}/\omega_0 = 0.95$. $C_3 : \omega_{SSG}/\omega_0 = 2.24$, $\omega_{CT}/\omega_0 = 1.87$. $C_4 : \omega_{SSG}/\omega_0 = 3.25, \omega_{CT}/\omega_0 = 2.72$. 132

List of Tables

2.1 Higher order material parameters a_i (eV/Å), c_i (eV/Å). 40
2.2 Higher order material parameters b_i (eV·Å). 41

4.1 Effects of higher order parameters to real and imaginary part of bending (ω/ω_0=30). 89
4.2 Effects of higher order parameters to real and imaginary part of tension (ω/ω_0=30). 90

5.1 Set of integer frequencies ω_i for 14, 15 and 16 parameters with M=4 (n is parameters number). 111
5.2 Sampling bounds for inputs. 111

Bibliography

[1] R. S. Langley, The response of two-dimensional periodic structures to point harmonic forcing, Journal of Sound and Vibration 197 (1996) 447–469.

[2] A. C. Eringen, D. G. B. Edelen, On nonlocal elasticity, International Journal of Engineering Science 10 (1972) 233–248.

[3] R. E. Miller, V. B. Shenoy, Size-dependent elastic properties of nano-sized structural elements, Nanotechnology 11 (3) (2000) 139.

[4] C. W. Lim, L. H. He, Size-dependent nonlinear response of thin elastic films with nano-scale thickness, International Journal of Solids and Structures 46 (11) (2004) 15–26.

[5] Z. J. Yang, R. B. Jiang, X. L. Zhuo, Y. M. Xie, J. F. Wang, H. Q. Lin, Dielectric nanoresonators for light manipulation, Physics Reports 701 (2017) 1–50.

[6] S. Jose, Expanding role in the field of surface protection supported by continuous technology innovations to spur opportunities for the growth of nanocoatings, Nanocoating-Market Analysis, Trends, and Forecasts (2018) 202.

[7] H. Askes, E. C. Aifantis, Gradient elasticity in statics and dynamics: an overview of formulations, length scale identification procedures, finite element implementations and new results, International Journal of Solids and Structures 48 (2012) 1962–1990.

[8] S. Momeni, M. Asghari, The second strain gradient functionally graded beam formulation, Composite Structures 188 (2018) 15–24.

[9] G. Zhu, C. Droz, A. M. Zine, M. N. Ichchou, Wave propagation analysis for a second strain gradient rod theory, Chinese Journal of Aeronautics (2019). doi:10.1016/j.cja.2019.10.006.

[10] B. I. Halperin, Quantized hall conductance, current-carrying edge states, and the existence of extended states in a two-dimensional disordered potential, Physical review B 25 (4) (1982) 2185.

[11] B. A. Bernevig, T. L. Hughes, S. C. Zhang, Quantum spin hall effect and topological phase transition in hgte quantum wells, Science 314 (5806) (2006) 57–61.

[12] F. Bloch, Uber die quantenmechanik der elektronen in kristallgittern, Zeitschrift fur Physik 52 (1929) 555–600.

[13] L. Brillouin, Propagation in periodic structures, Dover Publication, New York, 1953, Ch. Torsional vibration of shafts, pp. 11–35.

[14] M. I. Hussein, M. Leamy, M. Ruzzene, Dynamics of phononic materials and structures: historical origins, recent progress, and future outlook, Applied Mechanics Reviews 66 (2014) 10–11.

[15] M. Lazar, G. A. Maugin, E. C. Aifantis, Dislocation in second strain gradient elasticity, International Journal of Solids and Structures (2006) 1787–1817.

[16] R. D. Mindlin, Second gradient of strain and surface tension in linear elasticity, International Journal of Solids and Structures (1965) 147–438.

[17] F. Yang, A. C. M. Chong, D. C. C. Lam, P. Tong, Couple stress based strain gradient theory for elasticity, International Journal of Solids and Structures 10 (2002) 2731–2743.

[18] A. Eringen, Simple microfluids, International Journal of Engineering Science 2 (1964) 205–217.

[19] A. Eringen, Linear theory of micropolar elasticity, Journal of Applied Mathematics and Mechanics 15 (1966) 909–923.

[20] E. Kroner, Elasticity theory of materials with long range cohesive forces, International Journal of Solids and Structures 3 (1967) 731–742.

[21] A. C. Eringen, Vistas of nonlocal continuum physics, International Journal of Engineering 30 (1992) 1551–1565.

[22] M. Z. Nejad, A. Hadi, Neringen's non-local elasticity theory for bending analysis of bi-directional functionally graded euler–bernoulli nano-beams, International Journal of Engineering Science 106 (2016).

[23] M. E. Gurtin, A. I. Murdoch, A continuum theory of elastic material surfaces, Archive for Rational Mechanics and Analysis 57 (4) (1975) 291–323.

[24] J. Hamilton, J. Hamilton, Theories of surface elasticity for nanoscale objects, Surface Science 603 (2009) 1284–1291.

[25] R. Toupin, Elastic materials with couple-stresses, Archive for rational mechanics and analysis 11 (1) (1962) 385–414.

[26] M. Najafzadeh, M. M. Adeli, E. Zarezadeh, A. Hadi, Torsional vibration of the porous nanotube with an arbitrary cross-section based on couple stress theory under magnetic field, Mechanics Based Design of Structures and Machines (2020) 1–15.

[27] Z. WANG, Y. LI, W. BAI, Numerical modelling and analysis for elastic wave equations in the frame of the couple stress theory, Chinese Journal of Geophysics 64 (5) (2021) 1721–1732.

[28] H. Fan, L. Xu, Love wave in a classical linear elastic half-space covered by a surface layer described by the couple stress theory, Acta Mechanica 229 (12) (2018) 5121–5132.

[29] H. Shodja, A. Goodarzi, M. Delfani, H. Haftbaradaran, Scattering of an anti-plane shear wave by an embedded cylindrical micro-/nano-fiber within couple stress theory with micro inertia, International Journal of Solids and Structures 58 (2015) 73–90.

[30] B. Ghodrati, A. Yaghootian, A. Ghanbar Zadeh, H. Mohammad-Sedighi, Lamb wave extraction of dispersion curves in micro/nano-plates using couple stress theories, Waves in Random and Complex media 28 (1) (2018) 15–34.

[31] A. Nobili, V. Volpini, C. Signorini, Antiplane stoneley waves propagating at the interface between two couple stress elastic materials, Acta Mechanica 232 (3) (2021) 1207–1225.

[32] M. Espo, M. H. Abolbashari, S. M. Hosseini, Band structure analysis of wave propagation in piezoelectric nano-metamaterials as periodic nano-beams considering the small scale and surface effects, Acta Mechanica 231 (2020) 2877–2893.

[33] C. Liu, J. Yu, W. Xu, X. Zhang, B. Zhang, Theoretical study of elastic wave propagation through a functionally graded micro-structured plate base on the modified couple-stress theory, Meccanica 55 (5) (2020) 1153–1167.

[34] M. A. Khorshidi, Validation of weakening effect in modified couple stress theory: dispersion analysis of carbon nanotubes, International Journal of Mechanical Sciences 170 (2020) 105358.

[35] D. Soltani, M. Akbarzadeh Khorshidi, H. M. Sedighi, Higher order and scale-dependent micro-inertia effect on the longitudinal dispersion based on the modified couple stress theory, Journal of Computational Design and Engineering 8 (1) (2021) 189–194.

[36] B. Alizadeh Hamidi, F. Khosravi, S. A. Hosseini, R. Hassannejad, Free torsional vibration of triangle microwire based on modified couple stress theory, The Journal of Strain Analysis for Engineering Design 55 (7-8) (2020) 237–245.

[37] B. Karami, M. Janghorban, A. Tounsi, Variational approach for wave dispersion in anisotropic doubly-curved nanoshells based on a new nonlocal strain gradient higher order shell theory, Thin-Walled Structures 129 (2018) 251–264.

[38] M. Hosseini, H. H. Gorgani, M. Shishesaz, A. Hadi, Size-dependent stress analysis of single-wall carbon nanotube based on strain gradient theory, International Journal of Applied Mechanics 9 (06) (2017) 1750087.

[39] V. A. Eremeyev, G. Rosi, S. Naili, Comparison of anti-plane surface waves in strain-gradient materials and materials with surface stresses, Mathematics and mechanics of solids 24 (8) (2019) 2526–2535.

[40] A. Norouzzadeh, R. Ansari, H. Rouhi, Nonlinear wave propagation analysis in timoshenko nano-beams considering nonlocal and strain gradient effects, Meccanica 53 (13) (2018) 3415–3435.

[41] Y. Yang, J. Wang, Y. Yu, Wave propagation in fluid-filled single-walled carbon nanotube based on the nonlocal strain gradient theory, Acta Mechanica Solida Sinica 31 (4) (2018) 484–492.

[42] H. M. Shodja, F. Ahmadpoor, T. A., Calculation of the additional constants for fcc materials in second strain gradient elasticity: behavior of a nano-size bernoulli-euler beam with surface effects, Applied Mechanics 72 (2) (2010) 021008.

[43] M. Ghazavi, H. Molki, et al., Nonlinear analysis of the micro/nanotube conveying fluid based on second strain gradient theory, Applied Mathematical Modelling 60 (2018) 77–93.

[44] J. Torabi, R. Ansari, M. Bazdid-Vahdati, M. Darvizeh, Second strain gradient finite element analysis of vibratory nanostructures based on the three-dimensional elasticity theory, Iranian Journal of Science and Technology, Transactions of Mechanical Engineering 44 (3) (2020) 631–645.

[45] S. Khakalo, J. Niiranen, Form ii of mindlin's second strain gradient theory of elasticity with a simplification: For materials and structures from nano-to macro-scales, European Journal of Mechanics-A/Solids 71 (2018) 292–319.

[46] B. Babu, B. Patel, A new computationally efficient finite element formulation for nanoplates using second-order strain gradient kirchhoff's plate theory, Composites Part B: Engineering 168 (2019) 302–311.

[47] M. Delfani, S. Shojaeimanesh, V. Bagherpour, Effective shear modulus of functionally graded fibrous composites in second strain gradient elasticity, Journal of Elasticity 137 (1) (2019) 43–62.

[48] A. Eringen, Simple microfluids. int, Journal of Engng. Sci 2 (1964).

[49] A. C. Eringen, Linear theory of micropolar elasticity, Journal of Mathematics and Mechanics (1966) 909–923.

[50] A. C. Eringen, Micropolar fluids with stretch, International Journal of Engineering Science 7 (1) (1969) 115–127.

[51] E. Ogam, Z. E. A. Fellah, M. Fellah, C. Depollier, Theoretical and experimental study of micropolar elastic materials using acoustic waves in air, Journal of Sound and Vibration (2021) 116298.

[52] K. K. Kalkal, D. Sheoran, S. Deswal, Reflection of plane waves in a nonlocal micropolar thermoelastic medium under the effect of rotation, Acta Mechanica 231 (2020) 2849–2866.

[53] A. K. Yadav, Reflection of plane waves in a micropolar thermo-diffusion porous medium, Waves in Random and Complex Media (2021) 1–23.

[54] J. Kishine, A. Ovchinnikov, A. Tereshchenko, Chirality-induced phonon dispersion in a noncentrosymmetric micropolar crystal, Physical Review Letters 125 (24) (2020) 245302.

[55] M. Varygina, Numerical modeling of wave propagation in multilayered micropolar cylinder shells, in: AIP Conference Proceedings, Vol. 2302, AIP Publishing LLC, 2020, p. 090005.

[56] A. Chirilă, M. Marin, Wave propagation in diffusive microstretch thermoelasticity, Mathematics and Computers in Simulation 189 (2021) 99–113.

[57] B. Singh, A. Yadav, The effect of diffusion on propagation and reflection of waves in a thermo-microstretch solid half-space, Computational Mathematics and Modeling 32 (2021) 221–234.

[58] K. Lotfy, A. A. El-Bary, M. Allan, M. H. Ahmed, Generalized thermal microstretch elastic solid with harmonic wave for mode-i crack problem, Archives of Thermodynamics 41 (2020).

[59] G. Zhang, X.-L. Gao, C. Zheng, C. Mi, A non-classical bernoulli-euler beam model based on a simplified micromorphic elasticity theory, Mechanics of Materials 161 (2021) 103967.

[60] M. V. d'Agostino, G. Barbagallo, I.-D. Ghiba, B. Eidel, P. Neff, A. Madeo, Effective description of anisotropic wave dispersion in mechanical band-gap metamaterials via the relaxed micromorphic model, Journal of elasticity 139 (2020) 299–329.

[61] V. A. Eremeyev, L. P. Lebedev, M. J. Cloud, Acceleration waves in the nonlinear micromorphic continuum, Mechanics Research Communications 93 (2018) 70–74.

[62] E. A. C., Linear theory of nonlocal elasticity and dispersion of plane waves, International Journal of Engineering Science 10 (1973) 425–435.

[63] B. Arash, R. Ansari, Evaluation of nonlocal parameter in the vibrations of single-walled carbon nanotubes with initial strain, Phys E 42 (2010) 2058–64.

[64] W. Duan, N. Challamel, C. Wang, Z. Ding, Development of analytical vibration solutions for microstructured beam model to calibrate length scale coefficient in nonlocal timoshenko beams, Journal of Applied Physics 114 (2013) 104312.

[65] L. Huang, Q. Han, Y. Liang, Calibration of nonlocal scale effect parameter for bending single-layered graphene sheet under molecular dynamics, Nano 7 (2012) 3–8.

[66] J. Peddieson, G. Buchanan, R. McNitt, Application of nonlocal continuum models to nanotechnology, International Journal of Engineering Science 41 (2003) 305–12.

[67] L. Sudak, Column buckling of multiwalled carbon nanotubes using nonlocal continuum mechanics, Journal of Applied Physics 94 (2003) 7281–7.

[68] R. Moheimani, H. Dalir, Static and dynamic solutions of functionally graded micro/nanobeams under external loads using non-local theory, Vibration 3 (2) (2020) 51–69.

[69] I. Ghaffari, M. P. Yaghoobi, M. Ghannad, Complete mechanical behavior analysis of fg nano beam under non-uniform loading using non-local theory, Materials Research Express 5 (1) (2018) 015016.

[70] T. Bensattalah, M. Zidour, M. A. A. Meziane, T. H. Daouadji, A. Tounsi, Critical buckling load of carbon nanotube with non-local timoshenko beam using the differential transform method, International Journal of Civil and Environmental Engineering 12 (6) (2018) 637–644.

[71] S. A. Faghidian, On non-linear flexure of beams based on non-local elasticity theory, International Journal of Engineering Science 124 (2018) 49–63.

[72] H. Bourouina, R. Yahiaoui, R. Kerid, K. Ghoumid, I. Lajoie, F. Picaud, G. Herlem, The influence of hole networks on the adsorption-induced frequency shift of a perforated nanobeam using non-local elasticity theory, Journal of Physics and Chemistry of Solids 136 (2020) 109201.

[73] G. Alotta, M. Di Paola, G. Failla, F. P. Pinnola, On the dynamics of non-local fractional viscoelastic beams under stochastic agencies, Composites Part B: Engineering 137 (2018) 102–110.

[74] S. Vantadori, R. Luciano, D. Scorza, H. Darban, Fracture analysis of nanobeams based on the stress-driven non-local theory of elasticity, Mechanics of Advanced Materials and Structures (2020) 1–10.

[75] Z. Rahimi, W. Sumelka, X.-J. Yang, Linear and non-linear free vibration of nano beams based on a new fractional non-local theory, Engineering Computations (2017).

[76] Y. Wang, L. Bian, M. Gao, A non-local modeling for the influence of fluid forces on vibration characteristics of carbon nanotubes, Materials Science and Engineering: B 272 (2021) 115348.

[77] F. He, D. Qian, M. Zhai, Wave propagation in a non-local piezoelectric phononic crystal timoshenko nanobeam, Modern Physics Letters B 35 (03) (2021) 2150064.

[78] K. Rakrak, M. Zidour, H. Heireche, A. A. Bousahla, A. Chemi, Free vibration analysis of chiral double-walled carbon nanotube using non-local elasticity theory, Advances in nano research 4 (1) (2016) 031.

[79] A. Belhadj, A. Boukhalfa, S. A. Belalia, Carbon nanotube structure vibration based on non-local elasticity, Journal of Modern Materials 3 (1) (2017) 9–13.

[80] M. Arefi, Surface effect and non-local elasticity in wave propagation of functionally graded piezoelectric nano-rod excited to applied voltage, Applied Mathematics and Mechanics 37 (3) (2016) 289–302.

[81] M. Ö. Yayli, Torsional vibration analysis of nanorods with elastic torsional restraints using non-local elasticity theory, Micro and Nano Letters 13 (5) (2018) 595–599.

[82] P. Lu, P. Zhang, H. Lee, C. Wang, J. Reddy, Non-local elastic plate theories, Proceedings of the Royal Society A: Mathematical, Physical and Engineering Sciences 463 (2088) (2007) 3225–3240.

[83] B. Karami, D. Shahsavari, M. Janghorban, R. Dimitri, F. Tornabene, Wave propagation of porous nanoshells, Nanomaterials 9 (1) (2019) 22.

[84] S. Gopalakrishnan, Propagation of elastic waves in nanostructures, in: Nanosensors, Biosensors, and Info-Tech Sensors and Systems 2016, Vol. 9802, International Society for Optics and Photonics, 2016, p. 98020N.

[85] A. Cherednichenko, I. Y. Savelyeva, A. Shukhtin, Uniaxial tension of a two-dimensional plate, taking into account non-local effects, in: AIP Conference Proceedings, Vol. 2293, AIP Publishing LLC, 2020, p. 210003.

[86] W. Sumelka, Non-local kirchhoff–love plates in terms of fractional calculus, Archives of Civil and Mechanical Engineering 15 (1) (2015) 231–242.

[87] A. Madeo, P. Neff, I.-D. Ghiba, G. Rosi, Reflection and transmission of elastic waves in non-local band-gap metamaterials: a comprehensive study via the relaxed micromorphic model, Journal of the Mechanics and Physics of Solids 95 (2016) 441–479.

[88] M. Z. Nejad, A. Hadi, A. Omidvari, A. Rastgoo, Bending analysis of bi-directional functionally graded euler-bernoulli nano-beams using integral form of eringen's non-local elasticity theory, Structural engineering and mechanics: An international journal 67 (4) (2018) 417–425.

[89] M. E. Gurtin, A. I. Murdoch, A continuum theory of elastic material surfaces, Archive for rational mechanics and analysis 57 (4) (1975) 291–323.

[90] V. A. Eremeyev, G. Rosi, S. Naili, Transverse surface waves on a cylindrical surface with coating, International Journal of Engineering Science 147 (2020) 103188.

[91] M. Arefi, A. M. Zenkour, Employing the coupled stress components and surface elasticity for nonlocal solution of wave propagation of a functionally graded piezoelectric love nanorod model, Journal of Intelligent Material Systems and Structures 28 (17) (2017) 2403–2413.

[92] V. Eremeyev, Strongly anisotropic surface elasticity and antiplane surface waves, Philosophical Transactions of the Royal Society A 378 (2020) 20190100.

[93] L. Li, R. Lin, T. Y. Ng, Contribution of nonlocality to surface elasticity, International Journal of Engineering Science 152 (2020) 103311.

[94] B. Xie, S. Sahmani, B. Safaei, B. Xu, Nonlinear secondary resonance of fg porous silicon nanobeams under periodic hard excitations based on surface elasticity theory, Engineering with Computers 37 (2021) 1611–1634.

[95] B. Yang, C. Droz, A. M. Zine, M. N. Ichchou, Dynamic analysis of second strain gradient elasticity through a wave finite element approach, Composite Structures 263 (2021) 113425.

[96] D. De Domenico, H. Askes, E. C. Aifantis, Gradient elasticity and dispersive wave propagation: model motivation and length scale identification procedures in concrete and composite laminates, International Journal of Solids and Structures 158 (2019) 176–190.

[97] R. G. Nannapaneni, K. B. Nakshatrala, D. Stefaniuk, K. J. Krakowiak, Discrete lattice modeling of wave propagation in materials with heterogeneous microstructures, Journal of Engineering Mechanics 147 (10) (2021) 04021075.

[98] N. Liu, L.-Y. Fu, G. Tang, Y. Kong, X.-Y. Xu, Modified lsm for size-dependent wave propagation: Comparison with modified couple stress theory, Acta Mechanica 231 (4) (2020) 1285–1304.

[99] S. Sahmani, A. M. Fattahi, N. Ahmed, Develop a refined truncated cubic lattice structure for nonlinear large-amplitude vibrations of micro/nano-beams made of nanoporous materials, Engineering with Computers 36 (1) (2020) 359–375.

[100] J. Vila, J. Fernández-Sáez, R. Zaera, Nonlinear continuum models for the dynamic behavior of 1d microstructured solids, International Journal of Solids and Structures 117 (2017) 111–122.

[101] J. Wang, W. Zhou, Y. Huang, C. Lyu, W. Chen, W. Zhu, Controllable wave propagation in a weakly nonlinear monoatomic lattice chain with nonlocal interaction and active control., Applied Mathematics and Mechanics 39 (8) (2018).

[102] M. Song, W. Zhu, Elastic wave propagation in strongly nonlinear lattices and its active control, Journal of Applied Mechanics 88 (7) (2021) 071003.

[103] J. Hamilton, W. Wolfer, Theories of surface elasticity for nanoscale objects, Surface Science 603 (9) (2009) 1284–1291.

[104] V. A. Eremeyev, B. L. Sharma, Anti-plane surface waves in media with surface structure: Discrete vs. continuum model, International Journal of Engineering Science 143 (2019) 33–38.

[105] D. Karličić, M. Cajić, T. Chatterjee, S. Adhikari, Wave propagation in mass embedded and pre-stressed hexagonal lattices, Composite Structures 256 (2021) 113087.

[106] J. C. Hamilton, W. G. Wolfer, Theories of surface elasticity for nanoscale objects, Surface Science 603 (2009) 1284–1291.

[107] V. Tarasov, Lattice model with nearest-neighbor and next-nearest-neighbor interactions for gradient elasticity, Discontinuity, Nonlinearity, and Complexity 4 (2015) 11–23.

[108] F. Gómez-Silva, R. Zaera, Low order nonstandard continualization of a beam lattice with next-nearest interactions: Enhanced prediction of the dynamic behavior, Mechanics of Advanced Materials and Structures (2021) 1–15.

[109] G. Zhu, A. Zine, C. Droz, M. Ichchou, Wave transmission and reflection analysis through complex media based on the second strain gradient theory, European Journal of Mechanics-A/Solids (2021) 104326.

[110] V. E. Tarasov, Continuous limit of discrete systems with long-range interaction, Journal of Physics A 48 (39) (2006) 14895–14910.

[111] M. Feyzollahzadeh, M. Bamdad, A modified transfer matrix method to reduce the calculation time: A case study on beam vibration, Applied Mathematics and Computation 378 (2020) 125238.

[112] J.-M. Mencik, M. Ichchou, Multi-mode propagation and diffusion in structures through finite elements, European Journal of Mechanics A/Solids 24 (2005) 877—-898.

[113] V. Cotoni, R. Langley, P. Shorter, A statistical energy analysis subsystem formulation using finite element and periodic structure theory, Journal of Sound and Vibration 318 (2008) 1077–1108.

[114] S. Nemat-Nasser, T. Iwakuma, M. Hejazi, On composites with periodic structure, Mechanics of materials 1 (3) (1982) 239–267.

[115] V. F. Dal Poggetto, A. L. Serpa, Elastic wave band gaps in a three-dimensional periodic metamaterial using the plane wave expansion method, International Journal of Mechanical Sciences 184 (2020) 105841.

[116] V. F. Dal Poggetto, A. L. Serpa, Flexural wave band gaps in a ternary periodic metamaterial plate using the plane wave expansion method, Journal of Sound and Vibration 495 (2021) 115909.

[117] E. Riva, J. Marconi, G. Cazzulani, F. Braghin, Generalized plane wave expansion method for non-reciprocal discretely modulated waveguides, Journal of Sound and Vibration 449 (2019) 172–181.

[118] L. Xie, B. Xia, J. Liu, G. Huang, J. Lei, An improved fast plane wave expansion method for topology optimization of phononic crystals, International Journal of Mechanical Sciences 120 (2017) 171–181.

[119] A. Mock, Asymmetric band structure calculations using the plane wave expansion method with time-modulated permittivity, in: 2018 International Applied Computational Electromagnetics Society Symposium (ACES), IEEE, 2018, pp. 1–2.

[120] L. Han, Y. Zhang, Z.-Q. Ni, Z.-M. Zhang, L.-H. Jiang, A modified transfer matrix method for the study of the bending vibration band structure in phononic crystal euler beams, Physica B: Condensed Matter 407 (23) (2012) 4579–4583.

[121] M. Feyzollahzadeh, M. Bamdad, A modified transfer matrix method to reduce the calculation time: A case study on beam vibration, Applied Mathematics and Computation 378 (2020) 125238.

[122] M. Yang, X. Zhou, W. Zhang, J. Ye, Y. Hu, A modified transfer matrix method for bending vibration of cfrp/steel composite transmission shafting, Archive of Applied Mechanics 90 (3) (2020) 603–614.

[123] Y. Waki, B. Mace, M. Brennan, Free and forced vibrations of a tyre using a wave/finite element approach, Journal of Sound and Vibration 323 (3-5) (2009) 737–756.

[124] W. Zhou, M. Ichchou, Wave propagation in mechanical waveguide with curved members using wave finite element solution, Computer Methods in Applied Mechanics and Engineering 199 (33-36) (2010) 2099–2109.

[125] J. M. Renno, B. R. Mace, On the forced response of waveguides using the wave and finite element method, Journal of Sound and Vibration 329 (26) (2010) 5474–5488.

[126] A. Søe-Knudsen, S. Sorokin, On accuracy of the wave finite element predictions of wavenumbers and power flow: A benchmark problem, Journal of Sound and Vibration 330 (12) (2011) 2694–2700.

[127] F. Bouchoucha, M. N. Ichchou, M. Haddar, Diffusion matrix through stochastic wave finite element method, Finite Elements in Analysis and Design 64 (2013) 97–107.

[128] C. Droz, M. Ichchou, J. Lainé, Numerical prediction of dispersion characteristics for high-order waves in composite waveguides, in: Proceedings of the International Conference on Noise and Vibration Engineering, ISMA2014, 2014, pp. 4203–4216.

[129] J. M. Renno, B. R. Mace, Vibration modelling of structural networks using a hybrid finite element/wave and finite element approach, Wave Motion 51 (4) (2014) 566–580.

[130] C. Droz, J.-P. Lainé, M. Ichchou, G. Inquiété, A reduced formulation for the free-wave propagation analysis in composite structures, Composite Structures 113 (2014) 134–144.

[131] M. Kharrat, M. Ichchou, O. Bareille, W. Zhou, Pipeline inspection using a torsional guided-waves inspection system. part 2: Defect sizing by the wave finite element method, International Journal of Applied Mechanics 6 (04) (2014) 1450035.

[132] C. Droz, M. Ichchou, J.-P. Lainé, High-order wave propagation in multi-directional composite laminates, International Conference on Advances in Composite Materials and Structures (2015).

[133] A. Bhuddi, M.-L. Gobert, J.-M. Mencik, On the acoustic radiation of axisymmetric fluid-filled pipes using the wave finite element (wfe) method, Journal of Computational Acoustics 23 (03) (2015) 1550011.

[134] C. Zhou, J. Lainé, M. Ichchou, A. Zine, Multi-scale modelling for two-dimensional periodic structures using a combined mode/wave based approach, Computers and Structures 154 (2015) 145–162.

[135] C. Droz, C. Zhou, M. Ichchou, J.-P. Lainé, A hybrid wave-mode formulation for the vibro-acoustic analysis of 2d periodic structures, Journal of Sound and Vibration 363 (2016) 285–302.

[136] Y. Fan, M. Collet, M. Ichchou, L. Li, O. Bareille, Z. Dimitrijevic, Energy flow prediction in built-up structures through a hybrid finite element/wave and finite element approach, Mechanical Systems and Signal Processing 66 (2016) 137–158.

[137] E. Nobrega, F. Gautier, A. Pelat, J. Dos Santos, Vibration band gaps for elastic metamaterial rods using wave finite element method, Mechanical Systems and Signal Processing 79 (2016) 192–202.

[138] C. Droz, Z. Zergoune, R. Boukadia, O. Bareille, M. Ichchou, Vibro-acoustic optimisation of sandwich panels using the wave/finite element method, Composite Structures 156 (2016) 108–114.

[139] C. Droz, O. Bareille, M. N. Ichchou, A new procedure for the determination of structural characteristics of sandwich plates in medium frequencies, Composites Part B: Engineering 112 (2017) 103–111.

[140] Z. Zergoune, M. Ichchou, O. Bareille, B. Harras, R. Benamar, B. Troclet, Assessments of shear core effects on sound transmission loss through sandwich panels using a two-scale approach, Computers and Structures 182 (2017) 227–237.

[141] Y. Fan, M. Collet, M. Ichchou, L. Li, O. Bareille, Z. Dimitrijevic, Enhanced wave and finite element method for wave propagation and forced response prediction in periodic piezoelectric structures, Chinese Journal of Aeronautics 30 (1) (2017) 75–87.

[142] D. Chronopoulos, C. Droz, R. Apalowo, M. Ichchou, W. Yan, Accurate structural identification for layered composite structures, through a wave and finite element scheme, Composite Structures 182 (2017) 566–578.

[143] T. Gras, M.-A. Hamdi, M. B. Tahar, O. Tanneau, L. Beaubatie, On a coupling between the finite element (fe) and the wave finite element (wfe) method to study the effect of a local heterogeneity within a railway track, Journal of Sound and Vibration 429 (2018) 45–62.

[144] R. Boukadia, C. Claeys, C. Droz, M. Ichchou, E. Deckers, Model order reduction in unit cell modeling and its application to complex structures, in: Proceedings of the International Conference on Noise and Vibration Engineering, ISMA2018, 2018, pp. 4663–4678.

[145] T. Hoang, D. Duhamel, G. Forêt, J.-L. Pochet, F. Sabatier, Wave finite element method and moving loads for the dynamic analysis of railway tracks, in: 13th World Congress on Computational Mechanics (WCCM XIII), 2018, pp. 25–28.

[146] E. J. P. d. Miranda, J. M. C. D. Santos, Flexural wave band gaps in phononic crystal euler-bernoulli beams using wave finite element and plane wave expansion methods, Materials Research 20 (2018) 729–742.

[147] J. Hong, X. He, D. Zhang, B. Zhang, Y. Ma, Vibration isolation design for periodically stiffened shells by the wave finite element method, Journal of Sound and Vibration 419 (2018) 90–102.

[148] G. Tufano, C. Droz, O. Bareille, A. Zine, B. Pluymers, W. Desmet, M. Ichchou, Wavenumber identification technique for axial-symmetric structures, in: Proceedings of the International Conference on Noise and Vibration Engineering, ISMA2018, 2018, pp. 4627–4636.

[149] J.-M. Mencik, A wave finite element approach for the analysis of periodic structures with cyclic symmetry in dynamic substructuring, Journal of Sound and Vibration 431 (2018) 441–457.

[150] C. Droz, R. Boukadia, M. Ichchou, W. Desmet, Diffusion-based design of locally resonant sub-systems using a reduced wave finite element framework, in: Proceedings of the International Conference on Noise and Vibration Engineering, ISMA2018, 2018, p. e400.

[151] B. Lossouarn, M. Aucejo, J.-F. Deü, Electromechanical wave finite element method for interconnected piezoelectric waveguides, Computers and Structures 199 (2018) 46–56.

[152] E. Manconi, S. Sorokin, R. Garziera, A. Soe-Knudsen, Wave motion and stop-bands in pipes with helical characteristics using wave finite element analysis, Journal of Applied and Computational Mechanics 4 (Special Issue: Applied and Computational Issues in Structural Engineering) (2018) 420–428.

[153] C. Droz, O. Bareille, J.-P. Lainé, M. N. Ichchou, Wave-based shm of sandwich structures using cross-sectional waves, Structural Control and Health Monitoring 25 (2) (2018) e2085.

[154] M. Mallouli, M. B. Souf, O. Bareille, M. Ichchou, T. Fakhfakh, M. Haddar, Transient wave scattering and forced response analysis of damaged composite beams through a hybrid finite element-wave based method, Finite Elements in Analysis and Design 147 (2018) 1–9.

[155] M. Mirzajani, N. Khaji, M. Hori, Stress wave propagation analysis in one-dimensional micropolar rods with variable cross-section using micropolar wave finite element method, International Journal of Applied Mechanics 10 (04) (2018) 1850039.

[156] V. Thierry, L. Brown, D. Chronopoulos, Multi-scale wave propagation modelling for two-dimensional periodic textile composites, Composites Part B: Engineering 150 (2018) 144–156.

[157] R. Singh, C. Droz, S. De Rosa, F. Franco, O. Bareille, M. Ichchou, A study of structured uncertainties in wave characteristic of one-dimensional periodic structures, in: Proceedings of ISMA2018 International Conference on Noise and Vibration Engineering, 2018, pp. 4731–4740.

[158] R. F. Boukadia, C. Droz, M. N. Ichchou, W. Desmet, A bloch wave reduction scheme for ultrafast band diagram and dynamic response computation in periodic structures, Finite Elements in Analysis and Design 148 (2018) 1–12.

[159] J. Guo, Y. Xiao, S. Zhang, J. Wen, Bloch wave based method for dynamic homogenization and vibration analysis of lattice truss core sandwich structures, Composite Structures 229 (2019) 111437.

[160] F. Errico, M. Ichchou, F. Franco, S. De Rosa, O. Bareille, C. Droz, Schemes for the sound transmission of flat, curved and axisymmetric structures excited by aerodynamic and acoustic sources, Journal of Sound and Vibration 456 (2019) 221–238.

[161] C. Droz, O. Robin, M. Ichchou, N. Atalla, Improving sound transmission loss at ring frequency of a curved panel using tunable 3d-printed small-scale resonators, The Journal of the Acoustical Society of America 145 (1) (2019) EL72–EL78.

[162] M. J. Kingan, Y. Yang, B. R. Mace, Sound transmission through cylindrical structures using a wave and finite element method, Wave Motion 87 (2019) 58–74.

[163] C. Droz, O. Bareille, M. N. Ichchou, Generation of long-range, near-cut-on guided resonances in composite panels, Journal of Applied Physics 125 (17) (2019) 175109.

[164] C. Droz, O. Bareille, M. Ichchou, Data on full wave-field measurement of transient guided resonance pulses propagating in a composite structure, Data in brief 26 (2019) 104481.

[165] G. Tufano, F. Errico, O. Robin, C. Droz, M. Ichchou, B. Pluymers, W. Desmet, N. Atalla, K-space analysis of complex large-scale meta-structures using the inhomogeneous wave correlation method, Mechanical Systems and Signal Processing 135 (2020) 106407.

[166] R. Singh, C. Droz, M. Ichchou, F. Franco, O. Bareille, S. De Rosa, Stochastic wave finite element quadratic formulation for periodic media: 1d and 2d, Mechanical Systems and Signal Processing 136 (2020) 106431.

[167] C. Droz, R. Boukadia, E. Deckers, W. Desmet, Sub-wavelength damage detectability assessment in periodic assemblies using a bloch modelling framework, Proceedings of the XI International Conference on Structural Dynamics, EURODYN2020 (2020).

[168] A. Palermo, A. Marzani, A reduced bloch operator finite element method for fast calculation of elastic complex band structures, International Journal of Solids and Structures 191 (2020) 601–613.

[169] T. Hoang, D. Duhamel, G. Foret, Wave finite element method for waveguides and periodic structures subjected to arbitrary loads, Finite Elements in Analysis and Design 179 (2020) 103437.

[170] C. Boutin, P. Fossat, C. Droz, M. Ichchou, Dynamics of ribbed plates with inner resonance: Analytical homogenized models and experimental validation, European Journal of Mechanics-A/Solids 79 (2020) 103838.

[171] R. F. Boukadia, E. Deckers, C. Claeys, M. Ichchou, W. Desmet, A wave-based optimization framework for 1d and 2d periodic structures, Mechanical Systems and Signal Processing 139 (2020) 106603.

[172] S. Ahsani, R. Boukadia, C. Droz, C. Claeys, E. Deckers, W. Desmet, Diffusion based homogenization method for 1d wave propagation, Mechanical Systems and Signal Processing 136 (2020) 106515.

[173] W. Chai, A. Saidi, A. Zine, C. Droz, W. You, M. Ichchou, Comparison of uncertainty quantification process using statistical and data mining algorithms, Structural and Multidisciplinary Optimization 61 (2) (2020) 587–598.

[174] N. Guenfoud, C. Droz, M. N. Ichchou, O. Bareille, E. Deckers, W. Desmet, On the multiscale vibroacoustic behavior of multi-layer rectangular core topology systems, Mechanical Systems and Signal Processing 143 (2020) 106629.

[175] Y. Yang, C. Fenemore, M. J. Kingan, B. R. Mace, Analysis of the vibroacoustic characteristics of cross laminated timber panels using a wave and finite element method, Journal of Sound and Vibration 494 (2021) 115842.

[176] C. Droz, R. Boukadia, W. Desmet, A multi-scale model order reduction scheme for transient modelling of periodic structures, Journal of Sound and Vibration (2021) 116312.

[177] C. Wang, X. Yao, G. Wu, L. Tang, Vibration band gap characteristics of two-dimensional periodic double-wall grillages, Materials 14 (23) (2021) 7174.

[178] F. Qu, L. Van Belle, R. Boukadia, C. Claeys, E. Deckers, W. Desmet, Comparison between the wave finite element and shift cell operator method for calculating dispersion diagrams of periodic metamaterial structures, in: 2021 Fifteenth International Congress on Artificial Materials for Novel Wave Phenomena (Metamaterials), IEEE, 2021, pp. 353–355.

[179] B. Yang, C. Droz, A. Zine, M. Ichchou, Dynamic analysis of second strain gradient elasticity through a wave finite element approach, Composite Structures 263 (2021) 113425.

[180] R. F. Boukadia, C. Claeys, C. Droz, M. Ichchou, W. Desmet, E. Deckers, An inverse convolution method for wavenumber extraction (income): Formulations and applications, Journal of Sound and Vibration 520 (2022) 116586.

[181] A. Kessemtini, M. Taktak, M. Haddar, A reduced finite element model for sound propagation in straight and slowly varying cross section ducts, Finite Elements in Analysis and Design 201 (2022) 103692.

[182] W. Wang, Y. Fan, L. Li, Extending zhong-williams scheme to solve repeated-root wave modes, Journal of Sound and Vibration 519 (2022) 116584.

[183] D. Duhamel, J.-M. Mencik, Time response analysis of periodic structures via wave-based absorbing boundary conditions, European Journal of Mechanics-A/Solids 91 (2022) 104418.

[184] D. Mead, A general theory of harmonic wave propagation in linear periodic systems with multiple coupling, Journal of Sound and Vibration 27 (1973) 235–260.

[185] X. Xie, H. Zheng, S. Jonckheere, W. Desmet, Acoustic simulation of cavities with porous materials using an adaptive model order reduction technique, Journal of Sound and Vibration 485 (2020) 115570.

[186] V. Pereyra, Model order reduction with oblique projections for large scale wave propagation, Journal of Computational and Applied Mathematics 295 (2016) 103–114.

[187] V. Thierry, O. Mesnil, D. Chronopoulos, Experimental and numerical determination of the wave dispersion characteristics of complex 3d woven composites, Ultrasonics 103 (2020) 106068.

[188] R. Li, J. Yao, L. Wang, C. Jiang, F. Wu, N. Hu, A novel gap element for the coupling of incompatible interface in component mode synthesis method, International Journal of Computational Methods 17 (07) (2020) 1950033.

[189] M. Liu, D. Cao, D. Zhu, Coupled vibration analysis for equivalent dynamic model of the space antenna truss, Applied Mathematical Modelling 89 (2021) 285–298.

[190] M. M. Neves, H. Rodrigues, J. M. Guedes, Optimal design of periodic linear elastic microstructures, Computers and Structures 76 (1-3) (2000) 421–429.

[191] A. Gad, X.-L. Gao, K. Li, A strain energy-based homogenization method for 2-d and 3-d cellular materials using the micropolar elasticity theory, Composite Structures 265 (2021) 113594.

[192] P. Suttakul, T. Fongsamootr, Numerical study on bending response of auxetic 2d-lattice plates, in: IOP Conference Series: Materials Science and Engineering, Vol. 1137, IOP Publishing, 2021, p. 012025.

[193] M.-J. Jhung, J.-C. Jo, Equivalent material properties of perforated plate with triangular or square penetration pattern for dynamic analysis, Nuclear engineering and technology 38 (7) (2006) 689–696.

[194] D. Chronopoulos, B. Troclet, O. Bareille, M. Ichchou, Modeling the response of composite panels by a dynamic stiffness approach, Composite Structures 96 (2013) 111–120. doi:https://doi.org/10.1016/j.compstruct.2012.08.047.

[195] F. Errico, M. Ichchou, S. De Rosa, O. Bareille, F. Franco, The modelling of the flow-induced vibrations of periodic flat and axial-symmetric structures with a wave-based method, Journal of Sound and Vibration 424 (2018) 32–47.

[196] Y. Wang, X. Li, J. Li, Q. Wang, B. Xu, J. Deng, Debonding damage detection of the cfrp-concrete interface based on piezoelectric ceramics by the wave-based method, Construction and Building Materials 210 (2019) 514–524.

[197] T. Liu, A. Wang, Q. Wang, B. Qin, Wave based method for free vibration characteristics of functionally graded cylindrical shells with arbitrary boundary conditions, Thin-Walled Structures 148 (2020) 106580.

[198] L. Liu, F. Ripamonti, R. Corradi, Z. Rao, The modified weighted residual formulation in the wave based method for plate bending problems: A general formulation for different types of edge restraints, Journal of Sound and Vibration 511 (2021) 116329.

[199] A. L. Kalamkarov, E. M. Hassan, A. Georgiades, M. Savi, Asymptotic homogenization model for 3d grid-reinforced composite structures with generally orthotropic reinforcements, Composite structures 89 (2) (2009) 186–196.

[200] F. Fantoni, A. Bacigalupo, Wave propagation modeling in periodic elasto-thermo-diffusive materials via multifield asymptotic homogenization, International Journal of Solids and Structures 196 (2020) 99–128.

[201] D. Préve, A. Bacigalupo, M. Paggi, Variational-asymptotic homogenization of thermoelastic periodic materials with thermal relaxation, International Journal of Mechanical Sciences (2021) 106566.

[202] I. I. Andrianov, I. V. Andrianov, G. A. Starushenko, E. I. Borodin, Higher order asymptotic homogenization for dynamical problems, Mathematics and Mechanics of Solids (2021) 10812865211053035.

[203] A. Bacigalupo, M. L. De Bellis, G. Zavarise, Asymptotic homogenization approach for anisotropic micropolar modeling of periodic cauchy materials, Computer Methods in Applied Mechanics and Engineering 388 (2022) 114201.

[204] S. Khakalo, J. Niiranen, Form ii of mindlin's second strain gradient theory of elasticity with a simplification: For materials and structures from nano- to macro-scales, European Journal of Mechanics / A Solids 71 (2018) 292–319.

[205] M. Asghari, S. A. Momeni, R. Vatankhah, The second strain gradient theory-based timoshenko beam model, Journal of Vibration and Control 23 (13) (2015) 2155–2166.

[206] S. A. Momeni, M. Asghari, The second strain gradient functionally graded beam formulation, Composite Structures 188 (2018) 15–24.

[207] M. Attar, A. Karrech, K. Regenauer Lieb, Non-linear analysis of beam-like structures on unilateral foundations: A lattice spring model, International Journal of Solids and Structures 88 (2016) 192–214.

[208] V. E. Tarasov, Lattice with long-range interaction of power-law type for fractional non-local elasticity, International Journal of Solids and Structures 51 (2014) 2900–2907.

[209] H. Askes, E. C. Aifantis, Gradient elasticity in statics and dynamics: An overview of formulations, length scale identification procedures, finite element implementations and new results, International Journal of Solids and Structures 48 (2011) 1962–1990.

[210] C. Droz, J. P. Lainé, M. N. Ichchou, G. Inquiété, A reduced formulation for the free-wave propagation analysis in composite structures, Composite Structures 113 (2014) 134–144.

[211] V. Serey, N. Quaegebeur, P. Micheau, P. Masson, M. Castaings, M. Renier, Selective generation of ultrasonic guided waves in a bi-dimensional waveguide, Structural Health Monitoring 18 (2019) 1324–1336.

[212] B. R. Mace, D. Duhamel, M. J. Brennan, L. Hinke, Finite element prediction of wave motion in structural waveguides, Journal of the Acoustical Society of America 117 (2005) 2835–2843.

[213] M. Avcar, Free vibration analysis of beams considering different geometric characteristics and boundary conditions, International Journal of Mechanics and Applications 4 (3) (2014) 94–100.

[214] S. S. Rao, Vibration of continuous systems, Wiley, New Jersey, 2007, Ch. Torsional vibration of shafts, pp. 280–282.

[215] J. M. Mencik, M. N. Ichchou, Wave finite elements in guided elastodynamics with internal fluid, International Journal of Solids and Structures 44 (2007) 2148–2167.

[216] O. A. Kandil, E. F. Sheta, Coupled and uncoupled bending-torsion response of twin-tail buffet, Journal of Fluids and Structures 12 (1998) 677–701.

[217] J. Q. Zhao, P. Zeng, B. Pan, Improved hermite finite element smoothing method for full-field strain measurement over arbitrary region of interest in digital image correlation, Optics and Lasers in Engineering 50 (2012) 1662–1671.

[218] I. Bennamia, A. Badereddine, T. Zebbiche, Measurement of vibrations of composite wings using high-order finite element beam, Journal of Measurements in Engineering 6 (2018) 143–154.

[219] C. Droz, C. Zhou, M. N. Ichchou, J. P. Lainé, A hybrid wave-mode formulation for the vibro-acoustic analysis of 2d periodic structures, Journal of Sound and Vibration 363 (2016) 285–303.

[220] C. Zhou, J. Lainé, M. Ichchou, A. Zine, Multi-scale modelling for two-dimensional periodic structures using a combined mode/wave based approach, Computers and Structures 154 (2015) 145–162.

[221] R. S. Langley, On the modal density and energy flow characteristics of periodic structures, Journal of Sound and Vibration 2 (1994) 491–511.

[222] N. S. Bardell, The application of symbolic computing to the hierarchical finite element method, International Journal of Numerical Methods in Engineering 28 (1989) 1181–1204.

[223] A. M. Dehrouyeh-Semnani, M. Nikkhah-Bahrami, The influence of size-dependent shear deformation on mechanical behavior of microstructures-dependent beam based on modified couple stress theory, Composite Structures 123 (2015) 325–336.

[224] M. Ruzzene, F. Scarpa, F. Soranna, Wave beaming effects in two-dimensional cellular structures, Smart Materials and Structures 12 (2003) 363–372.

[225] C. Droz, R. F. Boukadia, M. Ichchou, W. Desmet, Diffusion-based design of locally resonant sub-systems using a reduced wave finite element framework, Proceedings of ISMA-International Conference on Noise and Vibration Engineering (2018) 3071–3083.

[226] K. Graff, Wave Motion in Elastic Solids, Oxford University Press, London, 1991, Ch. Longitudinal waves in the rods, pp. 75–130.

[227] S. Ahsani, R. Boukadia, C. Droz, C. Claeys, E. Deckers, W. Desmet, Diffusion based homogenization method for 1d wave propagation, Mechanical Systems and Signal Processing (2020). doi:10.1016/j.ymssp.2019.106515.

[228] G. Zhu, A. Zine, C. Droz, M. Ichchou, Wave transmission and reflection analysis through complex media based onthe second strain gradient theory, European Journal of Mechanics / A Solids (2021). doi:10.1016/j.euromechsol.2021.104326.

[229] J. Madeira, A. Araújo, C. Soares, C. Soares, Multiobjective optimization of viscoelastic laminated sandwich structures using the direct multisearch method, Computers Structures 147 (2015) 229–235.

[230] Y. Song, L. Feng, J. Wen, D. Yu, X. Wen, Reduction of the sound transmission of a periodic sandwich plate using the stop band concept, Computers Structures 128 (2015) 428–436.

[231] B. Clarkson, M. Ranky, Modal density of honeycomb plates, Journal of Sound and Vibration 91 (1983) 103–118.

[232] U. Arasan, F. Chevillotte, G. Tanner, On the accuracy limits of plate theories for vibro-acoustic predictions, Journal of Sound and Vibration (2020). doi:10.1016/j.jsv.2020.115848.

[233] J. H. Schaibly, K. E. Shuler, Study of the sensitivity of coupled reaction systems to uncertainties in rate coefficients. ii. applications, The Journal of Chemical Physics 59 (1973) 3873–3878.

[234] I. M. Sobol, Sensitivity analysis for nonlinear mathematical models, Mathematical Modeling and Computational Experiment 1 (1993) 407–414.

[235] A. Saltelli, S. Tarantola, K. P. S. Chan, A quantitative model-independent method for global sensitivity analysis of model output, Technometrics 41 (1999) 39–56.

[236] C. M. F. R. I. Cukier, K. E. Shuler, A. G. Petschek, J. H. Schaibly, Study of the sensitivity of coupled reaction systems to uncertainties in rate coefficients. i. theory, The Journal of Chemical Physics 59 (1973) 3873–3878.

[237] W. Chai, J.-L. Christen, A.-M. Zine, M. Ichchou, Sensitivity analysis of a sound absorption model with correlated inputs, Journal of Sound and Vibration 394 (2017) 75–89.

[238] D. Duhamel, B. R. Mace, M. Brennan, Finite element analysis of the vibrations of waveguides and periodic structures, Journal of Sound and Vibration 294 (2006) 205–220.

dernière page de la thèse

AUTORISATION DE SOUTENANCE

Vu les dispositions de l'arrêté du 25 mai 2016,

Vu la demande des directeurs de thèse

Messieurs M. ICHCHOU et A. ZINE

et les rapports de

M. M-A. HAMDI
Professeur - UTC - Laboratoire Roberval - Rue du docteur Schweitzer - CS 60319
60203 COMPIEGNE cedex

et de

M. N. KACEM
Maître de Conférences HDR - FEMTO ST - Mécanique Appliquée (UFC) - 24 rue de l'Epitaphe
25000 BESANCON

Monsieur YANG Bo

est autorisé à soutenir une thèse pour l'obtention du grade de **DOCTEUR**

Ecole doctorale Mécanique, Energétique, Génie civil, Acoustique

Fait à Ecully, le 22 avril 2022

Pour le directeur de l'Ecole centrale de Lyon
Le directeur des Formations

Grégory VIAL

ECOLE CENTRALE DE LYON
Service Scolarité
ECULLY